Development of Co-Fe Based Nanostructured Soft Magnetic Materials For High Temperature Applications

Thesis submitted in partial fulfillment of the requirement for the degree of

Doctor of Philosophy

By

OJASWINI MOHANTA

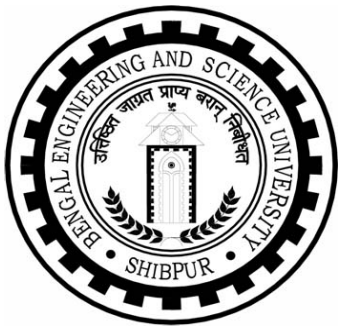

Department of Metallurgy & Materials Engineering
Bengal Engineering and Science University,
Shibpur, Howrah-711103
West Bengal, India

May 2010

Dedicated to my
Parents

Contents

Acknowledgements

I would like to express my deep and sincere gratitude to my supervisors, Dr. Amitava Basu Mallick, Prof. & Head of the Department of Metallurgy & Materials Engineering, Bengal Engineering & Science University, Shibpur, Howrah and Dr. Amitava Mitra, Scientist, National Metallurgical Laboratory, CSIR, Jamshedpur for the continuous support of my Ph.D. study and research. Their wide knowledge and logical way of thinking have been of great value for me. Their understanding, encouraging and personal guidance have provided a good basis for the present thesis.

I would like to thank Prof. S. P. Mehrotra (Ex-Director, National Metallurgical Laboratory, Jamshedpur) for kindly granting me permission to register for the Ph.D. Programme. I am thankful to the Head, (Dept. of Metallurgy & Materials Engineering, BESU, Shibpur, Howrah) and Head, (MST Division, N.M.L., Jamshedpur) for kindly providing me the administrative support during the Ph.D. Programme.

I am deeply grateful to Dr. A. K. panda, Scientist at NML, for helping me in instrumental analyses, troubleshooting during the experiments and cooperating with me in technical discussions. He has made himself available in a number of ways and has given constructive comments throughout this work.

I am thankful to Mr. Bhupeswar Mahato and Dr. Mainak Ghosh for providing me the technical help for XRD and TEM study. I am thankful to Dr. S. K. Tiwary for his help in the experimental and analytical part of the corrosion study.

I wish to express my gratitude to Dr. Ansu J. Kailath, Dr. Rajat Roy and Dr. Ranjan K. Sahu for inspiration and moral support.

I am thankful to my colleagues Jitendra, Seema, Arbind, Swapna, Partha, Satnam, Banoshree, Santiel, Samba, Abhisek to support me in various ways in the last five

years. Special thanks are also extended to my friends Anupama and Sankarshan for helping me get through the difficult times, for all the emotional support, encouragement through the hard times during the study.

My deepest gratitude goes to my entire family for providing a loving environment for me. My parents, brothers, sisters, my father in law, mother in law, sisters in law, brother in law, uncles, aunt for their moral support.

Last but not the least, I owe my loving thanks to my husband Manoj, for the stimulating discussions and for the sleepless nights he spent for revising the English of my manuscript before deadlines. Without his encouragement and understanding it would have been impossible for me to complete this work.

I am thankful to Council of Scientific and Industrial Research for granting me CSIR- Senior Research Fellowship for this research.

Ojaswini Mohanta

Abstract

Nanocrystalline FINEMET type alloys derived from amorphous precursors exhibit superior soft magnetic properties suitable for various types of applications like transformer cores, choke coils, magnetic sensors etc. However these materials lose their ferromagnetic stability at elevated temperature due to their low Curie temperature (below 700K) and hence are unsuitable for high temperature applications. To overcome this limitation, additional effort has been made to develop materials with high Curie temperature coupled with superior soft magnetic properties. It is observed that crystalline CoFe based alloy (HIPERCO) exhibits high Curie temperature. Hence, Willard *et al*. introduced a series of CoFe based alloys by the incorporation of cobalt in amorphous FeZrB alloy systems, which resulted in optimum material composition of $Co_{44}Fe_{44}Zr_7B_4Cu_1$ termed as HITPERM alloy. Even though this type of alloy had fairly high Curie temperature but its soft magnetic properties tended to deteriorate due to the presence of oxidation prone Zr in the system and put a limitation to use.

In the present work, an attempt is made to develop CoFe- based nanocrystalline alloys with good soft magnetic properties and high Curie temperature for high temperature applications. In the FeSiNbB system, the element cobalt was incorporated with an aim to increase the Curie temperature and also enhance the soft magnetic properties. To achieve the optimum alloy composition, a series of $Co_xFe_{72-x}Si_4Nb_4B_{20}$ (x = 10, 20, 36, 50 at%) alloys were prepared in the form of amorphous ribbons by the melt spinning technique. Partial substitution of Co by Fe in $Co_xFe_{72-x}Si_4Nb_4B_{20}$ (x = 10, 20, 36, 50 at%) series has an effect on the onsets of primary and secondary crystallization temperature. The size of nanoparticles tends to be smaller with increasing cobalt content. It was found that the alloy with stoichiometry x = 36 at% i.e., Co:Fe :: 50:50 exhibits better soft magnetic properties at elevated temperature compared to other measured alloys (x = 10, 20, 50 at%). The $Co_{36}Fe_{36}Si_4Nb_4B_{20}$ alloy exhibits excellent soft magnetic properties with coercivity less than ~106 Am^{-1}, susceptibility ~$0.5X10^3$, high Curie temperature ~1000K and low power loss in its nano-crystalline state (annealed at 925K). This is due to the lowering of magneto crystalline anisotropy attributed to the formation of bcc-FeCo nanoparticles. The combination of high Curie

temperature and superior soft magnetic properties makes this developed material a potential candidate for high temperature soft magnetic applications.

For further improvement of soft magnetic properties, Al was incorporated in the optimum $Co_{36}Fe_{36}Si_4Nb_4B_{20}$ alloy. The effect of Al substitution for Si in the above mentioned alloy system i.e. $Co_{36}Fe_{36}Si_{4-y}Al_yNb_4B_{20}$ (y = 0, 0.5, 1.0, 1.5, 2.0 at%) has been studied. The onset of crystallization temperature increases with Al content up to ($y \leq 1$), beyond which ($1 < y < 2$) it follows a decreasing trend. The glass transition temperature (T_g) lowers with increasing Al content. The alloy with Al = 1 at% exhibits low and stable coercivity values in its nanocrystalline state. This may be attributed to the reduction of magneto crystalline anisotropy and at the same time smaller nanoparticles of bcc-(CoFe)SiAl reduce effective anisotropy. The nanocrystalline alloy with Al = 1 at% (annealed at 925K) exhibits Curie temperature of 1100K in comparison to that of 1000K in the alloy without Al (y = 0 at%). It indicates higher ferromagnetic ordering at 925K in the alloy with y = 1 at% than the alloy without Al (y = 0 at%). Similarly the alloy with Al = 1 at% exhibited very low coercivity i.e. ~66 A/m whereas that without Al (y = 0) showed coercivity around ~106 A/m annealed at 925K.

The optimum $Co_{36}Fe_{36}Si_3Al_1Nb_4B_{20}$ nanocrystalline alloy exhibited better corrosion resistance in its nanocrystalline state due to the highest charge transfer resistance on the formation of bcc-(FeCo)SiAl nanoparticles. The spin wave stiffness constant and the mean square range of the exchange interaction of nanocrystalline $Co_{36}Fe_{36}Si_3Al_1Nb_4B_{20}$ alloy were found to decrease by magnetic softening on annealing at 850K. The excellent soft magnetic properties of $Co_{36}Fe_{36}Si_3Al_1Nb_4B_{20}$ alloy with the formation of nano-phases may be softening the spin waves. In addition, the smaller grain size of nanoparticles may also have an effect on magnetic softening.

Chapter-1

Introduction

1.1: Background

Some of the critical engineering systems such as jet engine and aerospace modules work in an adversely high temperature environment whereas inductors in power generation system and high frequency transformers work under high frequency environment [1]. The extreme high temperature conditions used to have an adverse effect on the associated devices such as magnetic core, rotor assembly in aircraft, inductor etc, as the property of the magnetic material is temperature-sensitive. Cooling devices are used to cater to the conditioning requirements in space power systems and high frequency transformers whereas the material is expected to work at high temperature without compromising the magnetic property. It is a challenge to explore for a material having sufficiently high Curie temperature along with good soft magnetic properties, so that it can be operated at a high temperature environment without losing its soft magnetic properties. The additional desired characteristics of the expected material are (i) low coercivity to minimize frequency independent losses, (ii) high resistivity to minimize frequency dependent eddy current losses and (iii) high magnetization. Therefore, the choice of materials for high temperature applications is limited to those that possess sufficiently high Curie temperature, high magnetization and low coercivity. The aforementioned requirements for use at high temperatures restrict the composition of the alloys to those containing Fe and Co due to the high Curie temperature of Co and its alloys. The conventional materials used for such type of applications were mainly polycrystalline materials like the Co:Fe :: 50:50 Permendur alloy, which has the limitations due to brittleness and high cost of cobalt. Though, ductility was achieved in materials like Hiperco-50 (49Co-49Fe-2V) with the incorporation of vanadium, its addition not only leads to rapid deterioration in energy efficiency due to magnetic losses, but also deterioration of its soft magnetic properties. These materials although have high Curie temperature ~1000K but inferior soft magnetic properties with coercivity above ~ 1Oe [2-3]. To overcome the above limitations of the existing crystalline alloys, attempts have been made to explore CoFe

based amorphous and nanocrystalline materials for high temperature applications. The advantage of the amorphous alloys is due to the reduction of the magneto crystalline anisotropy corresponding to the improvement in soft magnetic properties [4]. In addition, the random atomic structure in amorphous alloy leads to the increase in electrical resistivity than ordered structure in crystalline alloy, thus allowing for higher frequency application of the former. Historically, the discovery of nanocrystalline soft magnetic alloys seems to be originated from research aimed at the improvement of soft magnetic properties in amorphous alloys. In 1988 Yoshizawa, *et al*. of Hitachi Metals discovered that the magnetic softness of melt spun amorphous $Fe_{73.5}Si_{13.5}Nb_3B_9Cu_1$ alloy was being improved significantly by crystallization. This alloy, commercially known as FINEMET, exhibited an exceptionally high effective permeability ($\mu_e \sim 10^5$) with a saturation magnetization (Ms) of 1.25T [5-6]. This improved magnetic softness originated due to the formation of a unique microstructure composed of extremely fine grains such as DO_3- (Fe,Si) phases with a size of about 10-12 nm diameter embedded within the ferromagnetic amorphous matrix. Soon after the development of $Fe_{73.5}Si_{13.5}Nb_3B_9Cu_1$ alloy, Suzuki, *et al.* developed the new alloy NANOPERM in 1989 having a composition of $Fe_{88}Zr_7B_4Cu_1$ with higher content of transition metal than FINEMET [7]. The higher concentration of Fe in the alloy and the formation of α-Fe phase during primary crystallization enhance the magnetization of $Fe_{88}Zr_7B_4Cu_1$ alloy. The minor additives such as Nb, Zr and Cu in $Fe_{73.5}Si_{13.5}Nb_3B_9Cu_1$ and $Fe_{88}Zr_7B_4Cu_1$ alloy system play a large role in the crystallization kinetics. Rapid diffusion of Cu initiates local nucleation of crystalline FeSi in (FINEMET) or Fe in (NANOPERM) with random crystalline directions. Slow diffusion of Nb (FINEMET) or Zr (NANOPERM) inhibits growth of crystallites restricting to a typical size of ~10-20 nm. The combined effect of Cu and Nb/Zr leads to the stability of nanocrystalline structure. Both of these alloys have advantages due to their two phase microstructures amorphous and nanocrystalline because each phase improved the high frequency properties of the materials. The nanocrystalline phases provide high magnetization and the residual amorphous phase provides high resistivity that dampens the eddy currents.

Shortly after the development of nanocrystalline alloys, in 1989, Herzer analysed the magneto crystalline anisotropy energy of nanocrystalline materials based on the concept of random anisotropy model [8]. Herzer demonstrated that this model was

applicable to nanocrystalline materials having smaller grains i.e. less than 50 nm and pointed out that the coercivity of the nanocrystalline material was proportional to the 6^{th} exponential power of the grain size. Subsequent developments were made in lowering the magneto crystalline anisotropy, low magnetostriction and higher electrical resistivity of these nanocrystalline alloys. These additional features increased the potential of the above mentioned Fe-based nanocrystalline alloys in applications like transformer cores, choke coils, magnetic sensors, etc. [9] operating at room temperature. However, at elevated operating temperatures, these materials lose their ferromagnetic stability due to their low Curie temperature below 700K [10], and are unfit for the use in high temperature applications. To overcome this limitation of the existing Fe-based alloys, additional effort has been constrained by the necessity of high Curie temperature coupled with superior soft magnetic properties.

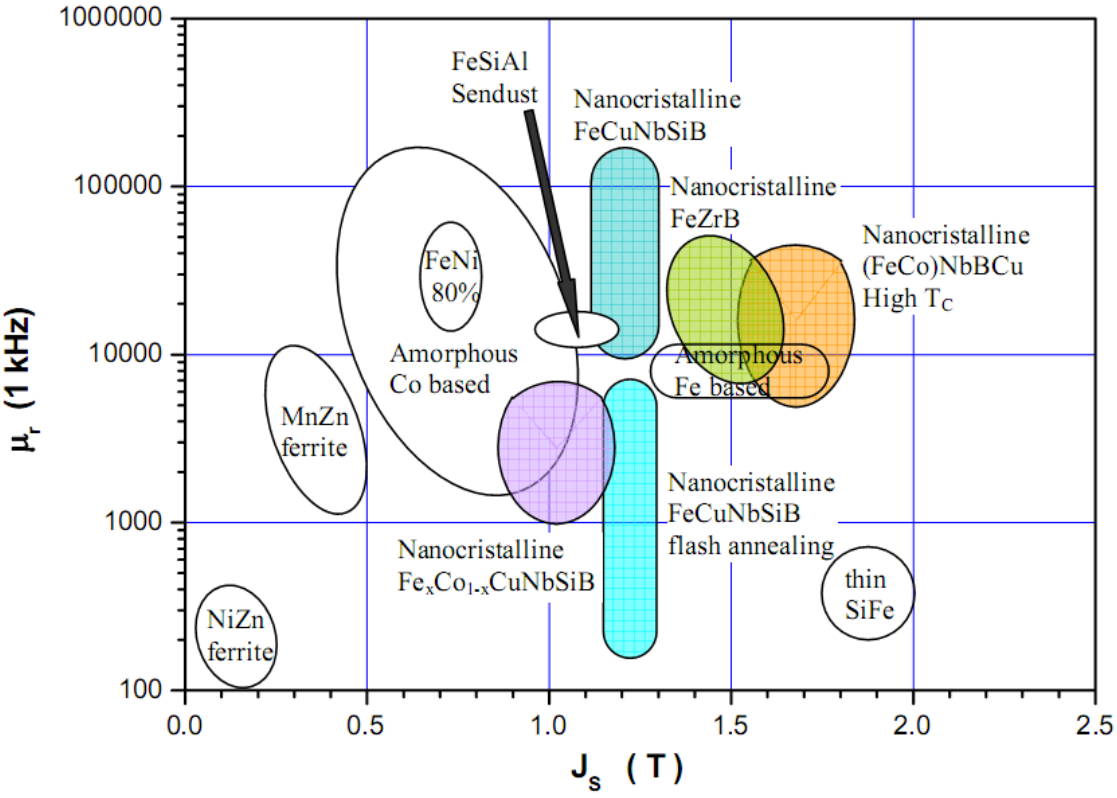

Fig-1.1: General view of soft magnetic materials for medium frequency applications [11]

Therefore the composition of the nanocrystalline alloys was tailored to Co- based or (Co,Fe)- based alloys, due to the high curie temperature of Co and its alloys for higher operation temperatures compared to their Fe based counterparts. Hence, Willard *et al*. introduced a series of CoFe based alloys by the incorporation of cobalt in FeZrB-based systems [12–14] which resulted in composition of $Co_{44}Fe_{44}Zr_7B_4Cu_1$, termed as HITPERM alloy. The HITPERM alloy offered large magnetizations to an elevated temperature over 1000K. Even though this type of alloy had a fairly high Curie temperature around ~1000K and was technologically promising for high temperature application, its soft magnetic properties tended to deteriorate due to the presence of oxidation-prone Zr in the system and put a limitation to use. In view of these limitations there was simultaneous work on the addition of Co to FeCuNbSiB-based nanocrystalline systems [15-16]. It was intended to the partial substitution of Co by Fe in CoFeCuNbSiB system to extend their outstanding soft magnetic properties to elevated temperatures. By varying the ratio of Co/Fe, the magnetization and magneto crystalline anisotropy was being controlled. This study emphasized that the addition of Cu in CoFe based alloys reduced the driving force for cluster formation because of the lower magnitude of the interaction between Co and Cu (25.8 KJ/mol) compared to that between Fe and Cu (42.9 KJ/mol). In Co containing alloys, Cu did not form cluster as Co had more affinity towards Cu compared to Fe. In addition, Cu reduced the crystallization temperature [17]. Recent study also suggests that Cu is not required as a nucleating agent in Co containing alloys [18]. The Co containing alloy exhibits both high glass transition temperature and wide super-cooled liquid region, favouring possible application in the form of bulk metallic glasses (BMG). Even though the Co based alloys have inferior magnetic properties compared to the Fe based alloys, they are magnetically more stable at elevated temperatures. Therefore in this present work an attempt was made (i) to optimize the Co/Fe stoichiometry in CoFeSiNbB alloy system and (ii) to study the effects of cobalt incorporation on nanostructure development and magnetic properties for high temperature applications. But Co containing alloy has a tendency of magnetic hardening. Hence, there was an interest to modify the alloy chemistry for further improvement of soft magnetic properties. Recently, some reports suggest that addition of extra alloying elements like Al in FeSiCuNbB alloy systems significantly improve the soft magnetic properties [19]. Therefore the present work is being extended to study the effect of Al addition in CoFeSiNbB alloy system. The detailed characterization such as structural behaviour,

magnetic behaviour and corrosion study with varying annealing temperature is discussed.

The present work will contribute to the understanding of the correlation between structural and magnetic properties of the nanostructure materials so as to tailor a potential material for high temperature and high frequency applications. Since our approach is an experimental one, a substantial effort has been made in the area of synthesis and characterization techniques. Details of the various experimental methods for synthesis of materials by melt spinning technique and characterization such as (i) Study of thermal behaviour with the aid of Differntial scanning calorimetry (DSC) and Thermal electrical resistivity (TER) (ii) Magnetic study by Magnetic hysteresis loop (MHL), Vibrating sample magnetometer (VSM) and AC hysteresis (iii) Structural study by X-ray diffraction technique (XRD) and Transmission electron microscopy (TEM) and corrosion study by Potentiostat used in this work are given in chapter-3. The influence of Co substitution for Fe in CoFeSiNbB system has been investigated in chapter-4. The results concerning the structural and magnetic properties of varying Co/Fe stoichiometry in $Co_xFe_{72-x}Si_4Nb_4B_{20}$ nanostructured alloys has been presented. Optimization of the alloy composition by varying Co/Fe ratio in $Co_xFe_{72-x}Si_4Nb_4B_{20}$ alloy system is being discussed in this chapter.

The detailed study on thermal behaviour, structural and soft magnetic properties is discussed in chapter-5. Thermal study includes the evaluation of crystallization temperature and glass transition temperature. Structural study includes phase identifications, grain size measurements. Magnetic study includes the evaluation of DC coercivity, AC coercivity, Curie temperature and saturation magnetization. The alloy is optimized with controlled annealing to achieve good soft magnetic properties and high Curie temperature. Effect of Al substitution for Si in the CoFeSiAlNbB alloy system is discussed in chapter-6. The improvement of soft magnetic properties as observed by the partial substitution of Al for Si is discussed in this chapter. In its optimum nanocrystalline state Al = 1 at% exhibits superior soft magnetic properties as well as high Curie temperature. The electrochemical behavior of the amorphous and nanocrystalline $Co_{36}Fe_{36}Si_{4-y}Al_yNb_4B_{20}$ (y=0, 1 at %) alloys is presented in chapter-7. The corrosion potential and corrosion current density of these alloys as evaluated from the cyclic anodic polarization curve are detailed in this chapter. The corrosion

behavior and electrochemical impedance spectroscopy with optimum stoichiometry $Co_{36}Fe_{36}Si_3Al_1Nb_4B_{20}$ alloy is discussed with special reference to annealing temperature.

The low temperature magnetic excitation of the amorphous and nanocrystalline with optimum stoichiometry $Co_{36}Fe_{36}Si_3Al_1Nb_4B_{20}$ alloy is discussed in chapter-8. The temperature dependent magnetization curve derived from VSM with cryostat operated from room temperature 273K to 77K. In this chapter the Bloch coefficients, spin wave stiffness constants and mean square range of exchange interaction of $Co_{36}Fe_{36}Si_3Al_1Nb_4B_{20}$ alloy has been evaluated using spin wave theory. The summary, conclusion and scope of the future work of this thesis are given in chapter-9.

1.2: Objective

The aim of this thesis is the optimization of nanocrystalline alloy to derive excellent soft magnetic properties along with high Curie temperature. To achieve the optimum alloy composition, a series of alloys has been prepared by varying Co/Fe stoichiometry in CoFeSiNbB alloy system. For further improvement of soft magnetic properties small amount of Si has been replaced by Al in optimum CoFeSiNbB alloy. The prepared alloys are being amorphous in state. The nano-phase development in amorphous matrix is optimized by varying annealing conditions.

References

[1] M.E. McHenry, M.A. Willard, H. Iwanabe, R.A. Sutton, Z. Turgut, A. Hsiao, and D.E. Laughlin., Bull. Mater. Sci. Vol. 22, p 495 (1999).

[2] A. Mitra, H.-Y. Kim, B. Shen, N.Nishiyama and A.Inoue., Mater. Trans. JIM Vol. 44, p 1562 (2003).

[3] Y. Waseda and K.T. Aust, J. Mater. Sci. Vol. 16, p 2337 (1981).

[4] H. Fujimori in "Amorphous Metallic alloys" edited by F.E. Lubrosky, Butterworths & Co, London, p 300 (1983).

[5] Y. Yoshizawa, K. Yamauchi, T. Yamane and H. Sugihara, J. Appl. Phys. Vol. 64, p 6047 (1988).

[6] Y. Yoshizawa, S. Oguma, and K. Yamauchi, J. Appl. Phys. Vol. 64, p 6044 (1988).

[7] K. Suzuki, M. Kikuchi, A. Makino, A. Inoue and T. Masumoto, Mat. Trans. JIM Vol.32, p 961 (1991).

[8] G. Herzer, IEEE Trans. Mag. Vol. 26(5), p 1397 (1990).

[9] G. Herzer, in Handbook of Magnetic Materials, edited by K.H.J. Buschow, Vol. 10 (Elsevier Science, North-Holland, 1997).

[10] A. Mitra, A.K. Panda, S.R. Singh, V. Rao and P. Ramachandra Rao, Phil. Mag. Vol. 83, p 1495 (2003).

[11] Makino A, Inoue A and Masumoto T, Mat. Trans. JIM Vol. 36, p 924 (1995).

[12] M.E. McHenry, M.A. Willard and D.E. Laughlin, Prog. Mater. Sci. Vol. 44, p 291 (1999).

[13] K. Gallagher, F. Johnson, E.M. Kirkpatrick, J.H. Scott, S. Majetich and M.E. McHenry., IEEE Mag. Vol. 32, p 4842 (1996).

[14] A. Mitra, H.Y. Kim, D.V. Louzguine, N. Nishiyama, B.L. Shen and A. Inoue, J. Magn. Magn. Mater. Vol. 278, p 299 (2004).

[15] Y. Yoshizawa, S. Fujji, D.H. Ping, M. Ohnuma and K. Hono., Scripta Mater. Vol. 48, p 863 (2003).

[16] C. Gomez-Polo, J.I. Perez-Landazabal and V. Recarte, Phys. Rev. B. Vol. 66, 012401 (2002).

[17] Y. Yoshizawa and K. Yamauchi, Mater. Trans., JIM, Vol. 31, No. 4, p 307 (1990).

[18] J.E. May, M.F. de Oliveira, C.R.M. Afonso, R.D. Sa´ Lisboa and S.E. Kuri, J. Non-Cryst. Solids Vol. 348, p 250 (2004).

[19] B.J. Tate, B.S. Parmar, I. Todd, H.A. Davies, M.R.J. Gibbs and R.V. Major, J. Appl. Phys. Vol. 83, p 6335 (1988).

Chapter-2

Literature review

2.1: Various synthesis routes of soft magnetic materials

The grain orientated silicon steel is widely used as a magnetic core material for transformers, generators and various electrical appliances [1-2]. The electromagnetic steel with low Si-content i.e. 2.5 - 4.5 wt% having a very high magnetic induction are used for the above mentioned applications. In conventional processes such type of low Si steel is developed in the form strip subjected to hot rolling, cold rolling and decarburization annealing. The electrical steel strip of thickness 2.5-5.0 mm is directly cast from molten alloy and hot rolled between 1000^0C-1100^0C, followed by a cold rolling at 50^0C-500^0C in one stage or in multiple stages with intermediate annealing to a final thickness between 0.15-1.0 mm. The strip is then continuously annealed to carry out the primary recrystallization followed by the oriented secondary recrystallization to develop oriented magnetic steel strip [3-4]. In the grain oriented electrical steel, good magnetic properties and very low A.C. losses are obtained in the rolling direction.

Amorphous metallic alloys are of interest because they do not have any long-range atomic order. As a result these materials have high resistivity, low magneto crystalline anisotropy and no microstructural in homogeneity [5]. These materials are observed to have small hysteretic and eddy current losses. Amorphous alloys are thermodynamically metastable, and hence, require non-equilibrium processing such as rapid solidification. In this section various methods of rapid solidifications process [6-8] are (i) Splat quenching (gun technique), (ii) Planer flow casting and (iii) Melt spinning.

2.1.1: Splat quench (gun technique)

Splat quench (gun technique) is the earliest melt quenching method used in the rapid solidification of metastable crystalline and amorphous material. Schematic diagram of this device is shown in fig-2.1(a). In this technique, small quantity of metal (< 100mg)

is melted in a crucible with a nozzle orifice of ~1 mm diameter in the bottom. The crucible holds the molten alloy by surface tension. The thin mylar diaphragm located between the high and low pressure chamber is ruptured by introducing an inert gas into the high pressure chamber with increasing pressure. The rupture of mylar diaphragm results in shock wave onto the crucible facilitating the ejection of molten alloy through the orifice onto a massive Cu substrate, in the shape of a sky-slide. The molten globule solidifies into a thin foil, typically ≤ 15 μm thick, at a solidification rate in the range of 10^6 to 10^{10} K/s.

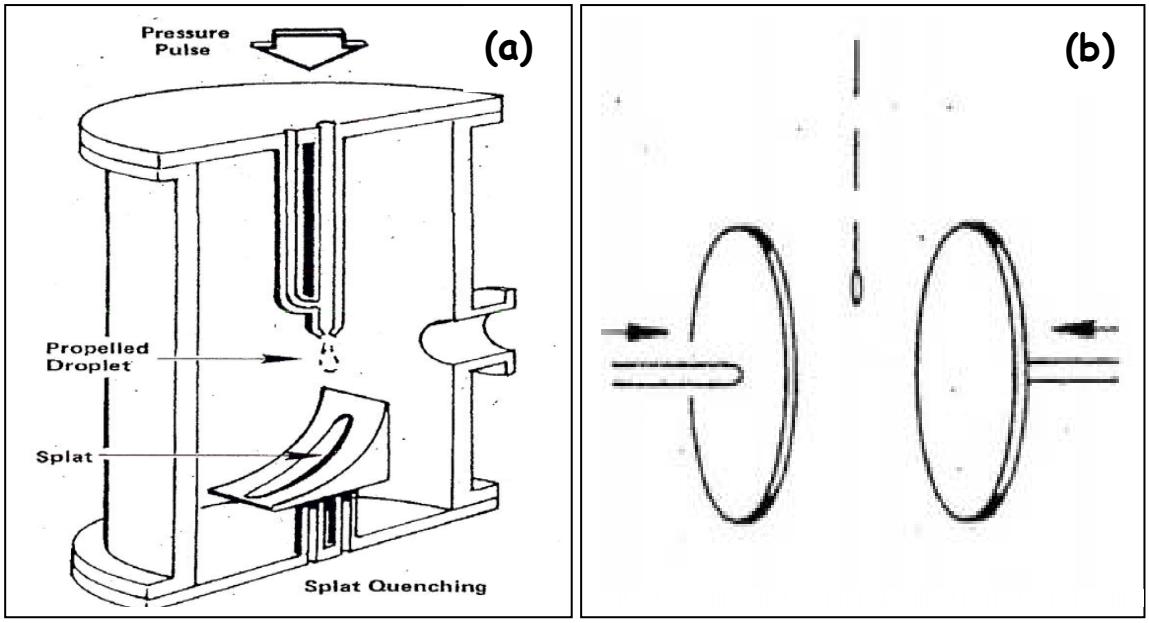

Fig-2.1: (a) Schematic diagram of gun technique [9] and (b) the piston and anvil technique [10].

The foils made by this technique are of non uniform thickness and only of limited research value. The piston and anvil technique is a variant of the "splat quenching" gun technique as shown in fig-2.1(b). In this process the molten drop is thinned by squeezing it between an anvil and piston or between two moving pistons. In some

variants the sample is melted by arc melting. In several methods, the falling droplet intercepts a beam of light between a source and a photocell and thus triggers the solenoid, which in turn releases the piston (or pistons). The cooling rate of a melt source and photocell is so arranged that the falling droplet intercepts a beam of light which is sensed by the device; in turn trigger the solenoid to release the piston (or pistons) in an optimum time. The cooling rate of this technique is in the range of 10^5-10^7 K/s. The foil produced in the piston and anvil apparatus has a uniform cross-section and is more useful for characterizations.

2.1.2: Melt spinning

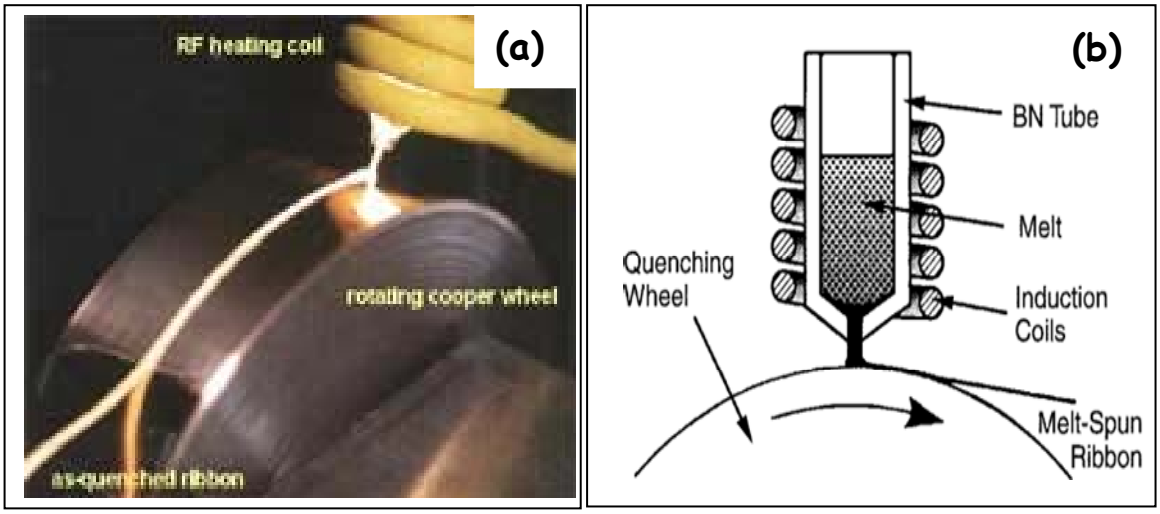

Fig-2.2: (a) Melt spinning process (b) Schematic diagram of melt spinning system [11-12]

Among the most common rapid solidification processing techniques, melt spinning technique is widely acceptable method to produce amorphous ribbons. The photograph and schematic diagram of a melt-spinning apparatus is presented in fig-2.2(a) and (b) respectively. In this system, the molten material is ejected through

an orifice onto a rotating copper wheel. This provides a quench rate of 10^5-10^7K/s sufficient to freeze the alloy as a glass devoid of nucleation and growth of crystallites. In this process, continuous amorphous ribbons are produced having a width of 10 mm and thickness around 20 μm. Morphology of the amorphous ribbon prepared by this (melt spinning) technique depends upon (i) composition, (ii) superheat of the melt, (iii) Diameter of the orifice in crucible nozzle, (iv) distance between the nozzle orifice and wheel surface, (v) wheel speed and (vi) ejection pressure of the melt. The compositions that are close to deep eutectics will allow the formation of glass at these quench rates.

2.1.3: Planer flow casting

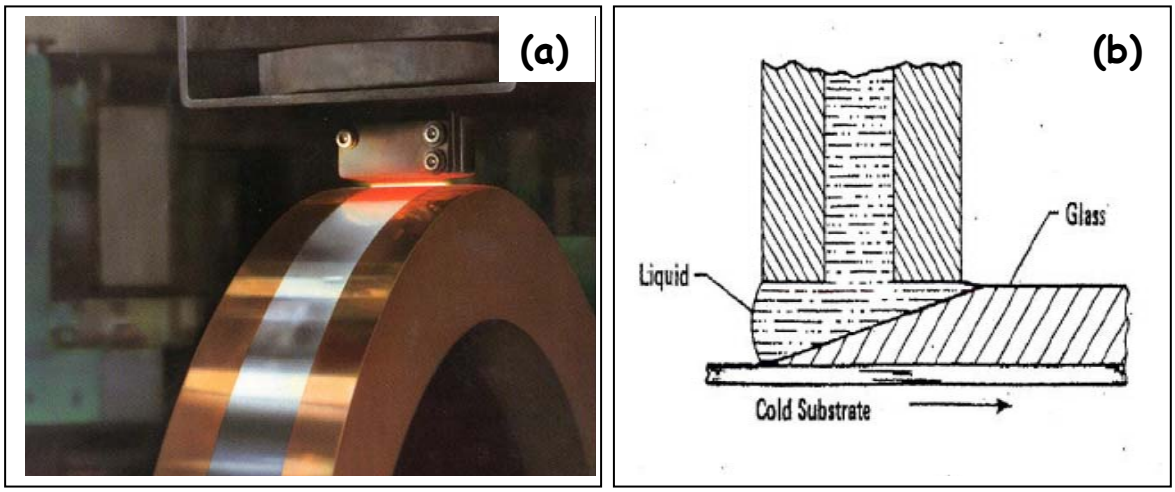

Fig-2.3: (a) Planer flow casting (b) Schematic diagram of the slotted nozzle of planer flow casting apparatus [13]

In Planer flow casting process the molten alloy is forced through a slotted nozzle in close proximity about 0.5 mm to a rotating chill substrate surface. The melt puddle is constrained to a stable, rectangular shape. The photograph and schematic diagram of

the slotted nozzle of planer flow casting apparatus is shown in fig-2.3(a) and (b) respectively. In this process, ribbons up to 10 cm wide can be produced. This process is now used commercially to prepare wide ribbons of several centimeters width (10cm) metallic glasses for applications as soft magnetic materials.

2.2: Magnetic properties of nanocrystalline alloys

The synthesis and characterization of Fe based soft magnetic materials has been intensively studied in last three decades. In an effort to improve their soft magnetic performance by controlling the microstructure and alloying element combinations have been used. In 1988, Yoshizawa, Oguma, and Yamauchi at Hitachi Metals, Ltd., developed the first nanocrystalline soft ferromagnetic alloy, of composition $Fe_{73.5}Si_{13.5}Nb_3B_9Cu_1$ with the trade name FINEMET [13]. The FINEMET ($Fe_{73.5}Si_{13.5}Nb_3B_9Cu_1$) alloy consists of a two-phase microstructure in its optimally annealed condition [14]. The microstructure is ferromagnetic DO3-(α-Fe_3Si) phases with grain diameters of 5 to 10 nm surrounded by a ferromagnetic amorphous matrix. This alloy exhibits an attractive combination of high saturation induction Bs ~1.2T, high permeability ~$10^4\mu$ at 1 kHz and Curie temperature T_c < 1040K. Shortly after the development of FINEMET, Suzuki, *et al*. developed the nanocrystalline Fe-M-B-Cu (M=Zr, Nb. Hf etc.) alloys patented with a trade name NANOPERM [15]. In NANOPERM, α-Fe nanocrystals with body centered cubic (A2) structure were dispersed in an amorphous matrix. The high concentration of Fe and the formation of α-Fe (bcc) during primary crystallization provided increased magnetization of the $Fe_{88}Zr_7B_4Cu_1$ alloy. NANOPERM alloys exhibited high saturation induction Bs in the range of ~ (1.5-1.8T), high permeability ~$10^4\mu$ at 1kHz and Curie temperature ~1050K. [16]. Both of these alloys (FINEMET and NANOPERM) were competitive with existing amorphous alloys, due to their high magnetization and ultra soft magnetic properties. The amorphous phase provides a high resistance path to eddy current formation, thus increasing the operation at high frequency compared to the crystalline alloys. These additional features increased the potential of these nanocrystalline alloys in applications like transformer core, choke coils, magnetic sensor etc. operating at room temperature [17]. FINEMET and NANOPERM alloys use to lose their magnetization upon the onset of the secondary crystallization of boride phase at around 975K and was a limiting factor for high temperature

applications. Fe based amorphous and nanocrystalline alloys of Fe-Si-B [18], Fe-Si-Nb-B-Cu [19-21], Fe-Nb-M-Si-B (M = Cu, Mn, Pt) [22-23] type has been prepared at National Metallurgical Laboratory, Jamshedpur and the change in magnetic property by the effect of nucleating element and metalloid is studied. Comparative study of nucleating element Cu, Mn, Pt in Fe-Nb-M-Si-B (M = Cu, Mn, Pt) system has suggested that Mn and Pt have high solubility with Fe resulting in the formation of intermetallics on devitrification, leading to lower nucleation efficiency thereby relatively weak soft magnetic property [22]. Effect of metalloids (Si, B) in the $Fe_{73.5}Nb_3Cu_1Si_{22.5-x}B_x$ (x = 5, 9, 10, 11.25, 19) alloy system was studied systematically by A.K Panda *et al.* [24]. The study indicates that superior soft magnetic property is achieved when 12.5 < Si < 13.5 in the alloy system as the formation of Fe_3Si nanophases is enhanced in its optimum nanocrystalline state, whereas the soft magnetic property deteriorates beyond the secondary crystallization temperature when strongly anisotropic Fe-boride phases form. It has been reported that addition of Al in FeNbCuMnSiB alloy system leads to considerable improvement in soft magnetic properties with coercivity ~ 0.32 A/m and susceptibility ~ $2.1X10^5$ in its optimum nanocrystalline state [25]. Recently, it is found that Co substitution for Fe in Fe-M-B-Cu (M = Nb, Hf or Zr) alloys can improve high temperature magnetic properties by increasing the Curie temperature of its nanocrystalline phase. Hence, subsequent reports have suggested the incorporation of cobalt in FeZrB-based systems [26-28] with a typical composition of $Co_{44}Fe_{44}Zr_7B_4Cu_1$ called as HITPERM. In $Co_{44}Fe_{44}Zr_7B_4Cu_1$ alloys, nanocrystalline α'-FeCo grains (B2 structure) are formed exhibiting significantly improved of high Curie temperature i.e. > 1250K, high saturation induction, 1.6-2.1 T and excellent thermal stability.

Table-2.1: Soft magnetic characteristic of nanocrystalline alloys

Alloy Trade Name	Typical composition	Nanocrystalline phases	B_s (T) (Magnetic moment)	T_c (K) Curie temperature
FINEMET	$Fe_{73.5}Si_{13.5}B_9Nb_3Cu_1$	DO3-(α-Fe_3Si)	1.0-1.2	< 1040K
NANOPERM	$Fe_{88}Zr_7B_4Cu_1$	α-Fe(BCC)	1.5-1.8	~ 1050K
HITPERM	$Fe_{44}Co_{44}Zr_7B_4Cu_1$	α-FeCo (BCC) α'-FeCo (B2)	1.6-2.1	> 1240K

The major advantage of HITPERM alloys is that their magnetization persists to the α-γ phase transformation at high temperature i.e.1250K [29]. This alloy achieves its properties by coupling the high magnetic moment of nanocrystalline α'-FeCo phase with low magnetic anisotropy as suggested by the random anisotropy model to the nanocrystalline structure. The soft magnetic characteristic of FINEMET, NANOPERM and HITPERM is listed in table-2.1.

2.2.1: Exchange coupled magnetism in nanocrystalline alloy

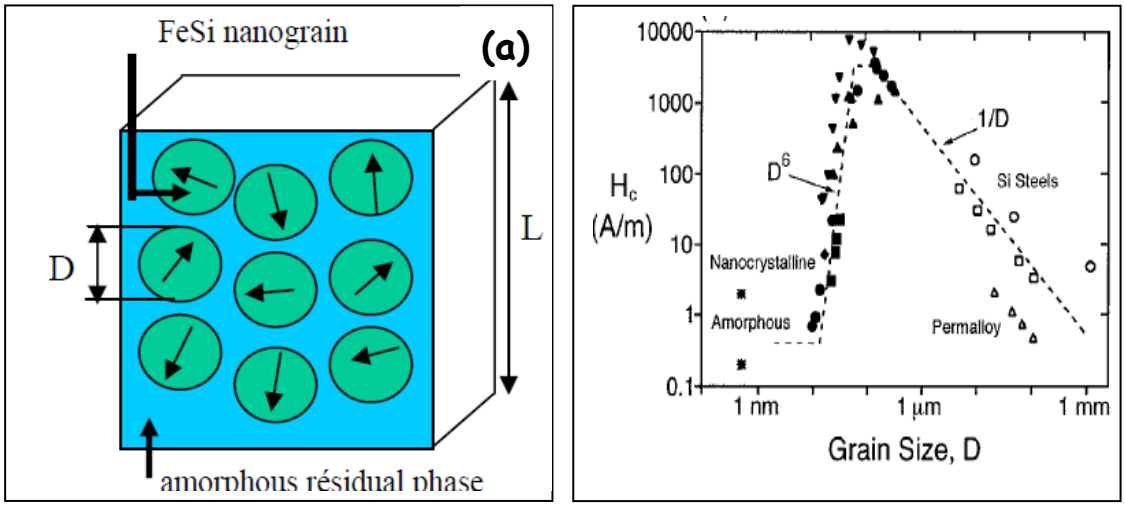

Fig-2.4: (a) Distribution of magnetization easy axes due to random crystallization (b) Evolution of coercivity with the grain size [25]

Nanocrystalline materials are formed by isothermal annealing of the amorphous alloy above the primary crystallization temperature. An optimal heat-treatment temperature is needed to obtain the desired nanocrystalline grains having 10-50 nm sizes in the amorphous matrix. After the discovery of the nanocrystalline alloys, Herzer offers a theory based on a random anisotropy model [17, 30]. The random anisotropy model, originally developed for amorphous alloys, explains this seemingly anomalous

behavior. The applications of this model to its nanocrystalline alloys shows that as the grain diameter is reduced below the exchange correlation length, the magneto crystalline anisotropy energy is averaged over the exchange volume resulting in very small values. This model requires the random orientation of nano grains smaller than the exchange correlation length as shown in fig-2.4. Using a coherent rotation model, for nanocrystalline alloys (grain size < 50 nm) the estimated coercivity is proportional to the sixth power of the grain sizes (D^6). The effective anisotropy <K> contribution of small randomly oriented grains is essentially reduced by the exchange interaction. The ferromagnetic exchange length is

$$Lo = \frac{\sqrt{A}}{K1} \qquad \ldots\ldots\ldots\ldots\ldots\ldots\ldots\ldots (2.1)$$

Where A is the exchange stiffness constant and Lo is the exchange correlation length. The randomly distribution of nano grains in amorphous matrix has shown in fig-2.4. According by the concept of random anisotropy model, an assembly of exchange coupled grains of size 'D' with magnetocrystalline anisotropies of K_1 oriented at random. The effective anisotropy <K> affecting the magnetization process results from averaging over the $N = (L_{ex}/D)^3$ grains the volume $V = L_{ex}^3$ determined by the exchange length L_{ex}. Thus the averaged anisotropy energy <K> is determined by the mean fluctuation amplitude of anisotropy N grains, i.e,

$$< K > \approx \frac{K1}{\sqrt{N}} = K1\sqrt[3]{D/Lex} \qquad \ldots\ldots\ldots\ldots (2.2)$$

The exchange length L_{ex} is normalized by substituting <K> for K1 in eq. 2.1. i.e. L_{ex} is related to the averaged anisotropy by

$$Lex = \sqrt{\frac{A}{< K >}} \qquad \ldots\ldots\ldots\ldots\ldots\ldots\ldots\ldots (2.3)$$

The combination of eq. 2.2 and 2.3 finally yields

$$\langle K \rangle \approx \frac{K1}{A^3} . D^6 \qquad \ldots\ldots\ldots\ldots\ldots\ldots\ldots\ldots (2.4)$$

Where 'D' is the grain size, which is smaller than the exchange length Lex. Using the coherent spin rotation, [31] the coercivity is related to <K>, which leads to

$$Hc = Pc \frac{\langle K \rangle}{Js} \approx Pc \frac{K1^4 D^6}{JsA^3} \qquad \ldots\ldots\ldots\ldots\ldots\ldots (2.5)$$

2.3: High temperature nanocrystalline alloy design

The design of nanocrystalline soft magnetic alloys is carried out by a two-statge process. In the first stage, amorphous alloy is prepared by rapid solidification techniques i.e. melt spinning. In the second stage, the amorphous alloy is heat treated above the primary crystallization temperature of the alloy for devitrification to nanocrystalline state. But the fabrication of nanocrystalline alloys requires the grains to be smaller in comparison to the ferromagnetic exchange length and preferably between 10-50 nm.

To synthesize the amorphous soft magnetic alloys, restriction limits the choice of ferromagnetic compositions Because of the magnetization of the alloy is directly related to the amount of magnetic transition metal elements such as Fe, Co, Ni or the rare earth metal Gd etc. and also the formation of amorphous structure by melt spinning is limited to compositions near deep eutectics. Early transition metal (i.e. Zr, Hf, Nb) and metalloid elements (i.e. B, Si, P) have been employed to produce the deep eutectics in ferromagnetic transition metal systems. But the addition of typical glass forming agents has a deleterious effect on the intrinsic magnetic properties such as the saturation induction and the Curie temperature. In the alloy chemistry the

transition metals were maximized and also contain metalloid elements (i.e. M = B, Si, P, C etc.) in order to stabilize the glassy phase. So the alloying addition with non-magnetic species has reduced average magnetic dipole moments by dilution. Therefore it is desirable to have the eutectic composition as close to pure Late Transition (TL) as possible so as to keep the magnetization high. The Early Transition (TE) elements such as Zr, Nb, Hf etc. provide a glass stabilizing function with added the extra features that they inhibit diffusion in these alloys. The binary phase diagrams for a TL-TE (Fe-Zr) and TL- M (Fe-B) are illustrated in fig-2.5. The TL-TE systems typically have much lower eutectic composition than the TL-M. Generally TL-M eutectic occurs near 20 at% M.

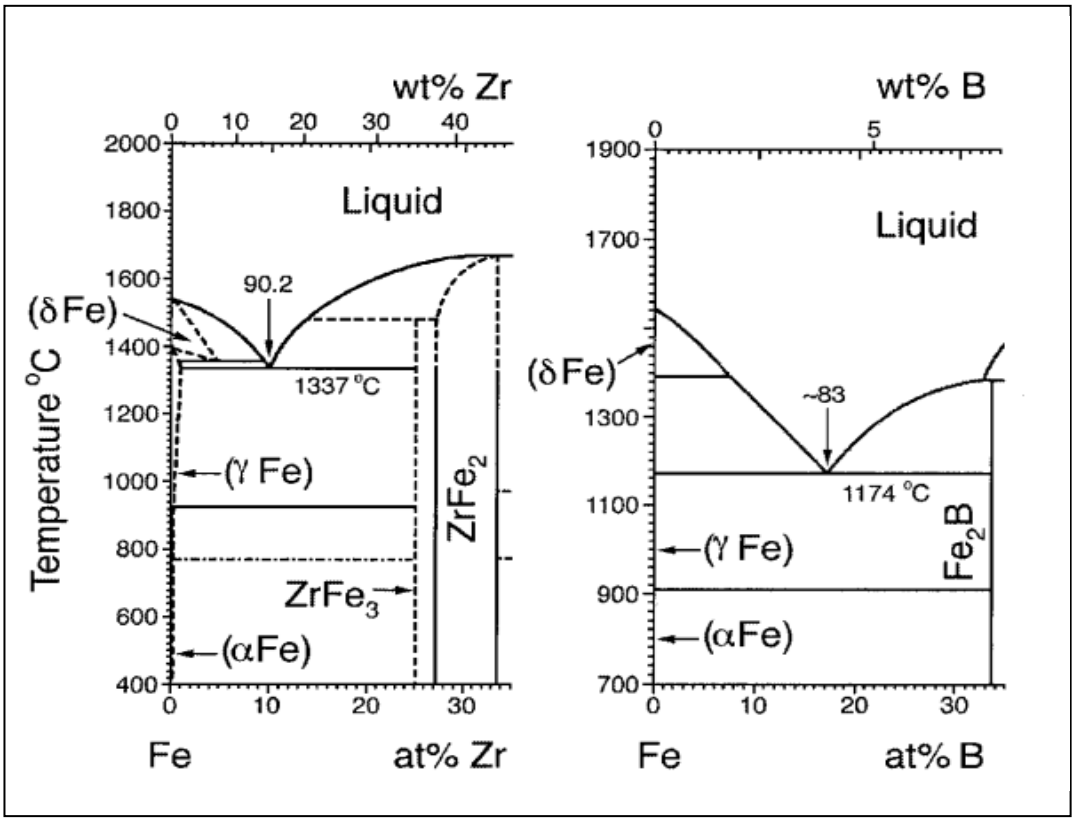

Fig-2.5: Equilibrium phase diagrams of the Fe-Zr and Fe-B alloy systems showing the eutectics for which amorphous alloys are easily produced [32]

On the other hand TL-TE eutectic that exists in Fe-Zr binary phase occurs near TL~90%. Therefore these elements allow for a greater fraction of TL provides subsequently a higher magnetization. This advantage is somewhat offset by the high cost of these elements and they are also highly reactive, that leads to greater degradation via oxidation. However, the design issues of conventional soft magnetic alloys for high temperature applications are additionally constrained by the requirements of high Curie temperature of the residual amorphous matrix along with its nanocrystalline phase. Therefore, the composition of these alloys is constrained to the Co and CoFe based nanocrystalline alloys because of the high Curie temperature of Co and its alloys. It has been noted that the position of the elements Fe and Co near the top of the Bethe-Slater curve [33].

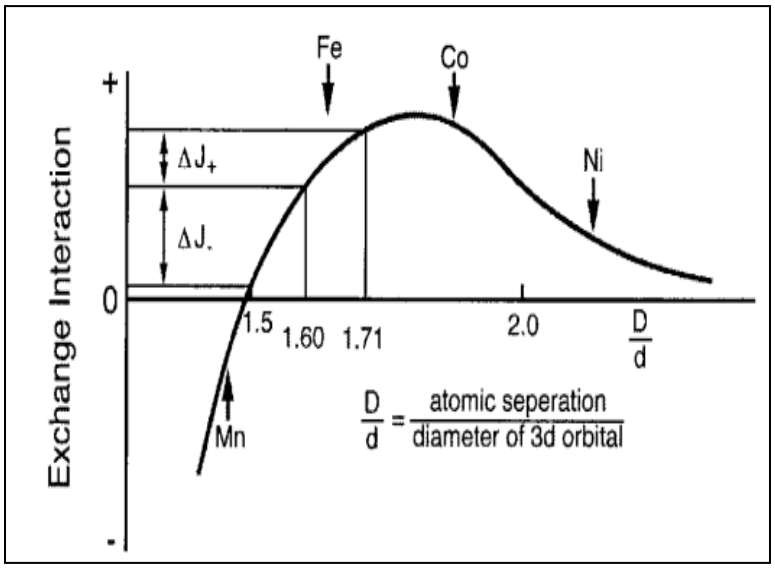

Fig-2.6: Bethe-Slater curve for the magnetic exchange interaction energy as a function of inter atomic spacing [33]

As a result the desired properties such as higher magnetization contain Fe and Co. Fe-rich alloys typically have larger inductions and lower Curie temperatures. On the other hand Co based alloys typically have smaller induction and larger Curie

temperature. Therefore the composition was constrained to Fe-Co based alloys, which is not only maintaining the high Curie temperature and relatively high magnetization than Fe based alloy hence are desirable for high temperature applications. But there is still a great amount of flexibility in alloy design because of that can be catered to specific applications, such as those requiring high permeability, low magnetostriction. Therefore, in this present work effort has been made to develop CoFe-based nanocrystalline alloys, which not only have a high Curie temperature but also possesses good soft magnetic properties.

2.4: Scope of the present work

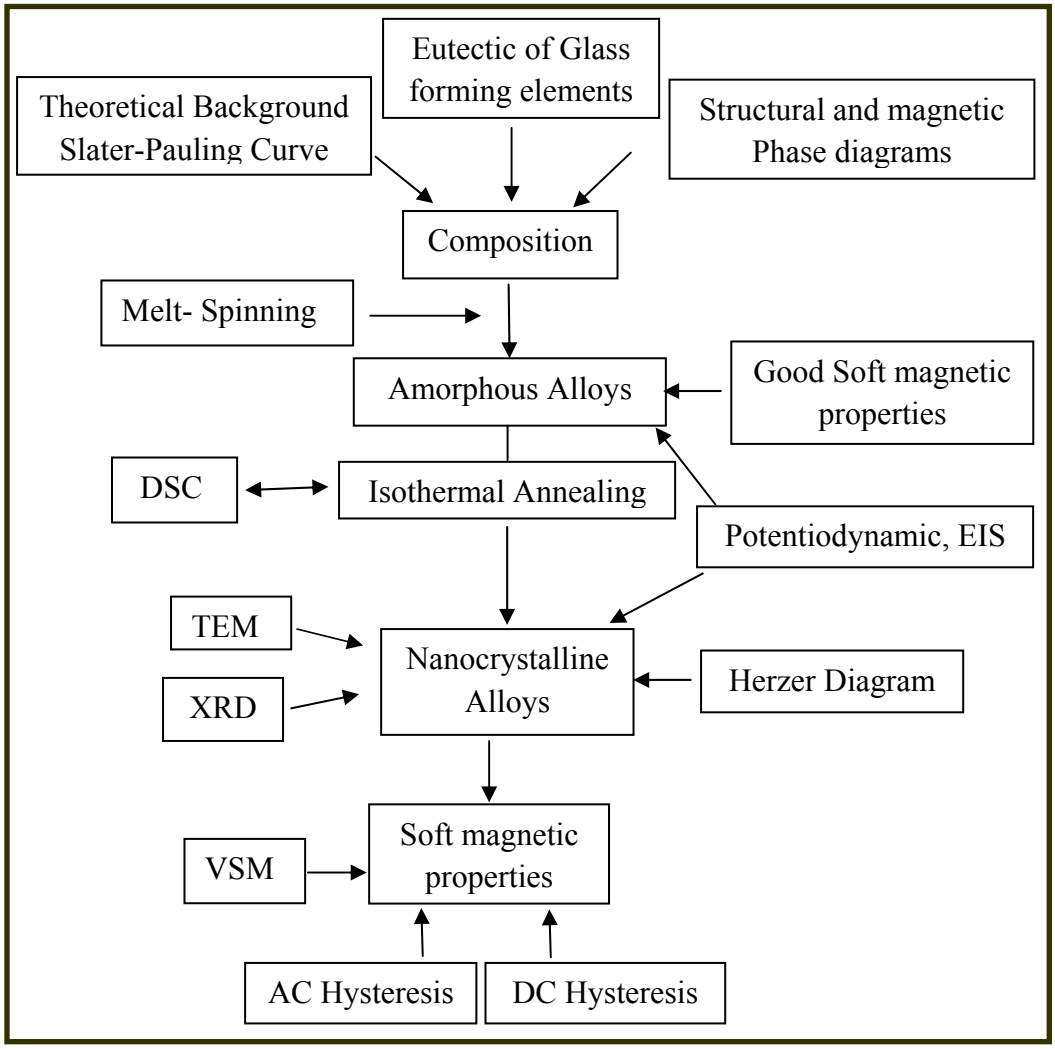

Fig-2.7: Flow chart of the scope of present work

In the present work attempts have made to optimize the Co-Fe stoichiometry in CoFeSiNbB nanostructured alloy system and correlating the effects of cobalt incorporation on nanostructured developments with magnetic properties. To achieve the optimum alloy composition, a series of alloys have been prepared by varying Co/Fe stoichiometry in CoFeSiNbB alloy system. It has been reported that the incorporation of the element cobalt in the FeSiNbB alloy system not only enhance the Curie temperature but also facilitate nanocrystallisation [34-35]. But in Co containing alloy has a tendency of magnetic hardening; hence there was an interest to modify the alloy chemistry for further improvement of soft magnetic properties. It is well known that the addition of Al in Fe-Si binary system i.e. Sendust class of alloys (FeSiAl) significantly improved the soft magnetic properties because lowering the magneto crystalline anisotropy [36]. Therefore the present work was aimed on the effect of addition of extra alloying elements like Al in CoFeSiNbB alloy system and investigate their crystallization, structural, soft magnetic properties and corrosion behavior in the as cast as well as in its nanocrystalline state.

References

[1] Honma H., Ushigami Y. and Suga, Y., J. Appl. Phys. Vol. 70, Issue 10, p 6259 (1991).

[2] T. Žák, Y. Jirásková, O. Schneeweiss, A. Sólyom and P. Marko, J. Magn. Magn. Mater. Vol. 157-158, p 453 (1996)

[3] Goto et al. U.S. Pat. 3940299, "Method for producing single-oriented electrical steel sheets having a high magnetic induction" February, (1976).

[4] Fiedler, U.S. Pat. 3957546, "Method of producing oriented silicon-iron sheet material with boron and nitrogen additions" May (1976).

[5] K. V. Rao in "Amorphous Metallic alloys" edited by F.E. Lubrosky, Butterworths & Co, London, p 401 (1983).

[6] Boettinger WJ. In: Kear BH, Giessen BC, Cohen M, editors "Rapidly solidified amorphous and crystalline alloys" New York: Elsevier, (1982).

[7] Davies HA. In: Steed S, Warlimont H, editors "Rapidly quenched metals" Vol.1. Amsterdam: North Holland, p 911 (1985).

[8] JH Perepezko and JS Paik, in Rapidly Solidified Amorphous and Crystalline Alloys, by BH Kear and BC Giessen **(**Elsevier**,** New York), p 125 (1984).

[9] Duwez P, Willens RH and Klement W. J. Appl. Phys. Vol. 31, p 1136 (1960).

[10] Duwez P. Trans. Am Soc Met. Vol. 60, p 607 (1967).

[11] Majetich SA, Artman JO, McHenry ME, Nuhfer NT and Staley SW. Phys. Rev. B Vol. 48, p 16845 (1993).

[12] Lim SH, Pi WK, Noh TH, Kim HJ and Kang IK. J. Appl. Phys. Vol.73, p 6591 (1993).

[13] Narasimhan, M. C., U.S. Pat. 4 142 571(1979).

[14] Y. Yoshizawa, S. Oguma, and K. Yamauchi, J. Appl. Phys. Vol. 64, p 6044 (1988).

[15] Y. Yoshizawa, K. Yamauchi, T. Yamane and H. Sugihara, J. Appl. Phys. Vol. 64, p 6047 (1988).

[16] K. Suzuki, M. Kikuchi, A. Makino, A. Inoue and T. Masumoto, Mat. Trans. JIM Vol.32, p 961 (1991).

[17] G. Herzer, in "Handbook of Magnetic Materials" edited by K.H.J. Buschow, Vol. 10 (Elsevier Science, North-Holland (1997).

[18] S.Palit, I.Chattoraj and A.Mitra, J.Physics D: Applied Physics Vol. 32, p 541 (1999).

[19] A.Mitra, S.Palit and I.Chattoraj, Phil Mag. B 77, p 1681 (1998).

[20] A.K. Panda, S.Roy, S.R.Singh, V.Rao, S.Pramanik, I.Chattoraj, A.Mitra, and P.Ramachandrarao, Materials Science & Engg. A, 304-306, p 457 (2001).

[21] A.Mitra, A.K.Panda, V.Rao, S.R.Singh and P.Ramachandrarao, Applied Surface Science, Vol. 182, p 321 (2001).

[22] A.K. Panda, I.Chattoraj, and A.Mitra, J. Magn. Magn. Mater. 222 p 263 (2000).

[23] A.K. Panda, I.Chattoraj and A.Mitra, Materials Science & Engg. A, 304-306 p 950-953 (2001).

[24] A.Panda, S.Basu and A.Mitra, J. Magn. and Magn. Mater. Vol. 260, p 70 (2003).

[25] A.Mitra, A.Panda, V.Rao, S.R.Singh and P.Ramachandrarao, Phil Mag. Vol. 83, p 1495 (2003).

[26] M.E. McHenry, M.A. Willard and D.E. Laughlin, Prog. Mater. Sci. Vol. 44, p 291 (1999).

[27] K. Gallagher, F. Johnson, E.M. Kirkpatrick, J.H. Scott, S. Majetich and M.E. McHenry., IEEE Mag. Vol. 32, p 4842 (1996).

[28] A. Mitra, H.Y. Kim, D.V. Louzguine, N. Nishiyama, B.L. Shen and A. Inoue, J. Magn. Magn. Mater. Vol. 278, p 299 (2004).

[29] Willard MA, Laughlin DE, McHenry ME, Thoma D, Sickafus K, Cross JO, et al. J. Appl. Phys. Vol. 84, p 6773 (1998).

[30] Herzer, IEEE Trans. Mag. Vol. 26(5), p 1397 (1990).

[31] R.M. Bozorth, Ferromagnetism, Princeton, N.J.: D. Van Nostrand, ch.18, p 811 (1951).

[32] Massalski T. "Binary alloy phase diagrams, Materials Park, OH ASM International" (1990).

[33] Chen CW. "Magnetism and metallurgy of soft magnetic Materials" New York: Dover Publications (1986).

[34] K. Hono, D.H. Ping, Y.Q. Wu, Proceedings of the 22nd Riso International Symposium on Materials Science, Vol. 35, p 52 (2001).

[35] D.H. Ping, Y.Q. Wu, K. Hono, M.A. Willard, M.E. McHenry and D.E. Laughlin, Scripta Mater. Vol. 45, 781 (2001).

[36] R. Boll, In: K.H.J. Buschow (Ed.), Electronic and Magnetic Properties of Metals and Ceramics, in: Materials Science and Technology, vol. 3B, Part II, VCH pub.,p. 446.

Chapter-3
Experimental methodology

The present work aims to the development of nanocrystalline soft magnetic materials and optimization of its magnetic properties. It involves the synthesis of amorphous alloys, optimization of annealing temperature to get nanocrystalline phases, characterization of magnetic properties, thermal properties, structural behaviour and corrosion behaviour of the nanostructured materials so that a potential material is tailored for a high temperature soft magnetic applications.

3.1: Introduction

Amorphous metals and alloys are synthesized by rapid solidification technique in last three decades. Rapid solidification is the process in which the melt gets quenched to glass at a rate greater than 10^4 K/s sufficient enough to avoid nucleation and growth of crystallites [1-2].

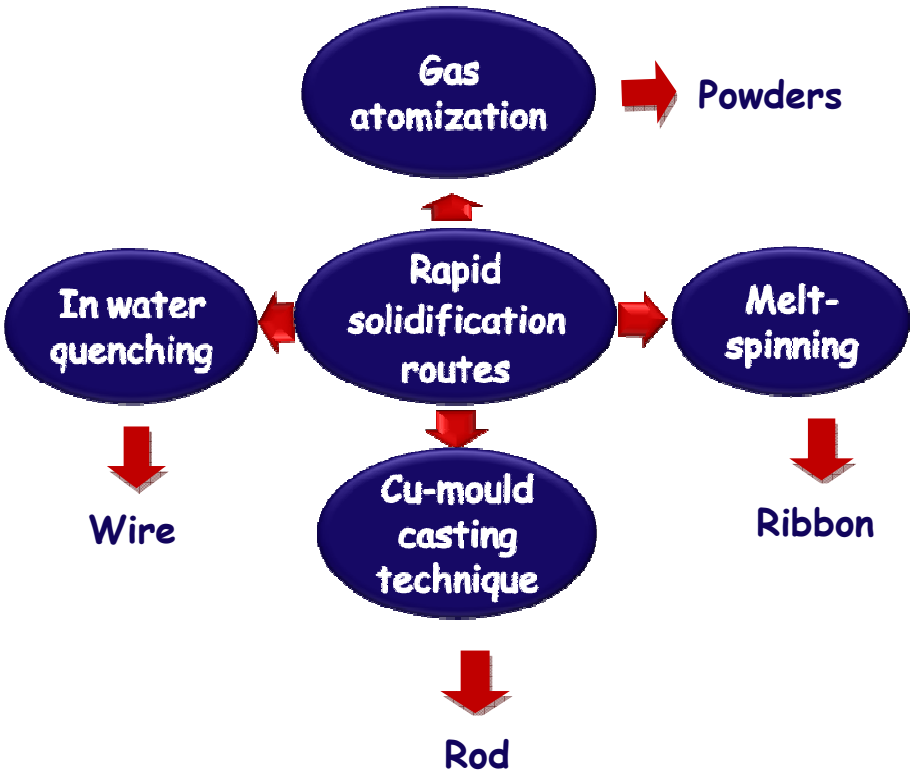

Fig-3.1: Different methods of rapid solidification routes

There are four methods of preparing alloys through rapid solidification technique and the shape of the product is shown in fig-3.1. The methods are such as 1- Gas atomization, 2- In-water quenching, 3- Cu-mould casting and 4- Melt spinning [3-6]. Out of which the melt spinning is the widely acceptable technique to produce amorphous ribbon.

3.2: Preparation of melt-spun ribbon

3.2.1: Equipments used

The synthesis of amorphous alloy in the present study was carried out by rapid solidification technique using melt-spinning apparatus, Model: 2M, make: Marko Materials, USA (Fig.-3.2).

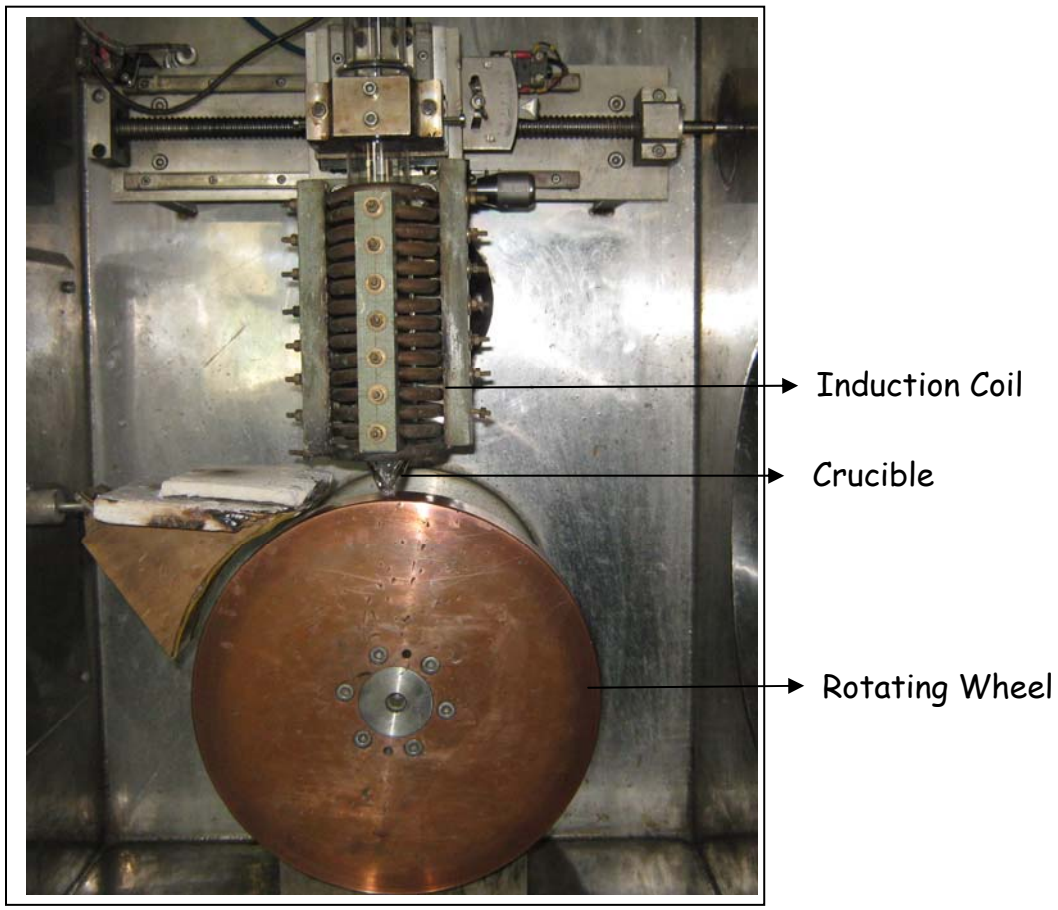

Fig-3.2: Melt spinning apparatus for preparation of amorphous ribbons.

The quenching copper wheel is made by Cu-Be alloy having diameter 305 mm and width 38 mm. The ingots for this purpose was prepared by Vacuum arc melting furnace, Model- L200d, make: Leybold Heraeus, Germay. The controlled annealing was carried out under argon atmosphere in infrared gold image furnace model: TER-2000, make: Sinku Riko, operated with a heating rate of 20 K/min. The nominal composition of these alloys used for the present study is given in table-3.1.

Table-3.1: Nominal chemical composition of the prepared alloys

Alloys	**Chemical composition in (at%)**
Alloy ≠ I	$Co_{10}Fe_{62}Si_4Nb_4B_{20}$
Alloy ≠ II	$Co_{20}Fe_{52}Si_4Nb_4B_{20}$
Alloy ≠ III	$Co_{36}Fe_{36}Si_4Nb_4B_{20}$
Alloy ≠ IV	$Co_{50}Fe_{22}Si_4Nb_4B_{20}$
Alloy ≠ V	$Co_{36}Fe_{36}Si_{3.5}\,Al_{0.5}Nb_4B_{20}$
Alloy ≠ VI	$Co_{36}Fe_{36}Si_3\,Al_1Nb_4B_{20}$
Alloy ≠ VII	$Co_{36}Fe_{36}Si_{2.5}\,Al_{1.5}Nb_4B_{20}$
Alloy ≠ VIII	$Co_{36}Fe_{36}Si_2\,Al_2Nb_4B_{20}$

3.2.2: Preparation method

Master alloys about 300 gm each was prepared by taking the pure elements (99.99%) of cobalt, iron, silicon, boron, niobium and aluminium. As the element boron and silicon are the volatile elements the quantities of the master alloys were calculated keeping in view the losses of boron and silicon at high temperature. So, 5 and 10 wt% losses for silicon and boron were considerable respectively. Initially the ingot of master alloys having nominal composition $Co_xFe_{72-x}Si_4Nb_4B_{20}$ (x = 10, 20, 36, 50 at%) and $Co_{36}Fe_{36}Si_{4-x}Al_xNb_4B_{20}$, (x = 0, 0.5, 1.0, 1.5, 2.0 at%) were arc melted in argon atmosphere by vacuum arc melting furnace. The melting was repeated several times to ensure effective homogenization and subsequently casted into ingots of master alloys. The alloy ingots were induction melted by induction furnace and rapidly solidified to obtain amorphous ribbon by melt spinning technique. In this system the molten alloy is ejected through a narrow orifice of quartz crucible by

flowing Ar gas at a pressure of 0.5 bar onto a high speed rotating copper wheel to produce amorphous ribbon. This provides a cooling rate in between 10^5-10^7 K/s sufficient to freeze the alloy to obtain the amorphous structure [7-8].

In this melt spinning system, the important process parameters which affect the ribbon quality are quench rate, melt puddle stability, crucible nozzle orifice diameter, distance between the nozzle orifice and surface of the wheel and the ejection pressure of the melt. To get the continuous ribbons of desired shape depends on the melt flow as well as the quench rate. In the present work the melt spinning process parameters such as (a) wheel speed, (b) melt temperature, (c) crucible nozzle orifice size, (d) distance between the nozzle orifice and surface of the wheel and (e) the ejection pressure of the melt has been optimized. The crucible with conical nozzle having 0.5mm orifice diameter has been used for all the alloys composition.

Table-3.2: Optimized process parameters

Process parameters	**Optimized value**
Wheel speed	1400 rpm
Crucible nozzle diameter	1.5 mm
Distance from the nozzle orifice and wheel surface	0.5 mm
Ejection pressure of the melt	0.5 bar

In the present work, the process parameters has been optimized and kept constant for all the alloy compositions. These optimized values of the wheel speed, crucible nozzle orifice diameter, distance between the nozzle orifice and surface of the wheel and the ejection pressure of the melt are given in table-3.2. By using these optimized parameters the continuous amorphous ribbons typically a few microns thick and width varying from 2 mm to 3 mm were prepared. As the materials prepared in melt spinning system are amorphous in state. Crystallization behavior has been studied to get the crystallization temperature. Based on the primary crystallization temperature (T_{X1}) from DSC data, the amorphous ribbons were subjected to control annealing at

various temperatures to develop nano-crystalline phase in amorphous matrix. The heating rate was constant at 20 K/min in argon atmosphere. The different annealing condition of these prepared alloys is given in table-3.3.

Table-3.3: Optimized properties with annealing behaviour

Alloys	Crystallization temp. (T_{x1})	Magnetic properties	Annealing conditions	
			875K/15min	925K/15min
Alloy ≠ III	845K	Hc (A/m) Tc (K)	50 A/m 738 K	106 A/m 1000 K
Alloy ≠ VI	856K	Hc (A/m) Tc (K)	37 A/m 731 K	66 A/m 1100 K

3.3: Experimental arrangement for crystallization study

3.3.1: Differential scanning calorimetry

The crystallization behaviour of these as prepared alloys was carried out using Differential scanning calorimeter (DSC), model: Diamond DSC, make: Perkin-Elmer. The DSC was run from room temperature to 975K at a scan rate of 20 K/s under argon environment. The equipment was calibrated against zinc and indium standard before each experimental run to ensure reproducibility. Variable scan rate was used for the calculation of activation energy by Kissinger equation. The amount of sample used for each run is about 20-30 mg. The DSC profile showed an exothermic peak preceded by an endothermic event called the glass transition temperature.

3.3.2: Thermal variation of electrical resistivity

The electron transport properties during phase transformations were evaluated from variation in electrical resistivity with thermal variation by using infra-red gold image programmable furnace, model: TER-2000, make: Sinku Riko. In the present work

thermal electrical resistivity was measured by four probe technique under a current of 5 mA. The current and voltage probes were spot welded on the surface of alloy. The sample was subjected to heating from room temperature to 1000K at a constant rate of 10K/min in an argon atmosphere. Thermal electrical resistivity was computed from the response of voltage and applied current (5mA).

3.4: Magnetic study

3.4.1: DC hysteresis loop measurement

The magnetic hysteresis loop was measured using the computer controlled hysteresis loop tracer developed at National Metallurgical Laboratory, Jamshedpur [9]. The schematic diagram of hysteresis measurement set up is shown in fig-3.3. The hysteresis measurements were carried out in open-flux configuration using a Helmholtz coil producing a field of 13.44 Oe per Ampere of current passing through it. The Helmholtz coil was driven by a power amplifier at a quasi-dc magnetizing frequency of 50 mHz.

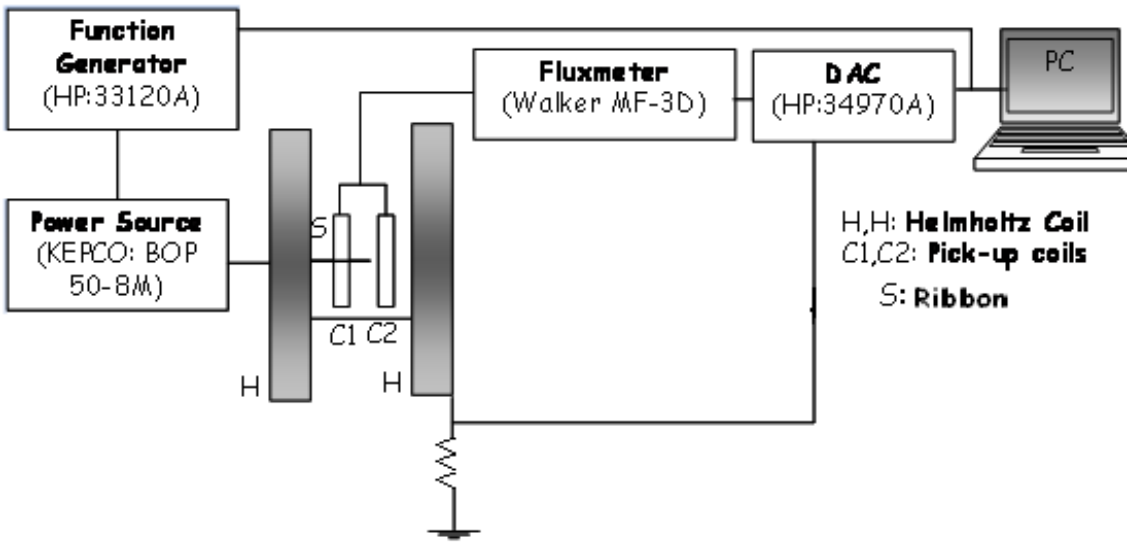

Fig-3.3: Schematic diagram of DC hysteresis loop measurement set up

Two oppositely wound coils (C1, C2) were placed at the centre of Helmholtz coil in such way that there was no output signal without sample. The sample was kept in the secondary coil and the sample parameters fed to the fluxmeter. When current passed through the Helmholtz coil, a magnetic field (H) is created and the sample got magnetized. The response of magnetization (B) was recorded as output signal by the connected personal computer through data logger and the hysteresis loop was recorded by plotting B vs H. DC coercivity was measured from hysteresis loop.

3.4.2: AC hysteresis loop measurement

The AC coercivity and core loss measurement were carried out using an AC hysteresis loop tracer Model: 401 AMH, make: Walker. The schematic diagram of high frequency automatic hysteresis graph systems is shown in the fig-3.4a. The AMH-401 has a test frequency range of 50 Hz to 1 MHz [10]. For AC magnetic hysteresis graph measurement the suitable sample geometry is the torroid shape because it forms a closed magnetic circuit that can be driven by a primary winding. In this present study the optimum alloys and its variant annealing conditions has been used to study the AC coercivity and coreloss behavior.

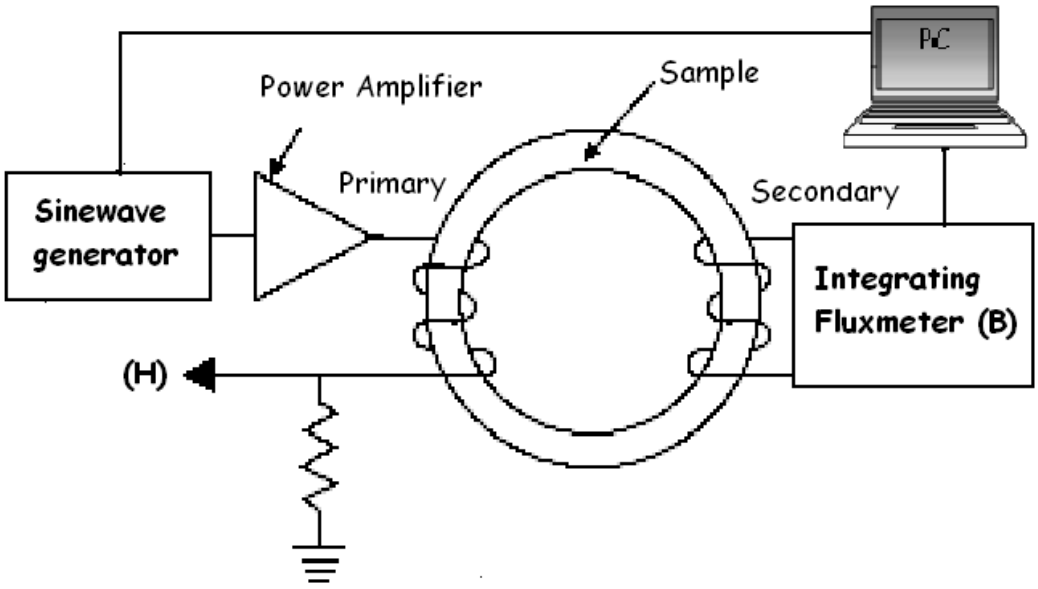

Fig-3.4a: Schematic diagram of AC hysteresis loop measurement set up

For AC hysteresis loop measurement the ribbons having approximate one meter length were wound onto a 13mm-o.d. quartz ring to make a torroid shape then wrapped with primary and secondary windings by copper wire. The computer-controlled function generator and power amplifier combination drive the primary winding. The applied magnetic field H, which magnetizes the sample, is calculated from the primary current using the equation [11]

$$H = \frac{\pi NI}{2.5L} \qquad \ldots\ldots\ldots\ldots\ldots\ldots\ldots (3.1)$$

Where, N = Number of primary turns, L = Magnetic path length of sample, H=Maximum desired H drive, (Oersteds), I = Maximum drive current (Amperes). The ring shaped sample is magnetized by applying field through the primary winding and the magnetic flux induced in the sample under test is measured using a computer-controlled integrating flux meter attached to the secondary windings. The induced flux F resulting from the variation of the driving magnetic field (H), generates a voltage (e) in the secondary windings, equal to

$$e = NK1\frac{d\phi}{dt} \qquad \ldots\ldots\ldots\ldots\ldots\ldots\ldots (3.2)$$

Therefore,

$$\Phi = \frac{1}{K1N}\int edt \qquad \ldots\ldots\ldots\ldots\ldots\ldots\ldots (3.3)$$

Where, F = total flux induced in the test sample by the driving magnetic field (H), dt=time differential, N = Number of secondary turns, K1 = 1 for S.I. system. A typical AMH-401 output hysteresis plot is shown in fig-3.4b. In this technique, the secondary winding voltage induced by the magnetic flux in the material is measured directly by a high-speed data acquisition system and the values of AC coercivity and core losses

of the samples were calculated using software. The test frequency range was in between 3 to 500 kHz. AC permeability measurements were performed with field amplitude of 5 Oe. A sinusoidal was used during the experiments. For nanocrystalline studied the toroid-shaped samples were annealed in an argon atmosphere above the primary crystallization temperature.

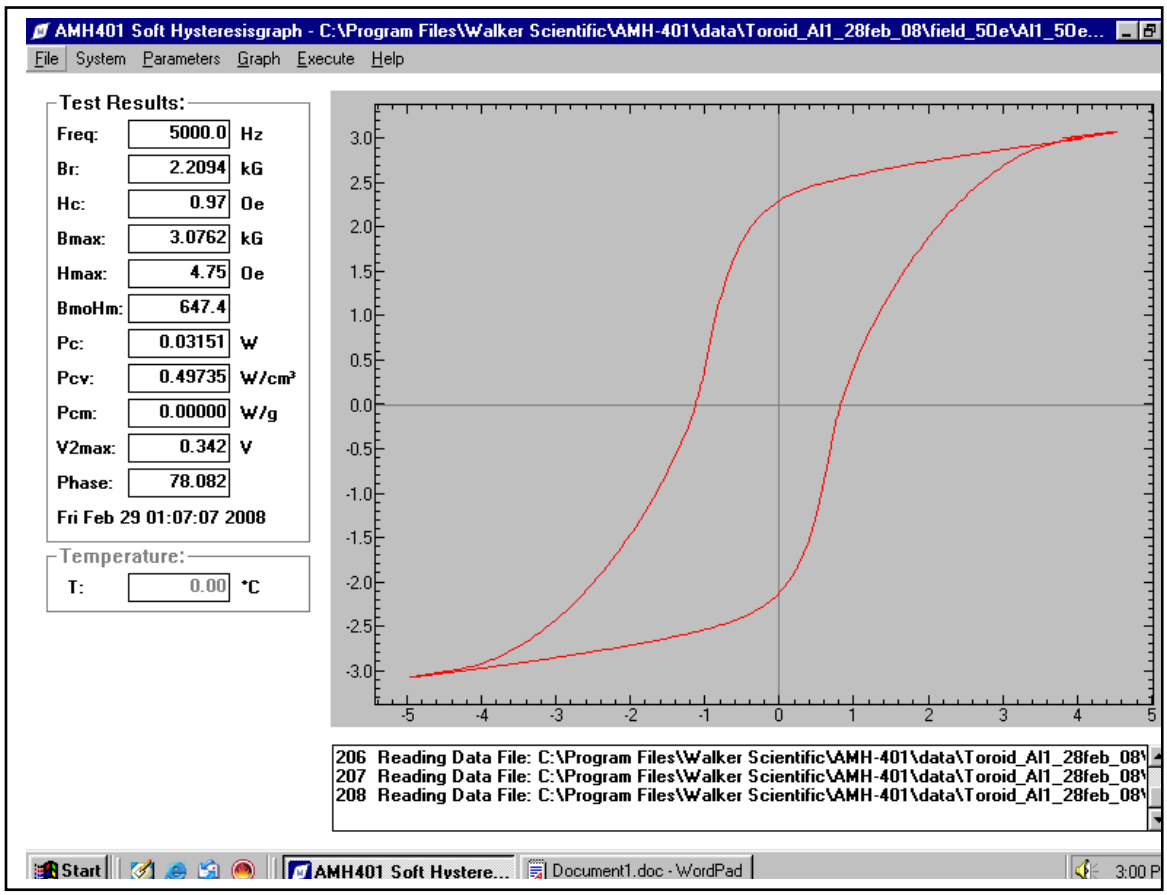

Fig-3.4(b): Typical output of AC hysteresis plot obtained from AMH-401.

3.4.3: Determination of Curie temperature and saturation magnetization

The Curie temperature and saturation magnetization were measured by vibrating sample magnetometer, Model 7404, make: Lake Shore in the present study. Saturation magnetization has been measured at the room temperature of the as cast along with

different heat treated alloys at a field 12 KG. Samples having 2mm length, 2mm width and 30 micron thickness were fixed in a side mounting holder and kept parallel to the magnetic field to reduce the demagnetization factor. The temperature dependence magnetization curve for the high temperature and low temperature study was carried out using a vibrating sample magnetometer (VSM, Lake Shore: Model 7404) attached with the high temperature furnace and cryostat respectively. For the high temperature study samples was heated from room temperature to 1175K in the rate of 5 K/min in an argon environment at a field of 2 KG. Curie temperature was evaluated from this study. For low temperature study sample was cooled from room temperature to 77K by using liquid nitrogen. Spin wave behavior has been investigated from the low temperature study.

3.5: Structural behaviour study

3.5.1: X-ray diffractogram

The amorphicity of the melt-spun ribbons and the different phases generated during crystallization were investigated by X-ray diffraction method using Philips D-500 X-ray equipment with CuKα radiation. The sample was scanned at room temperature from 20 degree to 90 degree at a scan rate of 2 degree/min. The magnitude of scattering vector has been evaluated from the major primary peak of the X-ray diffractograms using the equation 3.4 [12].

$$K - \frac{4\pi \mathrm{Sin}\theta}{\lambda} \qquad \ldots\ldots\ldots\ldots\ldots\ldots\ldots\ldots (3.4)$$

Where K is the scattering vector, Θ is the diffracting angle of the major primary peak obtained from X-ray diffractograms, and λ is the wavelength of the CuKα radiation.

3.5.2: Transmission electron microscopy

For micro structural behavior studies of the amorphous and heat treated ribbons samples were carried out using Transmission electron microscope of model Philips,

CM-200. The sample preparations were carried out by electro polishing technique followed by ion beam milling. A mixture of 90% glacial acetic acid and 10% perchloric acid at low temperature was used as electrolyte for thinning the sample.

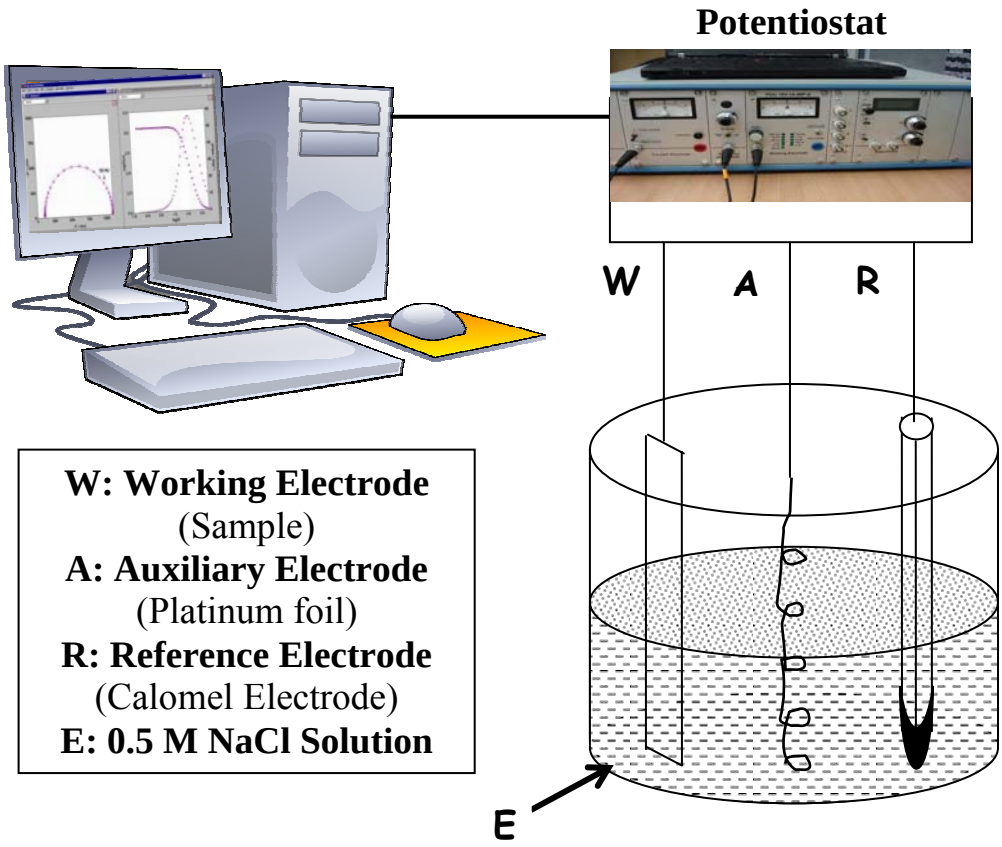

Fig-3.5: Schematic diagram of electrochemical cell.

3.6: Electrochemical behaviour study

The electrochemical behavior and corrosion process of the optimum alloys was studied in 0.5M NaCl solution. Both the polarization and electrochemical impedance spectroscopy (EIS) was carried out using computer controlled Potentiostat model No: PC4/750, make: M/s Gamry Instruments, USA and their accompanying software GPES (general purpose electrochemical system) and FRA (frequency response

analyzer system). The schematic diagram of the electrochemical cell has shown in figure-3.5. The auxiliary electrode was a platinum foil, the reference electrode was the saturated calomel electrode (SCE) and the ribbons were acted as the working electrode. A 0.5M NaCl solution was prepared from reagents grade chemicals and deionized water. The ribbons were cleaned in acetone and next covered protective layer exceptions of the tested part of surface having about 0.4 cm^2 area in each ribbons and dried in air. Both the polarization curve and electrochemical impedance spectroscopy data was obtained after holding the samples at open circuit potentials for 20 min in order to stabilize the circuit. In the anodic polarization test the alloy was scanned at the rate 2 mV/s from negative (cathodic) overpotential and ending at positive (anodic) overpotential at room temperature. The scan rate was chosen to be slightly high so as to avoid the total anodic dissolution of the very thin samples prior to the completion of the test. The corrosion potential E_{corr} (mV), corrosion current density i_{corr} (A/cm^2) have been determined using Tafel method. The value of i_{corr} can be calculated by fitting the experimental data to the following Tafel equation used by the theoretical model for the current-potential relationship [13]

$$i = i_{corr} [10^{(E- Ecorr)/ba} – 10^{-(E- Ecorr)/bc}]\ldots. \qquad (3.5)$$

The electrochemical impedance measurements were carried out in the frequency range between 10^5 Hz and 0.1 Hz.

3.7: Summary of the work done

Amorphous ribbons having more than a meter length, 2mm width and 30 micrometer thickness were obtained using melt spinning technique. The good quality ribbons were obtained by using the crucible with nozzle diameter of 1.5 mm placed at the distance of 0.5 mm from the quenching wheel. The wheel speed was 1400 rpm. The amorphous ribbons were annealed at different temperatures to optimize its nano-structured state. The crystallization behavior was studied using differential scanning calorimeter and Thermal electrical resistivity. DC magnetic hysteresis loop was

measured for the as cast and heat treated sample using a computer controlled hysteresis loop tracer developed at the laboratory. AC hysteresis loop was measured for the as cast and heat treated samples using AMH–401 automatic hysteresis graphs. Corrosion behavior was studied using the polarization curve and electrochemical impedance spectroscopy method.

References

[1] D. Raskin and C. H. Smith in "Amorphous Metallic alloys" edited by F.E. Lubrosky, Butterworths, London, p 381 (1983).

[2] M.Hagiwara, A.Inoue, in Rapidly Solidified Alloys: Processes, Structures, Properties, Applications, ed. H.H. Liebermann. Marcel Dekker Inc., New York, Chap. 6, p 139 (1993).

[3] H.Chiriac and T.A.Ovari, Prog. Mater. Sc. Vol. 40, p 333 (1996).

[4] H.S.Chen, Acta Metall. Vol. 22, p 1505 (1974).

[5] A.Inoue and T.Masumoto, Eng. Mater. Vol. 30, p 47 (1982).

[6] A.Mitra and M.Vazquez, J. Magn. Magn. Mater. Vol. 87, p 130 (1990).

[7] J.N.Nderu, Y.Shinokawa, J.Yamasaki, F.B. Humphrey and I.Ogasawara, IEEE Trans. Magn. Vol. 32, p 4878 (1996).

[8] Ohnaka, T.Fukusako and T.Matui, J. Jpn Inst. Met. Vol. 45, p 751 (1981).

[9] A.K.Panda, S.Basu and A.Mitra, J. Magn. Magn. Mater. 261(1-2) p 190 (2003).

[10] M. A. Willard, T. Francavilla and V.G. Harries, J. Appl. Phys. Vol. 97, 10F502 (2005).

[11] B.D. Cullity, C.D. Graham, Introduction to magnetic materials. Wiley IEEE Publ. 2nd edition p 16 (2008).

[12] "Elements of X-ray Diffraction" by B.D.Cullity, (Addison–Wesley publ.co) Massachusetts, p 554 (1978).

[13] D.C. Qiao, B. Green, M. Morrison and P.K. Liaw, Rev. Adv. Mater. Sci., Vol. 18, p 149 (2008).

Chapter-4

Optimization of Co-Fe stoichiometry in CoFeSiNbB system to get good soft magnetic properties and high Curie temperature

4.1: Introduction

Stability of ferromagnetic ordering has been a subject of immense concern in designing soft magnetic components for high temperature applications. These components typically include switches, cores, magnetic bearings, transformers and rotor assemblies in space power systems and jet engines [1-2]. The essential requirement of such magnetic applications is high Curie temperature (T_C). The efficiency of these components is a subject of study for the minimization of power loss at high thermal environments and frequency. For enhancing the working temperature, T_C of the material is conventionally enhanced by the incorporation of cobalt in Fe-based crystalline systems [3]. However, the inherent strong anisotropy constant of such materials is a major hurdle in achieving superior soft magnetic properties. The magnetic and electrical properties have been drastically improved with the advent of Fe-based nanostructured alloys [4]. The benefits arising out of such nano-regimed composite materials with cobalt incorporation for extension of ferromagnetic ordering has become a subject of intense research in recent years. However, the major challenges these investigations face is arriving at the optimal alloy composition, acceptable soft magnetic properties in combination with high T_C. The present investigation is an attempt to optimize the Co-Fe stoichiometry in CoFeSiNbB nanostructured alloy system and correlating the effects of cobalt incorporation on nanostructured developments with magnetic properties for high temperature applications.

4.2: Brief resume of previous work

The conventional soft magnetic crystalline alloys for high temperature applications are constrained to Co or (CoFe) based poly crystalline alloys, due to the relatively

high Curie temperature of Co and its alloys. The Co-Fe alloy with Co:Fe ratio of 50:50 exhibits large permeability, high saturation induction and high Curie temperature close to ~1200K, but inferior soft magnetic properties such as coercivity in the order of ~1Oe. The high coercivity is due to high crystalline anisotropy associated with restricted domain wall movement in a crystalline matrix. With the advent of methodology to develop nanocrystalline materials from amorphous precursor, it becomes simpler to lower crystalline anisotropy by taking the advantage of its inherent nanostructure. The most significant features in such materials are as follows: (1) the nanocrystals are dispersed within amorphous matrix, (2) the nanocrystals work as single domain, (3) the domain wall movement is smooth and efficient without any pinning effect because of the smoother interface between nanocrystal and matrix. So, efforts are made to tailor amorphous magnetic materials bearing low or negligible crystalline anisotropy with enhanced soft magnetic properties. It resulted in the development of new generation of FeNbCuSiB-based nanocrystalline alloy systems [4] with lower crystalline anisotropy, low magnetostriction and higher electrical resistivity. These additional features increased the potential of these Fe-based nanocrystalline alloys in applications like transformer cores, choke coils, magnetic sensors, etc. [5], operating at room temperature. However, at elevated operating temperatures these nano-materials lose their ferromagnetic stability due to their low Curie temperature below 700K [6]. Subsequently nanomaterials of Co substituted FeZrB-based system developed with a typical composition of $Co_{44}Fe_{44}Zr_7B_4Cu_1$ are reported to have a fairly high Curie temperature above 1000K [7–9]. As Zr tends to oxidize at high temperature, this material is oxidation prone and is not suitable for desired application. Simultaneously, the study on Co substituted FeCuNbSiB-based nanocrystalline systems [10-12] is in progress to extend their outstanding soft magnetic properties to elevated temperatures. The present study is focused to develop nanocrystalline alloy from an amorphous precursor of FeCuNbSiB system, partly substituted by Co.

4.3: Material composition

The alloys used for the present study are the melt spun amorphous ribbons of following compositions and their nanocrystalline progenies.

Alloy I: $Co_{10}Fe_{62}Si_4Nb_4B_{20}$

Alloy II: $Co_{20}Fe_{52}Si_4Nb_4B_{20}$

Alloy III: $Co_{36}Fe_{36}Si_4Nb_4B_{20}$

Alloy IV: $Co_{50}Fe_{22}Si_4Nb_4B_{20}$

The melt spun ribbons having a dimension of 10 cm in length, 0.2 cm in width and 30 micro-meters in thickness were used for DC magnetic measurement. The nanocrystalline alloy derivatives were prepared by the controlled annealing of amorphous ribbons in an argon atmosphere at a heating rate of 20 K/min.

4.4. Results

4.4.1: Crystallization study

4.4.1.1: Differential scanning calorimetry (DSC)

The crystallization temperature and glass transition material of melt spun ribbon of $Co_xFe_{72-x}Si_4Nb_4B_{20}$ (x = 10, 20, 36, 50 at%) alloys are measured by differential scanning calorimetry under argon atmosphere with a scan rate of 20K/min and the DSC curves are presented in fig.4.1. Differential scanning calorimetry (DSC) plots of all the alloys reveal distinct changes in heat flow profiles indicating exothermic transformation with the onset of crystallization at T_{X1}. This transformation is preceded by onset of glass transition represented by a low intensity endothermic peak at T_g. The evidence of onset of glass transition supports the glass formability of this cobalt substituted Fe-based alloy system under study [13]. The DSC profiles in the operatable range of 975K also exhibited high temperature secondary crystallization at T_{X2} observed only in alloys with higher cobalt contents. The crystallization onset T_{X2} increased with reduction in cobalt content and was thus not observed in the current operatable range of the instrument for $x < 36$ at% alloys. The characteristic temperatures obtained from DSC plots are shown in table-4.1. Both these temperatures indicated an almost similar drop by 75K as the cobalt content was increased from 10 at% to 50 at%. All the alloys displayed wide super cooled region of ΔT_X ($T_{X1} - T_g$) in the range of 45K to 55K. The activation energy (E_{X1}) for the primary crystallization (T_{X1}) was obtained from peak shift temperatures with different scan rate using the method of Kissinger equation [14].

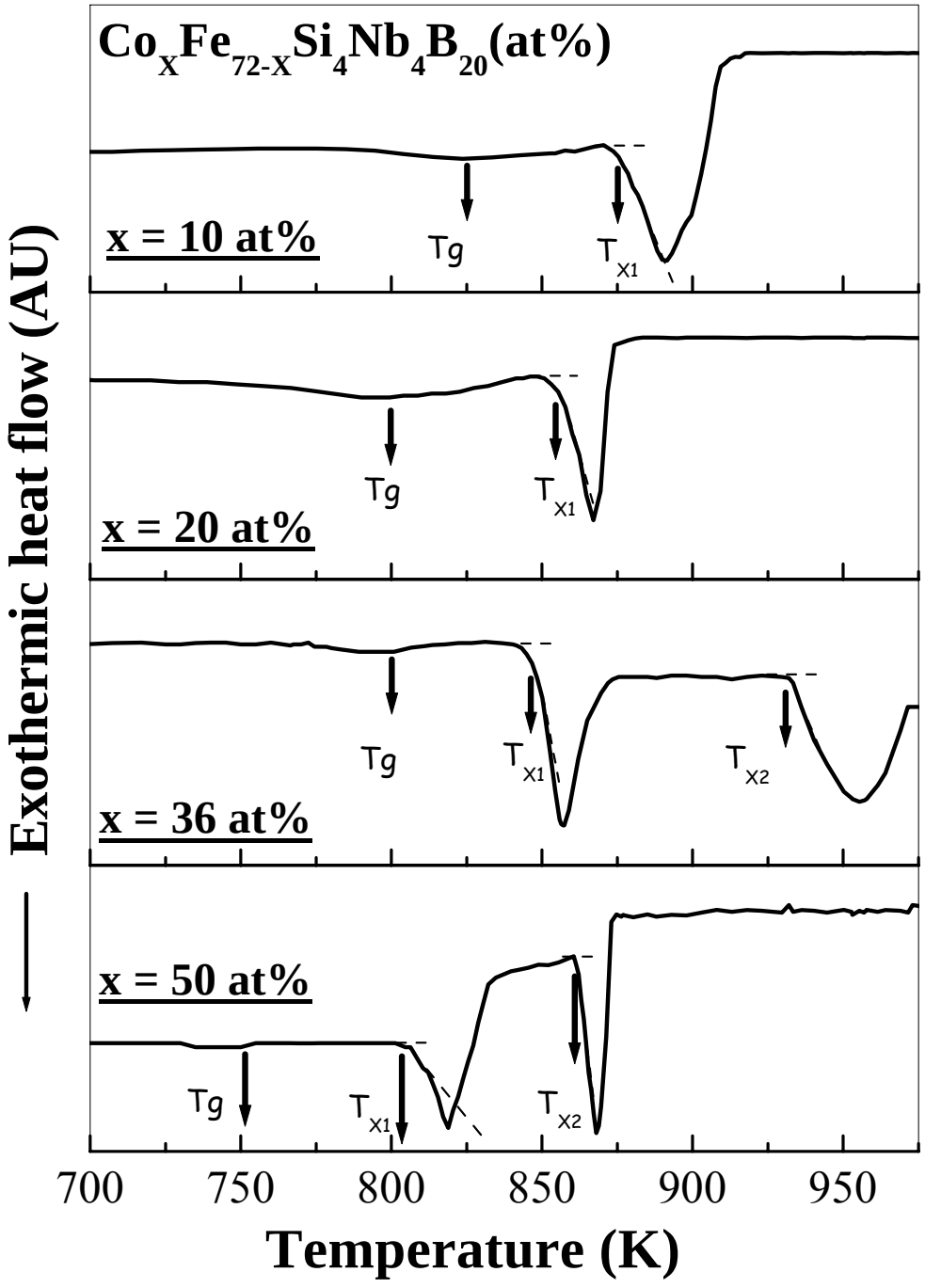

Fig- 4.1: DSC thermo grams of melt spun $Co_xFe_{72-x}Si_4\ Nb_4B_{20}$ (x=10, 20, 36, 50 at%) alloys at a heating rate of 20K/min

$$ln\left(\frac{\emptyset}{T_p^2}\right) = -\frac{E}{(RT_p)} + \text{constant} \ldots\ldots\ldots\ldots (4.1)$$

Where ϕ is the heating rates, R is the ideal gas constant, T_p is the peak temperature and the activation energy E allows for the energy barrier opposing the phase transformation to be quantitatively described. Fig-4.2 shows the Kissinger plot of the amorphous $Co_xFe_{72-x}Si_4Nb_4B_{20}$ (x = 10, 20, 36, 50 at%) alloys, which yields the activation energy. The trend of variation in T_{X1} and T_g and activation energy (E_{X1}) with cobalt content is also shown in fig-4.3. Though the variation in E_{X1} is small but it is observed to decrease with increasing Co-content in the alloys.

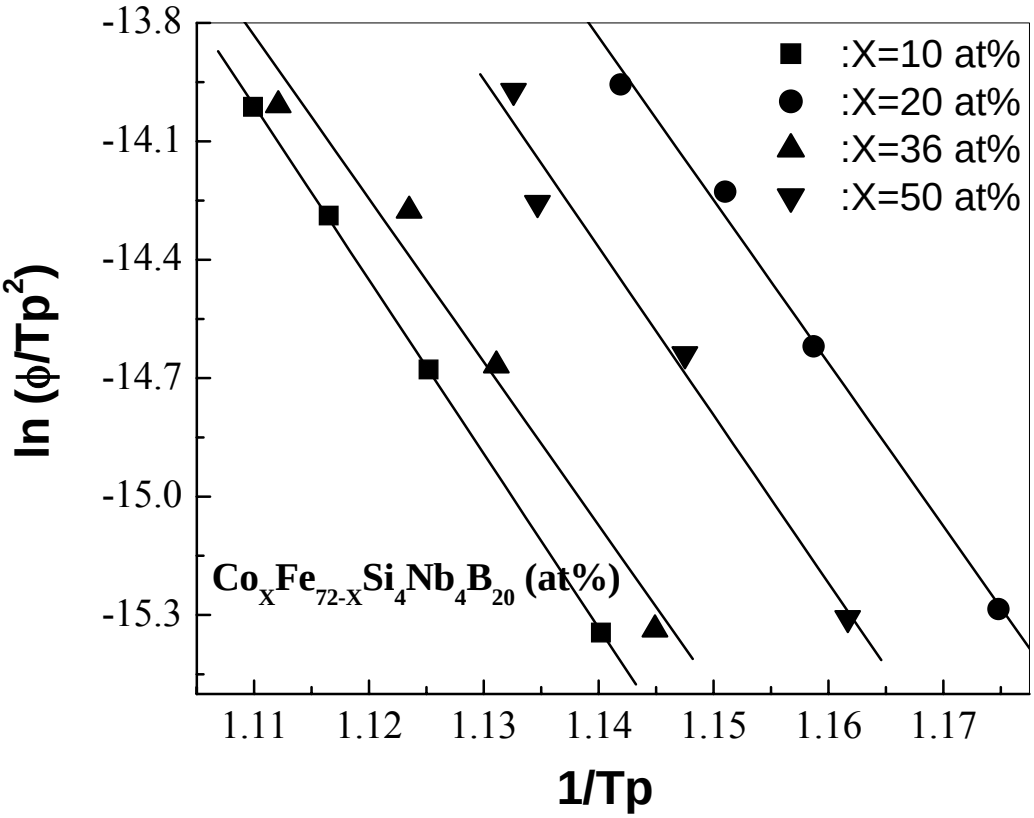

Fig- 4.2: Kissinger plot of $Co_xFe_{72-x}Si_4B_{20}Nb_4$ (x = 10, 20, 36, 50 at%) alloys

Table-4.1: Characteristic temperatures obtained from Differential scanning calorimetry measurements

Cobalt content (at%)	Glass transition temp.(T_g) (K)	Primary cryst. Temp.(T_{X1}) (K)	ΔT_X (T_{X1}- T_g) (K)	Secondary Cryst. temp.(T_{X2}) (K)
10	825	875	50	*
20	800	855	55	*
36	800	845	45	930
50	750	802	52	860

* Expected to be beyond current scope of measurement up to 975K

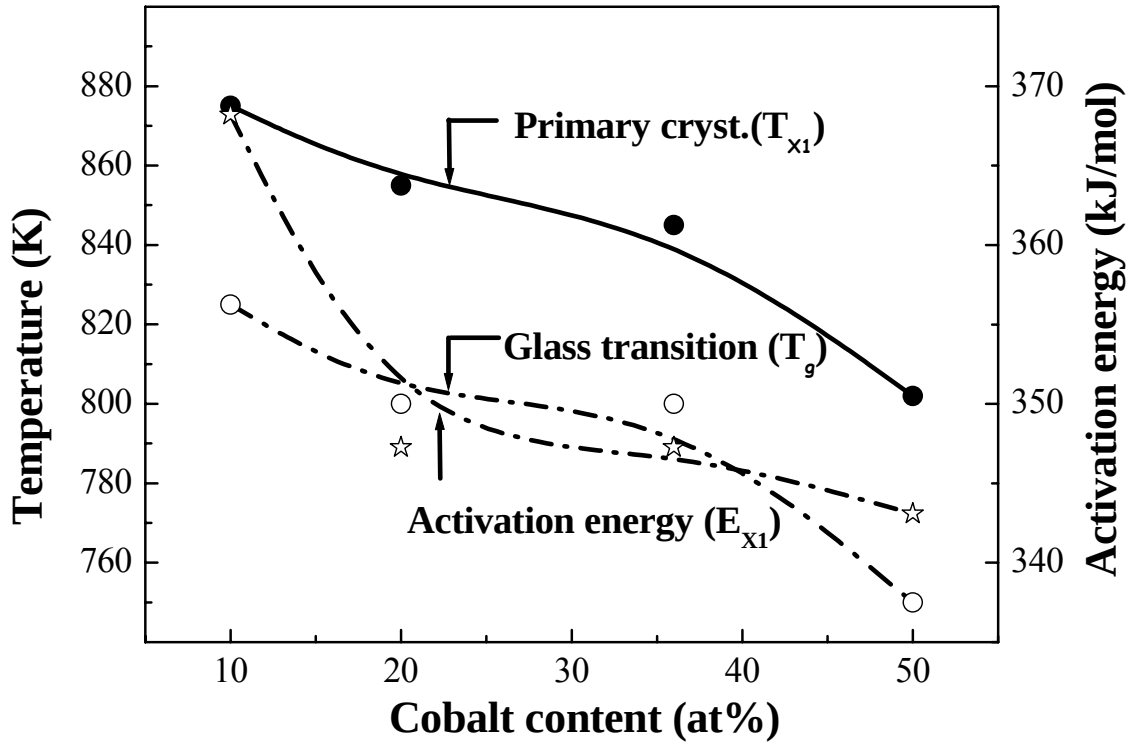

Fig-4.3: Variation in onset of primary crystallization (T_{X1}), glass transition (T_g) and activation energy (E_{X1}) with cobalt content in alloys

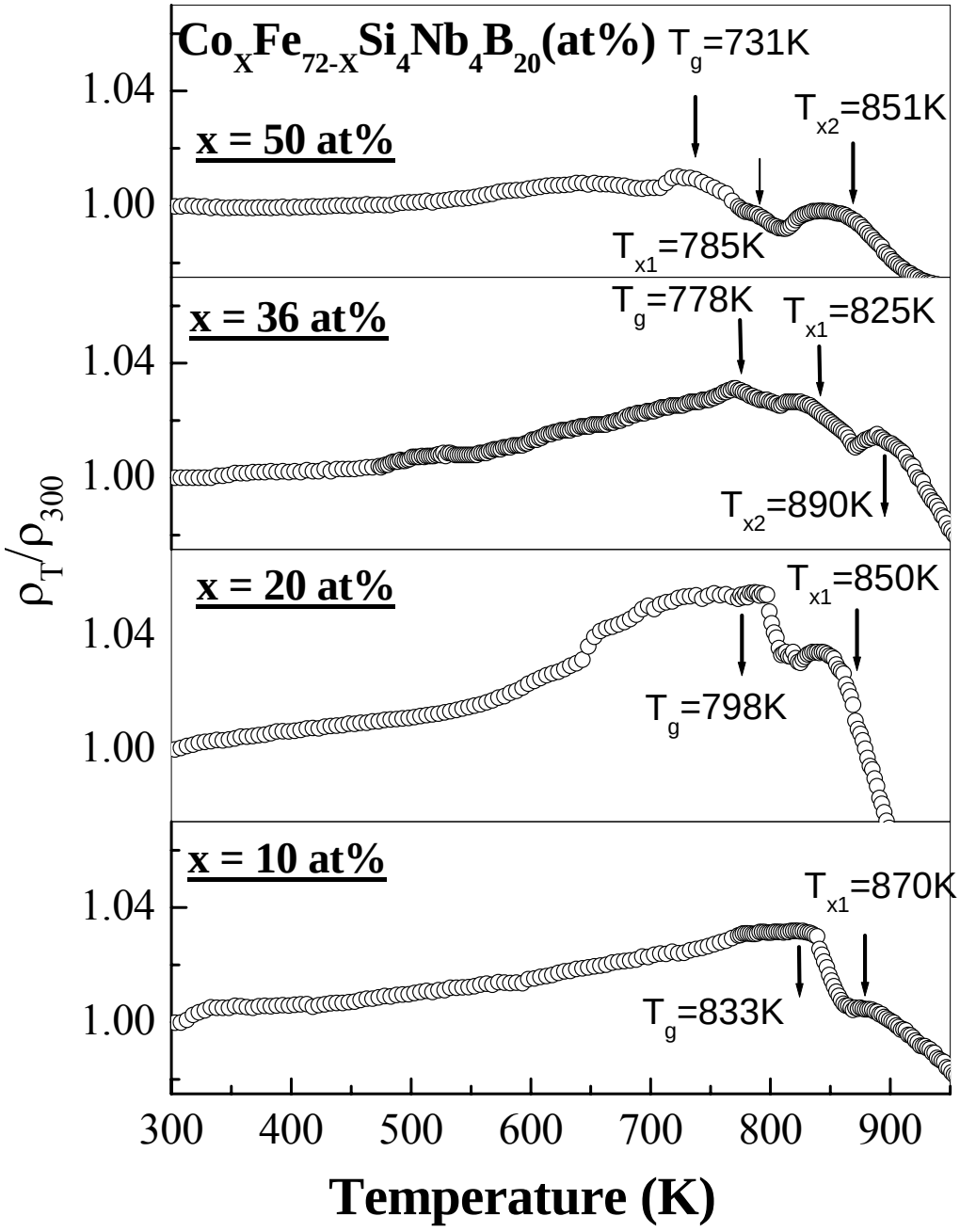

Fig-4.4: Thermal variation of electrical resistivity plot of as spun $Co_xFe_{72-x}Si_4B_{20}Nb_4$ (x = 10, 20, 36, 50 at%) alloys. Scan rate 10K min^{-1}

4.4.1.2: Thermal variation of electrical resistivity (TER)

Fig-4.4 shows the Temperature dependent electrical resistivity plot of $Co_xFe_{72-x}Si_4Nb_4B_{20}$ (x = 10, 20, 36, 50 at%) alloys obtained at scan rate of 10 Kmin^{-1}

in an argon atmosphere. The results are plotted after normalizing with respect to room temperature values. In all the four alloys, the electrical resistivity initially monotonically increases with the rise in temperature (from room temperature onwards), which is attributed to electron-magnon and electron-phonon scattering phenomena, and drops drastically in several steps at higher temperature. The first drop of electrical resistivity occurs at a temperature of 833K for the amorphous alloy with low Co content (x = 10 at%). This temperature systematically lowers to 798K, 778K and 731K with the increase in Co-content i.e., x = 20, 36 and 50 at% respectively. This characteristic temperature of first drop in resistivity is correlatable to the corresponding glass transition temperature 'T_g' of 825K, 800K, 800K and 750K for increasing Co-content of x = 10, 20, 36 and 50 at% respectively. Beyond T_g, the change in electrical transport behaviour becomes very significant with rapid changes in TER profile. Above the glass transition temperature, there is sharp decrease in resistivity in several steps corresponding to different crystallization stages at T_{X1}, T_{X2} and T_{X3} respectively.

4.4.2: Structural behaviour study

4.4.2.1: X-ray diffraction

The amorphous alloys were heat treated at a temperature close to crystallization temperature as suggested by DSC and TER and the phases were characterized by X-ray diffractograms (Fig.-4.5, 4.6). The X-ray diffraction pattern of as-spun ribbon shows a broad peak indicating the non-crystalline amorphous phase. Fig-4.5 and 4.6 represent the X-ray diffractograms of the alloy heat treated at 775K and 875K respectively. The XRD pattern for as cast alloy exhibits broad peak whereas that for heat-treated ones show sharp peaks suggesting partial devitrification of amorphous alloy to nanocrystalline state on controlled annealing. The alloys with high cobalt content (x = 50 at%) with the lowest temperature of primary crystallization 'T_{X1}' has been observed. This was evidenced from an early evolution of phases in the alloy with x = 50 at% indicating its lowest DSC onset T_{X1} at 802K. The X-ray analysis of samples annealed at 775K (fig-4.5) showed the incipient generation of bcc-FeCo phase in this alloy with a possible combination with Si while the other alloys with low Co-content still indicated a stable amorphous structure with a broad halo. The

X-ray diffractogram for this alloy indicated phase evolution around 25K lower than the DSC onset temperature which may be attributed to the higher sensitivity of the former technique.

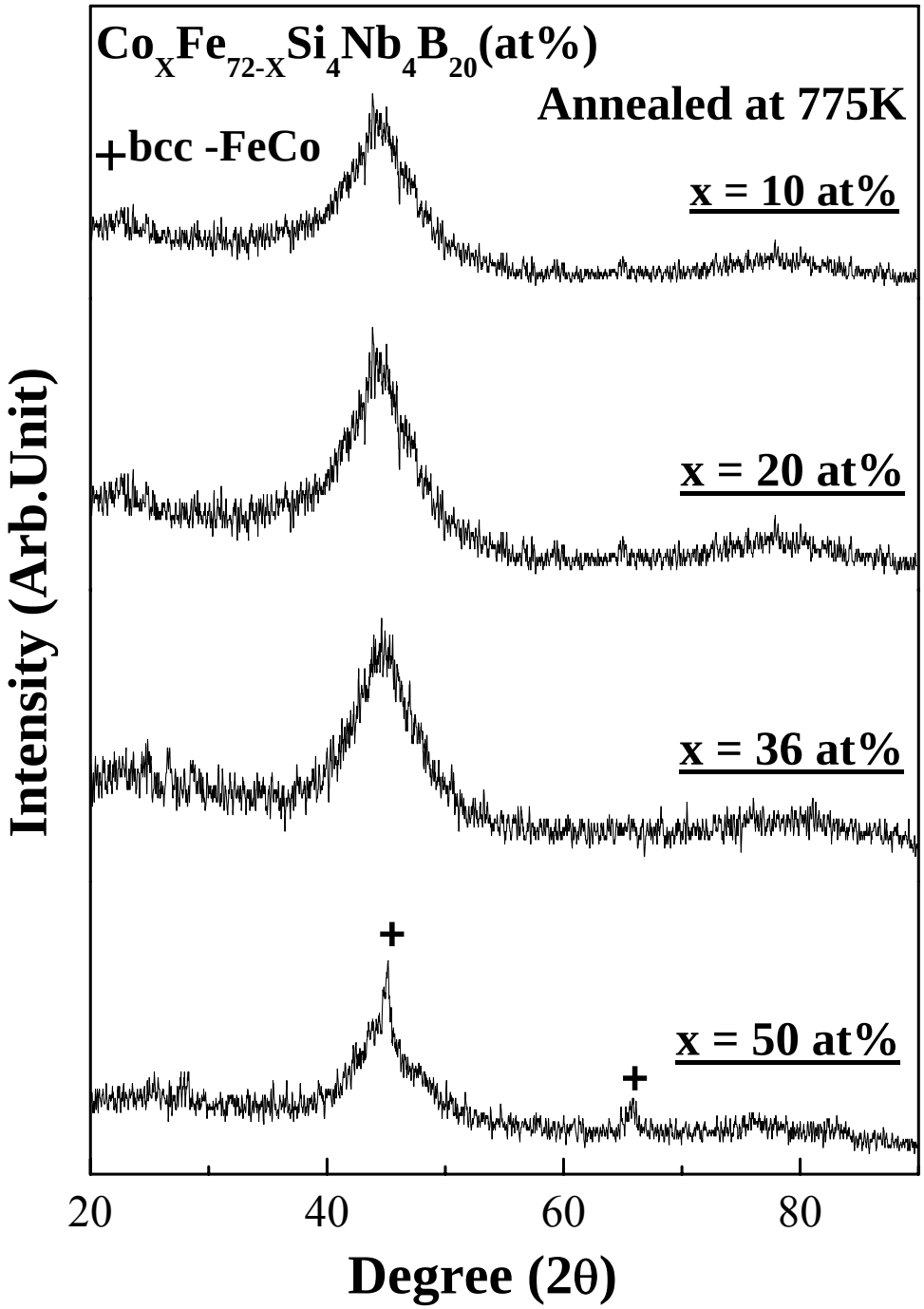

Fig- 4.5: XRD plots of $Co_xFe_{72-x}Si_4Nb_4B_{20}$ (x = 10, 20, 36, 50 at%) ribbons annealed at 775K

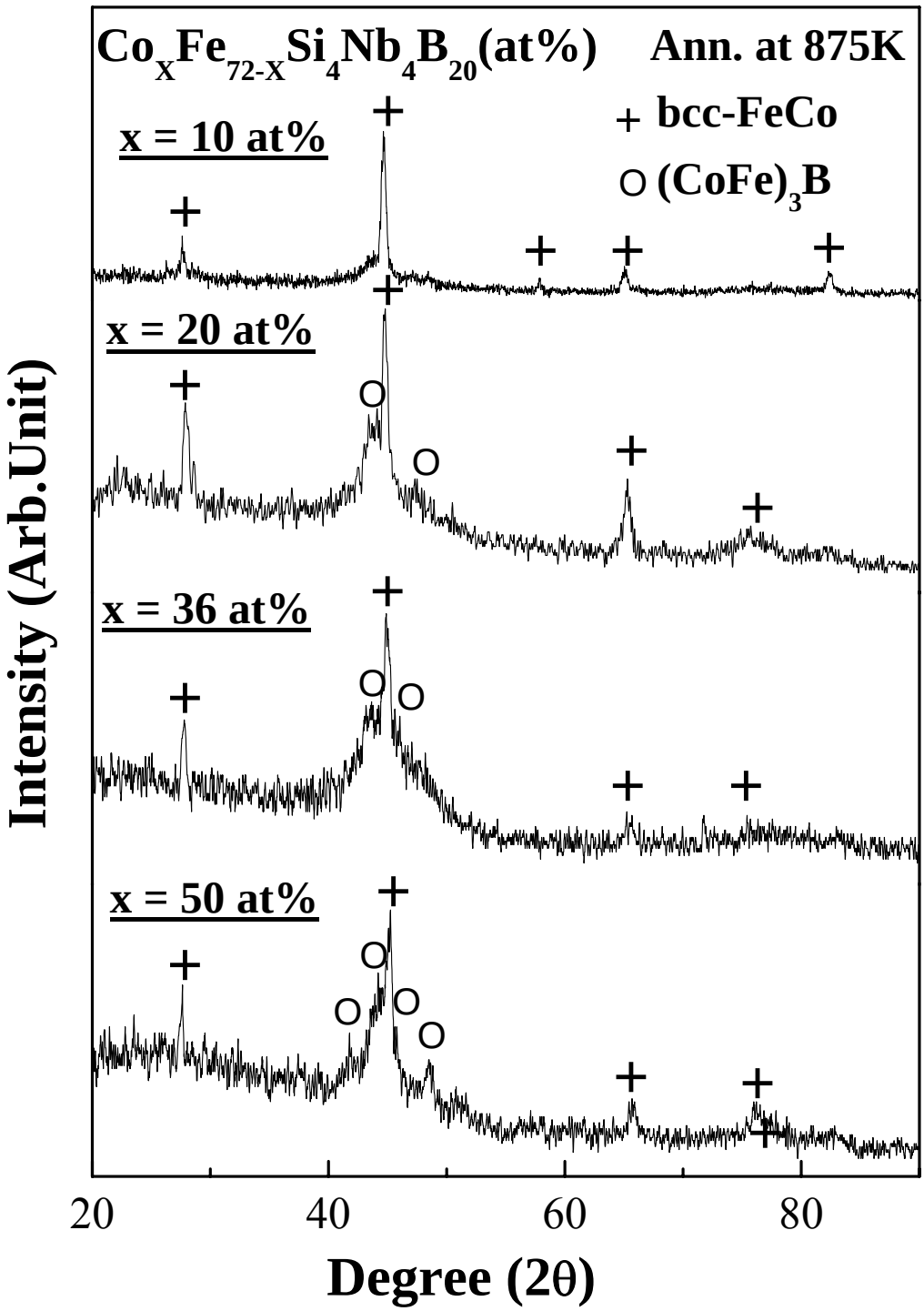

Fig- 4.6: XRD plots of $Co_xFe_{72-x}Si_4Nb_4B_{20}$ (x = 10, 20, 36, 50 at%) ribbons annealed at 875K

To investigate the phases obtained during annealing lower and higher temperature of the primary crystallization (T_{X1}) of all the alloys. XRD plots were obtained for samples annealed at 875K and shown in fig-4.6. The temperature at 875K corresponds to exactly T_{X1} for x = 10 at% alloy, therefore the formation of only bcc-FeCo was observed. However, the alloys with x ≥ 20 at% a low volume fraction of $(CoFe)_3B$ was incipiently generated whose increasing content was also revealed with a reduction in the onset of secondary crystallization temperature (T_{X2}).

4.4.2.2: Transmission electron microscopy

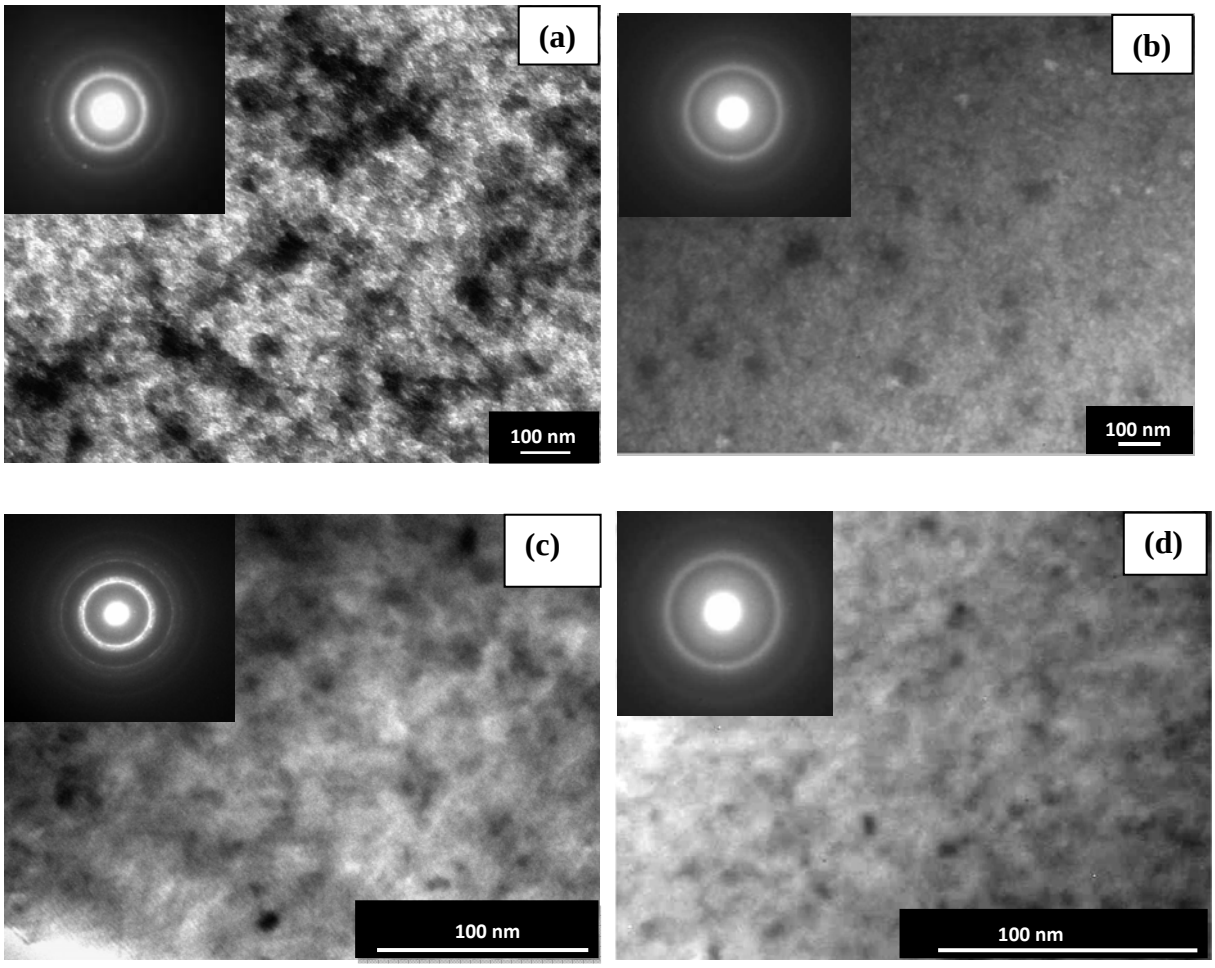

Fig- 4.7: Bright field images of (a) x = 10 (b) x = 20 (c) x = 36 and (d) x = 50 at% heat treated at 875K for 15 min. SAED patterns shown in the inset

Microstructures of these material were studied by transmission electron microscopy for the as cast and different heat treated samples. Fig- 4.7 shows TEM images and corresponding selected area electron diffraction (SAED) patterns of as spun along with heat-treated at 875K for x= 10, 20, 36, 50 at% alloys. The diffused halo SAED pattern which is shown in the inset of microstructure in as cast state of all alloys, which confirm the material to be in amorphous state. With annealing, the diffused SAED pattern transforms to ring pattern supporting the development of nanocrystalline phases in amorphous matrix. With increasing annealing temperature, the crystal size and the grain population increase. From the TEM micrograph it has been observed that the particle size decreases with increasing cobalt content.

4.4.3: Soft magnetic properties

4.4.3.1: DC coercivity

The phase transformation was also observed from the variation in coercivity with annealing temperature. Fig-4.8 presents the variation of DC coercivity with annealing temperature for $Co_xFe_{72-x}Si_4Nb_4B_{20}$ (x = 10, 20, 36, 50 at%) alloys. The alloys were annealed at different temperatures within the range from room temperature to 923K in an argon environment. It was observed that all the alloys exhibited fairly consistent coercivity till 850K. Beyond this temperature, the degradation in coercivity was evident in all the alloys. However, such deterioration in soft magnetic properties was minimal in alloy with an optimum content of cobalt of x = 36 at%, whereas cobalt content either above or below this concentration in the present alloy exhibited deleterious effects. The minimum coercivity is observed of x = 36 at% (Co:Fe::50:50) alloy of as cast and subsequent its nanocrystalline state. The stoichiometry close to Co:Fe :: 50:50 (at%) in alloys ($K_1 \sim 0$) crystalline anisotropy is minimum may be the reason of smaller coercive field [15]. The smaller grain size in the order of ~ 14-15nm may be responsible for softening the material with relatively consistent and smaller coercivity (< 50 A/m).

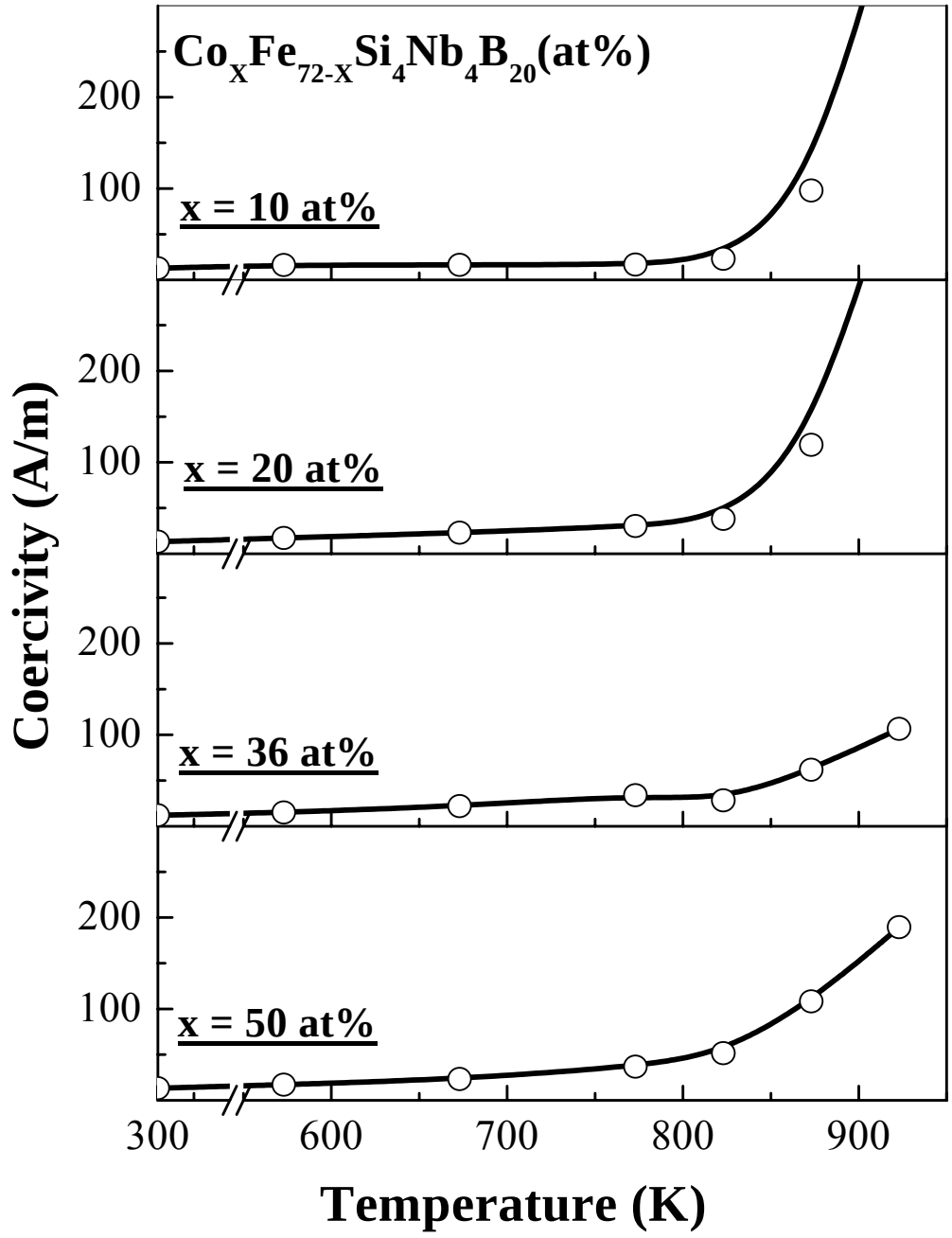

Fig- 4.8: Variation of coercivity with annealing temperature in $Co_xFe_{72-x}Si_4Nb_4B_{20}$ (x = 10, 20, 36, 50 at%) ribbons

4.4.3.2: Curie temperature and saturation magnetization

The temperature dependent magnetization curve of as spun $Co_xFe_{72-x}Si_4Nb_4B_{20}$ (x=10, 20, 36, 50 at%) alloys has shown in fig-4.9. In these plots the sharp drop in

magnetization indicated, the Curie temperature (T_c) of these alloys whereby its amorphous matrix transformed from its ferromagnetic to paramagnetic state.

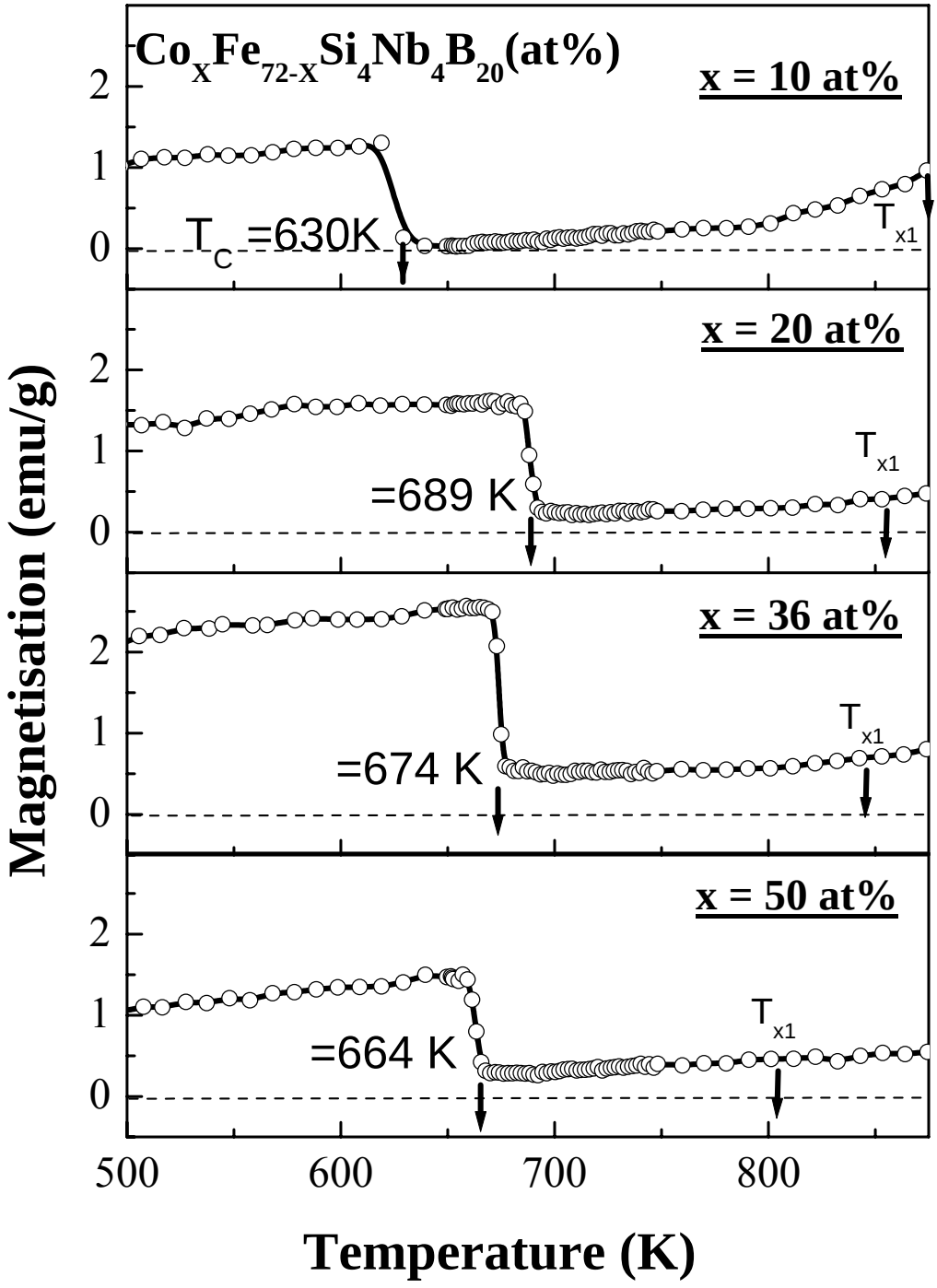

Fig- 4.9: Thermo-magnetization curves of as-cast $Co_xFe_{72-x}Si_4Nb_4B_{20}$ (x = 10, 20, 36, 50 at%) alloys

The estimated Curie temperature in amorphous phase was 630K, 689K, 674K and 664K for alloys x = 10, 20, 36, 50 at% respectively. However at elevated temperature beyond 800K, magnetization again increased due to the generation of ferromagnetic bcc-FeCo nanophases in amorphous matrix. In the case of all alloys the increase of magnetization was observed close to the crystallization temperature (T_{X1}). This may be attributed to the formation of bcc-FeCo nanophases in amorphous matrix. Fig- 4.10 shows the variation of Curie temperature with varying Co content of as cast along with heat treated at 875K. For as spun and heat treated alloys, the Curie temperature was found to increase and then drop down as shown in fig-4.10.

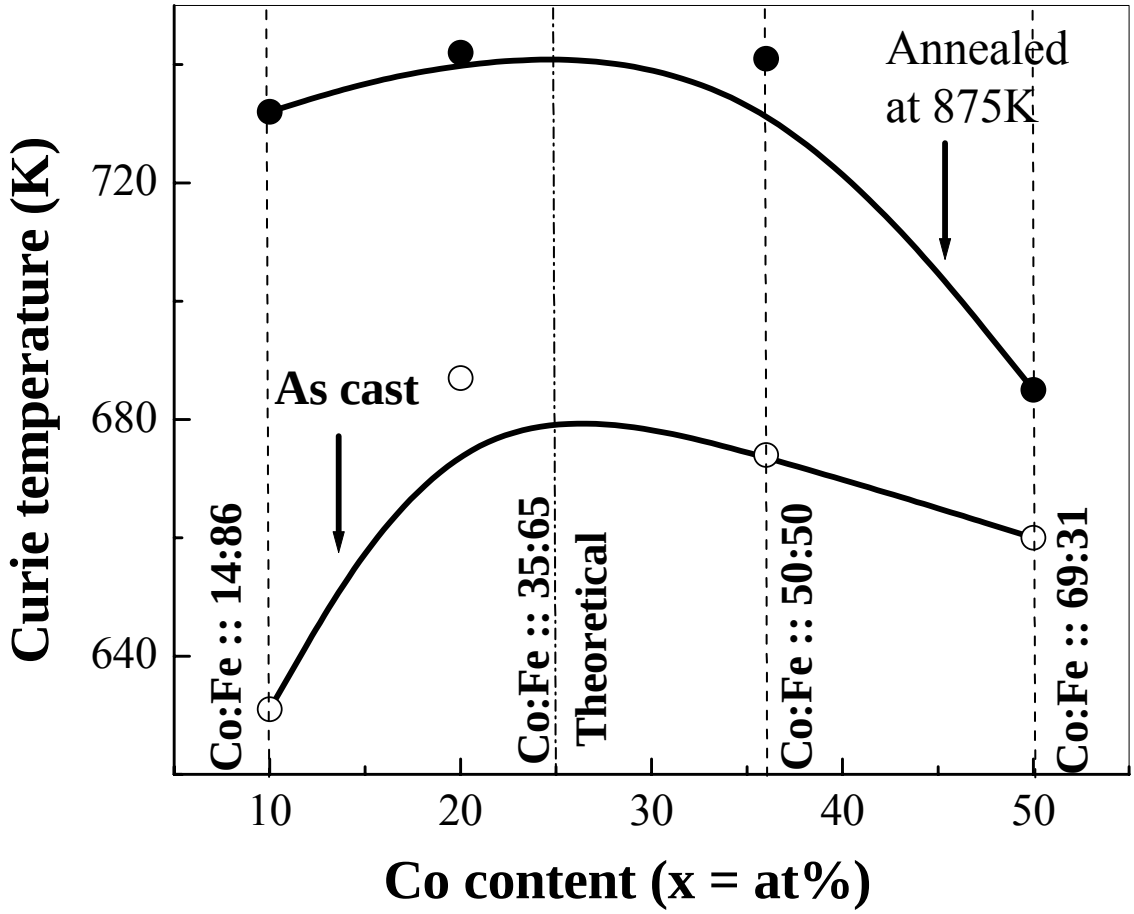

Fig-4.10: Variation of Curie temperature with cobalt content of as spun as well as annealed at 875K for 15 min

This is in accordance with the change in Co-Fe interaction as per Bethe-Slater curve [16] and is supposed to be strongly influenced by the compositional effect in amorphous state as this transition temperature is far below crystallization onsets. However, at elevated temperatures the magnetization exhibited an increasing trend beyond 800K which was due to the generation of bcc-FeCo phases in the amorphous matrix. In the case of x = 10 at% the increase in magnetization was observed at much lower temperature than the crystallization (T_{X1}) which may be attributed to formation of nanostructured α-Fe at lower temperature in Fe-riched alloy. It was also observed that at high Fe-content, the initial drop reaches a near zero magnetization value. However, as the cobalt content increase up to x = 36 at%, the magnetization does not drop to near zero value which may be attributed to the formation of CoFe-based fine crystallites in its as-cast material being responsible for raising the magnetization level. When x > 36 at%, the magnetization drop once again approaches near-zero value. Heat treatment to nanophase generation also affects the Curie temperature (T_c) of the system as observed in fig-4.10. In addition to the generation of bcc-FeCo phase, the Co-Fe stoichiometry also affected the T_c as shown in fig-4.10. It was observed that as the Co:Fe ratio changed from Co:Fe :: 14:86 to Co:Fe :: 69:31, the T_c varied in a non-linear fashion both in the amorphous state and nanocrystalline state with an expected highest theoretical value at Co:Fe :: 50:50 (indicated in fig-4.10) [17]. Amongst the studied alloys enhanced magnetic moments comparable to this equi-partitioned composition was achievable with stoichiometry close to Co:Fe :: 50:50 in the present alloy with x = 36 at% for the sample annealed at 875K.

4.5: Discussion

The incorporation of cobalt in Fe-based system as observed in previous section has been found to offer a complex effect of stoichiometric variation on magnetic and structural development for high temperature applications. From the range of cobalt content, the alloy with x = 36 at% revealed stable soft magnetic properties with an extended low coercivity with temperature (fig-4.8) in combination with enhanced ferromagnetic ordering (fig-4.10). Structural developments have a strong role in causing the deviation in these properties about a critical content of cobalt in the present alloys. During heat treatment of amorphous alloys with silicon as the metalloid, as and how the crystallization temperature T_{X1} approaches, there are

elemental combinations leading to the formation of silicide phases. This is distinctly evidenced from the shift in the primary X-ray diffraction peak of the samples annealed at 875K. The small span of diffraction angle about the primary reflection shows the peak shift towards higher angles indicating a decrease in lattice parameter. The lattice parameters were computed from the primary reflection peak (110) and corresponding Bragg's'd' spacing. Variation of lattice parameters with cobalt content at different temperatures is shown in fig- 4.11. Quantitatively, the lattice parameter 'a_α' for the formation of α-CoFe solid solution is given by the equation as follows [18-19]

$$a_\alpha\ (A) = [0.28236 + 6.4514 \times 10^{-5}\ (at\%Fe)]*10 \quad \text{----------(4.2)}$$

Using equation-4.2, the lattice parameter was calculated for the present alloys and its variation is shown in the inset of fig-4.11. The plot shows linear reduction in lattice parameter with cobalt substitution in Fe. However, in the present multi-component system, the lattice shrinkage is attributed not only due to the element Co going into solution with Fe [20] but also because of the metalloid Si combining with these ferromagnetic metals [21-22]. The decrease in lattice parameter also led to a reduction in particle size as observed from the Transmission electron micrographs of the samples annealed at 875K (fig-4.7) with selected area diffraction (SAD) patterns shown in the inset. However, a deviation in the trend of lattice parameters was found in the case of alloys with high cobalt content annealed at higher temperatures. It was observed that at elevated temperature of 925K, which was a temperature far above T_{X1}, the lattice parameter decreased in alloys with $x \leq 36$ at% while above this composition there was a rising trend. This increasing trend in alloys with $x > 36$ at% is attributed to the formation of different high temperature phase evolutions like CoFe-borides which drastically offsets the lattice shrinkage with cobalt addition in Fe. In amorphous magnetic alloy systems, the partitioning into fine crystalline phases particles led to variation in soft magnetic properties and has been modeled by Herzer [23]. The model is fitted in the present CoFe-based system for a temperature of 875K,

below which the lattice parameter shift has been found consistently decreasing irrespective of the alloying additions.

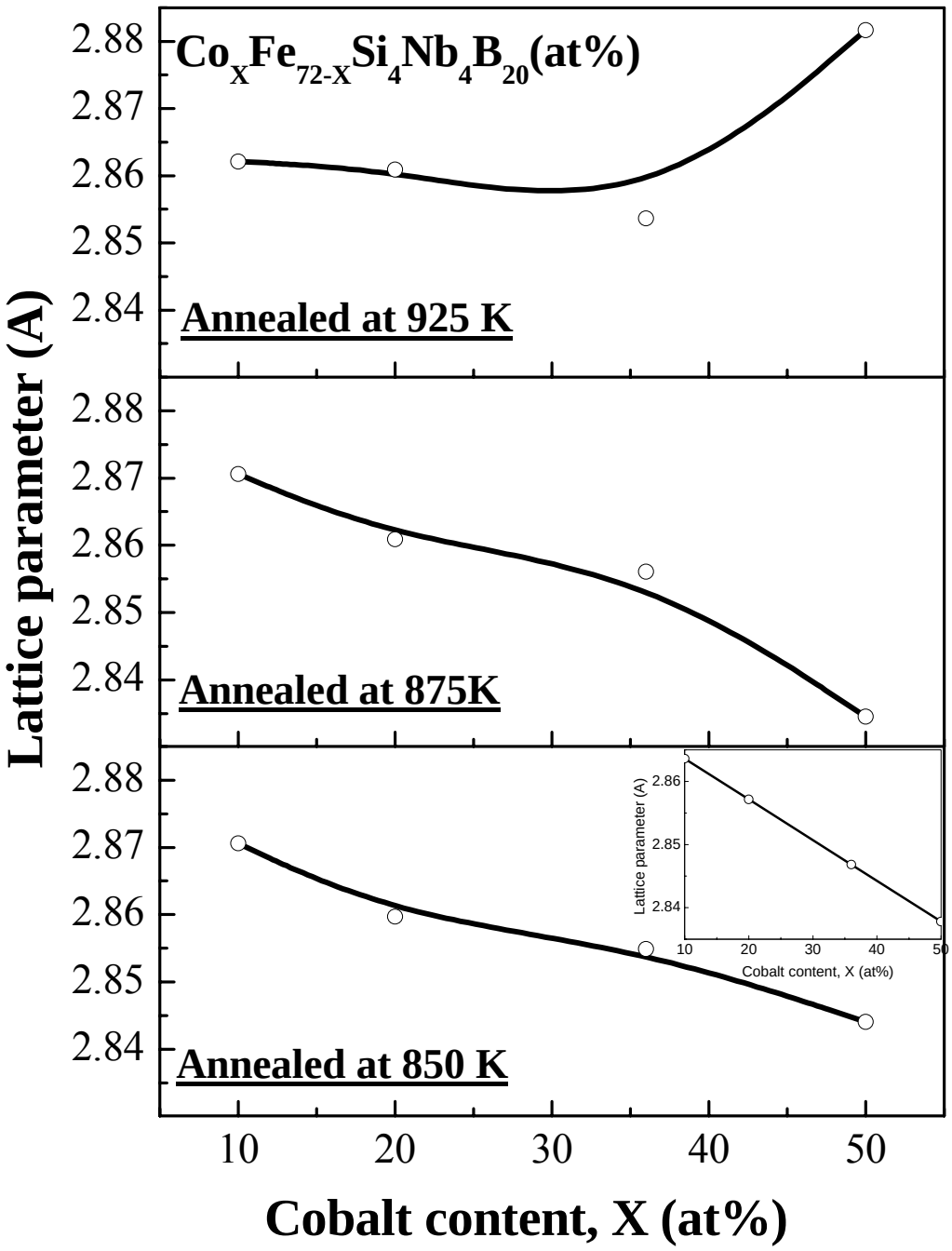

Fig-4.11: Variation of lattice parameters with cobalt content in $Co_xFe_{72-x}Si_4Nb_4B_{20}$ (x = 10, 20, 36, 50 at%) ribbons annealed at 850K, 875K and 925K. Lattice parameter from equation -4.2 shown in inset

The mathematical expression for this Random anisotropy model is;

$$H_C = P_C \frac{K_1^4 D^6}{A^3 J_S} \qquad \text{(4.3)}$$

Where H_C is the coercivity of the alloys annealed at 875K, P_C is a pre-factor that is according to the fine particle theory becomes 0.64 [10]. K_1 is the magneto crystalline anisotropy of the nanoparticles, which is 8 KJ/m^3 [24]. A= 10^{-11}J/m [25] is the exchange stiffness constant of the system. Js and D are saturation magnetization and particle size respectively the variations of which with cobalt content annealed at 875K are shown in fig-4.12(a). 'D' was determined from an assembly of particles bearing a deviation of ± 1nm in all the samples. The particle size 'D' was found to drop drastically above x = 20 at% compared to the gradual decrease in saturation magnetization 'Js' above x= 36 at%. These experimental data have been incorporated in Herzer's Random anisotropy model (equ. 4.3) and the coercivity determined is shown in fig-4.12(b). The coercivity values determined from the anisotropy model and magnetic hysteresis experiment follow similar trend till x = 36 at% with Co:Fe :: 50:50 stoichiometry indicating superior soft magnetic properties than the theoretical high magnetization stoichiometry of Co:Fe :: 35:65 alloy. At higher cobalt contents the experimental value indicated marked deviation from those of prediction through the model. The high magnetic hardness observed may be attributed to very fine cluster of highly anisotropic cobalt left in the matrix and that could not go into the nanophase [26] as well as due to the incipiently formed boride phases. This was also reflected from the deviation in lattice parameter (fig-4.11) in alloy with x > 36 at% though at a higher temperature of 925K whereby the shrinkage due to cobalt in Fe did not follow decreasing trend due to the clustering of cobalt in the matrix. It is also suggested that due to the presence of these cobalt clusters in matrix, the net magnetisation 'Js' did not drop down as drastically as that of nanoparticle size as shown in fig-4.12 (a). The partitioning behaviour of cobalt into nanophase with a critical increase in phase volume fraction was found to affect the magnetic moment of the system, an essential criterion for ferromagnetic ordering.

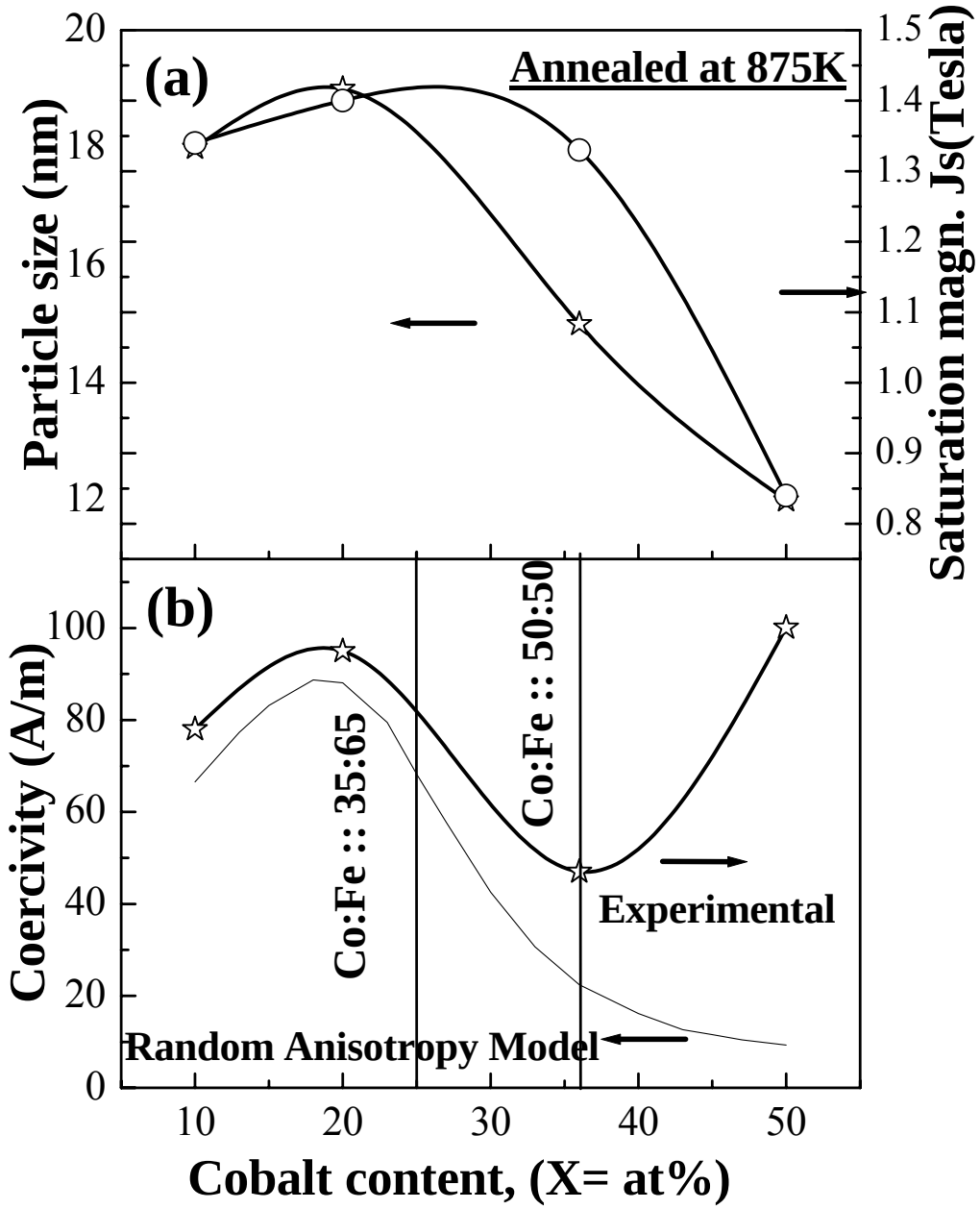

Fig-4.12: (a) Variation of particle size and saturation magnetization with cobalt content for the alloys annealed at 875K for 15 min (b) coercivity variation with cobalt content as per experimental data and Herzer's model for the alloys annealed at 875K

4.6 Conclusion

The $Co_xFe_{72-x}Si_4Nb_4B_{20,}$(x = 10, 20, 36, 50 at%) alloys were prepared in the form of amorphous ribbons by the melt spinning technique. The alloys exhibited reduction in

the onset of primary crystallization (T_{X1}), secondary crystallization (T_{X2}), glass transition (T_g), activation energy (E_{X1}) and the particle size (D) with increase in cobalt content. The bcc-FeCo nanophase and $(CoFe)_3B$ formation marked the thermodynamic onsets as T_{X1} and T_{X2} respectively. Both at high temperature range and high cobalt content were found the formation of borides leading to deviation in lattice shrinkage expected for increasing dissolution of Co and Si in the element Fe. The alloy with x = 36 at% with stoichiometry of Co:Fe :: 50:50 revealed superior soft magnetic properties at elevated temperatures compared to other alloys. This alloy when optimally annealed in the range of 875K to 925K generated bcc-FeCo nanophases enhanced the ferromagnetic ordering temperature to 1000K for suitability to applications at elevated temperature.

References

[1] Chu S-Y, Huang M-Q, Kline C, McHenry ME, Cross JO, Harris VG. J Appl. Phys., Vol. 85, p 6031 (1999).

[2] R.T.Fingers and C.S. Rubertus, IEEE.Trans.Magn., Vol. 36, p 3373 (2000).

[3] F.Pfeifer and C.Radeloff, J.Magn. Magn.Mater, Vol. 19, p 190 (1980).

[4] Y. Yoshizawa, S. Oguma and K. Yamauchi, J. Appl. Phys. Vol. 64, p 6044 (1988).

[5] G. Herzer, Handbook of Magnetic Materials, edited by K.H.J. Buschow, Vol. 10 (Elsevier Science, North-Holland) (1997).

[6] A. Mitra, A.K. Panda, S.R. Singh and P. Ramachandrarao Phil. Mag. Vol. 83, p 1495 (2003).

[7] M.E. McHenry, M.A. Willard and D.E. Laughlin, Prog. Mater. Sci. Vol. 44, p 291 (1999).

[8] K. Gallagher, F. Johnson, E.M. Kirkpatrick, J H Scott, S Majetich and M E McHenry., IEEE Mag. Vol. 32, p 4842 (1996).

[9] A. Mitra, H.Y. Kim, D.V. Louzguine, N. Nishiyama, B.L. Shen and A. Inoue., J. Magn. Magn. Mater. Vol. 278, p 299 (2004).

[10] Y. Yoshizawa, S. Fujji, D.H. Ping, M. Ohnuma and K. Hono., Scripta Mater. Vol. 48, p 863 (2003).

[11] C. Gomez-Polo, J.I. Perez-Landazabal and V. Recarte, Phys. Rev. B Vol. 66, 012401 (2002).

[12] Y. Yoshizawa, K. Yamauchi, Mater. Trans., JIM, Vol. 31, No. 4, p 307 (1990).

[13] A.Inoue, B.Shen, J.Mater.Res., Vol. 18, p 2799 (2003).

[14] E.J.Mittemeijer, L.Chang, P.J.Van Der Schaaf, C.M.Brakman, and B.M.Korevaar, Metall.Trans.A, Vol. 19, p 925 (1988).

[15] T. Sourmail, Prog. in Mater. Science Vol. 50, p 816 (2005).

[16] K.A.Gallagher, M.A Willard., V.N. Zabenkin., D.E.Laughlin and M.E.Mchenry, J. Appl. Phys, Vol. 85, p 5130 (1999).

[17] F.Johnson, C.Y.Um, M.E.McHenry and H.Garmestani, J. Magn. Magn, Mater, Vol. 93, p 297 (2006).

[18] I. Ohnuma, H.Enoki, O.Ikeda, R.Kainuma, H.Ohtani, B.Sundman and K. Ishida, Acta Mater, Vol. 50, p 379 (2002).

[19] T.Sourmail, Scripta Mater., Vol. 52, p 1347 (2005).

[20] R.M. Bozorth., Ferromagnetism (New York: Van Nostrand) (1959).

[21] M.Muller, N.Mattern and L.Illgen. Z.Metallkde, Vol. 82, p 895 (1991).

[22] A.K. Panda, B.Ravikumar, S.Basu and A.Mitra, J. Magn. Magn, Mater Vol. 260, p 70 (2003).

[23] G.Herzer. IEEE Trans. Magn. Vol. 26, p 1397 (1990).

[24] H. Gengnagel and H. Wagner, Z. Angew. Physik, Vol. 8, p 174 (1961).

[25] K. Huller, J. Magn. Magn. Mater, Vol. 61, p 347 (1986).

[26] X.Mao, F.Xu, J.Tang, W.Gao, S.Li and Y.Du, J.Magn.Magn.Mater, Vol. 288, p 106 (2005).

Chapter-5

Structural and magnetic properties of optimized $Co_{36}Fe_{36}Si_4Nb_4B_{20}$ nanocrystalline alloy

5.1: Introduction

The study on melt spun ribbon of $Co_xFe_{72-x}Si_4Nb_4B_{20}$ (x = 10, 20, 36, 50 at%) alloys subjected to nanocrystallisation by heat treatment, as discussed in chapter-4, reveals that variation in the Co-Fe stoichiometry had effect on the magnetic property. Amongst all, $Co_{36}Fe_{36}Si_4Nb_4B_{20}$ exhibits better soft magnetic properties such as low coercivity and high Curie temperature [1]. Hence, extensive study was carried out on the nanocrystalline material of this optimum composition. This chapter includes the detailed aspects of crystallization kinetics, analysis of nano-phases and magnetization behaviour of this alloy. Phase analysis is carried out by XRD and measurement of dimension of the nano-grains by TEM. The variation of DC coercivity, AC susceptibility and Curie temperature was carried out with the systematic variation of annealing temperature. The AC coercivity and core loss measurement was carried out with variation of frequency of amorphous and nanocrystalline state of the optimum alloy.

5.2: Brief resume of previous work

With the development of aviation and space technology, there arise the demands of soft magnetic materials for high temperature and high frequency applications. Many researchers have studied that Fe based soft magnetic nanocrystalline materials, under the conditions of room temperature and low frequency, have excellent soft magnetic properties, which are related to its microstructure and depend on the exchange coupling between these grains through the amorphous boundaries [2]. But this exchange coupling among the crystallites is reduced as the temperature increased and finally suppressed when the temperature is above the Curie temperature of the amorphous alloy [3]. A rapid increase in core losses leads to a poor quality factor for this type of alloys when frequency is above 20 kHz [4]. The low Curie temperature

and high core losses indicate alloys cannot satisfy the demands of high temperature and high frequency application. So much attention was given that partial substitution of Co for Fe is an effective way to improve the high temperature and high frequency properties [5-10].

5.3: Results and discussion

5.3.1: Crystallization study

5.3.1.1: Differential scanning calorimetry (DSC)

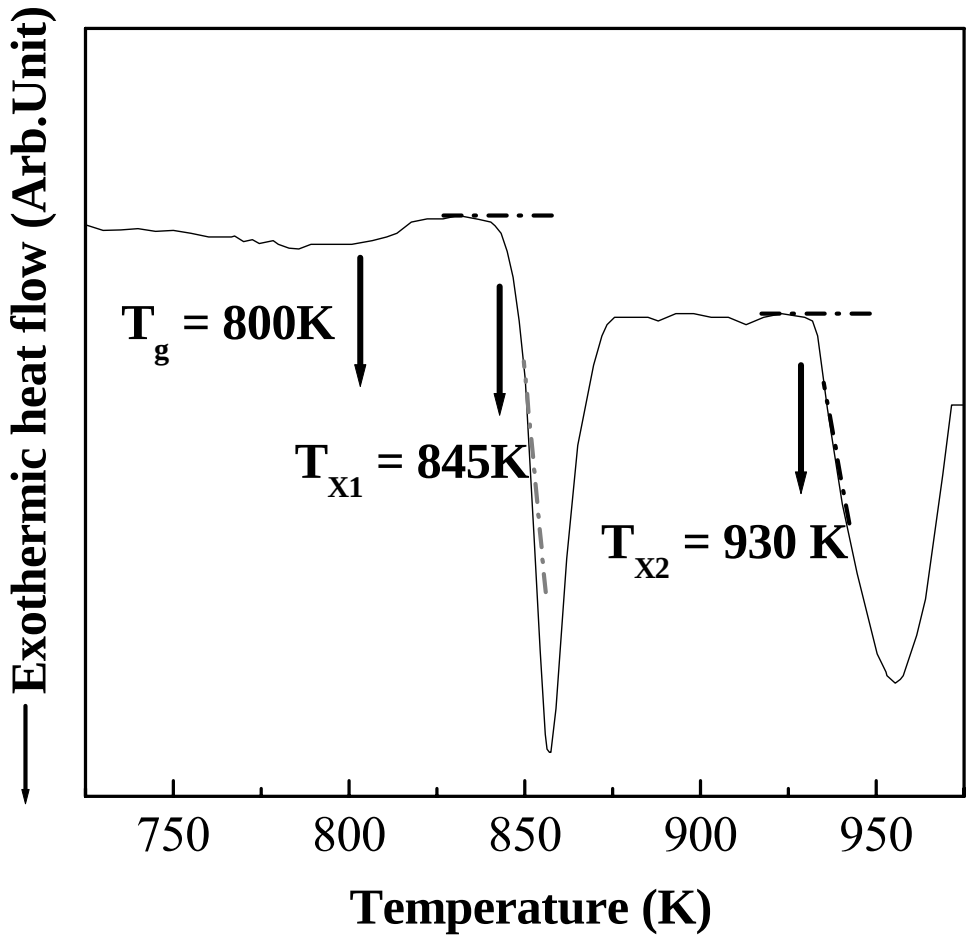

Fig- 5.1: Differential scanning calorimetry plot of the as-cast $Co_{36}Fe_{36}Si_4Nb_4B_{20}$ (at%) ribbon at scan rate 20 K/min

The DSC plot of the $Co_{36}Fe_{36}Si_4Nb_4B_{20}$ (at%) alloy shows the thermodynamic phase transformation as a function of heat flows with respect to temperature. Fig-5.1 shows the DSC plot of as-cast ribbon obtained at a heating rate of 20 K/min in an argon atmosphere. The DSC exotherms indicate two stages of crystallization represented by temperatures T_{X1} and T_{X2} at 845K and 930K respectively. The alloy also exhibited a distinct glass transition (T_g) with an onset of an endothermic peak at 800K. The T_g, which is attributed to mechanical softening due to lowering of viscosity, was observed about 45K below the first crystallization temperature suggesting a fairly wide super cooled region also observed in some bulk glassy alloys [11]. As the primary crystallization process is the major factor for the change in the magnetic properties, the activation energy involved during this transformation was calculated using a modified Kissinger's equation [12] written as

$$ln\left(\frac{T_p^2}{S}\right) = \frac{E_{act}}{RT_p} + \ln\left(\frac{E_{act}}{RK_0}\right) \ldots\ldots\ldots\ldots (5.1)$$

Where T_p is the temperature of the maximum of the peak, E_{act} is the effective activation energy for the process associated with the peak, S is the rate of thermal scanning, R is the gas constant and K_0 is the pre-exponential factor in the arrhenius equation for the rate constant k. The Kissinger plot shown in fig-5.2(a) was obtained with a good linear fit of <R> = 0.99 from where the activation energy was found to be 83 kcal/mol. The time constant [3] for the primary crystallization process was also determined from Kissinger analysis and shown in fig-5.2(b). A good linear fit with a correlation factor <R> = 0.99 was obtained with the following expressions:

$$\ln \tau = \left(\frac{41.37 \times 10^3 \times 1}{T}\right) - 42.737 \ldots\ldots\ldots\ldots\ldots (5.2)$$

The stability of the amorphous phase at any desired temperature could be obtained by using equation (5.2).

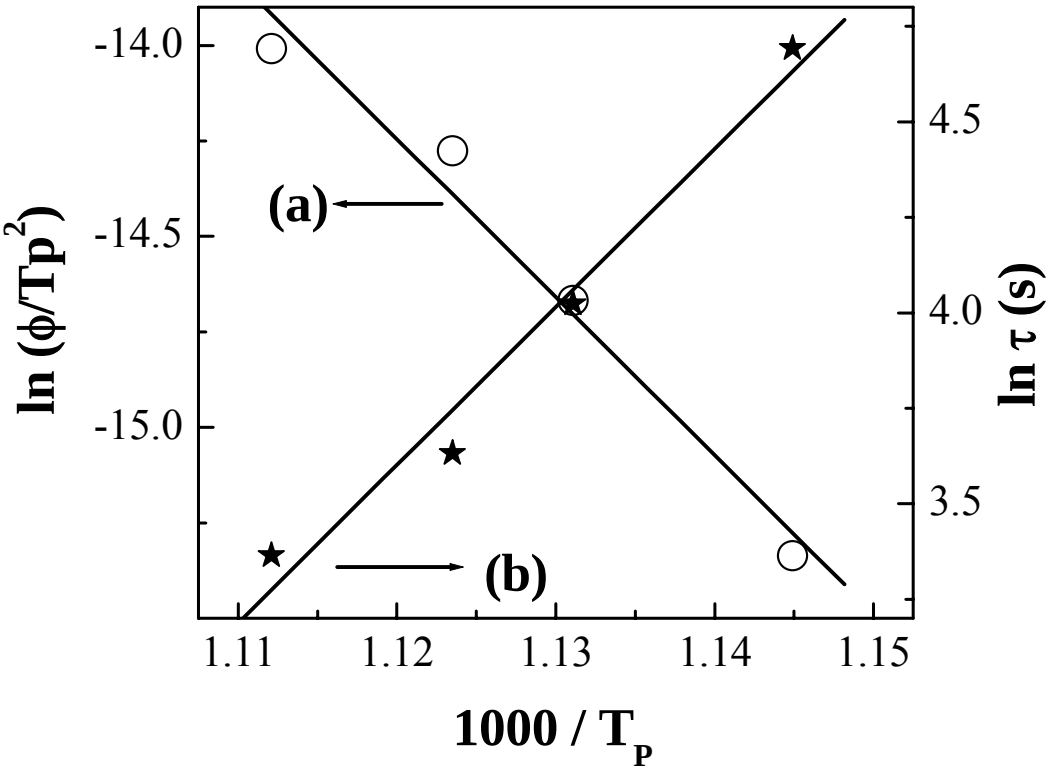

Fig-5.2: Kissinger plots of as-cast $Co_{36}Fe_{36}Si_4Nb_4B_{20}$ (at%) ribbon obtained using different scan rates

5.3.1.2: Thermal variation of electrical resistivity (TER)

Temperature variation of electrical resistivity of the $Co_{36}Fe_{36}Si_4Nb_4B_{20}$ (at%) ribbon obtained at a scan rate of 10 $Kmin^{-1}$ in an argon atmosphere is shown in fig-5.3. The resistivity data have been normalized with respect to room temperature resistivity values. The resistivity increased monotonically from room temperature onwards, which is attributed to electron–magnon and electron–phonon scattering till the first drop in resistivity was observed at 770K. This characteristic temperature was identified as the glass transition temperature T_g that was observed at 800K in the DSC plot. The electrical resistivity exhibited a drastic decrease above T_g shown by a negative temperature coefficient, α_g, as reported by other researchers [13-16]. Although the exact phenomenon of electron transport behaviour is yet to be determined, recent reports suggest that such a resistivity drop is due to transition from a state of super cooled random structure with high resistivity to a glassy state with low

resistivity [15]. In addition to this theory, it is known that with an increase in temperature, the viscosity drop around the glass transition leads to mechanical softening. As a result of this mechanical softening, stress relaxation takes place thereby increasing the conductivity of electrons leading to a decrease in thermal electrical resistivity at the glass transition, T_g. Beyond T_g, the change in electron transport behaviour became very significant and showed rapid changes in the TER profile, as shown in fig-5.3. The changes in the profile were analyzed and their coefficients of resistivity (TCR) around the characteristic temperatures are shown in table-1. Above the glass transition, the TER plot showed drastic drops in resistivity representing three crystallization stages at T_{X1}, T_{X2} and T_{X3}, i.e. temperatures of 825K, 890K and 1000K, respectively.

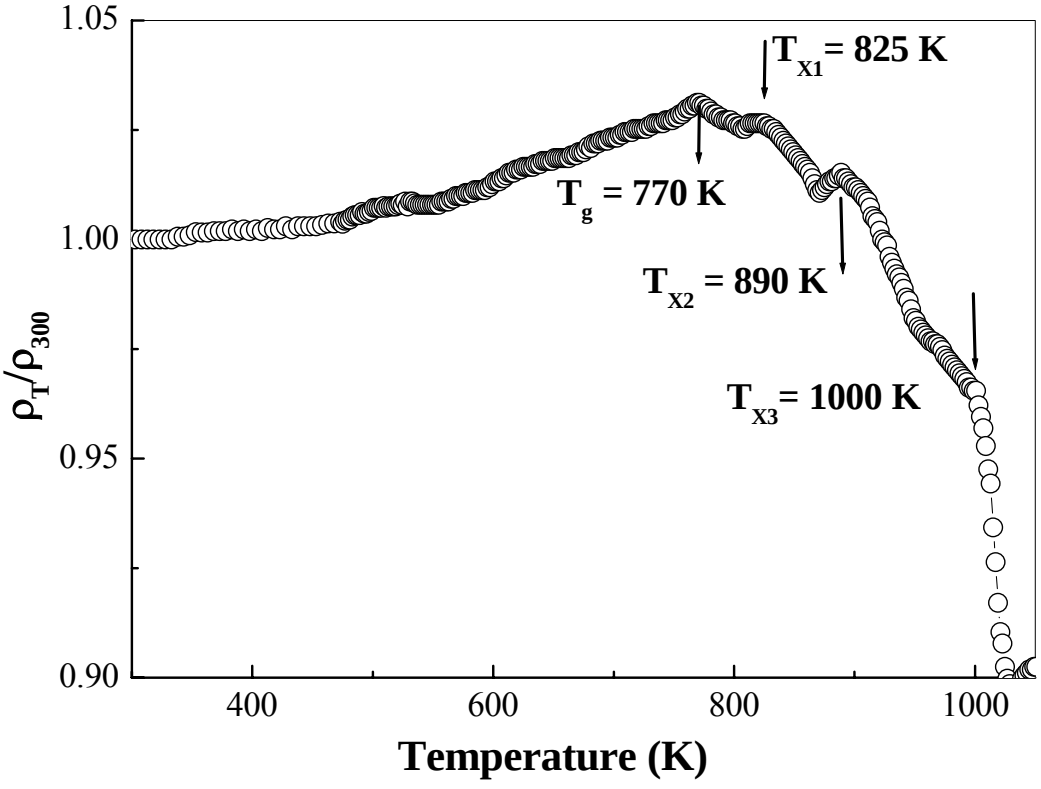

Fig-5.3: Thermal variation of electrical resistivity plot of as-cast $Co_{36}Fe_{36}Si_4Nb_4B_{20}$ (at%) ribbon, scan rate 10K/min

Table-1: Temperature coefficients determined from TER measurements

Characteristic temperature (K)	Temperature range (K)	Temperature coefficient, α (X10 $^{-4}$)	
$T_g < T < T_{X1}$	771–807	α_g	- 1.537
$T_{X1} < T < T_{X2}$	825–871	α_1	- 3.409
$T_{X2} < T < T_{X3}$	891–999	α_2	- 4.984
$T_{X3} < T$	1001–1025	α_3	- 28.400

The first two crystallizations corroborate with the DSC data; it was beyond the operating range of the DSC instrument to monitor the high temperature transition at T_{X3}. It was observed that the negative temperature coefficients of resistivity showed an increasing trend beyond T_{X1}. However, it was noted that above T_{X1} there was a gradual drop in resistivity shown by a slow increase in TCR value from α_1 = - 3.409 to α_2 = - 4.984. This indicates that a phenomenon like electron scattering by nanoparticles [17-18] occurs beyond T_{X1}, which restricted the drastic decrease in resistivity. This was evidenced from the structural evolution during nanocrystallization of the amorphous state initially shown by salt–pepper contrast in a TEM micrograph (fig-5.4) and its corresponding selected area diffraction (SAED). This exhibits the characteristics of diffused ring pattern indicating an absence of crystallinity. A broad maximum in the XRD peak (fig-5.5) also indicated the amorphous nature of as-cast alloy. When annealed beyond first crystallization temperature i.e. at 875K, dispersion of nanoparticles (~ 14–15 nm) appears within the amorphous matrix. The second phase occurs in the form of isolated islands as well as clusters of varying shape (fig-5.4b). The distribution of fine second phases within the matrix is confirmed by the presence of few concentric diffraction maxima (fig-5.4b). The indexed ring pattern indicates the zone axis as Z = B = [121]. The nanoparticles formed at this temperature, as per TER measurements, were identified to be nanophase bcc-FeCo as observed from XRD (fig-5.5). This nanocrystallization stage was also shown by DSC exothermic (fig-5.1) temperature at 845K due to its low sensitivity than electrical resistivity measurements. Beyond the second and third crystallization temperature, T_{X2} and T_{X3}, respectively, the resistivity drop became drastic with the negative TCR value increases from α_2 = - 4.984 to α_3 = - 28.400. This

rapid fall in resistivity was attributed to ordering phenomena occurring during amorphous to crystalline transformation [19]. X-ray diffractograms of material annealed at 875K showed the formation of bcc-FeCo nano phases. Whereas beyond 875K showed the formation of such crystalline phases like $(CoFe)_3B$ along with bcc-FeCo phases was the cause of drastic decrease in resistivity around the third crystallization temperature T_{X3} = 1000K.

5.3.2: Structural behaviour

5.3.2.1: Transmission electron microscopy

The microstructure of the as cast, annealed at 875K and 925K of the $Co_{36}Fe_{36}Si_4Nb_4B_{20}$ alloy is investigated by the transmission electron microscope as shown in fig-5.4. The as cast alloys exhibited featureless micrograph with diffused selected area electron diffraction patterns (SAED) confirmed that material is in amorphous state. Annealed at 875K (beyond first crystallization temperature) material undergoes partial devitrification to nanocrystalline state, which is evidenced by ring SAED patterns (Fig.-5.4).

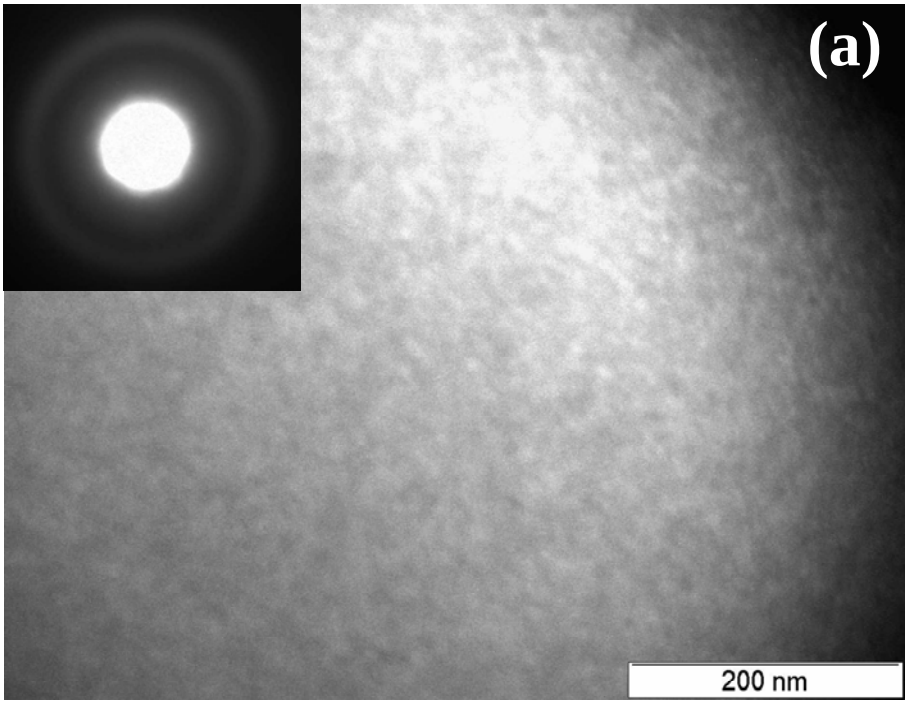

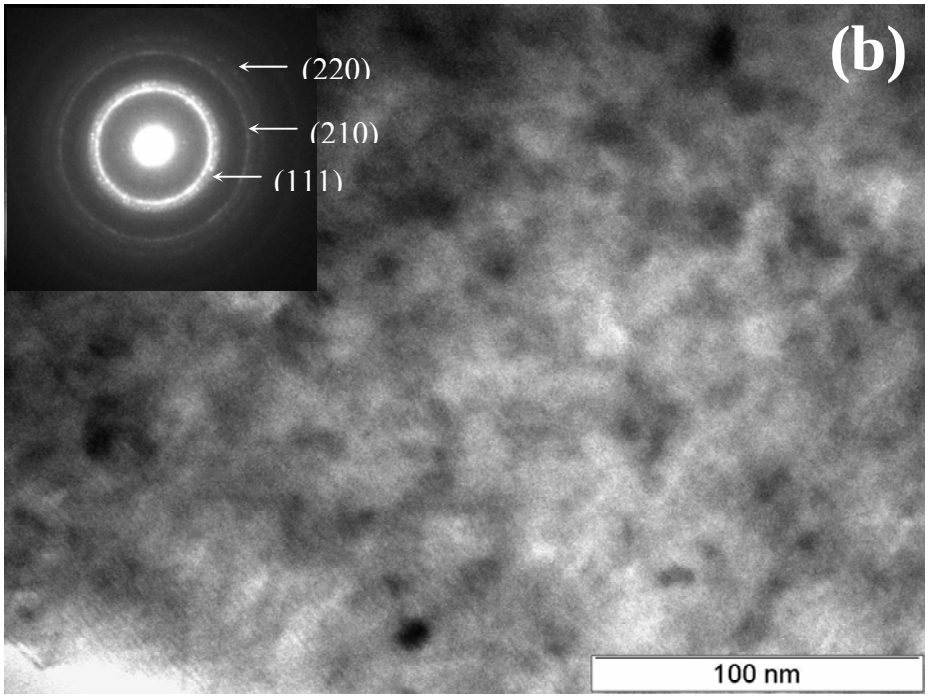

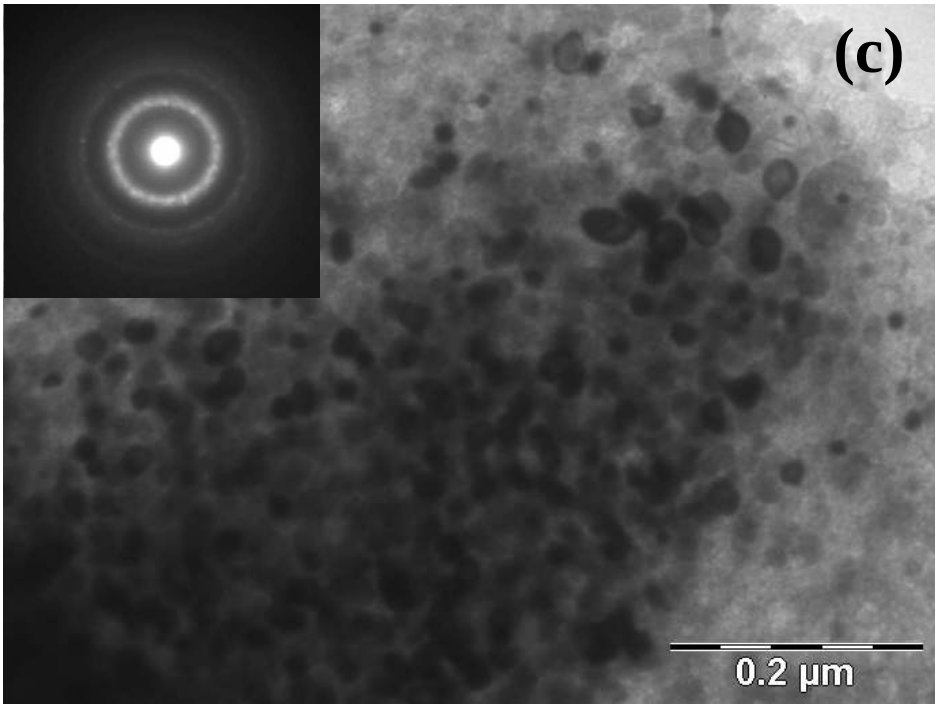

Fig-5.4: TEM micrograph of the alloy in the (a) as-cast (b) annealed at 875K and (c) annealed at 925K SAED pattern shown in the inset.

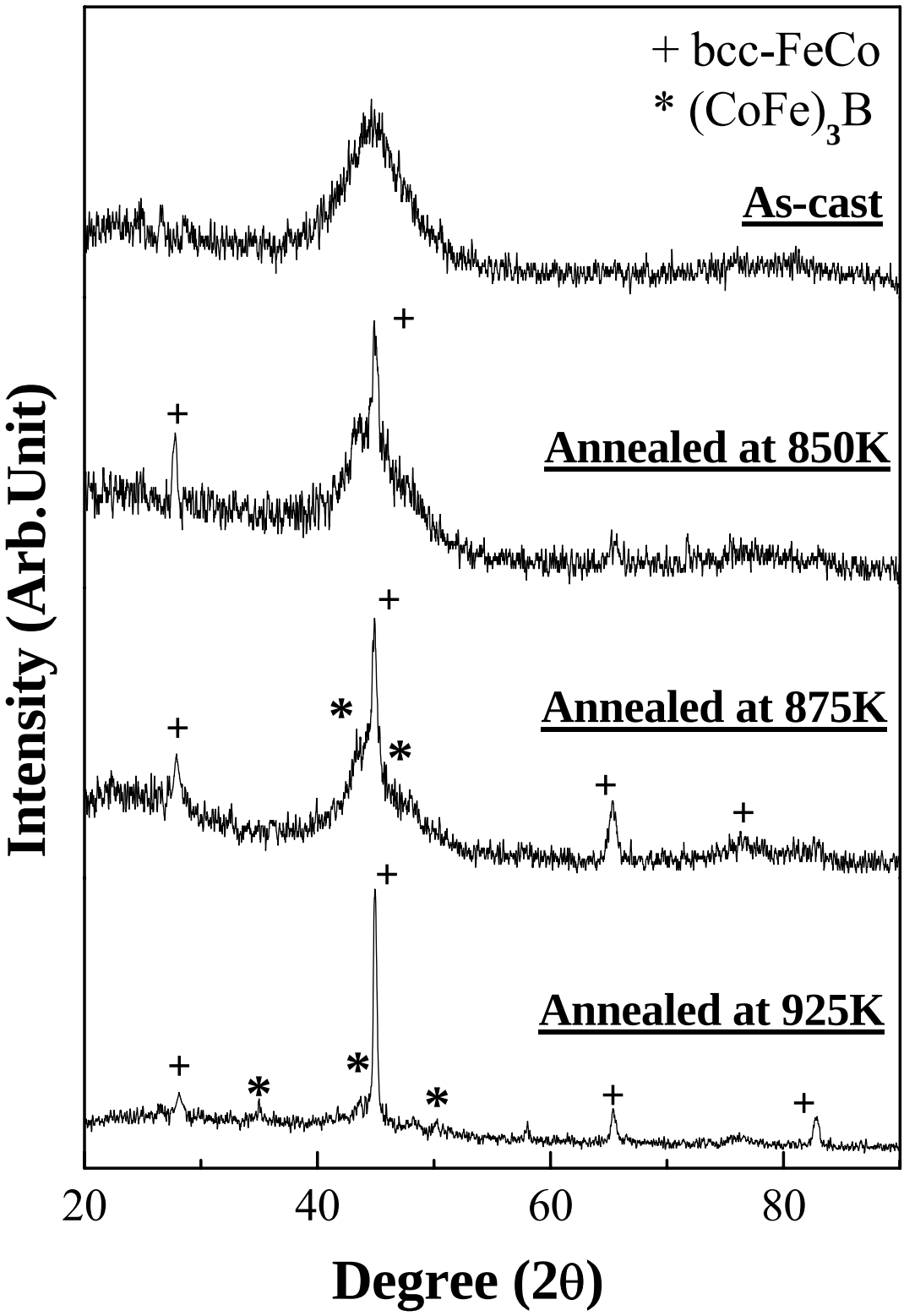

Fig-5.5: XRD plot of the as cast and annealed at different temperature of $Co_{36}Fe_{36}Si_4Nb_4B_{20}$ (at%) alloy

It is seen that the ultrafine grains about ~ 14-15 nm are dispersed in amorphous matrix of the annealed at 875K. Annealing at higher temperature, close to the secondary crystallization temperature i.e. 925K, grain sizes increases about 20-22 nm. To identify the different phases that formed after annealing, X-ray diffractograms were taken for different heat-treated samples. The X-ray diffraction patterns of the as quenched and annealed ribbons for $Co_{36}Fe_{36}Si_4Nb_4B_{20}$ alloys are shown in fig- 5.5. The as quenched alloy shows a broad hallo pattern typical in amorphous nature. On the other hand, annealed at 875K close to first crystallization temperature XRD peak showed the formation of nanocrystalline bcc-FeCo and $(CoFe)_3B$ phases. Annealing close to the secondary crystallization, that is around at 925K, more $(CoFe)_3B$ phases also found together with the phases that existed near to the first crystallization. The formations of these strongly anisotropic phases pinned the domain wall movement and led to drastic magnetic hardening above 925K.

5.3.3: Magnetic characterization

5.3.3.1. DC coercivity and AC susceptibility

Fig.-5.6 shows the effect of annealing on the coercivity and ac susceptibility of the $Co_{36}Fe_{36}Si_4Nb_4B_{20}$ (at%) alloy. On heat treatment above room temperature, the material did not show any significant change in coercivity. However, the susceptibility value showed an increasing trend with annealing up to 800K owing to its measurement at low applied field that bore a sensitive change to magneto elastic anisotropy. Hence, the improvement in soft magnetic property below the first crystallization onset was attributed to structural relaxation. At an annealing temperature of 850K, the alloy exhibited soft magnetic properties with coercivity ~$14Am^{-1}$ and susceptibility ~ 4 X 10^3. The bcc-FeCo nanoparticles formed at this temperature (fig-5.5) have a tendency to randomly average out their individual anisotropies and thereby reduce the overall anisotropy of the system to exhibit soft magnetic properties [20]. According to this model, the relation between coercivity and magneto crystalline anisotropy of the nanoparticles derived from effective anisotropy of the system [21] could be approximated as

$$H_C = P_C \frac{K_1^4 D^6}{A^3 J_S} \qquad \text{(5.3)}$$

Where, Pc is a pre-factor that according to the fine-particle theory becomes 0.64. K_1 is the magneto crystalline anisotropy of the nanoparticles, which is $8kJm^{-3}$[22]. $A=10^{-11}$ Jm^{-1} [23] is the exchange stiffness constant of the system. In the present $Co_{36}Fe_{36}Si_4Nb_4B_{20}$ (at%) alloy, Js was found to be 1.13 T obtained from approach to saturation at high magnetizing field. D is the particle size which was ~ 14 nm for sample annealed at 850K.

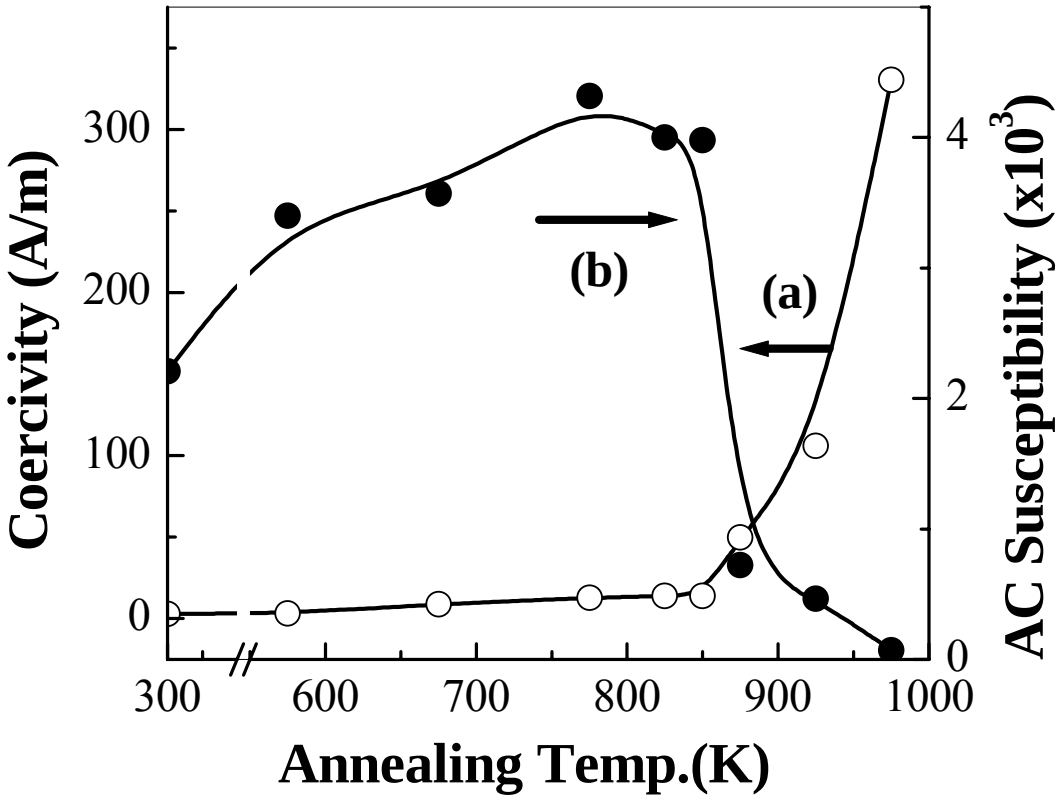

Fig-5.6: Variation of coercivity (a) and susceptibility (b) of $Co_{36}Fe_{36}Si_4Nb_4B_{20}$ (at%) alloy with annealing temperature

With the above material parameters, coercivity was calculated according to equ.5.3 and was found to be 17.44 Am^{-1} close to the experimental value of 14 Am^{-1}. Annealing beyond 850K led to gradual deterioration in soft magnetic properties with

increase in coercivity and a decrease in susceptibility which may be attributed to increase in size of bcc-FeCo nanoparticles. However, in this temperature range, the thermal degradation of soft magnetic properties was slow enough to corroborate its effect with the retarded growth of bcc-FeCo nanoparticles. Such restriction to anomalous growth of nanoparticles was brought about by the presence of large sized refractory element Nb [24]. The distribution of these slowly growing nanoparticles even up to 875K were effectively averaging their individual anisotropy thereby reducing the net anisotropy of the system and thus maintaining fairly soft magnetic properties with coercivity ~ 49.9Am^{-1} and susceptibility ~ 0.72 X 10^3. Above 875K, magnetic hardening became prominent with increase in coercivity and corresponding decrease in susceptibility. This deterioration in the soft magnetic properties above 875K is attributed to the formation of strongly anisotropic boride phases identified using X-ray analysis (fig-5.5). The magnetic degradation became drastic above 925K which was caused not only by the enhanced anisotropy with the formation of additional $(CoFe)_3B$ crystalline phases but also by their rapid growth which impeded domain wall movement.

5.3.3.2 Curie temperature and saturation magnetization

The present alloy exhibited consistent soft magnetic properties; therefore Curie temperature behaviour was a significant issue for high temperature applications. For this, the temperature dependent magnetization curve of as cast and annealed at 875K, 900K and 925K samples is shown in fig-5.7. The sharp drop in magnetization indicated the transformation of the material from ferromagnetic to paramagnetic state. The Curie temperature was calculated from the derivative of the normalized magnetization plot. The initial drop in magnetization was elevated to higher temperature when annealed at 875K which was around the primary onset for bcc-FeCo nanophase formation. This drop shifted to lower temperature for 900K annealed sample which may be attributed to the depletion of cobalt and iron from the ferromagnetic matrix. The subsequent enhancement of magnetization level at 800K and above is attributed to the increase in volume fraction of nanophase generated. A typical heat treatment at 925K raised the level of magnetization considerably with a ferromagnetic stability till 1000K (fig-5.7, inset). Beyond this temperature the ferromagnetic disordering started due to the formation of CoFe-borides in high volume fraction which also affected the trend of lattice contraction due to cobalt

partitioning into bcc-FeCo nanophase. Annealed at 925K the nanophases revealed good soft magnetic properties with coercivity below ~106 Am^{-1} and susceptibility ~$0.5X10^3$ and raised the overall magnetization of the alloy system with a Curie temperature above 1000K.

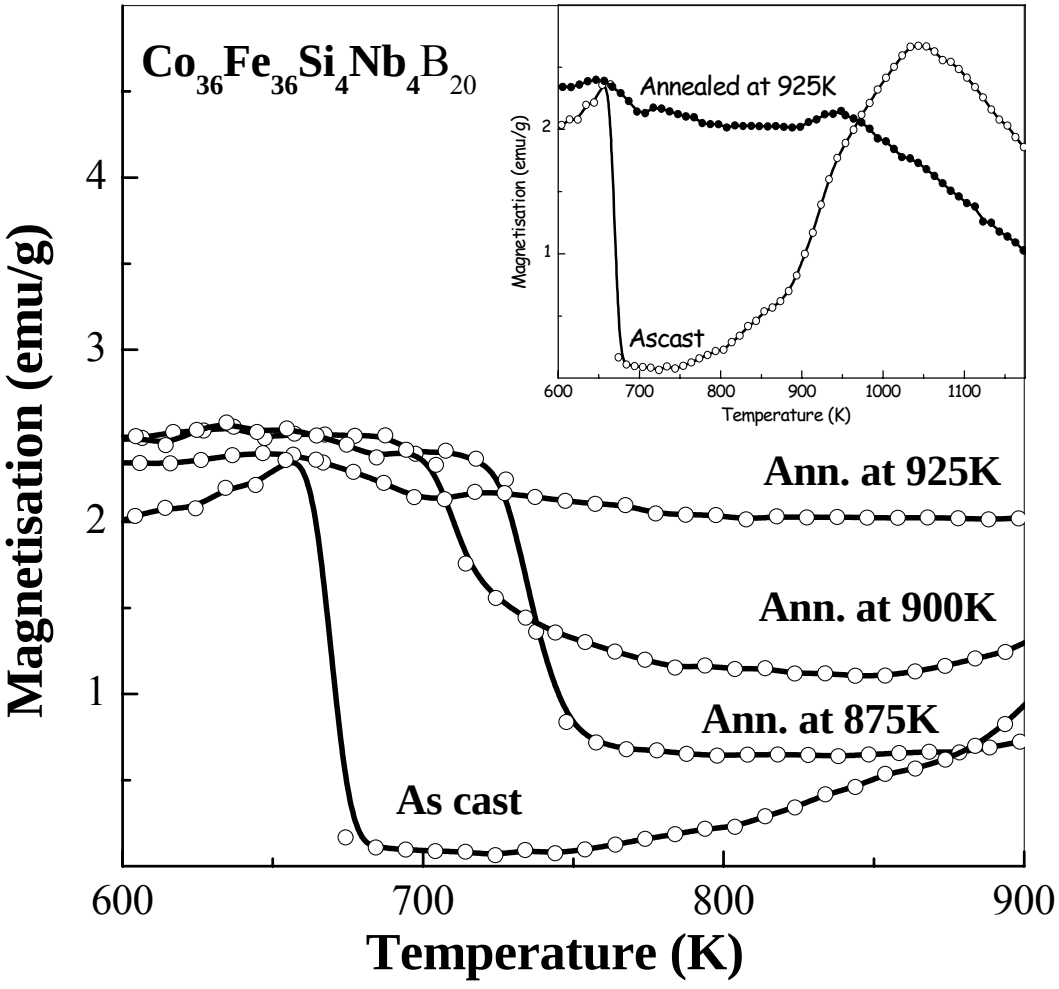

Fig-5.7: Thermal variation of magnetization of as cast and annealed $Co_{36}Fe_{36}Si_4Nb_4B_{20}$ at% alloy. Inset shows the profile for as-cast and 925K annealed sample, at a magnetizing field of 2Oe

5.3.3.3: AC magnetic properties

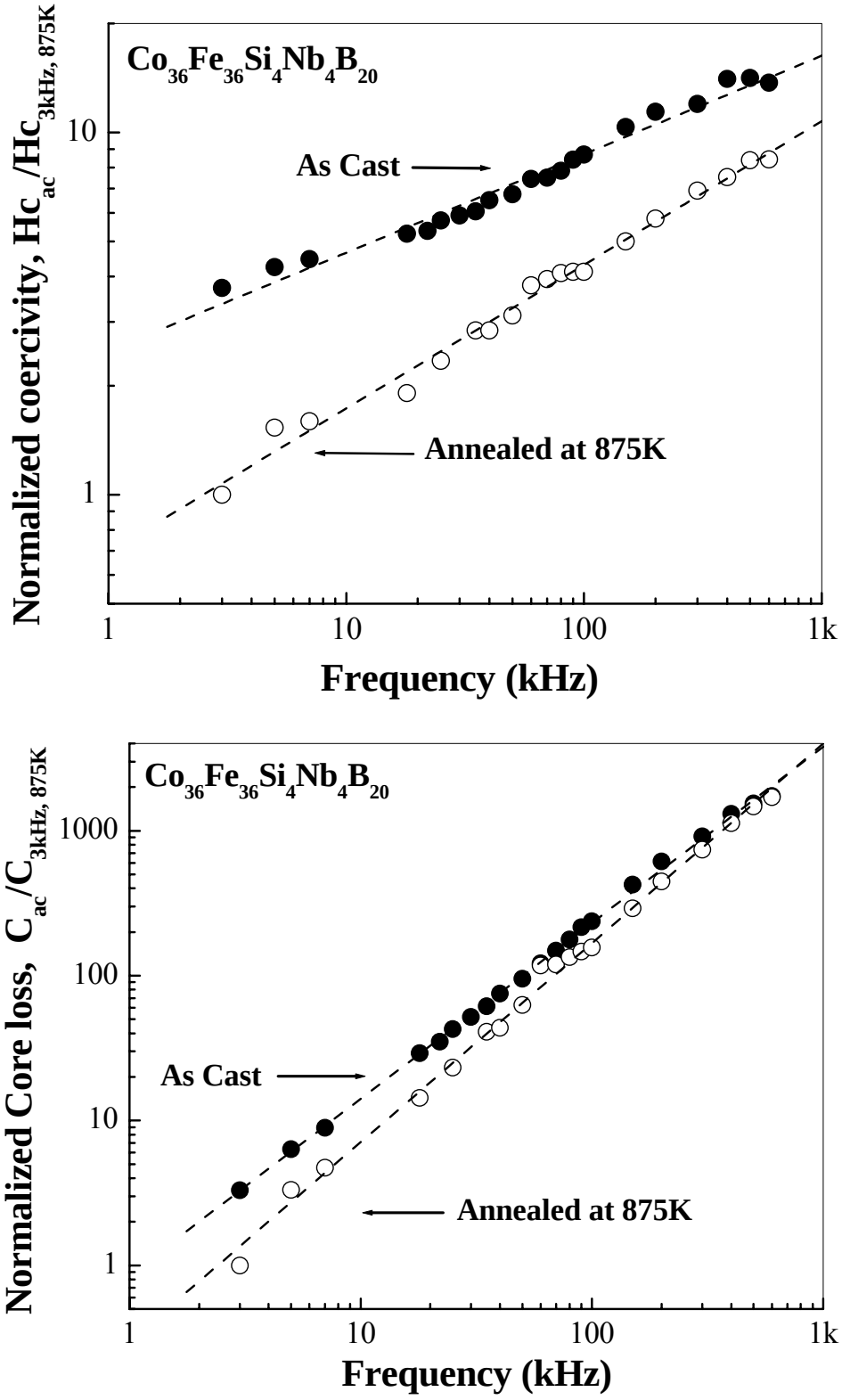

Fig-5.8: (a) Variation of AC coercivity and (b) Core loss normalized with respect to 875K annealed data measured at 3 kHz and at a magnetizing field of 5 Oe

In high frequency transformer and rotor assemblies with a soft magnet core, flux lines in alternating current would contribute towards power losses adding a major concern for high temperature soft magnetic applications [25]. The coercivity and core loss variation with frequency for the as-cast and sample annealed at 875K is shown in fig-5.8(a) and fig-5.8(b) respectively. The measurements have been carried out at magnetizing field of 5 Oe starting from a frequency of 3 kHz. To observe the effect of nanocrystallisation, all the data has been normalized with respect to the data for 875K annealed sample obtained at a starting frequency of 3 kHz. This optimally heat treated sample exhibited lower AC coercivity and core loss compared to the as-cast material. Linear fittings of the data indicated that the nanocrystallised sample has a tendency to approach as-cast material behaviour with increasing frequency. However, the soft magnetic behaviour (coercivity) was stable towards higher frequency compared to the eddy current loss (core loss).

5.4: Conclusion

An optimum $Co_{36}Fe_{36}Si_4Nb_4B_{20}$ (at%) alloy was prepared in the form of amorphous ribbons by the melt-spinning technique. Differential scanning calorimetry (DSC) and thermal variation of electrical resistivity (TER) studies indicated a glass transition stage before the occurrence of subsequent crystallization stages. Annealed at 875K alloy exhibited fairly soft magnetic properties with coercivity ~ 49.9 Am^{-1} and susceptibility ~ 0.72 X 10^3 because of the formation of ~ 14-15 nm sized bcc-FeCo phases in the amorphous matrix, which is evidenced by X-ray analysis and TEM study. A typical temperature, annealed at 925K the nanophases not only revealed good soft magnetic properties with coercivity below ~106 Am^{-1} and susceptibility ~0.5 X 10^3 but also raised the overall magnetization of the alloy system with a Curie temperature above 1000K. The combination of high Curie temperature and superior soft magnetic properties makes the material a potential candidate for high temperature soft magnetic applications. The alloy in its nanostructure state also exhibited low power losses.

References

[1] Ojaswini Mohanta, M. Ghosh, A. Mitra and A. K. Panda, J. of Phys. D, Appl. Phys. V. 42, 065007 (2009).

[2] Y. Yoshizawa, S. Oguma and K. Yamauchi, J. Appl. Phys. V. 64 p 6044 (1988).

[3] K. Gallagher, F. Johnson, E.M. Kirkpatrick, J H Scott, S Majetich and M E McHenry., IEEE Mag. Vol. 32 p 4842 (1996).

[4] A. Mitra, H.Y. Kim, D.V. Louzguine, N. Nishiyama, B.L. Shen and A. Inoue., J. Magn. Magn. Mater. Vol. 278 p 299 (2004).

[5] Y. Yoshizawa, S. Fujji, D.H. Ping, M. Ohnuma and K. Hono., Scripta Mater. Vol. 48 p 863 (2003).

[6] C. Gomez-Polo, J.I. Perez-Landazabal and V. Recarte, Phys. Rev.B V. 66 012401 (2002).

[7] M. A. Willard, D. E. Laughlin, M. E. McHenry, D. Thoma, K. Sickafus, J. O. Cross, and V. G. Harris, J. Appl. Phys. V. 84 p 6773 (1998).

[8] M.E. McHenry, M.A. Willard, D.E. Laughlin, Mater. Sci. Prog. V. 44 p 291 (1999).

[9] D. H. Ping, Y. Q. Wu, K. Hono, M. A. Willard, M. E. McHenry, and D. E. Laughlin, Scr. Metall Mater. V. 45 p 781 (2001).

[10] K. Krištiakova, P. Švec, and D. Janičkovič, Mater. Trans. JIM V. 42 p 1523 (2001).

[11] A. Inoue, Mater. Trans. JIM V. 36 p 866 (1995).

[12] E.J.Mittemeijer, L.Chang, P.J.Van Der Schaaf, C.M.Brakman, and B.M.Korevaar, Metall.Trans.A, Vol. 19, p 925 (1988).

[13] O. Haruyama, H. Kimura, N. Nishiyama and A Inoue., Mater. Sci. Engng A 304–306 740 (2001).

[14] O. Haruyama, H. Kimura, N. Nishiyama and A Inoue., J. Non-crystallne Solids 250–252 p 781, (1999).

[15] J. Guo, F. Zu, Z. Chen, S. Zheng and Y. Yuan., Solid St. Commun. V. 135 p. 103 (2005).

[16] D.N. Perera and A.P. Tsai, J. Phys. D V. 33 p 1937 (2000).

[17] K. Pekala, P. Jaskiewicz, M. Pekala and T. Kulik., Nanostruct. Mater. V. 6 p 497 (1995).

[18] A.K. Panda, B. Ravikumar, S. Basu and A Mitra., J. Magn. Magn. Mater. V. 260 70 (2003).

[19] A. Mitra, S. Palit and I. Chattoraj, Phil. Mag. B V. 77 p 1681 (1998).

[20] G. Herzer, IEEE Trans. Magn. V. 26 p 1397 (1990).

[21] G. Herzer, Mater. Sci. Engg A 1331 (1990).

[22] H. Gengnagel and H. Wagner, Z. Angew Phys. V. 8 p 174 (1961).

[23] K. Huller, J. Magn. Magn. Mater. V. 61 p 347 (1986).

[24] Y. Yoshizawa and K. Yamauchi, Mater. Sci. Engg A 133 176 (1991).

[25] Varga L K, Kov´acs Gy, K´akay A, Mazaleyrat F, Gercsi Zs, Ferenc J, Fazakas E, Kulik T and Conde C J. Magn. Magn. Mater. V. 272 p 1506 (2004).

Chapter- 6

Substitution of Al in CoFeSiNbB alloy system for further improvement of soft magnetic properties

6.1: Introduction

Optimization of Co-Fe stoichiometry in CoFeSiNbB nanostructured alloy system to achieve materials with low coercivity and high Curie temperature has been discussed in the previous chapter. As cobalt containing alloys are susceptible to magnetic hardening, there is an interest to explore a modification of alloy chemistry with the addition of other alloying element for further improvement of soft magnetic properties. Some recent investigations suggested improvement in soft magnetic properties with the incorporation of aluminum. This idea originated from the fact that addition of Al in Sendust class of alloys (FeSiAl), significantly improved the soft magnetic properties as the magneto crystalline anisotropy is lowered due to the addition of Al to Fe-Si binary system [1-3]. It is expected that addition of Al to CoFeSiNbB type of alloy may have an effect on magnetostriction and magnetic anisotropy with a cumulative effect on the magnetic property.

In the present work, the effect of Al substitution for Si in $Co_{36}Fe_{36}Si_{4-y}Al_yNb_4B_{20}$ alloy system is taken into consideration. This chapter includes the study of thermal behavior, structural behavior and soft magnetic properties of alloy with partial substitution of Al in its stoichiometric composition and its annealed products developed at varied annealing temperature.

6.2: Brief resume of previous work

Many researchers have studied that the incorporation of element cobalt in Fe based soft magnetic nanocrystalline materials not only enhance the Curie temperature but also facilitate nanocrystallisation [4]. Such effect of nanocrystallisation has been reported by the present author at National Metallurgical Laboratory, Jamshedpur,

India for the optimum CoFeSiNbB alloy with Co/Fe in the stoichiometry of 50:50 [5]. However, the addition of Co leads to the enhancement in magnetic anisotropy and thus, to deleterious effect on soft magnetic properties. Therefore, attempts were made to improve the soft magnetic properties with the addition of other alloying element. The observation of Zeleňáková *et al*. (2003) suggests that aluminium influences magnetic properties and the domain structure in the ($Fe_{71.5}Si_{15.5-x}Cu_1Nb_3B_9Al_x$) FINEMET alloys [6]. Since the crystallization temperature of these alloys decreases with increasing Al content, the Al-substituted samples did not show any improvement of soft magnetic properties. A. Zorkovsk´a *et al*. observed that aluminum influence on intrinsic magnetic properties of the nanocrystalline FINEMET ($Fe_{73.5-x}Al_xCu_1Nb_3Si_{13.5}B_9$) alloys, such as saturation magnetization, Curie temperature and spin-wave stiffness constant [7]. The strengthening effect of Al on the exchange interaction was observed for the alloys with small Al content (up to 3at%). Higher concentration of Al (5–7 at%) led to considerably suppressed exchange interaction. I. Todd *et al*. observed that the improvements in DC coercivity (Hc) and AC permeability are attributed to a reduction in magneto crystalline anisotropy (K_1) of the FeSiBNbCu based nanocrystalline alloy by the introduction of Al [8]. Thus, these attributes are further important for alloy modifications through substitution of Al for Si in the CoFe-based nanostructured systems.

6.3: Material studied

The alloys used for the present study were the melt spun amorphous ribbon of $Co_{36}Fe_{36}Si_{4-y}Al_yNb_4B_{20}$ type with following composition.

Alloy I : $Co_{36}Fe_{36}Si_{3.5}Al_{0.5}\ Nb_4B_{20}$

Alloy II : $Co_{36}Fe_{36}Si_3Al_1Nb_4B_{20}$

Alloy III: $Co_{36}Fe_{36}Si_{2.5}Al_{1.5}Nb_4B_{20}$

Alloy IV: $Co_{36}Fe_{36}Si_2Al_2Nb_4B_{20}$

The continuous amorphous ribbons having more than a meter length, 0.2 cm width and 30 micro-meter thickness were prepared by melt spinning technique. The alloys were subjected to annealing in an argon atmosphere at a heating rate of 20 K/min for developing corresponding nanocrystalline variants. The amorphous and their nano-crystalline variants of each were subjected to DC magnetic measurement.

6.4: Results

The alloys prepared by melt spinning system exhibit broad peak in the X-ray diffraction pattern indicating amorphous nature of the as-spun ribbons irrespective of all Al-content alloys. Out of which two patterns of alloy with Al 0 atomic percent and 1 atomic percent (y = 0 and y = 1) are shown as representative X-ray diffractogram (Fig-6.1).

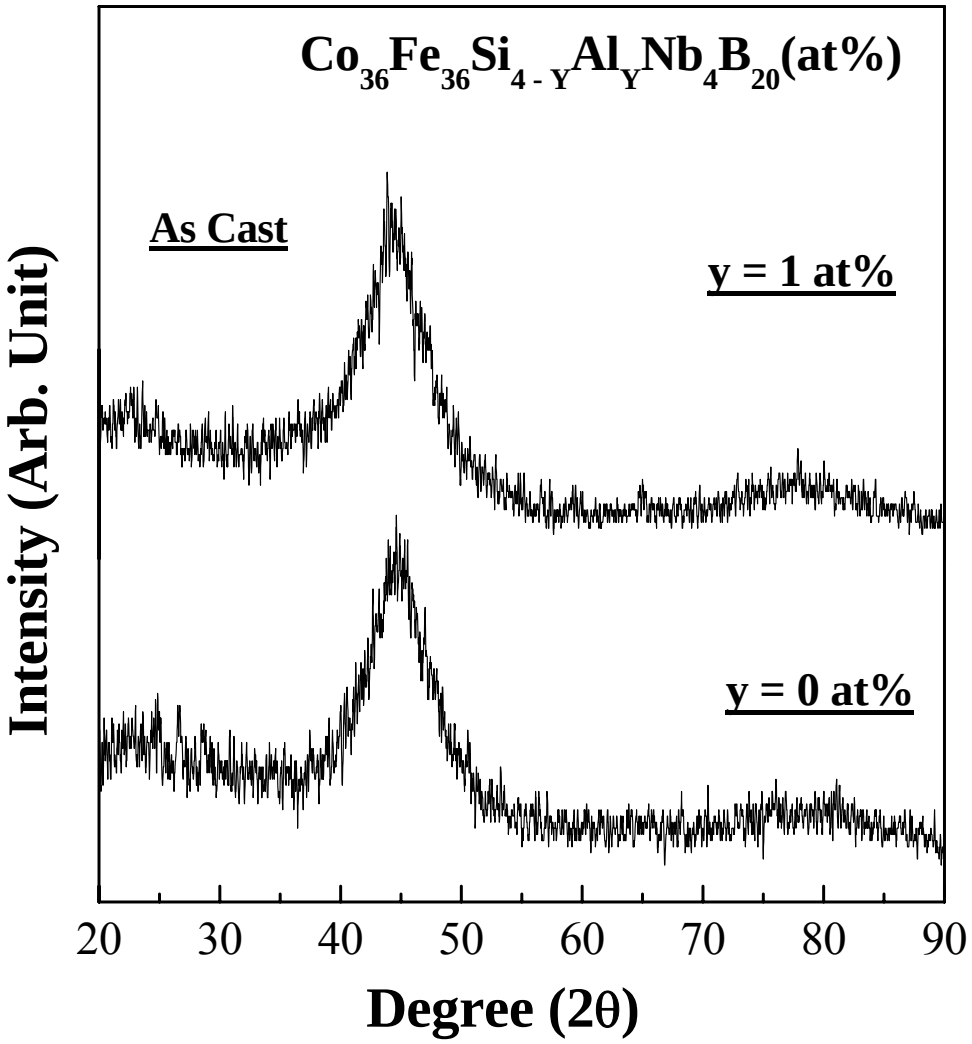

Fig-6.1: X-ray diffractogram of as cast $Co_{36}Fe_{36}Si_{4-y}Al_yNb_4B_{20}$ (y = 0, 1 at%) alloys

6.4.1: Crystallization study

6.4.1.1: Differential scanning calorimetry (DSC)

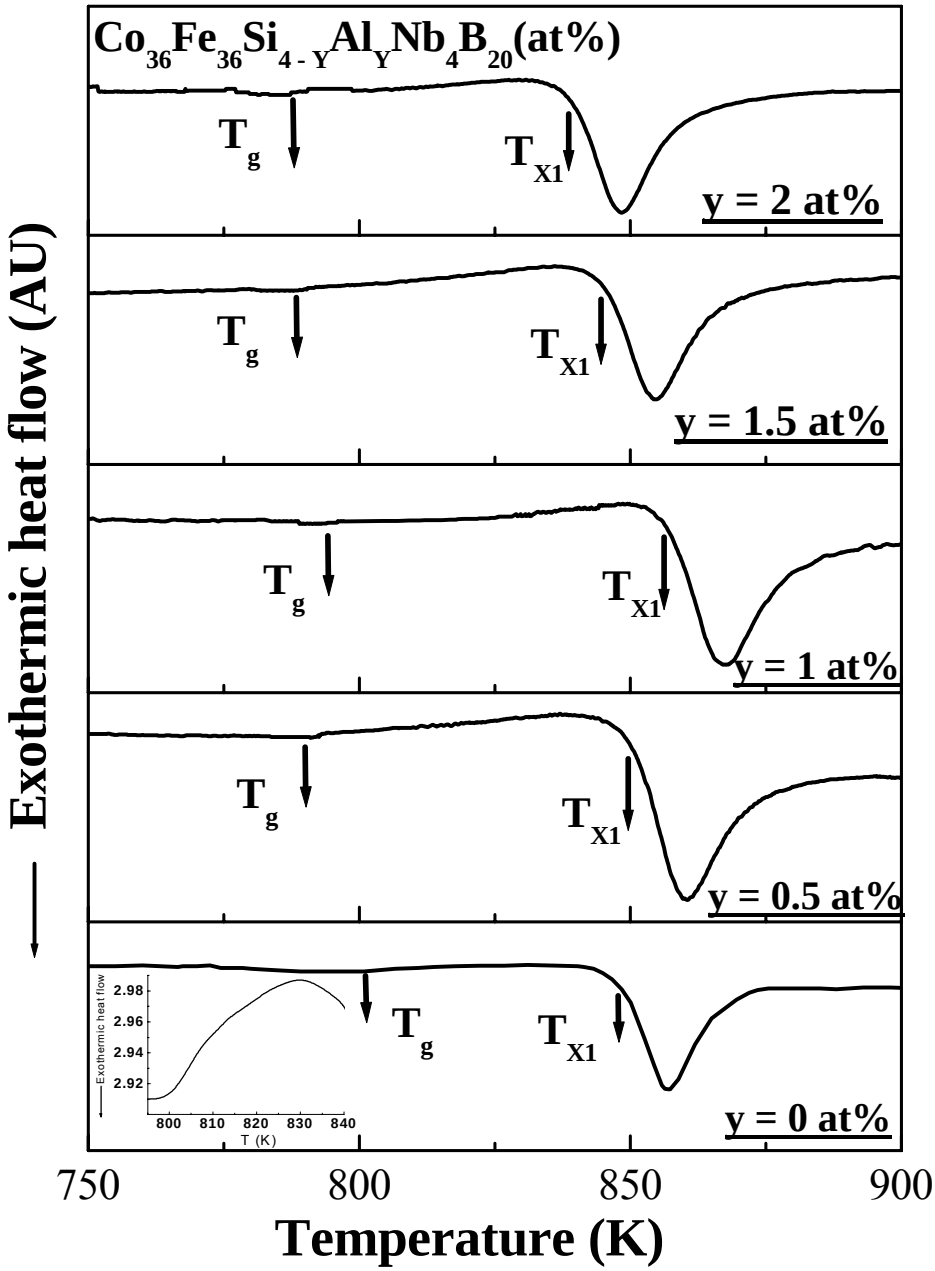

Fig-6.2: Differential scanning calorimetry (DSC) plots of as- spun $Co_{36}Fe_{36}Si_{4-y}Al_yNb_4B_{20}$, y = 0, 0.5, 1.0, 1.5, 2.0 at% alloys at a heating rate of 20 K/min

Fig-6.2 shows the DSC curve of melt spun ribbon of $Co_{36}Fe_{36}Si_{4-y}Al_yNb_4B_{20}$, (y = 0, 0.5, 1.0, 1.5, 2.0 at%) alloys measured at a scan rate of 20 K/min in an argon atmosphere. These alloys on thermal scanning up to 900K revealed exothermic transformation with an onset of crystallization at T_{X1} [9]. The crystallization temperature increases with Al content up to $y \leq 1$ at% and then displayed a decreasing trend when aluminium content was $1 < y < 2$ at% as shown in fig-6.3.

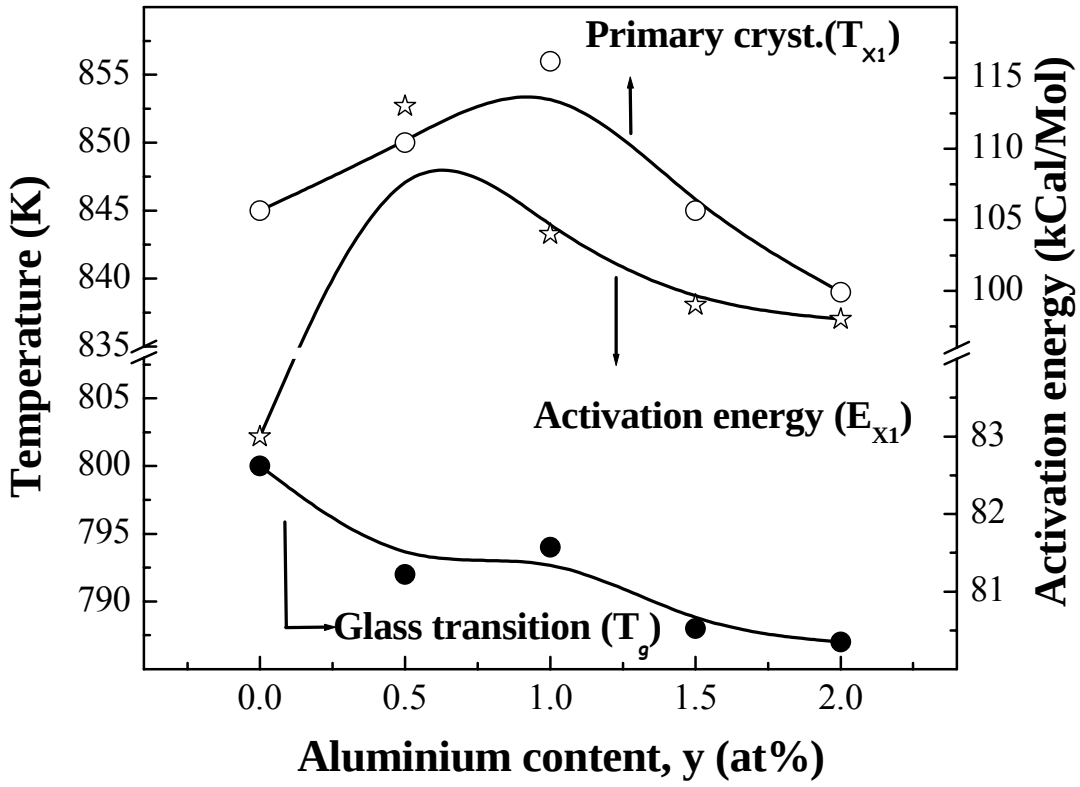

Fig-6.3: Variation of crystallization onset (T_{X1}), glass transition temperatures (T_g) and activation energy (E_{X1}) of $Co_{36}Fe_{36}Si_{4-y}Al_yNb_4B_{20}$, y = 0, 0.5, 1.0, 1.5, 2.0 at% alloys

An endothermic peak before the onset of primary crystallization in DSC plots corresponds to the glass transition temperature 'T_g'. The distinct endothermic onset is

shown in inset of fig-6.2 as an example for the alloy with y = 0. The 'T_g' was found to decrease with increasing Al content as shown in fig-6.3. The activation energy (E_{X1}) for the primary transformation was calculated using the modified Kissinger's equation [10] as given in eq. 6.1.

$$ln\left(\frac{T_p^2}{S}\right) = \frac{E_{act}}{RT_p} + \ln\left(\frac{E_{act}}{RK_o}\right) \ldots\ldots\ldots\ldots (6.1)$$

Where T_p is the temperature of the maximum of the peak, E_{act} is the effective activation energy for the process associated with the peak, S is the rate of thermal scanning, R is the gas constant and K_o is the pre-exponential factor in the Arrhenius equation for the rate constant k. The variation of E_{X1} followed similar trend as T_{X1} with Al incorporation has shown in fig-6.3.

6.4.2: Phase evolutions by XRD and TEM

Fig-6.4(a) shows the X-ray diffraction pattern of $Co_{36}Fe_{36}Si_{4-y}Al_yNb_4B_{20}$, y = 0, 0.5, 1.0, 1.5, 2.0 at% alloys annealed at 850 K. The diffractograms showed the formation of bcc-(CoFe)Si nanophase in the alloys with a predominant Si content [11]. However, the Al bearing alloys showed the formation of bcc-(CoFe)SiAl nanophase along with bcc-(CoFe)Si phases. This suggested the incorporation of Al into the bcc-(CoFe)Si phase with increased Al content. Fig-6.5 showed the TEM micrograph and corresponding selected area electron diffraction (SAED) patterns for $Co_{36}Fe_{36}Si_3Al_1Nb_4B_{20}$ alloy heat treated at 875K and 925K respectively. It is seen that the ultrafine grains about ~ 6-8 nm are dispersed in amorphous matrix annealed at 875K, at a temperature close to its onset of crystallization. It was observed that the nanoparticles formed in Al containing alloy is much finer scale compared to the Al free alloy which was around ~ 14-15 nm. Such finer nanoparticles found in Al bearing alloys may be responsible for improvement in soft magnetic properties marked by reduction of coercivity. The aluminium containing alloys revealed nanoparticle size about ~ 15 nm after annealing at much higher temperature at 925K which is comparable to that of y = 0 annealed at 875K.

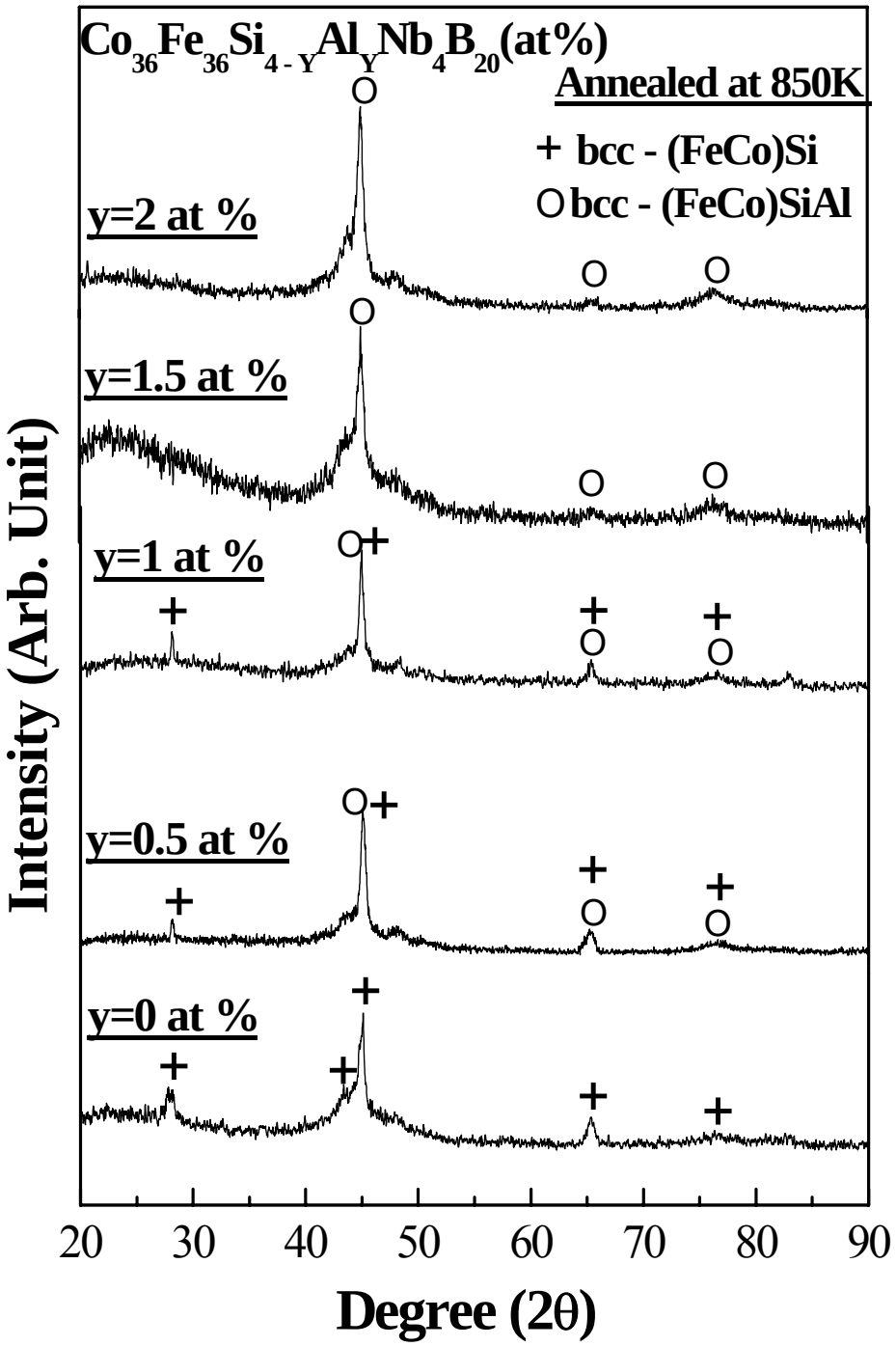

Fig-6.4a: XRD plots of $Co_{36}Fe_{36}Si_{4-y}Al_yNb_4B_{20}$, y = 0, 0.5, 1.0, 1.5, 2.0 at% alloys annealed at 850 K

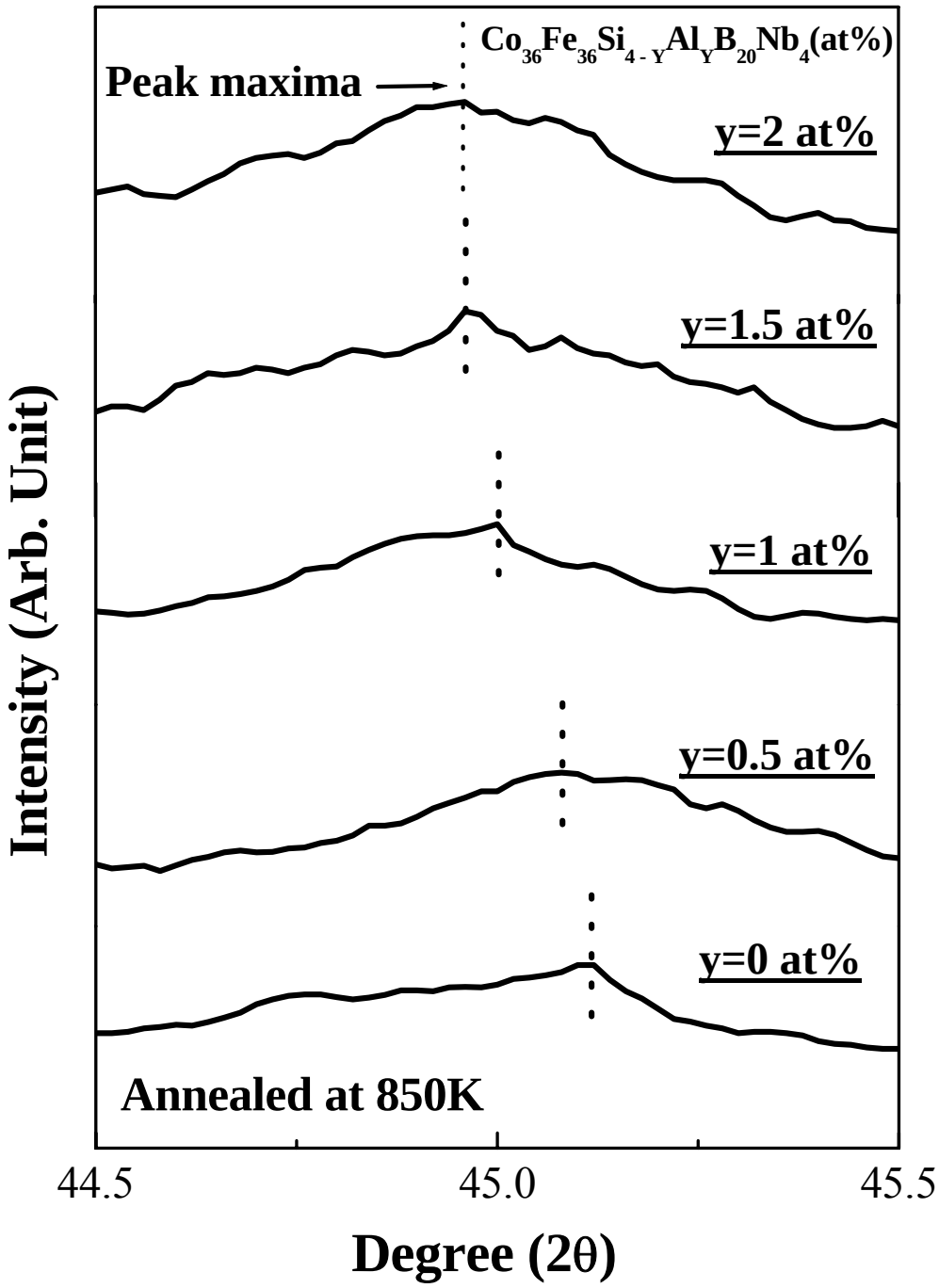

Fig-6.4b: The primary peak shift of XRD plots of $Co_{36}Fe_{36}Si_{4-y}Al_yNb_4B_{20}$ (y= 0, 0.5, 1.0, 1.5, 2.0 at%) alloys annealed at 850K. Plots are shown for the small span of 2^0 about primary peak

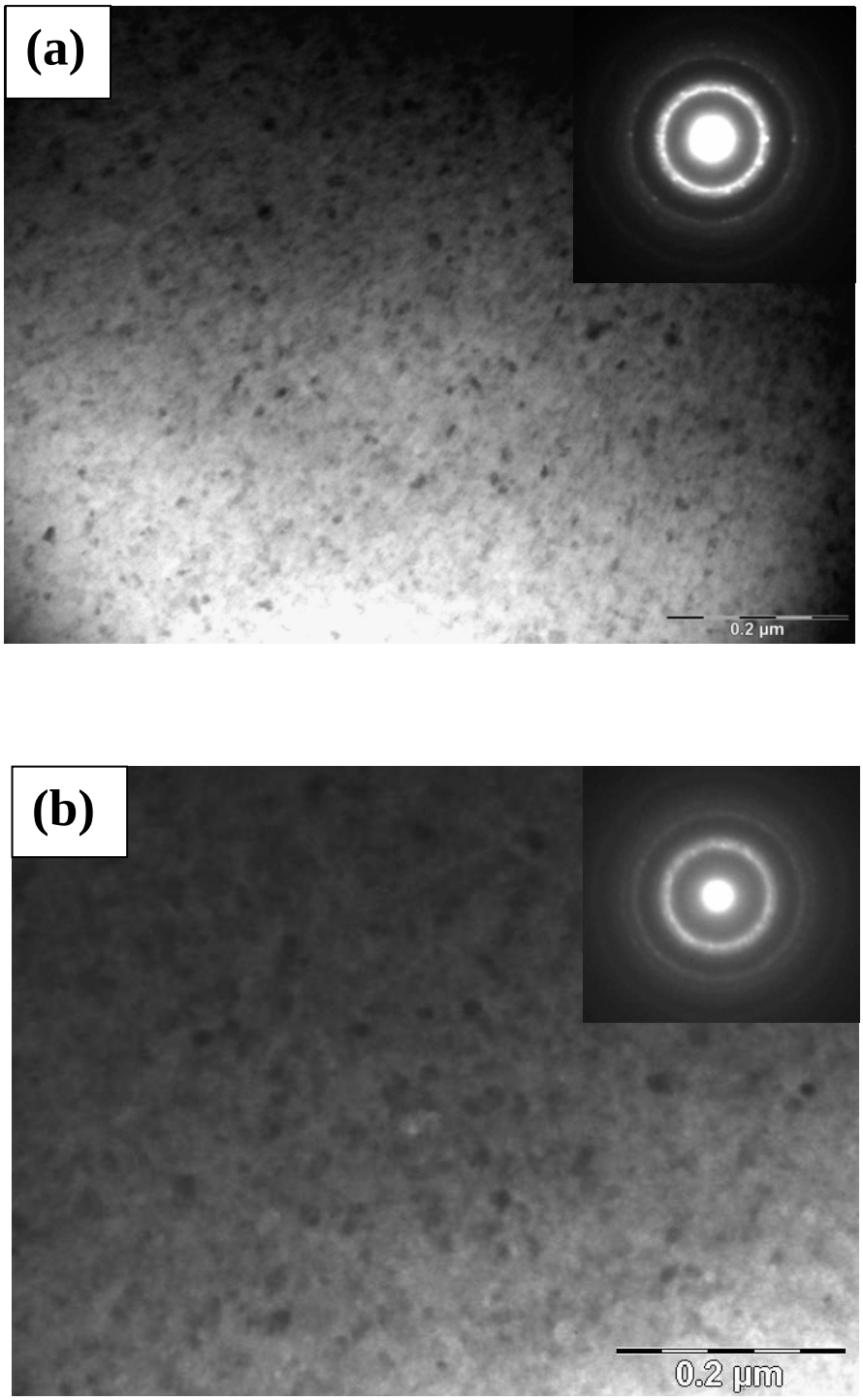

Fig-6.5: TEM micrograph of $Co_{36}Fe_{36}Si_3Al_1Nb_4B_{20}$ alloy annealed (a) at 875K and (b) at 925K. Corresponding SAED is given in the inset

6.4.3: Soft magnetic properties

6.4.3.1: Evolution of DC magnetic properties

The variation of DC coercivity with annealing temperature of $Co_{36}Fe_{36}Si_{4-y}Al_yNb_4B_{20}$, (y= 0, 0.5, 1.0, 1.5, 2.0 at %) alloys is shown in fig-6.6.

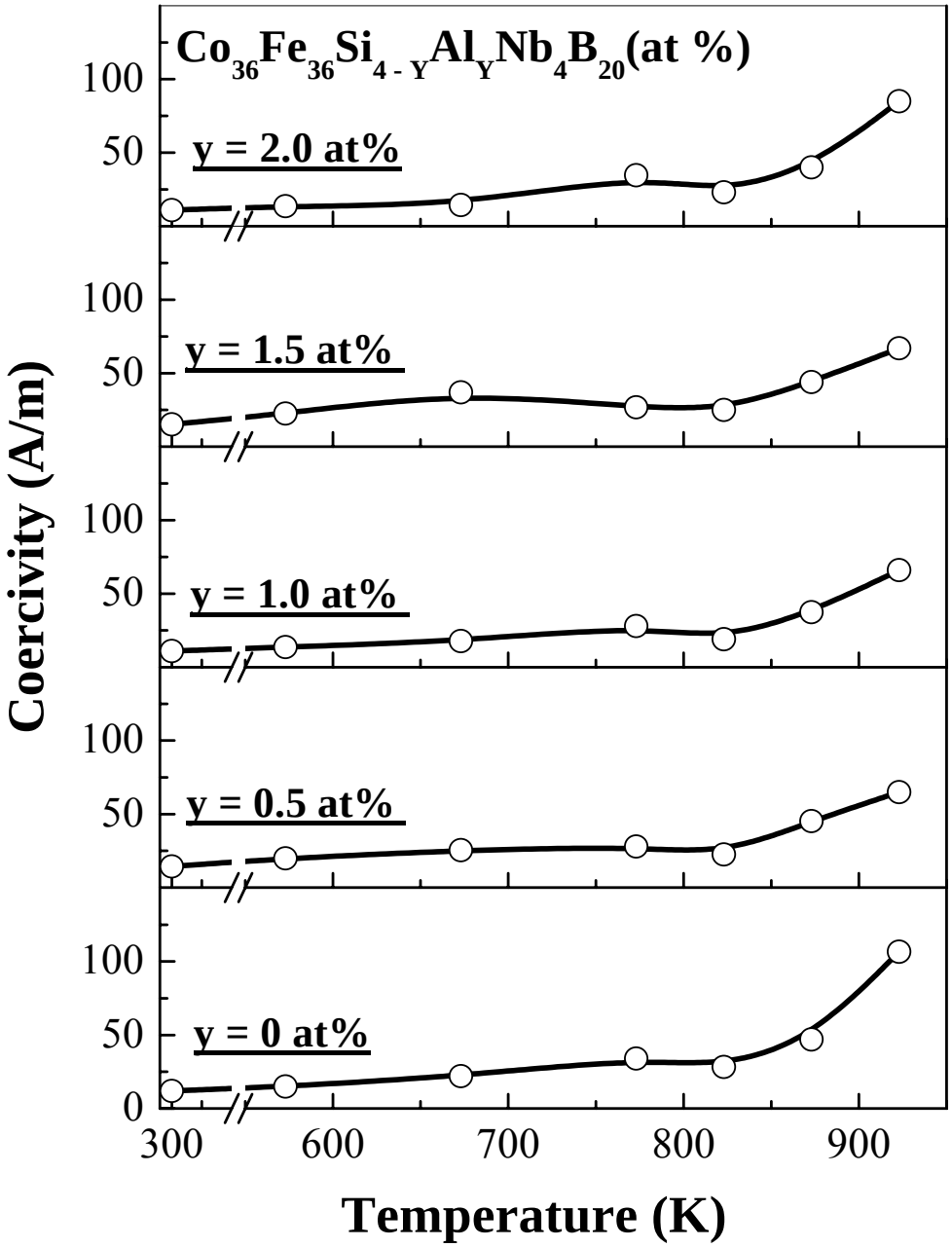

Fig-6.6: Variation of coercivity with annealing temperature of $Co_{36}Fe_{36}Si_{4-y}Al_yNb_4B_{20}$ (y = 0, 0.5, 1.0, 1.5, 2.0 at%) alloys

It has been noted that the coercivity of all the alloys after the initial rise remained consistent coercivity values up to 850K beyond which there was rapid degradation. The initial magnetic hardening with the rise in coercivity may be due to some Fe segregates on the grain boundary region before crystallization.

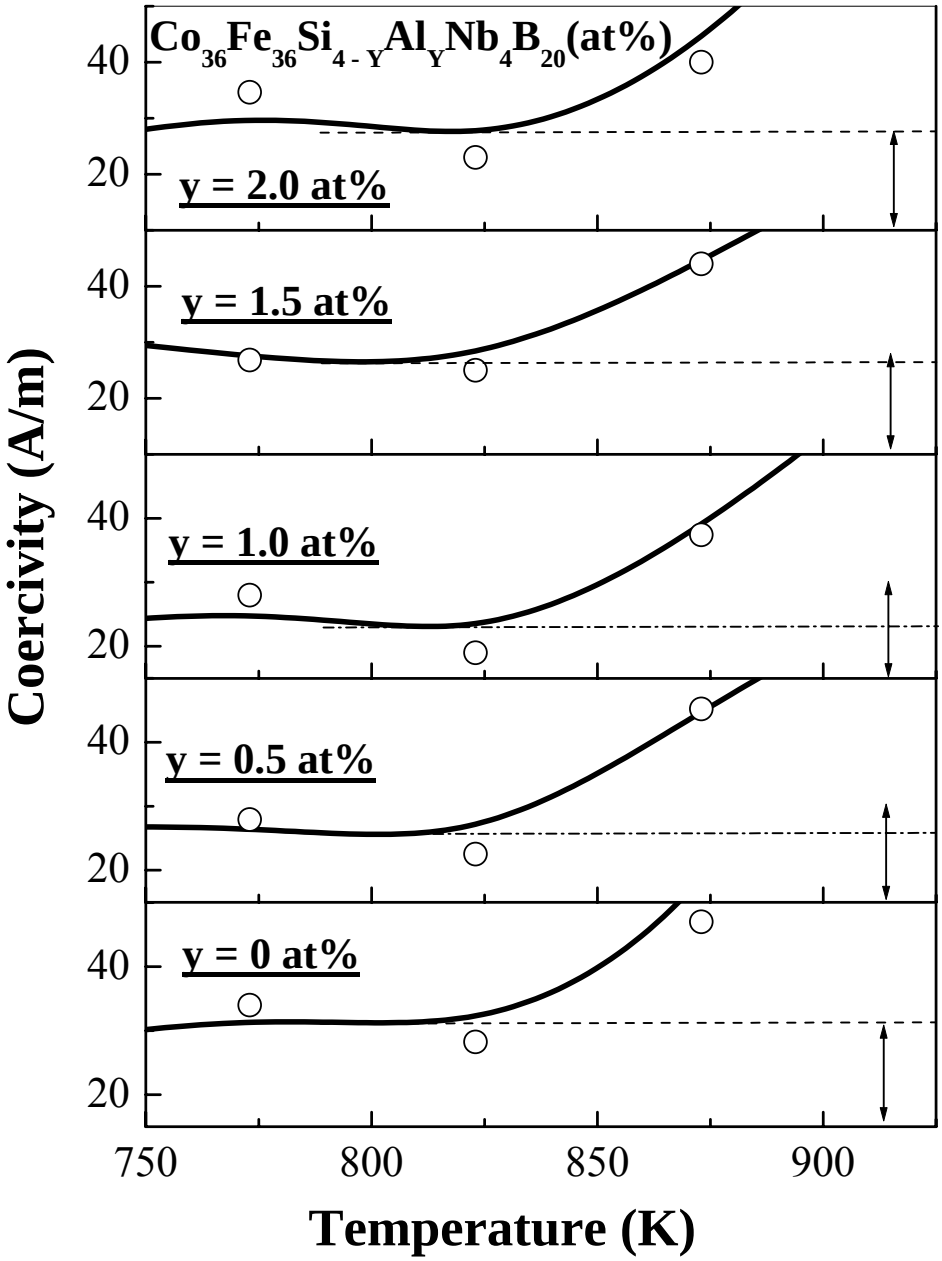

Fig-6.7: Optimal values of coercivity variation with annealing temperature in $Co_{36}Fe_{36}Si_{4-y}Al_yNb_4B_{20}$, (y = 0, 0.5, 1.0, 1.5, 2.0 at%) alloys. Extended arrow indicates minimal coercivity observed

A guide to minimum coercivity before this deterioration was indicated with an extended arrow of range 18A/m as shown in rescaled fig-6.7.

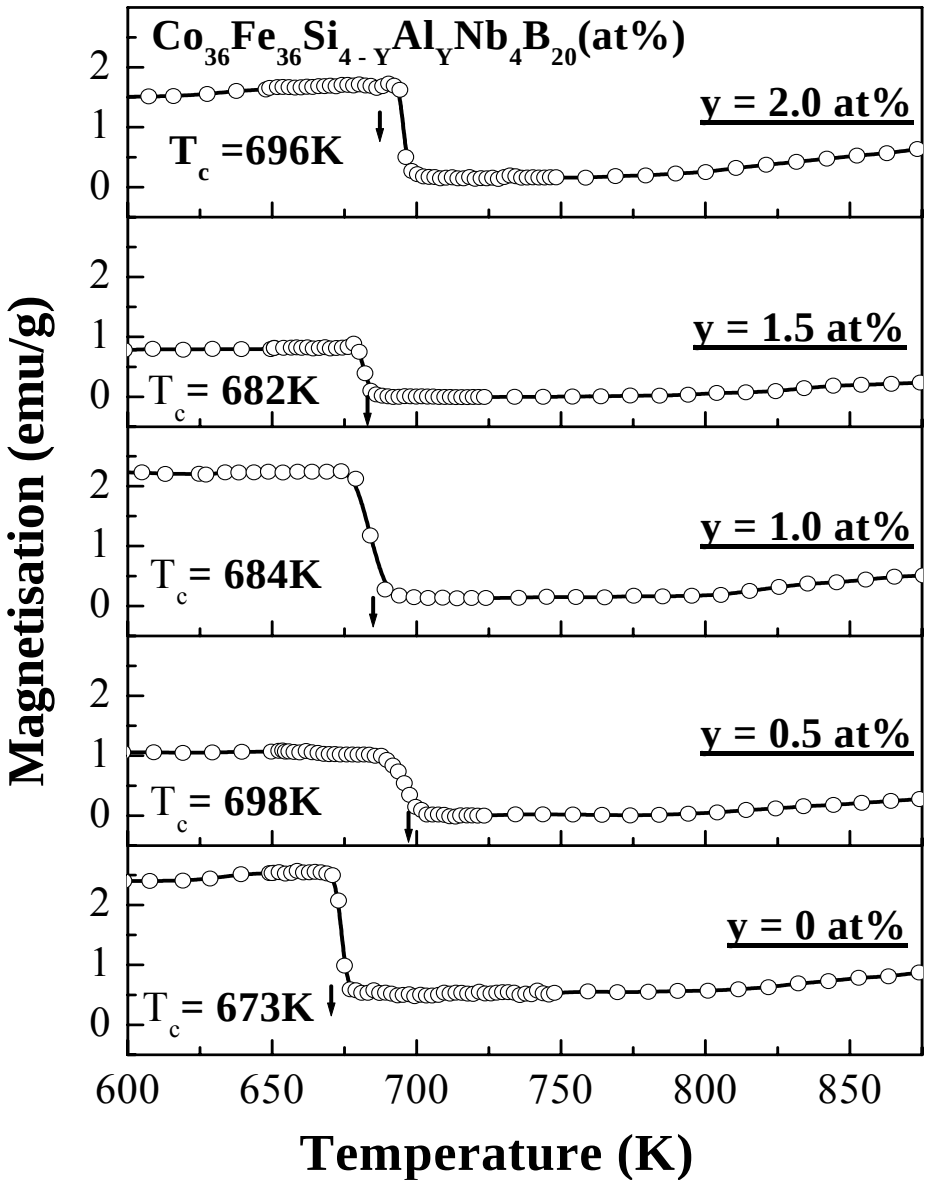

Fig-6.8: Temperature dependent magnetization curve of as spun $Co_{36}Fe_{36}Si_{4-y}Al_yNb_4B_{20}$ (y = 0, 0.5, 1.0, 1.5, 2.0 at%) alloys, at a magnetizing field of 2 Oe

This guide revealed that in Al devoid (y = 0 at %) and Al substituted (y = 2 at%) alloys, the minimal coercivity values were much higher than the alloys with

intermediate Al concentration ($0.5 \leq y \leq 1.5$). The consistent coercivity prior to degradation was observed in alloy with aluminium content of y = 1 at%.

6.4.3.2: Curie temperature

Thermal variation of magnetization of as spun $Co_{36}Fe_{36}Si_{4-y}Al_yNb_4B_{20}$, (y = 0, 0.5, 1.0, 1.5, 2.0 at%) alloys has shown in fig-6.8. The initial drop in magnetization indicated transition of ferromagnetic to paramagnetic state i.e. the Curie temperature 'T_C'. The estimated Curie temperature in amorphous phase was 673K, 698K, 684K, 682K, 696K for alloys y = 0, 0.5, 1.0, 1.5, 2.0 at% respectively. However at elevated

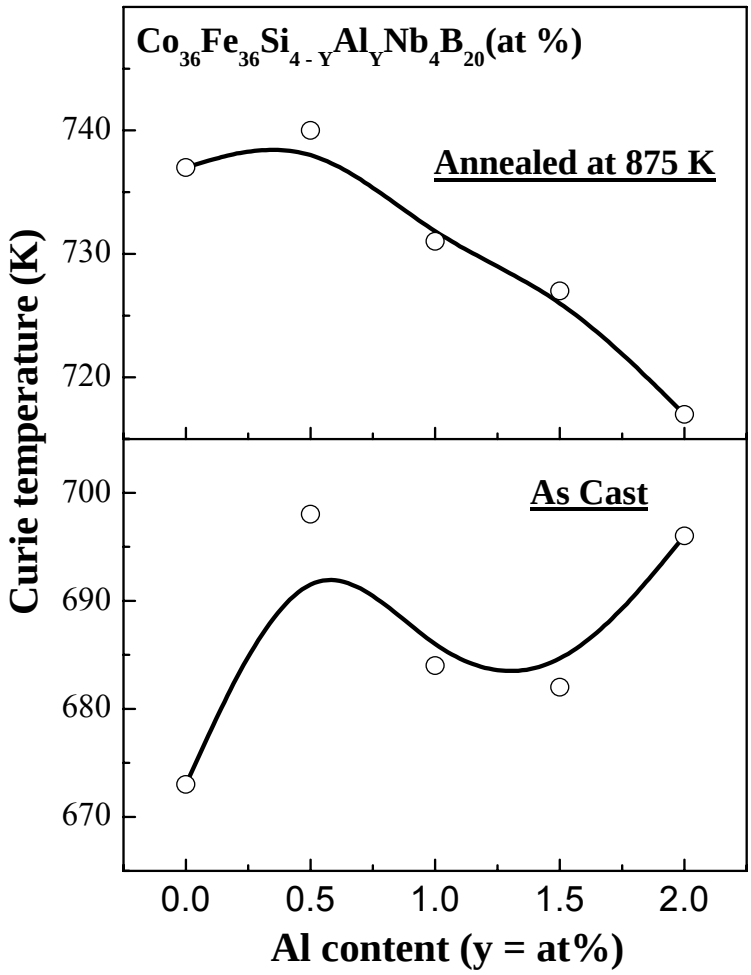

Fig-6.9: Variation of Curie temperatures with Al content of as spun as well as annealed at 875K for 15 min

temperature (Fig-6.8) beyond 850K, magnetization again increased due to the generation of ferromagnetic nanophases in amorphous matrix, which induced ferromagnetic exchange coupling with amorphous matrix. In the case of all alloys, the enhancement in magnetization was observed close to the crystallization temperature (T_{X1}). This may be attributed to the formation of bcc-(CoFe)Si and bcc-(CoFe)SiAl nanophases in amorphous matrix. Fig-6.9 shows the variation of Curie temperature with varying Al content of as cast along with heat treated at 875K. The trend in 'T_C' of the as-cast ribbon with Al content indicated non-linear variations. However, after annealing at 875K, 'T_C' showed a decreasing trend with increasing Al content though the drop was only by 25K with up to 2 at% of Al (y = 2 at%). This indicated that alloys, in their nanocrystalline state, exhibited higher Curie temperature towards lower Al concentration. It is possibly attributed to the preferential substitution of nanocrystalline phase by Al. These Al-enriched nano-phases exhibit magnetic moment with inverse proportional relation to Al content and Curie temperature. It is supported by the possibility of Si substitution by Al in FeSiAl alloy system.

6.5: Discussion

Detailed analysis of the effect of Al on the magnetic properties is shown in fig-6.10. In the as-cast state, the coercivity varied non-linearly thereby exhibiting the competing role of Al and Si in the amorphous structure. On annealing at a temperature of 875K, close to the onset of crystallizations, the alloys with y = 0 at% and y = 2 at% show much rapid degradation in coercivity compared to those with intermediate Al content. The alloys annealed at an elevated temperature of 925K, exhibit further deterioration in coercivity. At higher annealing temperatures, the variation of coercivity with Al-content shows a shallow profile with a minima at Al-content of y = 1. This enhancement in property (low coercivity) may be attributed to some sort of Al partitioning into a nano-phase bcc-(CoFe)Si modifying it to bcc-(CoFe)SiAl during the process of nanocrystallisation. Such modification of nanophase is supported by the peak shift in x-ray diffractogram (Fig-6.4b) towards higher d-spacing (lower angle). In the alloys with y = 0 the high Si content led to peak shift towards higher diffracting angle as shown in fig-6.4b. As the silicon to aluminium ratio increases, the diffraction angle 2θ of the crystallizing nano-crystal

increases. This is attributed to lattice shrinkage due to Si partitioning into solid solution of

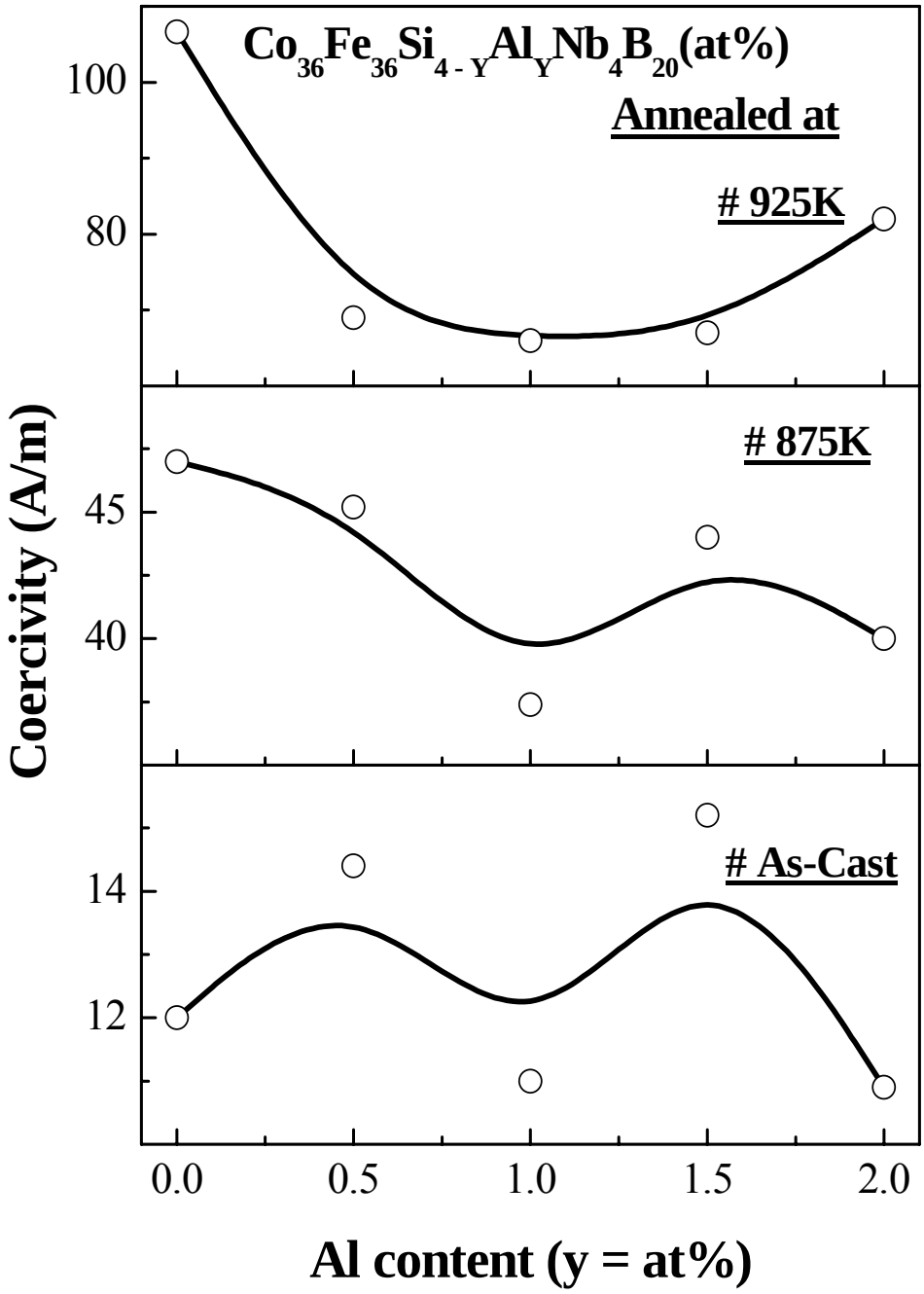

Fig-6.10: Variation of coercivity with aluminium content of as cast and annealed at 875K and 925K of $Co_{36}Fe_{36}Si_{4-y}Al_yNb_4B_{20}$ (y = 0, 0.5, 1.0, 1.5, 2.0 at%) alloys

bcc-(CoFe) to form the nanostructured silicide phase around crystallization temperature T_{X1} [12]. With subsequent replacement of Si by Al, the lattice shrinkage effect was counteracted by lattice expansion [13] and consequent peak shift towards low angle. The variation of lattice parameter as derived from the primary peak of X-ray diffractogram of sample annealed at 850K with Al addition is shown in fig-6.11. Al substitution up to 1 at% showed rapid increase in lattice parameter (inset of fig-6.11) beyond which this rise had a tendency to reach a limiting value. The limiting tendency at an approach of 2 at% Al may be attributed to a competing role of Si and Al towards lattice shrinkage and expansion respectively.

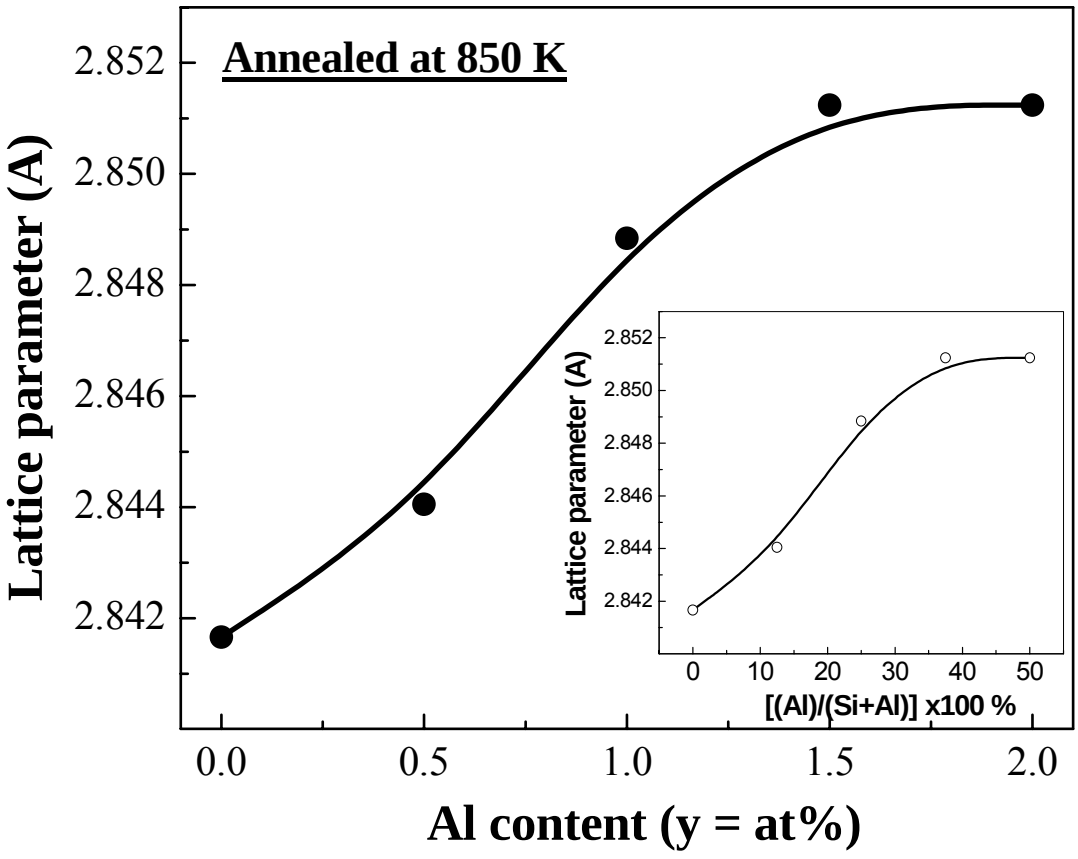

Fig-6.11: Variation of lattice parameter obtained from major peak of X-ray diffractograms of $Co_{36}Fe_{36}Si_{4-y}Al_yNb_4B_{20}$ (y = 0, 0.5, 1.0, 1.5, 2.0 at%) alloys annealed at 850K. Inset shows lattice parameter versus [Al(Si+Al)]X100%

Al substitution for Si has been found to alter T_X and T_g indicating its influence on the amorphous structure. Scattering factor was determined from the major peak of x-ray diffraction pattern of alloys annealed at 850K. The replacement of Si by Al led to a decrease in scattering factor as shown in fig-6.12. The scattering factor was determined [14] from the primary peak using the equation

$$K = \frac{4\pi \mathrm{Sin}\theta}{\lambda} \quad \ldots\ldots\ldots\ldots\ldots\ldots\ldots\ldots (6.2)$$

Where Θ is the diffracting angle of the major primary peak obtained from X-ray diffractograms, and λ is the wavelength of the CuKα radiation.

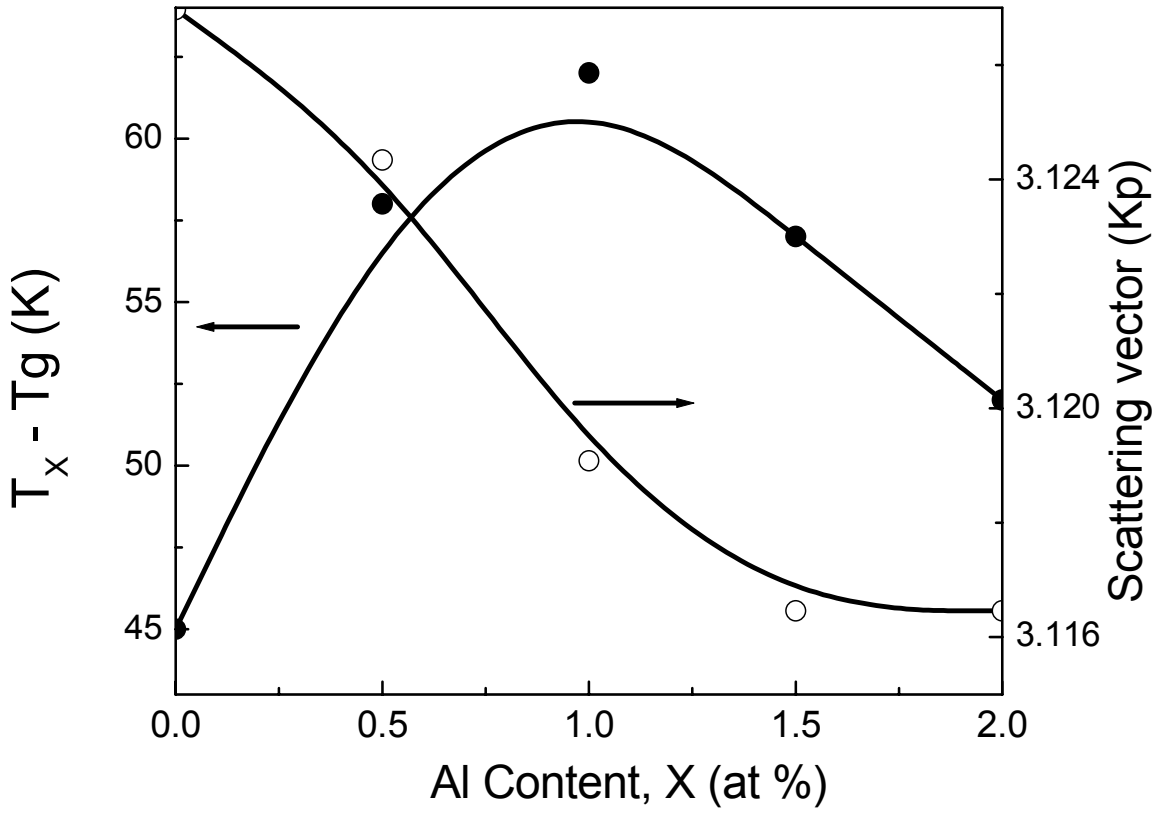

Fig-6.12: Variation of super cooled region (T_X – T_g) and the magnitude of the scattering vector of 850K annealed $Co_{36}Fe_{36}Si_{4-y}Al_yNb_4B_{20}$ (y= 0, 0.5, 1.0, 1.5, 2.0 at%) alloys

This decreased scattering constant 'k_p' is due to an increase in Fe-Fe, Fe-Co and Co-Co atomic pair distance for the addition of larger element Al [15]. The increase in atomic spacing with Al incorporation leads to an increase in the vacant regions for enhanced dissolution of the metalloid required for the amorphous structure. However, the relative reduction in metalloid Si content with Al addition beyond y = 1 did not contribute much towards the amorphous stabilization and as a result the glass transition temperature 'T_g' and the corresponding super cooled region [16] was affected. The extent of super cooled region, ΔT_X obtained as ($T_X - T_g$) and shown in fig-6.12 suggests that such an effect on amorphous phase stability is observed with Al substitution up to y = 1 at%.

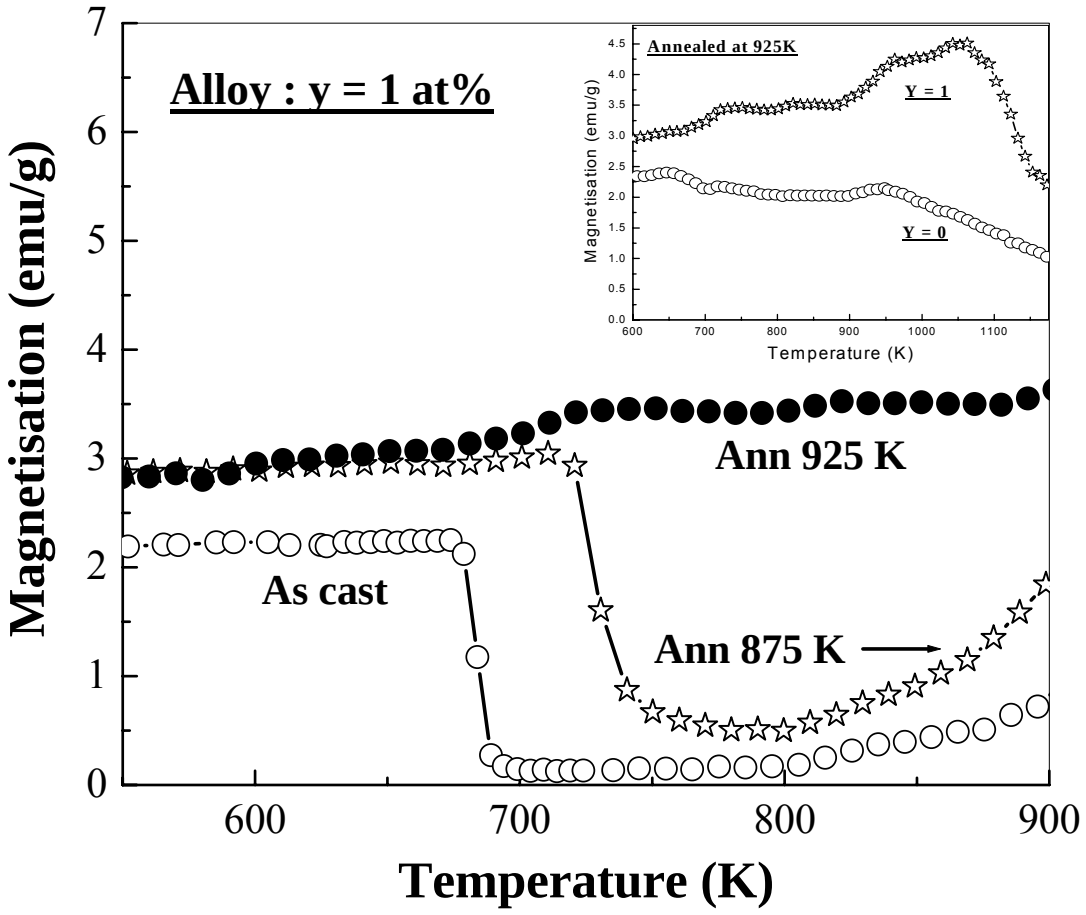

Fig-6.13: Effect of annealing temperature on thermal variation of magnetization in $Co_{36}Fe_{36}Si_3Al_1Nb_4B_{20}$ alloys. Inset shows the profile for y = 0 and y = 1 alloys annealed at 925K, at a magnetizing field of 2Oe

ΔT_X increased continuously up to y = 1 beyond which there was a decreasing trend with Al content. Beyond this Al content, the scattering vector also tended to reach a limiting trend. The effect of Al addition was also observed in inducing enhanced amorphous stability as observed from microstructural evaluations. The substitution of Al for Si has also been known to favorably enhance the magnetic moment of system as the element Al having one less p-electron than Si atom, promotes smaller charge transfer from Al to Fe atoms thereby raising the magnetization [17]. This was observed from higher level of magnetization in alloy with y = 1 at% for samples annealed at 875K as observed from thermal variation of magnetization in fig-6.13. This may be attributed the process of nanocrystallisation whereby the partitioning of Al along with reduced fraction of Si in y = 1 at% formed (CoFe)SiAl nanophase with enhanced magnetic moment. This plot which also revealed the thermal variation of ferromagnetic ordering also revealed that in y = 1 at% alloy, the drastic fall in magnetization was subsequently followed by rise in moment around 800K whereas the alloy without aluminium maintained a low moment range after the drop. This enhanced behaviour of ferromagnetic ordering in the former case was further manifested by a more stable ferromagnetic ordering (inset of fig-6.13) up to 1100K in Al containing alloy (y = 1 at%) compared to reduction in magnetization around 1000K in y = 0 at% alloy. The bcc (CoFe)SiAl due to its enhanced magnetization is supposed to shift the exchange coupling of nanoparticles through paramagnetic amorphous matrix towards high temperature regions [18-20].

In high temperature applications the efficiency of soft magnetic components in transformers and rotor assemblies depend on the frequency response of coercivity and core loss [21]. As seen in fig-6.14 and fig-6.15, the as-cast alloy with aluminium content of y = 1 at% revealed lower values of coercivity and core loss respectively than the alloy without Al (y = 0 at%). In the as-cast state, both the alloys revealed a consistent difference in their properties (coercivity, core loss) throughout the evaluated span of frequencies. This behaviour suggests that Al incorporation enhanced the as-cast disordered structure for lower coercivity and higher resistivity for low eddy current loss leading to reduction in core loss. However, in the nanocrystalline state through annealing at 875K, the alloy with y = 1 at% revealed distinct divergence from y = 0 at% for coercivity and core loss at higher frequencies.

This behaviour may attributed to the reduction in anisotropy with Al incorporation into (CoFe)SiAl nanophase. Additionally, the lower particle size ~ 6 nm in the former alloy compared to 15nm for y = 0 at% attributed towards greater electron scattering (higher resistivity) for lower core losses at higher frequencies.

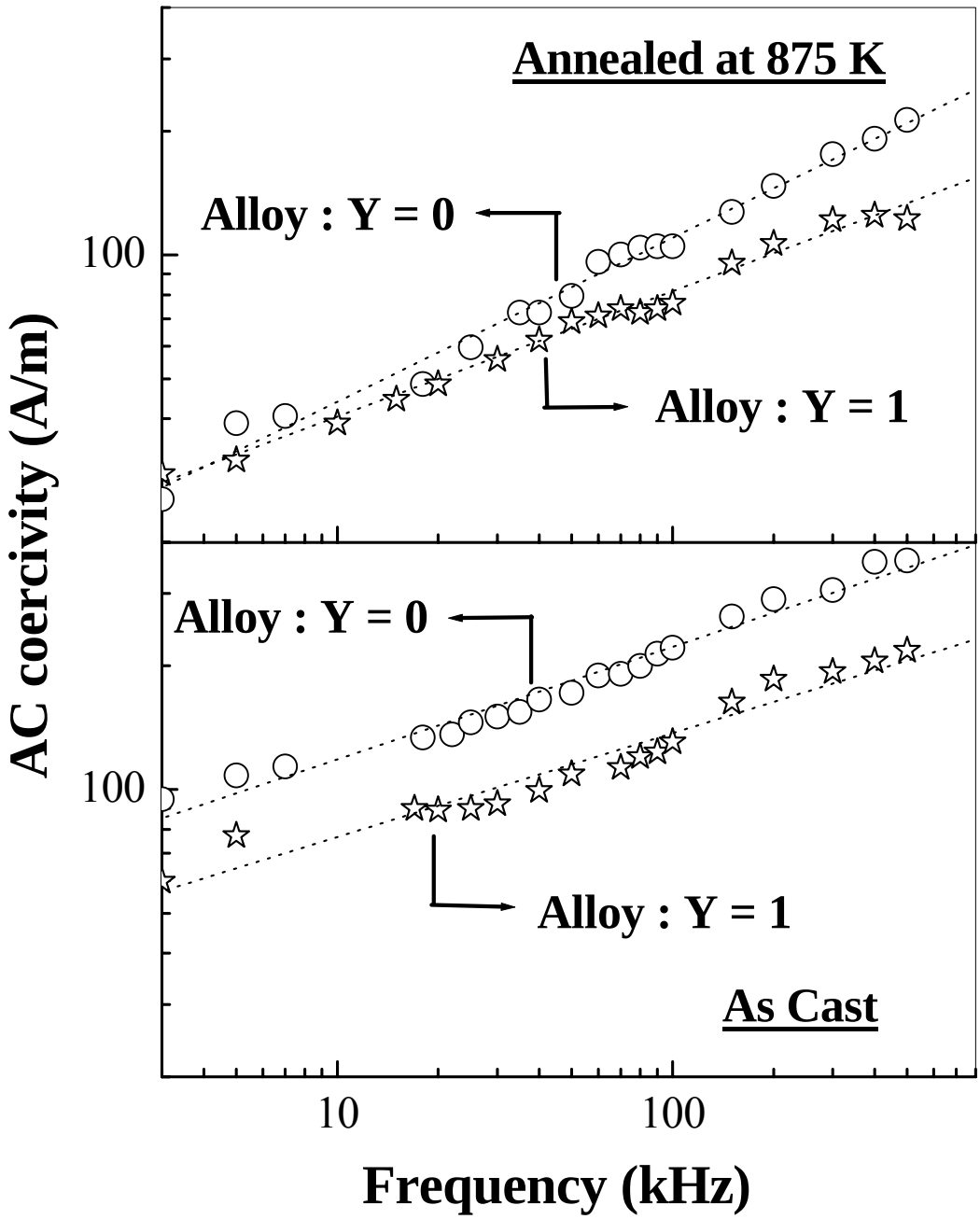

Fig-6.14: AC coercivity for as- spun and annealed at 875K for y = 0 and y = 1 of $Co_{36}Fe_{36}Si_3Al_1Nb_4B_{20}$ alloys

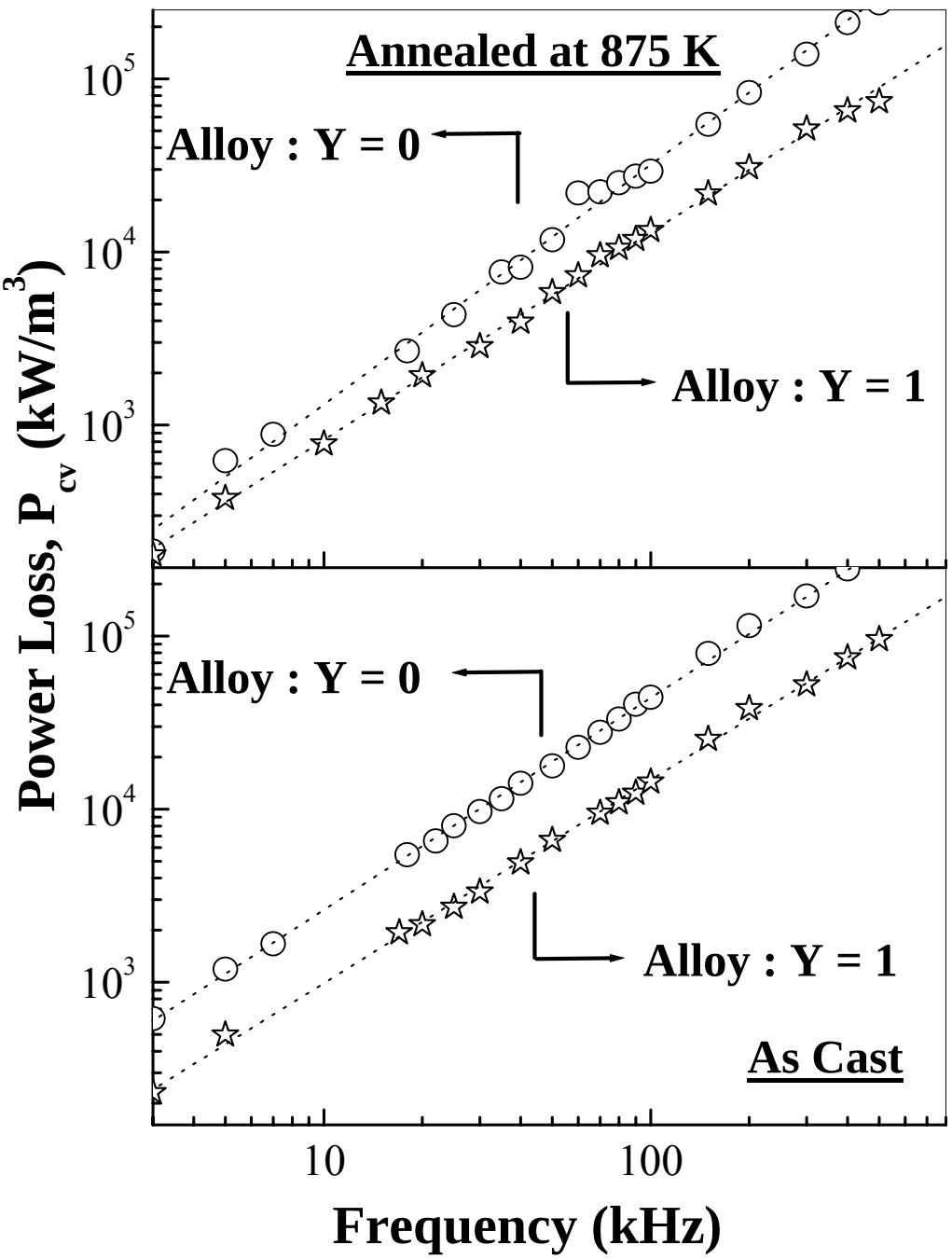

Fig-6.15: AC power loss for as- spun and annealed at 875K for y = 0 and y = 1 of $Co_{36}Fe_{36}Si_3Al_1Nb_4B_{20}$ alloys

6.6: Conclusion

The $Co_{36}Fe_{36}Si_{4-y}Al_yNb_4B_{20}$, (y = 0, 0.5, 1.0, 1.5, 2.0 at%) alloys were prepared in the form of amorphous ribbons by the melt spinning technique. The onset of crystallization temperature increased with Al content up to ($y \leq 1$), whereas at higher Al content there was a decreasing trend. The glass transition temperature (T_g) reduced with increasing Al content. Compared to all the other compositions, the alloy with optimum Al content for y = 1 at% exhibited stable coercivity values at high temperature. This may be attributed to reduction of magneto crystalline anisotropy with Al incorporation and at the same time smaller nanoparticles bcc-(CoFe)SiAl to induce effective averaging of anisotropy. In the nanostructured state when annealed at 925K, the alloy without Al (y = 0) showed reduction in ferromagnetic ordering above 1000K. However, the Al containing alloy with y = 1 at% exhibited stable ferromagnetic ordering up to 1100K i.e. additionally by 100K. This optimal Al containing alloy also revealed better frequency response of coercivity and low core losses compared to the alloy without Al (y = 0 at%).

References

[1] B.J. Tate, B.S. Parmar, I. Todd, H.A. Davies, M.R.J. Gibbs and R.V. Major, J. Appl. Phys. Vol. 83, p 6335 (1988).

[2] I. Todd, B.J. Tate, H.A. Davies, M.R.J. Gibbs, D. kendall and R.V. Major, J. Magn. Magn. Mater., Vol. 215-216, p 272 (2000).

[3] R.Boll in Electronic and Magnetic Properties of Metals and Ceramics in Materials Science and Technology, Part II edited by K.H.J.Buschow, Vol. 3B (VCH pub.) p 446.

[4] J.E. May, M.F. de Oliveira, C.R.M. Afonso, R.D. Sa Lisbio and S.E. Kuri, J. Non-crystalline solids, Vol. 348, p 250 (2004).

[5] A.K.Panda, O. Mohanta, A.Kumar, M.Ghosh and A.Mitra, Philosophical Magazine, Vol. 87, No. 11, p 1671 (2007).

[6] A. Zelenakova, M. Kuzminski", J. Fuzer, P. Kollar and T. Svec., J. Magn. Magn. Mater. Vol. 215-216, p 459 (2000).

[7] A. Zorkovsk´a, P. Petrovi˘c, P. Sov´ak and J. Kov´a˘ "Presented at 11th Czech and Slovak Conference on Magnetism, Ko˘sice, 20–23 August 2001", Czechoslovak Journal of Physics, Vol. 52, No. 2, (2002).

[8] I. Todd, B.J. Tate, H.A. Davies, M.R.J. Gibbs, D. kendall and R.V. Major, J. Magn. Magn. Mater., Vol. 215-216, p 272 (2000).

[9] C.F. Conde and A. Conde, Mater. Sci. Forum Vol. 179, p 587 (1995).

[10] E.J. Mittemeijer, L. Chang, P.J. Van Der Schaaf, C.M. Brakman and B.M. Korevaar., Metall. Trans. A 19, p 925 (1988).

[11] C. Gomez-Polo, P. Marin, L. Pascual, A. Hernando and M. Vásquez., Phys. Rev. B Vol. 65, 024433(2002).

[12] M. Muller, N. Mattern, L. Illgen, Z. Metallk. Vol. 82, p 895 (1991).

[13] E. Apinaniz, E. Legarra, F. Plazaola and J.J.S. Garitaonandia, J. Magn. Magn. Mater. Vol. 320, e692 (2007).

[14] B.D. Cullity, "Elements of X-ray diffraction", Addison–Wesley publ.co, Massachusetts (1978).

[15] A. Inoue, H. Yamamoto and T. Masumoto, Mater. Trans., JIM Vol. 31, p 1021 (1990).

[16] A. Inoue, Mater. Trans. JIM Vol. 36, p 866 (1995).

[17] E. Apinaniz, E. Legarra, F. Plazaola and J.J.S. Garitaonandia, J. Magn. Magn. Mater. Vol. 316, e470 (2007).

[18] A. Hernando, I. Navarro, and P. Gorria., Phys. Rev. B Vol. 51, p 3281 (1995).

[19] A. Hernando and T. Kulik, Phys. Rev. B Vol. 49, p 7064 (1994).

[20] A. Slawska-Wanieska, A. Ślawska-Waniewska, P. Nowicki, H. K. Lachowicz, P. Gorria, J. M. Barandiarán, and A. Hernando., Phys. Rev. B Vol. 50, p 6465 (1994).

[21] M.E. Mc. Henry and D.E. Laughlin, Acta Mater. Vol. 48, p 223 (2000).

Chapter-7

Influence of annealing on the electrochemical behaviour of CoFeSiAlNbB alloy

7.1: Introduction

Nanocrystalline $Co_{36}Fe_{36}Si_4Nb_4B_{20}$ alloy is found to be a good soft magnetic alloy for high temperature applications as discussed in Chapter-4 and Chapter-5 and is reported by our group [1-2]. The soft magnetic property can be further enhanced with the addition of Al as discussed in Chapter-6 and as reported by us [3]. Limited work is reported on the electrochemical properties of nanocrystalline materials of similar type (Fe-based alloy) and about the influence of corrosion on magnetic properties [4–6]. Depending on the applications, Fe based nanocrystalline alloy may have to work in a wet industrial and marine atmosphere containing sulphide and chloride ions, and it is difficult to eliminate the interaction between materials and environment. This may lead to an electrochemical corrosion. On the other hand, high ambient temperature is an additional factor accelerating the corrosion rate. The corrosion products forming on the surface of a ferromagnetic alloy may cause a partial degradation of soft magnetic properties. Therefore, the study of electrochemical and corrosion behaviour of the developed alloy is essential for its industrial applications.

The electrochemical and corrosion behavior of $Co_{36}Fe_{36}Si_{4-y}Al_yNb_4B_{20}$ (y = 0, 1 at%) alloys in 0.5M NaCl solution were studied by using cyclic anodic polarization experiment and electrochemical impedance spectroscopy (EIS). The change in magnetic properties of the optimum alloy on exposure to 0.5M NaCl solution was also investigated.

7.2. Brief resume of previous work

Corrosion resistance of amorphous metallic materials mostly depends on their structure and phase compositions. Limited data is published on the electrochemical behavior of Fe based amorphous and nanocrystalline alloys in corrosive solution.

There are reports on substitution of alloying elements in the FINEMET type alloys and its effect on the electrochemical behavior [7-9]. The corrosion products formed on the surface of the alloys may change their structural properties [10] resulting in the partial degradation of soft magnetic properties of Fe-based alloys [11].

7.3: Material studied

The present study is carried out on the melt spun $Co_{36}Fe_{36}Si_{4-y}Al_yNb_4B_{20}$ (y = 0, 1 at%) amorphous ribbons and their nano-crystalline progenies formed by the heat treatment at 850K and 875K for 15 minutes. The cyclic anodic polarization (AP) and electrochemical impedance spectroscopy (EIS) is carried out in 0.5 molar solution of NaCl. The ribbon sample of dimension approximately 4cm x 2mm x 30µm (length x breadth x thickness) used for experiment is degreased by acetone. A test part of 0.4 cm^2 is created on it by covering rest of the surface with a protective layer. The magnetic property of the samples exposed to 0.5M NaCl solution for 15 days is evaluated. Both AP and EIS tests were conducted using potentiostat Gamry Instruments and accompanying software for 'general purpose electrochemical system' and 'frequency response analyzer system'.

7.4: Results and discussion

Corrosion behavior of the optimum $Co_{36}Fe_{36}Si_{4-y}Al_yNb_4B_{20}$ (y = 0, 1 at%) alloys is studied by cyclic voltametry and electrochemical impedance spectroscopy. The polarization curve and impedance data were obtained after holding the samples at open circuit potential for 20 minutes. In the cyclic polarization experiments, the alloys were scanned from negative (cathodic) overpotential to positive (anodic) overpotential and reverse to negative (cathodic) overpotential at a scan rate of 2mV/s. The scan rate was chosen to be slightly high so as to avoid total anodic dissolution of very thin samples prior to the completion of test. The corrosion resistance of the $Co_{36}Fe_{36}Si_{4-y}Al_yNb_4B_{20}$ (y = 0, 1 at%) alloys was evaluated based on the measurement of the corrosion potential E_{corr} (mV) and the corrosion current density i_{corr} (A/cm^2) using first Tafel method. The cyclic anodic polarization curves of amorphous alloy variants (y = 0, 1 at%) and corresponding nanocrystalline materials (heat treated at 825K and 875K respectively, for y = 0, 1 at% alloys) are shown in fig-7.1a, 7.1b and 7.1c respectively. It is observed that in amorphous state, both the alloys with y =0 at%

and y = 1 at% do not show any pitting behavior (Fig-7.1a). The heat treated alloys exhibit pitting corrosion (Fig-7.1b & c). The corrosion potential E_{corr} (in mV) and the corrosion current density i_{corr} (in A/cm^2) are evaluated from the anodic polarization curves using Tafel method. The value of i_{corr} (the current density at the open circuit or corrosion current density) can be calculated by fitting the experimental data to the following Tafel equation used by the theoretical model for the current-potential relationship

$$i = i_{corr} [10^{(E- E_{corr})/b_a} - 10^{-(E- E_{corr})/b_c}]\ldots. \qquad (7.1)$$

where 'i' is the current density, 'E' is the potential, 'E_{corr}' is the potential at the open circuit, 'b_a' is the slope of the anodic polarization curve (anodic beta Tafel constant in volts/decade), 'b_c' is the negative slope of the cathodic polarization curve (cathodic beta Tafel constant in volts/decade).

It is observed that the addition of 1 at% Al in place of Si in $Co_{36}Fe_{36}Si_{4-y}Al_yNb_4B_{20}$ alloy displaces the anodic polarization curves to lower current density (Fig-7.1b & c). It exhibits more noble corrosion potential with lower i_{corr} compared to Al free alloy in both amorphous and nanocrystalline state (Fig-7.1b & c). Apparently, former (the alloy with y = 1 at%) has higher resistance to corrosion. The obtained result also shows that the increase in annealing temperature from 825K to 875K shifts the corrosion potential anodically in the case of alloy with 1 at% Al. The kinetic parameters including corrosion potential (E_{corr}), corrosion current density (i_{corr}) and Tafel slopes (b_c, cathodic beta Tafel constant in volts/decade) of $Co_{36}Fe_{36}Si_{4-y}Al_yNb_4B_{20}$ (y = 0, 1 at%) alloys are calculated from Tafel plots through the software and the data is summarized in table-7.1. Tafel slope is 0.11 V/decade for as cast alloy whereas 0.14 V/decade for nanocrystalline alloy of optimum composition. The enhanced resistance to corrosion of the optimum alloy $Co_{36}Fe_{36}Si_3Al_1Nb_4B_{20}$ can be explained by its nanocrystalline structure. The optimum $Co_{36}Fe_{36}Si_3Al_1Nb_4B_{20}$ alloy upon nanocrystallization at 875K, transforms to an alloy with bcc-(FeCo)SiAl and bcc-(FeCo)Si nanocrystals dispersed within an amorphous matrix (Fig-6.4a, 6.5) as discussed earlier in Chapter-6.

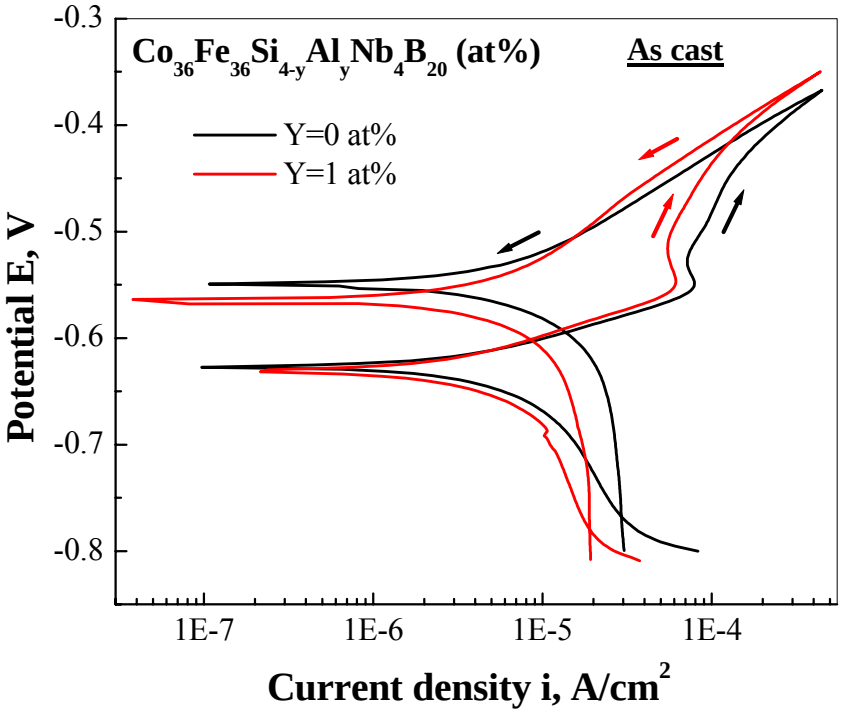

Fig-7.1a: Comparison of cyclic polarizations curves of the as quenched $Co_{36}Fe_{36}Si_{4-y}Al_yNb_4B_{20}$ (y = 0, 1 at%) alloys

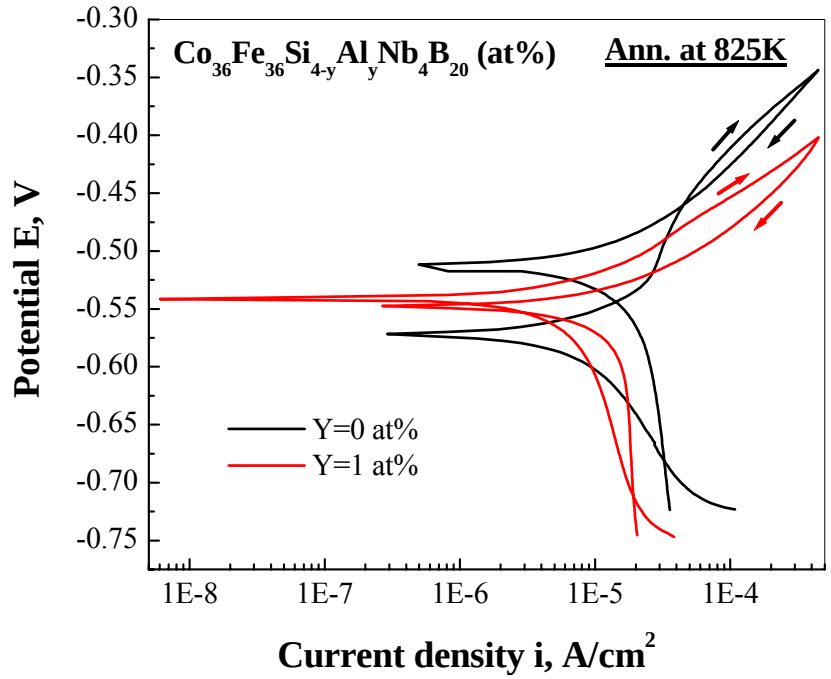

Fig-7.1b: Comparison of cyclic polarizations curves of the $Co_{36}Fe_{36}Si_{4-y}Al_yNb_4B_{20}$ (y = 0, 1 at%) alloys heat treated at 825K

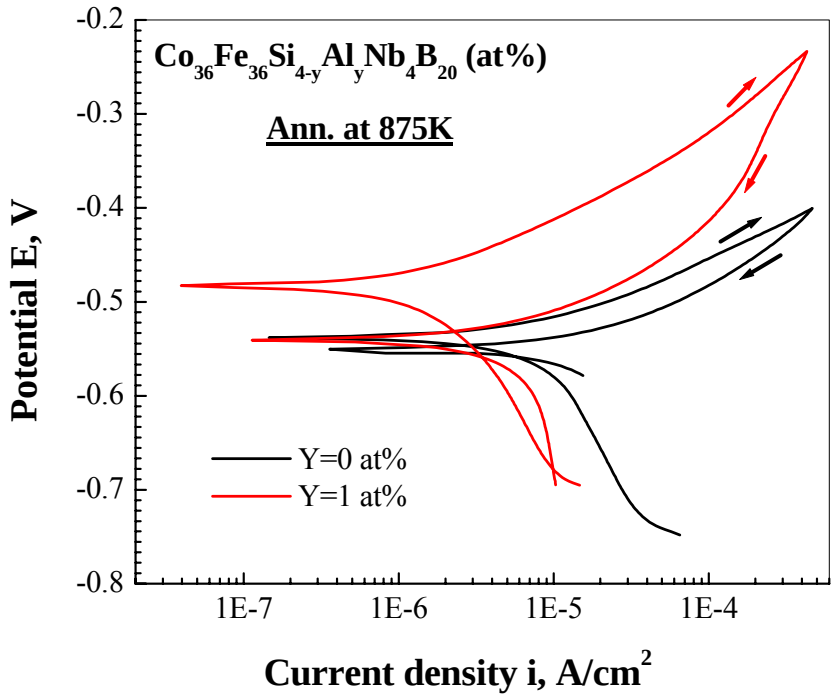

Fig-7.1c: Comparison of cyclic polarizations curves of $Co_{36}Fe_{36}Si_{4-y}Al_yNb_4B_{20}$ (y = 0, 1 at%) alloys heat treated at 875K

Table-7.1: Data extracted from the Tafel plots in fig-7.1)

Annealing temperature (K)	y = 0 at% alloy			y = 1 at% alloy		
	E_{corr} (V)	i_{corr} (A/cm^2)	b_c ($Vdec^{-1}$)	E_{corr} (V)	i_{corr} (A/cm^2)	b_c ($Vdec^{-1}$)
as cast	-0.627	$4.47 X10^{-6}$	0.102	-0.631	$4.54X10^{-6}$	0.1162
825	-0.572	$1.6 X10^{-5}$	0.362	-0.54	$1.8X10^{-6}$	0.041
875	-0.538	$6.73 X10^{-6}$	0.1754	-0.483	$1.23X10^{-6}$	0.1441

As the grain size is of nano scale, there is a possibility of large number of crystal-glass interface boundaries along which fast diffusion of atoms is possible on higher

temperatures. So, at an annealing temperature of 875K, the Si and Al atom in the bcc-(FeCo)SiAl and bcc-(FeCo)Si nanograins segregate to interface boundaries where they can diffuse to the surface of the sample. At the surface, both Si and Al interact with oxygen to form a passive layer of SiO_2 and Al_2O_3 which hinders further oxidation as supported by [12].

The detailed information about the corrosion behaviour of the optimum $Co_{36}Fe_{36}Si_3Al_1Nb_4B_{20}$ alloy in 0.5M NaCl solution is drawn from electrochemical impedance spectroscopy (EIS). The study is carried out on this alloy in amorphous (as cast), amorphous relaxed (annealed at 825K) and nanocrystalline (annealed at 875K) state. The electrochemical impedance measurements (EIS) are carried out in the frequency range between 10^5 Hz and 0.1 Hz. The impedance (Z) is a mathematical complex quantity with a magnitude and a phase shift, which depends on the frequency of the signal, and can be represented in Cartesian as well as polar co-ordinates. In polar co-ordinates the impedance of the data is represented by equation 7.2.

$$Z(\omega) = |Z(\omega)|\, e^{\phi(\omega)} \qquad \ldots\ldots\ldots\ldots \quad (7.2)$$

Where |Z| is magnitude of the impedance and ø is the phase shift. In Cartesian co-ordinates the impedance is given by equation 7.3.

$$Z(\omega) = Z'(\omega) + jZ''(\omega) \ldots\ldots\ldots\ldots\ldots\ldots (7.3)$$

where Z' is the real part of the impedance and Z" is the imaginary part of the impedance, $j = (-1)^{1/2}$. The plot of the real part of impedance against the imaginary part gives the Nyquist plot used in this work and is corroborated by Bode plots ($\log f$ versus $\log|Z|$ and $\log f$ versus phase angle). The arc in Nyquist diagram is a part of the circle with centre at $[R_a/2, R_a/2\mathrm{ctg}(n\pi/2)]$ (respective x, y coordinates of centre) , and the radius of the circle is $[R_a/4\sin(n\pi/2)]$ where R_a is the resistance of the electrode, and n is the power of Z [$Z=(j\omega)^{-n}/Y_0$] [13]. The Nyquist diagrams of the as cast alloy and heat treated ones at 825K and 875K are shown in fig-7.2. All the curves appear to be similar (Nyquist plots), consisting of a single semicircle in the high frequency region signify the charge controlled reaction. Though these curves appear to be similar with respect to their shape, they differ considerably in their size. This indicates

that the same fundamental processes must be occurring on all these variants. The amorphous relaxed and nanocrystalline variants are developed by annealing at a temperature of 825K and 875K respectively close to the temperature of crystallization (856K).

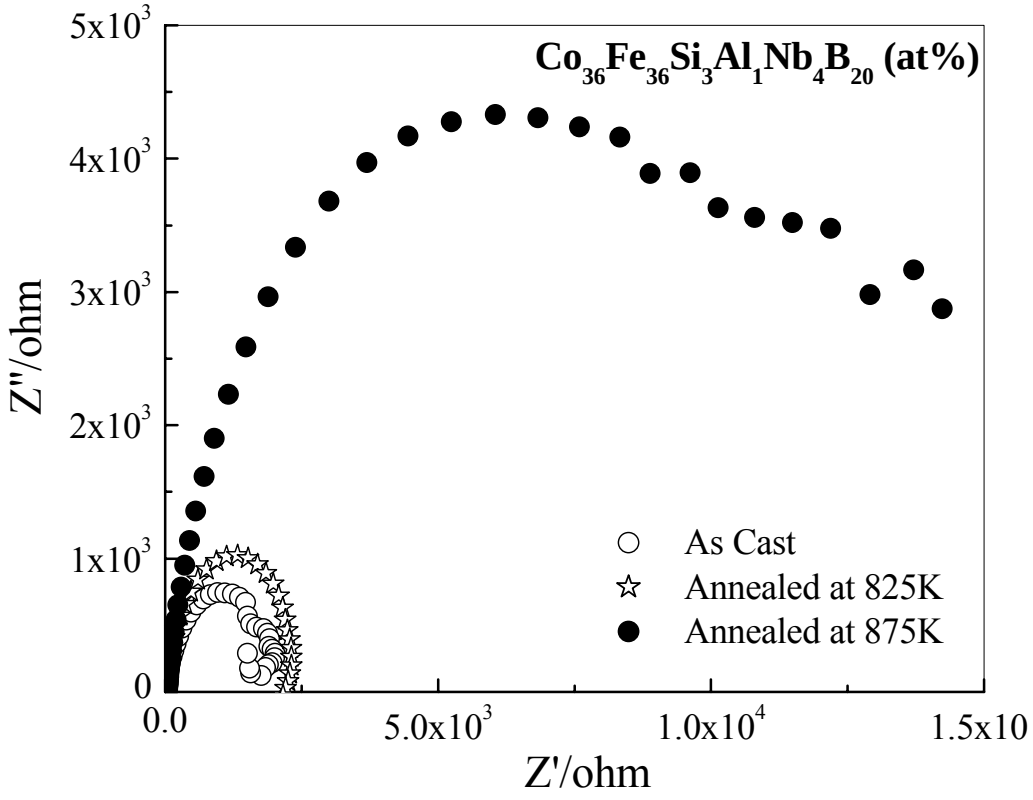

Fig-7.2: Nyquist plot of $Co_{36}Fe_{36}Si_3Al_1Nb_4B_{20}$ alloy of as cast and annealed at 825K and 875K in 0.5M NaCl solution at 25^0C

The Nyquist plot (Fig-7.2) shows that the loci follow semi-circular trend, and the radius of the plot for as cast alloy is very small, that for the alloy annealed at 825K is close but slightly larger, and that for alloy annealed at 875K is very large about four times larger. As these semi-circular loci pass through the origin of plot, the x-coordinate for the centre of plot will be the smallest for as cast alloy and the largest for alloy annealed at 875K. Thus the radius of circle, that can be computed out, will be smallest for the as cast alloy, intermediate but small for the alloy annealed at 825K

and the highest for the alloy annealed at 875K. The radius being representative of charge transfer resistance, it is apparent that the charge transfer resistance increases with the annealing temperature upto 875K, and thus the enhancement in corrosion resistance. Annealing at 825K causes a small change in the charge transfer resistance due to structural relaxation. On further enhancement in the annealing temperature to 875K, at the onset of crystallization, there occurs a significant enhancement in the charge transfer resistance. Both structural relaxation and nanocrystallization improve corrosion resistance. However, nanocrystallization seems to be more effective to corrosion resistance than structural relaxation.

Fig-7.3 (a) and (b) describe the Bode figures ('log *f*' versus log|Z| and 'log *f*' versus phase angle) of $Co_{36}Fe_{36}Si_3Al_1Nb_4B_{20}$ alloy of as cast and the alloy heat treated at 825K and 875K. Bode plot of 'log *f*' versus log|Z| in Fig-7.3 (a) shows a single inflection point. Bode plot of 'log *f*' versus phase angle (Z_{phz}) in Fig-7.3 (b) shows a single phase angle extremum. The negative value of phase angle will give the plot a curve with maxima at the extremum [14]. The maximum phase angle obtained in the annealed materials (Fig-7.3) corresponds to the electron-transfer rate. The greater maximum phase angle corresponds to lower electron-transfer rate, indicating to larger corrosion resistance. In comparison, it can be observed that the maximum phase angle is the lowest for amorphous alloy, and the highest (about-75°) for nanocrystalline alloy and is intermediate for amorphous relaxed alloy. It can be construed that corrosion resistance enhances from amorphous alloy to amorphous relaxed alloy and is the highest for crystalline alloy. The observation from Bode plot and Nyquist diagram corroborate this conclusion. The single inflection point in'log *f*' versus log|Z| and single maxima in 'log *f*' versus phase angle indicates that the corrosion process involves only one time constant for all the variants of the alloy tested. The magnetic behaviour of three variants (as cast, annealed at 825K, annealed at 875K) of optimum alloy composition $Co_{36}Fe_{36}Si_3Al_1Nb_4B_{20}$ under corrosive environment is shown by hysteresis loop in Fig-7.4 (a), (b) and (c) respectively. Each plot gives a comparative hysteresis loop of the alloy before and after the exposure to corrosive environment. The corrosive environment was imposed by exposing respective samples to 0.5 M NaCl solution for 15 days. The magnetic properties of the amorphous and nanocrystalline alloy are strongly affected by the surface quality of the amorphous ribbons.

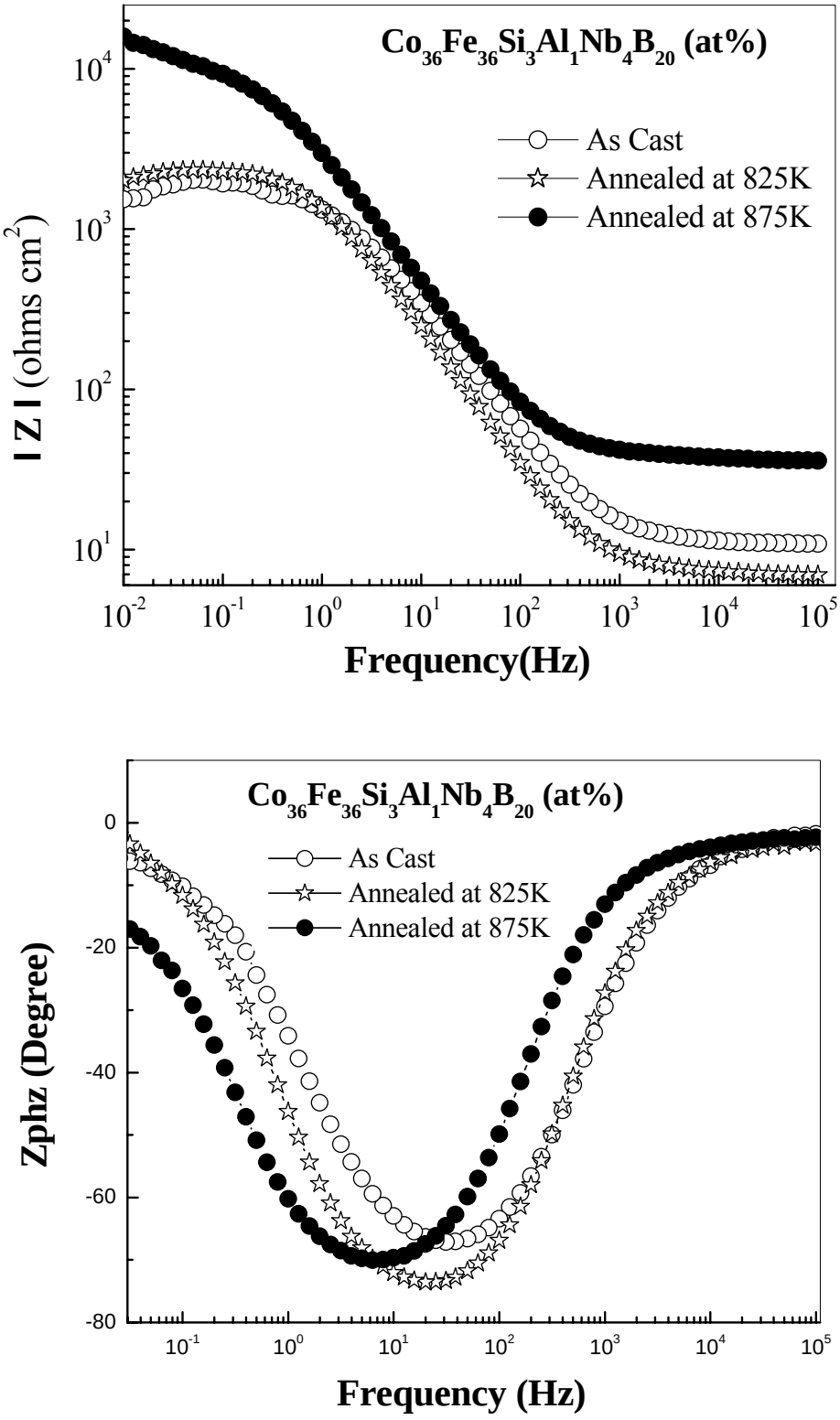

Fig-7.3: (a) Bode figures of |Z| versus log frequency and (b) Bode figures Zphz versus log frequency of $Co_{36}Fe_{36}Si_3Al_1Nb_4B_{20}$ alloy of as cast and heat treated at 825K and 875K

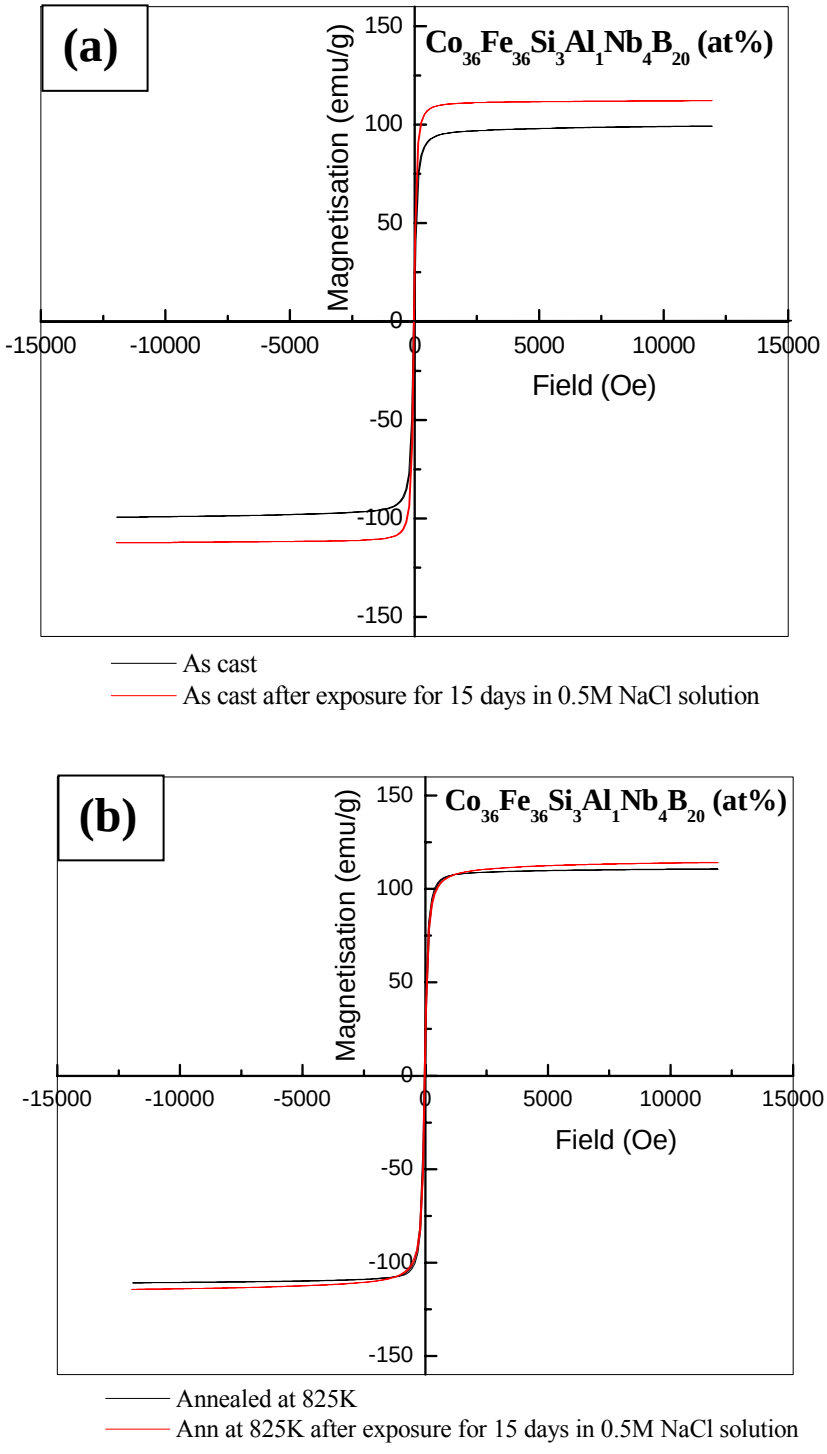

Fig-7.4: Hysteresis loop of (a) as cast alloy and alloy annealed at (b) 825K of $Co_{36}Fe_{36}Si_3Al_1Nb_4B_{20}$ alloy before and after exposure to 0.5M NaCl solution for 15 days

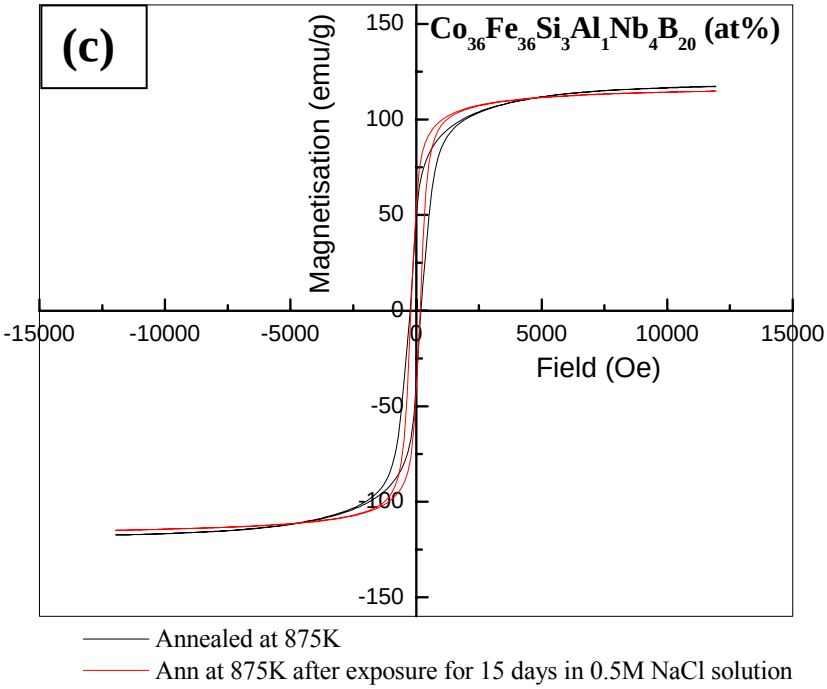

Fig-7.4: (c) Hysteresis loop of $Co_{36}Fe_{36}Si_3Al_1Nb_4B_{20}$ alloy annealed at 875K before and after exposure to 0.5M NaCl solution for 15 days

Corrosion medium is not the cause of straightforward degradation of the magnetic properties of the alloys. In some case the improvement in soft magnetic properties has been observed. The alloy with y= 1 at%, in its amorphous state and annealed at 825K and 875K improves the soft magnetic behavior after exposure to corrosive medium. Similar observation is also reported for FINEMET alloy system [11]. The improvement in soft magnetic property is due to reduction of unwanted stress, which blocks the movement of magnetic domains on the surface of the ribbon.

7.5: Conclusion

The study on influence of annealing temperature on corrosion behavior of $Co_{36}Fe_{36}Si_{4-y}Al_yNb_4B_{20}$ (y= 0, 1 at%) alloys by using cyclic anodic polarization method reveals that Al containing alloy (y = 1 at %) exhibits better corrosion resistance compared to the Al free alloy. Corrosion behaviour of the alloy depends directly on its microstructure evolution. The corrosion resistance increases with annealing temperature due to a structural relaxation in amorphous state, and due to the

crystallization of bcc-(FeCo)SiAl and bcc-(FeCo)Si nano-phases within its amorphous matrix. In optimum nanocrystalline state $Co_{36}Fe_{36}Si_3Al_1Nb_4B_{20}$ alloy not only improve its soft magnetic properties, but also appreciably improves its corrosion resistance.

References

[1] Ojaswini Mohanta, M. Ghosh, A. Mitra and A. K. Panda., J. Phys. D, Appl. Phys. Vol. 42, 065007 (2009).

[2] A.K. Panda, O. Mohanta, A. Kumar, M. Ghosh and A. Mitra., Philosophical Magazine, Vol. 87, No. 11, p 1671 (2007).

[3] Ojaswini Mohanta, A. Basumallick, A. Mitra, A.K. Panda, J. Magn. Magn. Mater.Vol.322, p 112 (2010).

[4] A. Altube, H. Takenouti, L. Beaunier, M. Keddam, S. Joiret, S. Borensztajn, F. Pillier and A. R. Pierna., Corros Sci, V. 45 p 685 (2003).

[5] G. Vara, A.R. Pierna, J.A. García, J.A. Jimenez and M. Delamar, J Non-Cryst Solids, V. 353 p 1008 (2007).

[6] F.F. Marzo, A.R. Pierna, J. Barranco, G. Vara, A. Perez and T. Gómez-Acebo, J Non-Cryst Solids, V. 353 p 875 (2007).

[7] F. F. Marzo, A. Altube and A. R. Pierna., Electrochimica Acta, V. 47 p 2265 (2002).

[8] A. Altube and A. R. Pierna, Electrochimica Acta, V. 49 p 303 (2004).

[9] Rammelt U and Reinhard G, Electrochim Acta, V. 35–6: L199 (1988).

[10] A. Baron, D. Szewieczek and G. Nawrat, Electrochimica Acta Vol. 52, p 5690 (2007).

[11] D. Szewieczek and A. Baron, J. Mater. Process. Tech. Vol. 164-165, p 940 (2005).

[12] H. A. Shivaee, A. N. Golikand, H. R. M. Hosseini and M. Asgari, J. Mater. Sci., DOI 10.1007/s10853-009-3972-z (2009).

[13] D.C. Qiao, B. Green, M. Morrison and P.K. Liaw, Rev. Adv. Mater. Sci., Vol. 18, p 149 (2008).

[14] R. Nowosielski, A. Zajdel, A. Baron, S. Lesz, J. Achievements in Materials and Manufacturing Engineering, Vol. 20, Iss.1-2, p 167 (2007).

Chapter-8

Low temperature magnetization behaviour of $Co_{36}Fe_{36}Si_3Al_1Nb_4B_{20}$ (at%) nanostructured alloy

8.1. Introduction

The low temperature magnetization is particularly important in predicting the interactions within discrete magnetic phases and spin freezing phenomena which may be useful in analyzing the itinerant magnetism in nanostructured materials. In the past few years a number of studies have been reported for the low temperature magnetic excitations of the amorphous metallic ferromagnetic materials especially of the metal-metalloid class [1-3]. According to Bloch, the elementary excitation of a spin system has a wave like form and is called a spin wave. In general, it has been found that at long wavelengths many such glasses exhibit well-defined spin wave excitations with a normal ferromagnetic dispersion relation [4].

$$\hbar\omega(q) = \Delta + Dq^2 + Eq^4 + \cdots\cdots\cdots\cdots \; (Dq^2/\Delta >> 1) \cdot \qquad (8.1)$$

Where, Δ is an effective anisotropy gap due to the dipole-dipole interactions. At low temperature, the magnetization is observed to exhibit the usual ferromagnetic behavior is given by

$$M(T) = M_0 (1 - BT^{3/2} - CT^{5/2} \cdots) \qquad (8.2)$$

Such low temperature magnetization behaviour has been mostly interpreted in term of crystalline or glassy systems. However, in the nanostructured systems obtained from amorphous precursors, the magnetization at low temperature is supposed to be more complex. The complexity is due to the existence of both amorphous phase and the

nanostructured phase whereby the nanoparticles have to maintain ferromagnetic coupling across the amorphous matrix.

In this chapter, the low temperature magnetization study of $Co_{36}Fe_{36}Si_3Al_1Nb_4B_{20}$ alloy in the as-quenched and nanostructured state has been investigated. This study is useful to evaluate spin wave stiffness constants and the parameters of exchange coupling.

8.2: Material studied

The alloy used for the present study was the melt spun $Co_{36}Fe_{36}Si_3Al_1Nb_4B_{20}$ amorphous and annealed samples (annealed temperature at 775K, 825K, 850K, 875K and 900K for 15 mins). The heat treatment was carried out in argon atmosphere using an infrared gold image furnace. The heating rate was 20 K/min. Magnetic measurements were performed in a vibrating sample magnetometer (VSM, Lake Shore: Model 7404) attached with cryostat. The square shaped samples had dimensions of approximately 2mm X 2mm X 30μm was used to minimize demagnetizing field effects. Saturation magnetization was measured at an applied field of 12 kOe. The samples were cooled from room temperature to 77K at zero field and magnetization was measured from 77K to 300K at an applying field of 5 kOe.

8.3: Results and discussion

Differential scanning calorimetry (DSC) plot (fig-8.1) showed broad exothermic peak indicating the transformation from amorphous to nanostructure state. The onset of nanocrystallisation (T_X) is at 856K. Transmission electron microscopy was carried out on a sample annealed at 875K, which was the just above of primary crystallization temperature. The inset of the figure-8.1 shows the TEM micrograph of the annealed ribbon revealing bcc-(FeCo)SiAl nanoparticles dispersed in the amorphous matrix. The formation of these nanophases enhanced the ferromagnetic coupling across the matrix and influenced the magnetization behaviour. This was evident from the thermal variation of magnetization plots (fig-8.2). The alloy annealed at 875K not only raised the magnetization level but also shifted the ferro-para transition (Curie temperature) towards higher temperature. The Curie temperature was raised by 47K in the nanostructured sample (684K to 731K) compared to the as-spun ribbon.

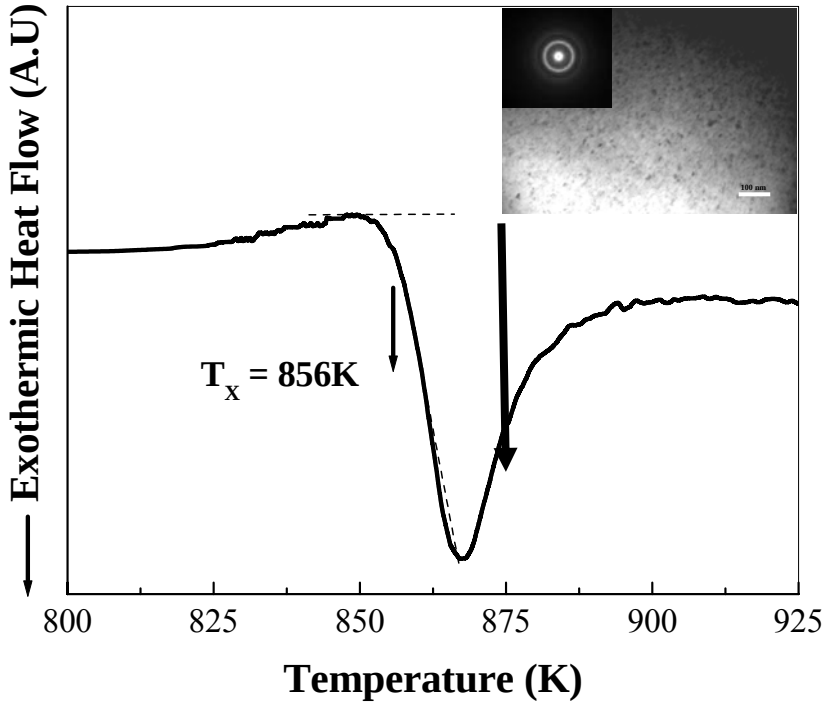

Fig-8.1: DSC plot of as-spun $Co_{36}Fe_{36}Si_3Al_1Nb_4B_{20}$ at% ribbon showing onset of nanocrystallisation. Inset shows TEM micrograph of the ribbon annealed at 875K

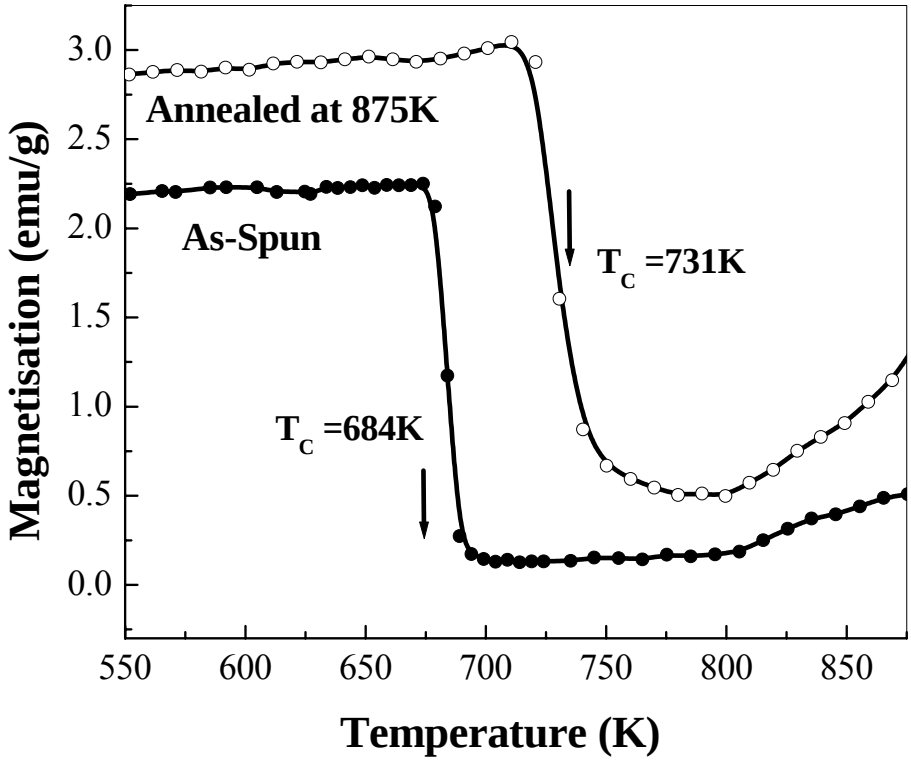

Fig-8.2: Thermal variation of magnetization of as-spun ribbon and ribbon annealed at 875K, applied field 2 Oe

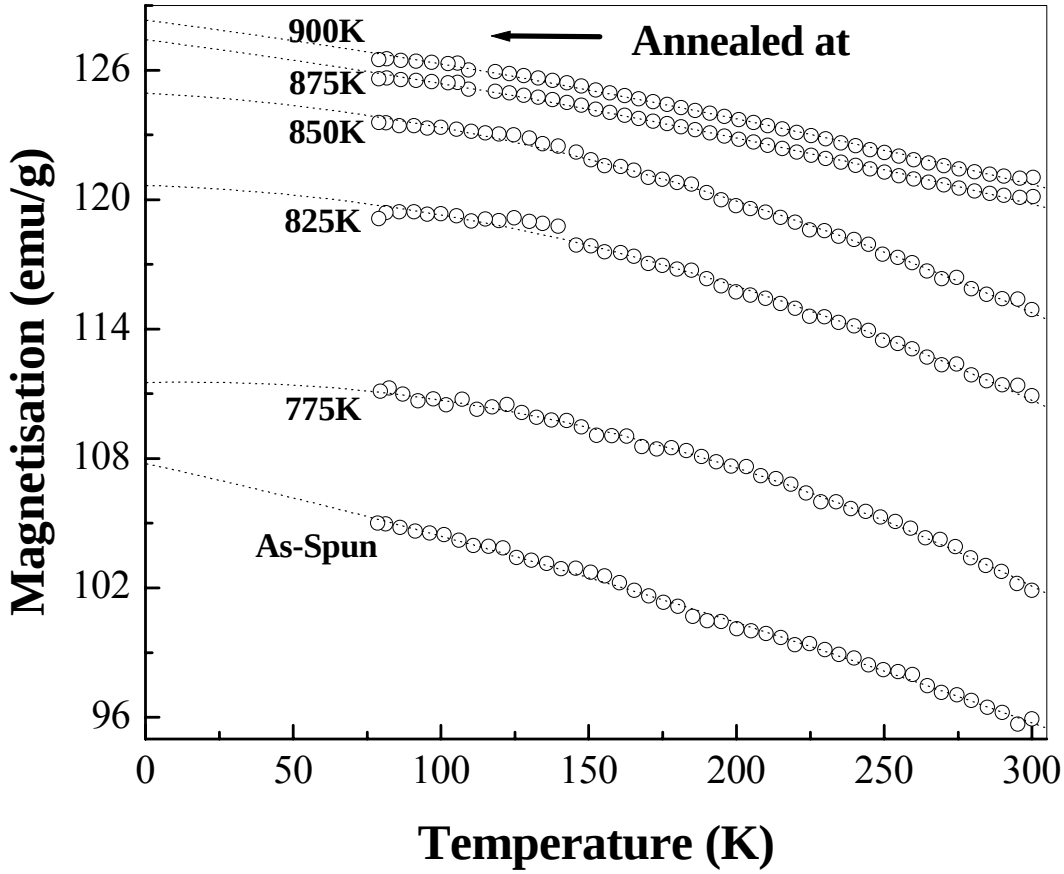

Fig-8.3: Thermal variation of magnetization of as-spun ribbon and annealed ribbons in the temperature range of 77K to 300K. Applied field 5kOe. Curve fits up to 0K indicated

In this plot, the applied magnetizing field was 2 Oe. However, high magnetizing field of 5 kOe was applied to find the variation of saturation magnetization 'Ms' at low temperatures ranging between 77K to 300K (fig-8.3). With the rise in temperature above 77K, the Ms values decreased in the as-spun and annealed samples. It was interesting to find that the rate of decrease was low in the samples annealed at 875K and 900K. When annealed at these temperatures, the nanophase generation as evidenced from micro structural analysis was responsible for the enhanced ferromagnetic coupling via the amorphous matrix. Such enhancement in the coupling between nanophases maintained its stability towards thermal effects. The decreasing profiles of Ms showed that thermal effects strongly influenced the magnetization

behaviour although the temperature range was sub-ambient. The magnetization plots of all the samples consistently followed second order polynomial fit to $Y=A+B_1x+B_2x^2$ with a high regression $\langle r^2 \rangle \sim 0.99$. The regression analysis coefficients are shown in table-8.1.

Table-8.1: Fitting parameters of the thermo magnetic plots in the range of 77K to 300K for estimation of magnetization at 0K

As-spun/ annealed (K)	Polynomial fitting (0K to 300K)				Magnetisation, Ms(emu/g) at temperatures		
	A	B_1	B_2	$\langle r^2 \rangle$	0 K	77K	300K
As-Spun	107.7778	-0.03051	-3.19407E-5	0.99685	108	105	96
773K	111.521	0.00364	-1.1693E-4	0.99734	112	111	102
823K	120.6625	-0.00396	-9.7326E-5	0.9931	121	119	111
848K	124.9448	-0.00707	-8.96391E-5	0.99657	125	124	115
873K	127.4167	-0.01766	-2.58241E-5	0.99634	127	126	120
898K	128.3167	-0.01766	-2.58241E-5	0.99634	128	127	121

The Y-intercept 'A' of regression equation gave the magnetization value at zero Kelvin (0K) as presented in the table-8.1. The M_S(0K), M_S(77K) and M_S(300K) data as function of annealing temperature are shown in fig-8.4. Compared to ambient temperature (300K), a reduction in temperature to 77K led to a drastic rise in magnetization which was found to increase further for zero Kelvin obtained through mathematical fit. It was also observed that the linear rise in magnetization had a saturating tendency at higher annealing temperatures. When the measurement temperatures were low (0K and 77K) the magnetization values had a saturating tendency beyond 850K which was much earlier than measured in ambient (300K) whereby such limiting tendency was observed beyond a higher temperature of 875K.

This also showed that at low temperatures, the magnetic coupling between the incipiently generated nanophases could be sensitively detected. The overall magnetic interactions become much more prominent in view of minimisation of thermally induced excitations. At low temperature the decrease in magnetization with increasing temperature has been observed in both amorphous and crystalline magnetic materials. The thermo magnetization curve at low temperature is found to obey the Bloch law [5] in terms of the spin wave approximation as follows:

$$Ms\ (0)\text{-}Ms\ (T)/\ (Ms\ (0) = 1 - BT^{3/2} - CT^{5/2} \ldots\ldots \quad (8.3)$$

Where M(0) is the saturation magnetization at 0K, and B and C are the Bloch coefficients related to the spin wave stiffness constant 'D' through the expressions.

$$B = \xi\ (3/2)[g\mu_B/M_s(0)]\ (k_B/4\pi D)^{3/2} \qquad \ldots\ldots\ldots\ldots (8.4)$$

$$C = \xi\ (5/2)\ [g\mu_B/M_s(0)]\ (k_B/4\pi D)^{5/2}\ 3\pi\langle r^2\rangle/4 \ldots\ldots (8.5)$$

Where ξ (3/2) and ξ (5/2) are the Riemann zeta function, g is the spectroscopic splitting g-factor, μ_B is the Bohr magneton, k_B is the Boltzmann constant and $\langle r^2\rangle$ is the mean square range of the exchange interactions. The Bloch coefficients, B and C were determined by fitting $[\Delta M_s(T) / M_s(0)]$ magnetization curve vs. $T^{3/2}$ and $T^{5/2}$ respectively. For high enough temperatures, the spin wave excitation has followed the equation-8.3. As the value of the coefficient B is generally larger than C and fluctuations in $T^{5/2}$ is high at elevated temperatures, the later part of eq. 8.3 is neglected for the estimation of the Bloch coefficient B. Fig-8.5 shows the variation of $[\Delta M_s(T) / M_s(0)]$ versus $T^{3/2}$. The linear fits are valid in the range of temperature up to 244K, which is one-third of the Curie temperature of sample annealed at 875K. The Bloch coefficient (B) and M_s were calculated from the experimental curves fitting the

data according to equation-8.3 and shown in table-8.2. From these experimental results, spin wave stiffness constant (D) of the alloys with the different annealing condition were determined. The value of 'D' depends on the saturation magnetization (Bs) at 77K and the value of Bloch coefficient (B). Rearranging the equation (8.4) yields

$$D = (2.612)^{2/3} [g\mu_B/M_s (0)B]^{2/3} [k_B/4\pi)] \ldots\ldots\ldots\ldots\ldots\ldots (8.6)$$

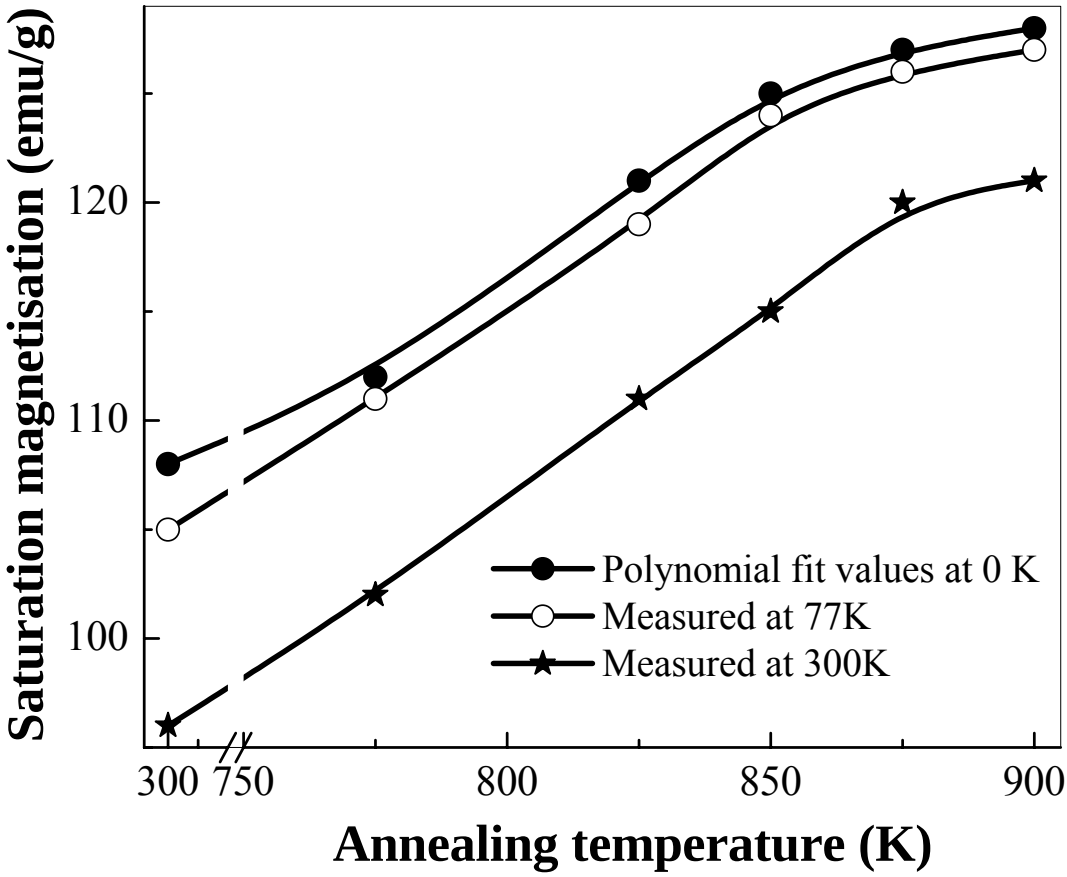

Fig-8.4: Variation of saturation magnetization of as-spun and annealed ribbons measured at 77K to 300K. Values obtained from curve fittings up to 0K also indicated for comparison

The values of spectroscopic splitting 'g' factor are estimated to be 2.1 for the alloys. Using the values of B, Ms and 'g' the spin wave stiffness constant 'D' was calculated. The variation of Bloch coefficient 'B' and Stiffness constant 'D' with respect to annealing temperature has been plotted in fig-8.6. The as-spun ribbon which was amorphous showed high values of 'B' and low values of 'D' as expected in disordered systems [2]. Both these low temperature excitation determinants 'B' and 'D' indicated a decreasing and increasing trend respectively with a rise in annealing temperature. However, the profiles became flattened around 850K indicating a distinct reduction in the change in Bloch coefficient as well as stiffness constant.

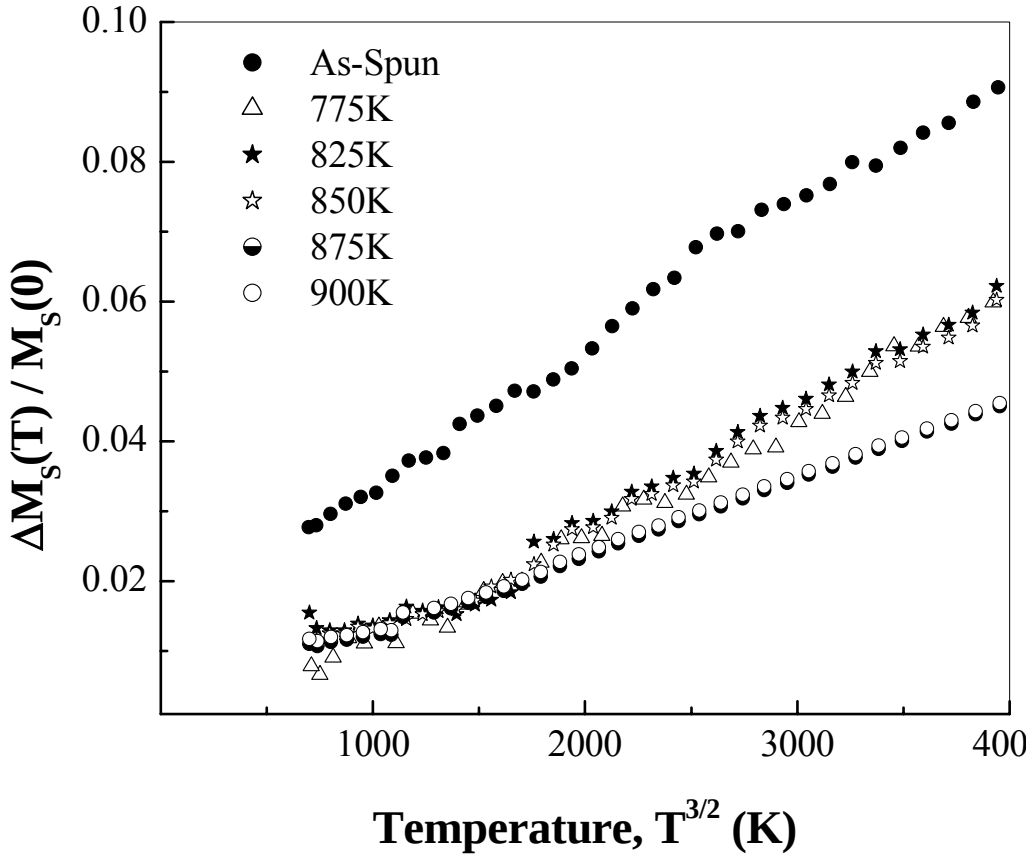

Fig-8.5: Variation of change in magnetization $\Delta M_S(T)/M_S(0)$ with respect to temperature $T^{3/2}$

Table-8.2: Fitting parameters of estimation of Bloch coefficient 'B' and Spin wave stiffness constant 'D' from variation of magnetization with respect to $T^{3/2}$K.

As-spun/ annealed (K)	A	B (Bloch coeff.) (10^{-5})	<r>	D (meVA^{o2})
As-Spun	0.01361	2.00117	0.99691	147
773K	-0.00572	1.6307	0.99489	164
823K	-0.00264	1.59111	0.98896	158
848K	-0.00291	1.55461	0.99459	158
873K	0.00167	1.09653	0.99877	197
898K	0.00244	1.08796	0.99877	197

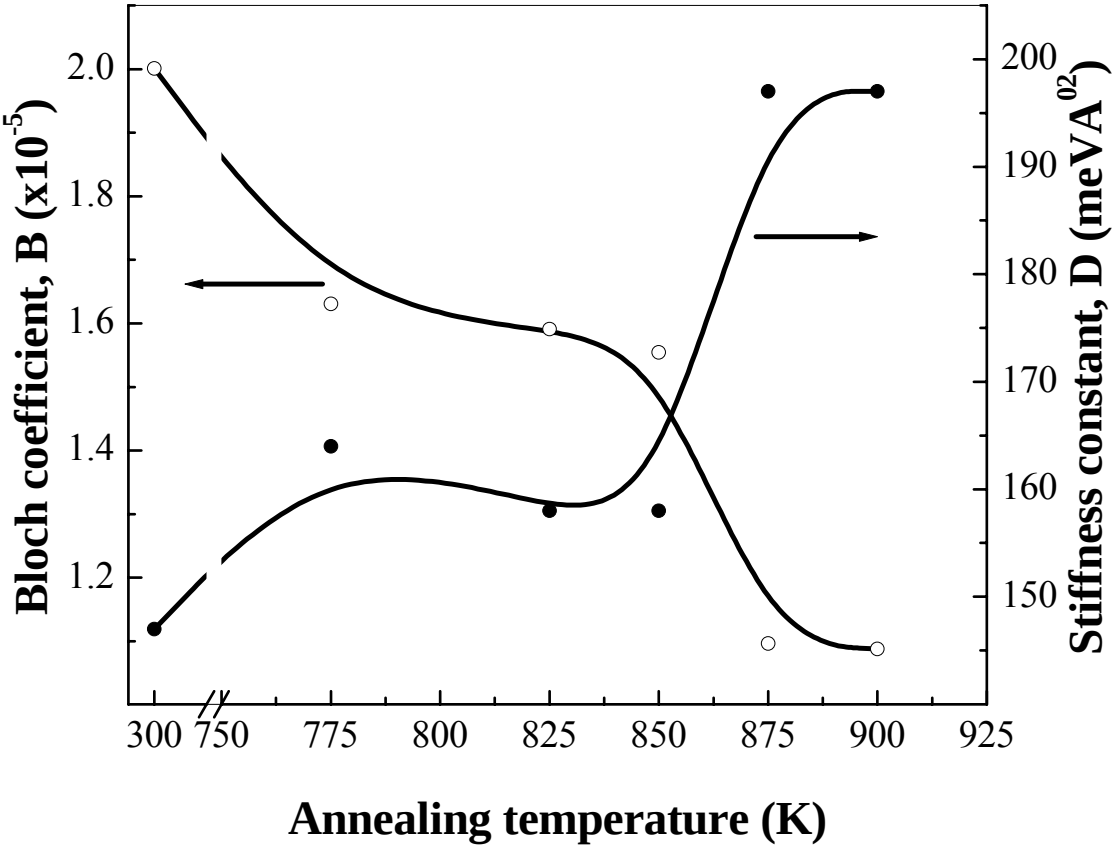

Fig-8.6: Variation of Bloch coefficient (B) and Spin wave stiffness constant (D) with respect to annealing temperature

For analyzing the changes in these coefficients (B and D) and to extract the basis of such phenomena, the variation of coercivity and stiffness constant 'D' was plotted as a function of annealing temperature and shown in fig-8.7. It was observed that stiffness constant indicated a drop around 850K annealed sample at which magnetic softening was also revealed with a reduction in coercivity. This comparative plot clearly indicated that stiffness constant was reduced around the nanocrystallisation onset temperature of 856K as observed from DSC plot. The enhanced ferromagnetic coupling amongst the nanoparticles via amorphous matrix reduced the spin wave stiffness constant 'D'. Subsequently the rise in 'D' and increase in coercivity beyond 850K was due to growth of the nanoparticles. Therefore, the source of excellent soft magnetic properties is due to formation of ultrafine particles and softening (decrease) of the spin wave [5].

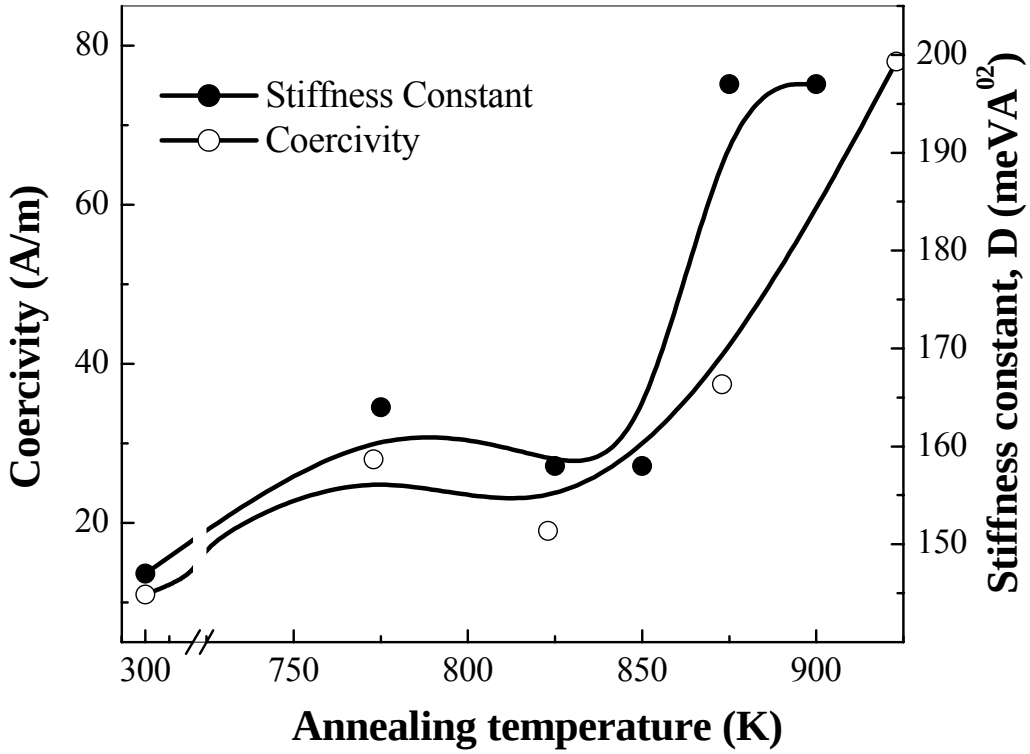

Fig-8.7: Variation of coercivity and Spin wave stiffness constant (D) with annealing temperature

The nanophase generation also affected the $T^{3/2}$ component subsequently restricting the monotonous drop in Bloch coefficient which is observed when amorphous to crystalline transformation takes place with increase in annealing temperature [3]. The spin wave stiffness constant 'D' has been closely correlated to Curie temperature 'T_C' of various metallic and glassy systems to find the range of exchange interaction given by D/T_C (= r). The range of exchange interaction in non-crystalline ferromagnets has been found to be typically smaller than crystalline magnets [2]. Its low value indicates short range nature of interactions.

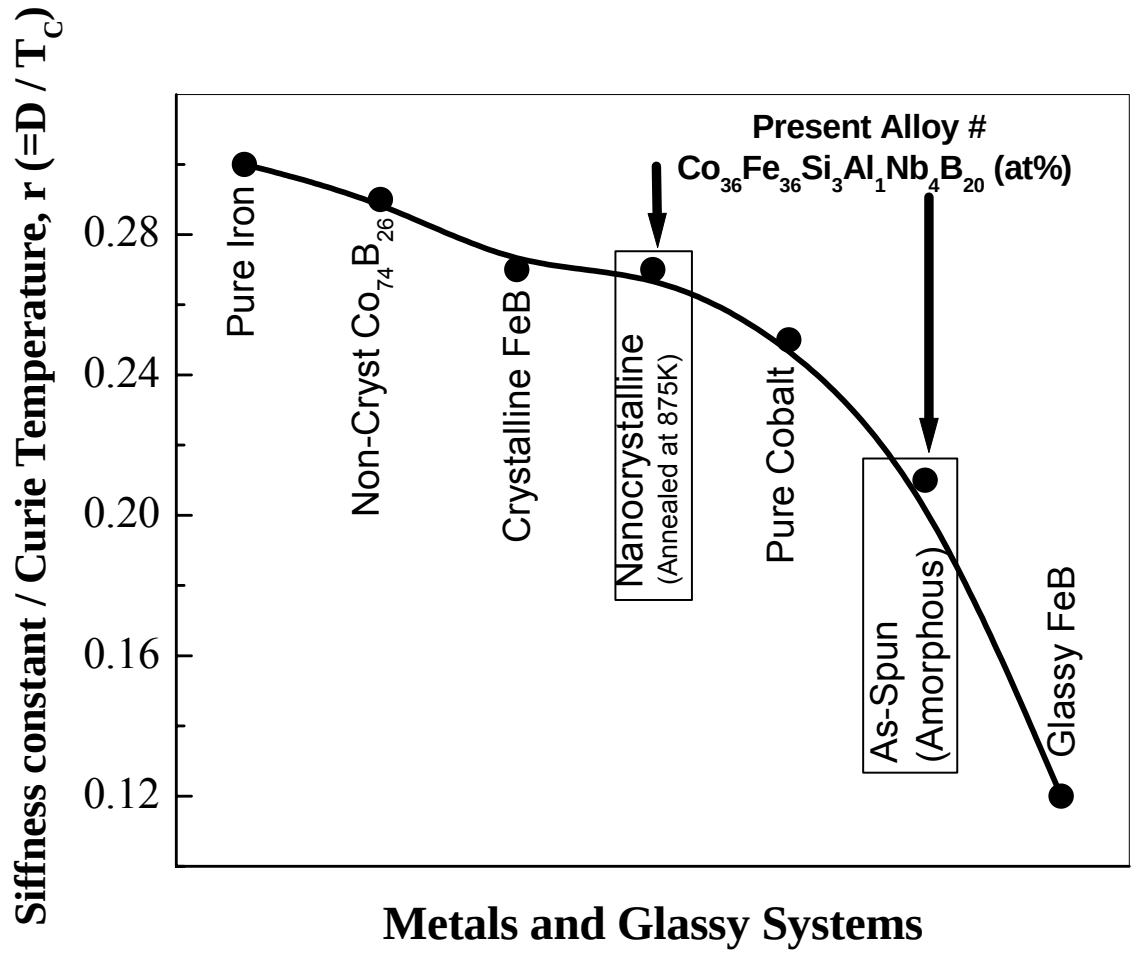

Fig-8.8: A comparative plot showing the stiffness constants of present as-spun and annealed nanostructured ribbons with respect to known metals and their glassy alloys

Calculations showed that the present $Co_{36}Fe_{36}Si_3Al_1Nb_4B_{20}$ alloy had high exchange interaction value of 0.27 for the 875K annealed nanostructured sample compared to 0.21 for the as-spun amorphous state. The relative positions of 'r' in the present as-spun (amorphous) and nanostructured system with respect to ferromagnetic metals and some well known glassy systems are shown in fig-8.8. The value of exchange interaction for the CoFe-based as-spun ribbon lies below that for pure iron (0.30) and pure cobalt (0.25) [6]. However, in the annealed nanostructured state the formation of bcc-(FeCo)SiAl nanoparticles raised the exchange interaction value to 0.27 which was lying between that of iron and cobalt.

8.4. Conclusion

Low temperature magnetization behaviour of $Co_{36}Fe_{36}Si_3Al_1Nb_4B_{20}$ (at%) alloy has been investigated. The nanocrystallisation of amorphous ribbon was evidenced in TEM micrograph of samples annealed at 875K whereby bcc-(FeCo)SiAl nanoparticles were dispersed in amorphous matrix. The Bloch coefficient 'B' and stiffness constant 'D' were influenced by nanostructured formation through annealing treatment. Optimum annealing temperature revealed magnetic softening and also lowering of stiffness constant. The range of exchange interaction given by D/T_C (= r) was higher in its optimum nanocrystalline state (annealed at 875K) compared to its as-spun amorphous state. The enhanced ferromagnetic coupling between nanoparticles across amorphous matrix was responsible for such higher values of 'r' compared to its disordered state.

References

[1] J. D. Axe, G. Shirane, T. Mizoguchi and K. Yamauchi, Phys. Rev. B15 p 2763 (1977).

[2] C. L. Chien and R. Hasegawa, Phys. Rev. B16, p 2115 (1977).

[3] S. N. Kaul, Phys. Rev. B Vol. 24 p 6550 (1981).

[4] H.Hamouda, D.Saifaoui and H.Lassri, Condensed Mater, Vol. 3 p 115 (2000).

[5] S. C. Yu, K. S. Kim, Y-S.Cho and T-K Kim, IEEE Trans. Magn. Vol. 28, p 2421, (1992).

[6] M.W. Stringfellow, J. Phys C1 p 950 (1968).

Chapter-9

Summary, conclusion and future scope of work

9.1: Summary and conclusion

In the present work, we have made an effort to find a high temperature nanocrystalline soft magnetic material with good soft magnetic properties and high Curie temperature. Synthesis protocol and process parameters are being optimized and analytical protocols are being developed during this work. To achieve the optimum alloy composition, we have prepared alloys having composition $Co_xFe_{72-x}Si_4Nb_4B_{20}$ (x = 10, 20, 36, 50 at%) with varied Co-Fe stoichiometry. These materials are being prepared in melt spinning system by rapid solidification process. The process parameters of the melt spinning system at National Metallurgical Laboratory are being optimized at wheel speed of 1400 rpm, crucible nozzle orifice diameter of 1.5 mm, ejection pressure of 0.5 bar and distance between the nozzle orifice and surface of the wheel to 0.5 mm. This parameter setting is maintained in the preparation of all the alloy compositions. The continuous and good quality of amorphous ribbons of about 30 micro meter thickness was obtained in the optimum processing condition.

All the alloys prepared in this study exhibit glass transition temperature. Partial substitution of Co for Fe in $Co_xFe_{72-x}Si_4Nb_4B_{20}$ (x = 10, 20, 36, 50 at%) series has an effect on the onsets of primary and secondary crystallization temperature. The onset of primary crystallization and glass transition temperature is observed to decrease with increasing cobalt content. The generation of bcc-FeCo and $(CoFe)_3B$ phases are observed from X-ray diffractometry (XRD) at the onset of primary and secondary crystallization respectively. The reduction in the size of nanoparticles with increasing cobalt content is being observed from Transmission electron microscopy (TEM). It is found that the alloy with stoichiometry x = 36 at% i.e. Co:Fe :: 50:50 exhibits better soft magnetic properties at elevated temperature compared to other alloys (x = 10, 20, 50 at%). The detailed studies on crystallization kinetics, structural behavior and

magnetic properties are being carried on the optimum alloy composition, $Co_{36}Fe_{36}Si_4Nb_4B_{20}$. The optimum alloy exhibits good soft magnetic properties with coercivity ~ 106 Am^{-1}, susceptibility ~ 0.5 X 10^3, high Curie temperature ~1000K and low power loss in its nano-crystalline state (annealed at 925K). This is due to the lower magneto crystalline anisotropy attributed to the formation of bcc-FeCo nanoparticles. The combination of high Curie temperature and superior soft magnetic properties makes the material a potential candidate for high temperature soft magnetic applications.

Al is also incorporated in the optimum $Co_{36}Fe_{36}Si_4Nb_4B_{20}$ alloy for further improvement of soft magnetic properties. The effect of Al substitution in place of Si in the $Co_{36}Fe_{36}Si_{4-y}Al_yNb_4B_{20}$ (y = 0.5, 1.0, 1.5, 2.0 at%) alloys is being studied systematically. It is observed that the onset of crystallization temperature increased with Al content up to $y \leq 1$ at%, whereas at higher Al content there is a decreasing trend. In its annealing temperature of 875K, the alloy achieves bcc-(CoFe)SiAl nanoparticles with 6-8 nm size in amorphous matrix which is evident from X-ray analysis and transmission electron microscopy. Compared to all, the alloy with optimum Al content for y = 1 at% exhibited low and stable coercivity values at higher annealing temperature. This may be attributed to the reduction of magneto crystalline anisotropy of bcc-(CoFe)SiAl nanoparticles and also to the further reduction in particle size as compared to materials without Al. The nanocrystalline alloy derived from the same optimized stoichiometry of $Co_{36}Fe_{36}Si_{4-y}Al_yNb_4B_{20}$ (y = 1 at%) annealed at 925K, exhibits Curie temperature of 1100K in comparison to that of 1000K in the alloy without Al (y = 0 at%). It indicates higher ferromagnetic ordering at 925K in the former (y = 1 at %) than the latter (y = 0 at %). The former alloy with 1 at% of Al maintains stable ferromagnetic ordering up to 1100K, which is 100K higher than that without Al. This optimal Al containing alloy also exhibits better frequency response of AC coercivity and low core loss compared to the Al free alloy (y =0 at%).

As this type of nanocrystalline alloy, may have to work in a wet industrial and marine atmosphere containing sulphide and chloride ions. The electrochemical and corrosion behavior of $Co_{36}Fe_{36}Si_{4-y}Al_yNb_4B_{20}$ (y = 0, 1 at%) alloys are being studied in 0.5M NaCl solution. It is found that Al bearing alloy with optimum (y = 1 at%) exhibits better corrosion resistance compared to the Al free alloy. Detailed studies on the

corrosion behaviour is being carried out for nanocrystalline variants derived from optimum stoichiometry $Co_{36}Fe_{36}Si_3Al_1Nb_4B_{20}$ alloy with varying annealing temperature (300K, 850K, 875K). The study shows that the corrosion resistance enhances with annealing temperature. It is due to the highest charge transfer resistance in the nanocrystalline alloy compared to amorphous alloy because of stress relaxation and on the formation of bcc-(FeCo)SiAl nanoparticles. It is observed that nanocrystalline $Co_{36}Fe_{36}Si_3Al_1Nb_4B_{20}$ alloy has improved soft magnetic and corrosion resistance properties compared to the material with Al.

To develop a better understanding on the magnetic exchange interaction, we have studied the low temperature magnetization of $Co_{36}Fe_{36}Si_3Al_1Nb_4B_{20}$ alloy. At low temperature, the thermo-magnetization curve of the $Co_{36}Fe_{36}Si_3Al_1Nb_4B_{20}$ nanocrystalline alloy is found to obey the Bloch law in compliance to spin wave theory. The spin wave stiffness constant and the mean square range of the exchange interaction of this alloy are found to decrease by magnetic softening on annealing at 850K. The excellent soft magnetic properties of $Co_{36}Fe_{36}Si_3Al_1Nb_4B_{20}$ alloy with the formation of nano-phases may be softening the spin waves. In addition, the smaller grain size may also have an effect on magnetic softening.

9.2: Future scope of work

A nanocystalline $Co_{36}Fe_{36}Si_3Al_1Nb_4B_{20}$ alloy is successfully developed in the present work for high temperature soft magnetic applications. As the Curie temperature of this soft magnetic alloy is high, it has the potential for use at high temperature and high frequency application. Future work will be directed to develop high frequency transformer using the developed materials. Attempts will be made to use the developed material as a core for magnetic sensing device which can be utilized at high temperature and at hostile environment.

The amorphous ribbon has poor load bearing capacity and it becomes very brittle on annealing. Therefore, this material cannot be given any desired shape during fabrication. This may restrict the use of this excellent material for different applications. As the prepared alloys exhibit glass transition temperature and wide super cooled region of ΔT_x ($T_{X1} - T_g$) in the range of 50K, the material has the

potential to form bulk metallic glass using Cu-mould casting technique. Attempts will be made to develop bulk metallic glass having composition $Co_{36}Fe_{36}Si_3Al_1Nb_4B_{20}$ with high tensile strength, superior soft magnetic properties and high Curie temperature.

PUBLICATIONS

List of journal papers

1. A.K. Panda, **O. Mohanta**, A. Kumar, M. Ghosh and A. Mitra, "A Potential $Co_{36}Fe_{36}Si_4B_{20}Nb_4$ Nanocrystalline Alloy for High Temperature Soft Magnetic Applications" Philosophical Magazine, V-87, No. 11, pp. 1671-1682, (**2007).**
2. A.K. Panda, **O. Mohanta**, A. Mitra, D. C. Jiles, C.C.H. Lo, Y. Melikhov "Soft magnetic Properties of a high temperature CoFeSiBNb nanocrystalline alloy" Journal of Magnetism and Magnetic Materials V-316, No. 2, pp. 886-889, (**2007).**
3. **Ojaswini Mohanta**, M. Ghosh, A. Mitra and A. K. Panda "Enhanced ferromagnetic ordering through nanocrystallisation in cobalt incorporated FeSiBNb alloys" Journal of physics D, Applied physics V-42, 065007 (8 pp), (**2009)**
4. A.K. Panda, **O. Mohanta**, M. Ghosh and A. Mitra, "Development of nanostructured CoFe based alloys for High Temperature Magnetic Applications" Journal of Nanoscience and Nanotechnology Vol-9, pp. 1-4, (**2009)**
5. **Ojaswini Mohanta**, A. Basu Mallick, A. Mitra, A.K. Panda, "Enhancement in Soft magnetic and Ferromagnetic Ordering Behaviour through Nanocrystallisation in Al Substituted CoFeSiBNb Alloys" Journal of Magnetism and Magnetic Materials V-322, pp. 112-118, (**2010).**

List of Conference papers

International Conferences

1. **O. Mohanta**, A. Mitra and A.K. Panda "Crystallisation and Soft magnetic properties of CoFe- based nanocrystalline alloy for high temperature applications" Presented on International Conference on Advances in Materials and Materials Processing (**ICAMMP-2006)**, 3-5 February **2006**, IIT, Kharagpur, Page No. 479-485.

2. A.K. Panda, **O. Mohanta**, A. Mitra, D.C. Jiles, C. Lo and Y. Melikhov, "Soft Magnetic Properties of a High temperature CoFeSiBNb Nanocrystalline alloy" Presented at III Joint European Magnetic Symposia, San Sebastian, 26-30 June, **2006**.
3. **O. Mohanta**, A.K. Panda and A. Mitra, "Crystallisation behaviour and soft magnetic properties of Co_{10} Fe_{62} Si_4 B_{20} Nb_4 nanocrystalline alloy for high temperature applications" Presented on International Symposium on steel for Automotives, 44^{th} National Metallurgists day and 60^{th} Annual Technical Meeting, IIM and TATA steel Limited, Jamshedpur, 13-16 Nov **2006.**
4. A. Mitra, **O. Mohanta**, A.Kumar and A.K. Panda, "Structural and soft magnetic properties of high temperature CoFe based nanocrystalline alloys" Presented on International conference on Recent trends in Nanoscience and technology**, ICRTNT-06**, Jadavpur University, Kolkata, 7-9 December, **2006**.
5. A.K. Panda, **O. Mohanta**, M. Ghosh and A. Mitra, " Effect of Al substitution for Si in CoFeSiBNb nanocrystalline alloys for high temperature soft magnetic application" Proc. of International conference on soft magnetic materials (SMM 18), Cardiff University, UK, Sep 2-5, **2007.**
6. **O. Mohanta**, A.K Panda, A. Mitra, "Influence of Co substitutions on magnetic properties and thermal behaviour of $Fe_{72-x}Co_xSi_4B_{20}Nb_4$ amorphous alloys for high temperature applications" Presented on 10^{th} International Conference on Advanced Materials (IUMRS-ICAM 2007), Bangalore, India, 8-13 Oct **2007**.
7. A.K. Panda, **O. Mohanta**, M. Ghosh and A. Mitra, "Development of nanostructured CoFe based alloys for High Temperature Magnetic Applications" Proc. of International Conference on Nanoscience and Technology (ICONSAT), Chennai, Feb 27-29, **2008**.
8. Amitava Mitra, **O. Mohanta**, P. Sarkar and Ashis Panda, "Nanostructured Materials for High temperature soft magnetic and GMI-based Sensor Applications" Presented on International conference on Magnetic materials and their applications for 21^{st} century (MMA-21), NPL, New Delhi and MSI, 21-23 Oct **2008**.
9. Partha Sarkar, **O. Mohanta**, S.K. Pal, A.K. Panda, A. Mitra, "Effect of Al addition on the Giant magneto-impedance behavior of CoFeNbSiB rapidly

solidified alloys" Presented on International conference on Magnetic materials and their applications for 21st century (MMA-21), NPL, New Delhi and MSI, 21-23 Oct 2008.

National Conferences/seminars

1. A.K. Panda, **O. Mohanta**, A. Mitra, "Development of a CoFeSiBNb based nanocrystalline alloy for high temperature Soft magnetic applications" Presented in National Conference on Materials for Electrical, Electronic & Magnetic Applications: Characterization & Measurements (**MEEMA- 2005**), 2-3 September, DMRL, Hyderabad.
2. Partha Sarkar, **O. Mohanta**, S.K. Pal, A.K. Panda, A. Mitra, " Giant magneto impedance effects in the Co-Fe based rapidly solidified alloys" Presented on National symposium for materials (MR08), IIT Bombay, May 17-18, **2008 (Best Poster Awarded)**

IOP PUBLISHING JOURNAL OF PHYSICS D: APPLIED PHYSICS

J. Phys. D: Appl. Phys. **42** (2009) 065007 (8pp) doi:10.1088/0022-3727/42/6/065007

Enhanced ferromagnetic ordering through nanocrystallization in cobalt incorporated FeSiBNb alloys

Ojaswini Mohanta, M Ghosh, A Mitra and A K Panda[1]

National Metallurgical Laboratory, Jamshedpur 831 007, India

E-mail: akpanda@nmlindia.org and akpanda2_in@rediffmail.com

Received 3 October 2008, in final form 3 February 2009
Published 3 March 2009
Online at stacks.iop.org/JPhysD/42/065007

Abstract

This investigation addresses the effect of nanocrystallization on ferromagnetic ordering in a series of $(Fe_{72-X}Co_x)Si_4B_{20}Nb_4$, ($X = 10$, 20, 36, 50 at%) alloy ribbons prepared by the melt-spinning technique. Partial substitution of Fe by Co throughout this series affected the primary and secondary crystallization onsets observed from differential scanning calorimetry and the consequent generation of bcc-FeCo and $(CoFe)_3B$, respectively, as observed from x-ray diffractometry. The reduction in the size of nanoparticles with increasing cobalt content was observed from transmission electron microscopy. At an elevated temperature, the alloy with $X = 36$ at% was found to reveal superior soft magnetic properties compared with other alloys. In the nanostructured state, this alloy also showed enhanced ferromagnetic ordering and low power losses exhibited its scope as a material for high temperature soft magnetic application.

1. Introduction

Stability of ferromagnetic ordering has been a subject of immense concern in designing soft magnetic components for high temperature applications. These components typically include switches, cores and magnetic bearings in transformers and rotor assemblies in space power systems and jet engines [1]. The essential requirement of such magnetic applications is a high Curie temperature (T_c). The efficiency of these components is subject to minimization of power loss at high thermal environments and frequencies. The ferromagnetic operable range, i.e. T_c, is conventionally enhanced by incorporation of cobalt in Fe-based crystalline systems [2]. However, their inherent strong anisotropy constants are major hurdles in achieving superior soft magnetic properties. High magnetic losses are also a direct consequence of it. Additionally the high degree of crystalline ordering lowers their electrical resistivity due to enhanced electron transport. The retarded resistivity due to ordering reduces the eddy current ultimately leading to high core losses.

The magnetic and electrical properties have been drastically improved with the advent of Fe-based nanostructured alloys [3]. The benefits arising out of such nano-regime composite materials with cobalt incorporation for extension of ferromagnetic ordering has become a subject of intense research in recent years. However, the major challenges these investigations face are arriving at the optimal alloy concentrations and acceptable soft magnetic properties in essential combination with high T_c.

This investigation is an attempt to optimize the Co–Fe stoichiometry in the CoFeSiBNb nanostructured alloy system by correlating the effects of cobalt incorporation on nanostructured development with magnetic properties for high temperature applications.

2. Experimental

Elements of 99.99% purity were melted several times for effective homogenization and subsequently cast into ingots of master alloys with a nominal composition of $Fe_{72-X}Co_xSi_4B_{20}Nb_4$ ($X = 10$, 20, 36, 50 at%). From these ingots, ribbons were obtained by the melt spinning technique. Crystallization behaviour of these rapidly quenched ribbons was evaluated using a differential scanning calorimeter (Perkin–Elmer DSC-7). Different phases generated during crystallization were investigated by the x-ray diffraction method (Philips: D-500) with Cu Kα radiation at a scan

[1] Author to whom any correspondence should be addressed.

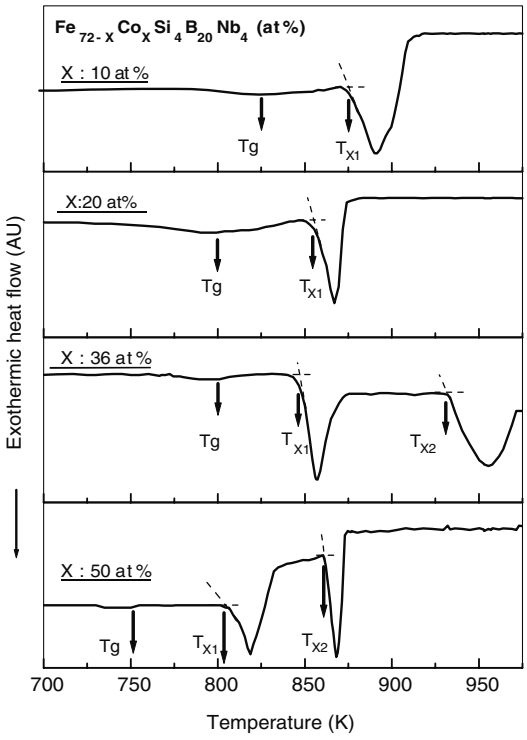

Figure 1. DSC thermograms of melt spun $Fe_{72-X}Co_xSi_4B_{20}Nb_4$ ($X = 10, 20, 36, 50$ at%) alloys at a heating rate of 20 K min^{-1}.

rate of 2° min^{-1}. Microstructural evolutions were observed using a transmission electron microscope (Philips, CM-200). Magnetic coercivity was measured from the hysteresis loop obtained by a computer controlled hysteresis loop tracer at a dc magnetizing frequency of 50 mHz. The saturation magnetization and Curie temperature measurements were carried out using a vibrating sample magnetometer (LakeShore VSM Model: 7404). The ac coercivity and core loss were measured using an ac hysteresis loop tracer (Walker, Model: 401 AMH).

3. Results

3.1. Crystallization behaviour

Differential scanning calorimetry (DSC) plots of all the alloys (figure 1) revealed distinct changes in the heat flow profiles indicating exothermic transformation with an onset of crystallization at T_{X1}. This transformation was preceded by a low intensity endothermic onset exhibiting a glass transition at T_g suggesting the contribution of cobalt towards glass formation in Fe-based alloys [4]. The DSC profiles in the operable range of 975 K also exhibited high temperature secondary crystallization at T_{X2} observed only in alloys with higher cobalt content. The crystallization onset T_{X2} increased with a reduction in the cobalt content and was thus not observed

Table 1. Characteristic temperatures obtained from DSC measurements.

Cobalt content (at%)	Glass transition (T_g)	Primary cryst. (T_{X1})	ΔT_X ($T_{X1} - T_g$)	Secondary cryst. (T_{X2})
10	825	875	50	[a]
20	800	855	55	[a]
36	800	845	45	930
50	750	802	52	860

[a] Expected to be beyond current scope of measurement up to 975 K.

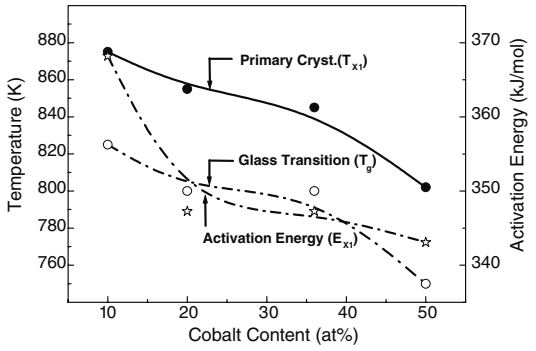

Figure 2. Variation in the onset of primary crystallization (T_{X1}), glass transition (T_g) and activation energy (E_{X1}) with the cobalt content in alloys.

in the current operable range of the instrument for $X < 36$ at% alloys. The characteristic temperatures obtained from the DSC plots are shown in table 1. The trend of variation in T_{X1} and T_g with cobalt is shown in figure 2.

Both these temperatures indicated an almost similar drop by 75 K as the cobalt content was increased from 10 to 50 at%. All the alloys displayed a wide super cooled region of ΔT_x ($T_{X1} - T_g$) in the range 45–55 K. The activation energy (E_{X1}) for the primary crystallization (T_{X1}) was obtained from the peak shift temperatures with different scan rates using the method of the Kissinger equation [5]:

$$\ln(\phi/T_p^2) = -E/(RT_p) + \text{constant}, \quad (1)$$

where ϕ is the heating rate, R is the ideal gas constant, T_p is the temperature of the maximum of the peak and the activation energy E allows for the energy barrier opposing the phase transformation to be quantitatively described. The activation energy is also shown in figure 2. Though the variation in E_{X1} was small it was observed to decrease with increasing Co-content in the alloys.

3.2. Evolution of phases

The alloys with a high cobalt content indicated much earlier onsets of primary crystallization T_{X1}. This was evidenced from an early evolution of phases in the alloy with $X = 50$ at% indicating its lowest DSC onset T_{X1} at 802 K. The x-ray analysis of samples annealed at 775 K (figure 3) showed

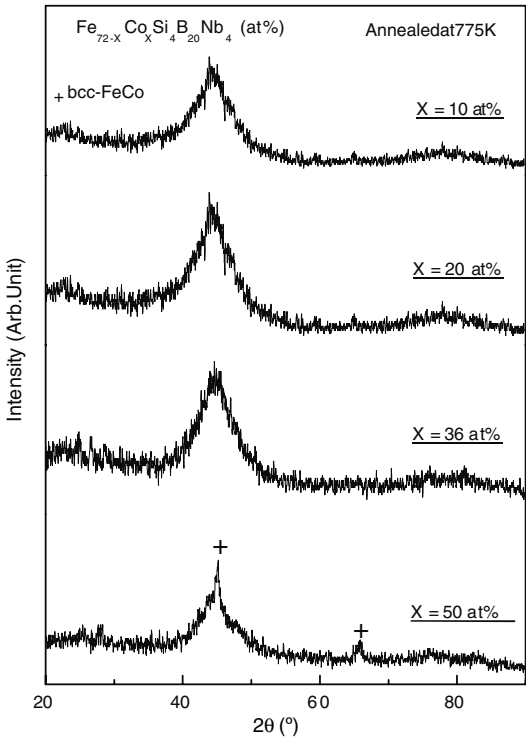

Figure 3. XRD plots of $Fe_{72-X}Co_xSi_4B_{20}Nb_4$ ($X = 10$, 20, 36, 50 at%) ribbons annealed at 775 K.

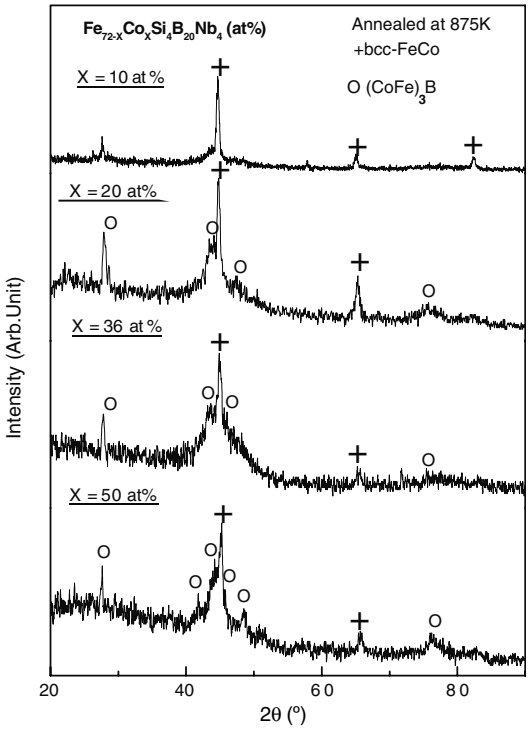

Figure 4. XRD plots of $Fe_{72-X}Co_xSi_4B_{20}Nb_4$ ($X = 10$, 20, 36, 50 at%) ribbons annealed at 875 K.

the incipient generation of the bcc-FeCo phase in this alloy with a possible combination with Si, while the other alloys with a low Co content still indicated a stable amorphous structure with a broad halo. The x-ray diffractogram for this alloy indicated phase evolution around 25 K lower than the DSC onset temperature which may be attributed to the higher sensitivity of the former technique. To investigate phase evolution before and after the primary crystallization (T_{X1}) of all the alloys, x-ray diffractometry (XRD) plots were obtained for samples annealed at 875 K and shown in figure 4. At this temperature, which corresponds to exactly T_{X1} for the $X = 10$ at% alloy, the formation of only bcc-FeCo was observed. However, for the alloys with $X \geqslant 20$ at% a low volume fraction of $(CoFe)_3B$ was incipiently generated whose increasing content was also revealed with a reduction in the secondary crystallization onset T_{X2}.

3.3. Soft magnetic properties and Curie temperature

Phase transformation was also observed from the variation in coercivity with temperature as shown in figure 5. It was observed that all the alloys exhibited fairly consistent coercivity till 850 K. Beyond this temperature, the degradation in coercivity was evident in all the alloys. However, such a deterioration in the soft magnetic properties was minimal in alloys with an optimum content of cobalt of $X = 36$ at% whereas the cobalt content either above or below this concentration in the present alloy exhibited deleterious effects. Such a non-linear effect of cobalt substitution for Fe was also observed from the temperature variation of magnetization of as-spun alloys as shown in figure 6. In these plots the sharp drop in magnetization indicated the Curie temperature, T_c, of these alloys whereby its amorphous matrix transformed from the ferromagnetic to the paramagnetic state. T_c was found to increase and then drop as shown in figure 7. This is in accordance with the change in the Co–Fe interaction as per the Bethe–Slater curve [6] and is supposed to be strongly influenced by the compositional effect in the amorphous state as this transition temperature is far below the crystallization onsets. However, at elevated temperatures the magnetization exhibited an increasing trend (figure 6) beyond 800 K which was due to the generation of bcc-FeCo phases in the amorphous matrix. In the case of $X = 10$ the increase in magnetization was observed at a much lower temperature than the crystallization (T_{X1}) which may be attributed to the formation of nanostructured α-Fe at a lower temperature in Fe-rich alloys. It was also observed that at a high Fe content, the initial drop reaches a near zero magnetization value. However, as the cobalt content increases up to $X = 36$ at%, the magnetization does not drop to a near zero value which may be attributed to the formation of CoFe-based fine crystallites in its as-cast material being responsible

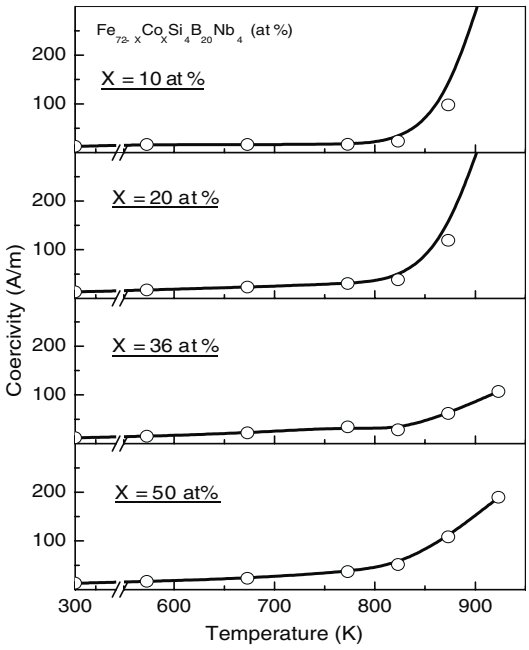

Figure 5. Variation of coercivity with the annealing temperature in $Fe_{72-X}Co_xSi_4B_{20}Nb_4$ ($X = 10, 20, 36, 50$ at%) ribbons.

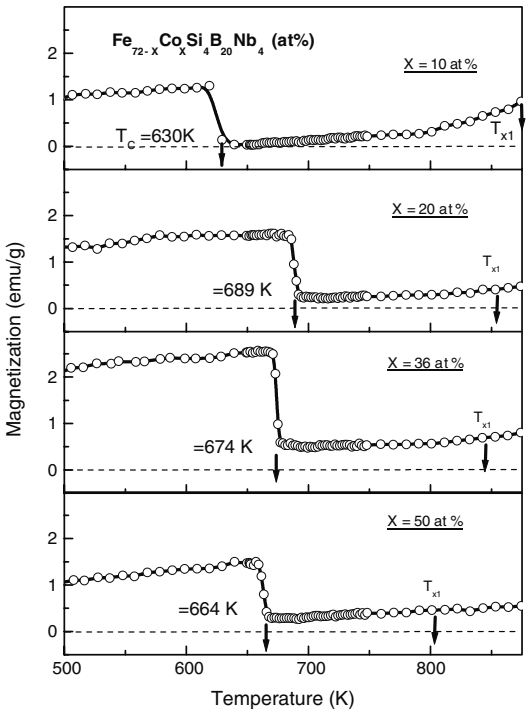

Figure 6. Thermo-magnetization curves of as-cast $Fe_{72-X}Co_xSi_4B_{20}Nb_4$ ($X = 10, 20, 36, 50$ at%) alloys. T_{X1} (↓) indicated in the figure.

for raising the magnetization level. When $X > 36$ at%, the magnetization drop once again approaches a near zero value. Heat treatment for nanophase generation also affects the Curie temperature (T_c) of the system as observed in figure 7. In addition to the generation of the bcc-FeCo phase, the Co–Fe stoichiometry also affects the T_c as shown in figure 7. It was observed that as the Co : Fe ratio changed from 14Co–86Fe to 69Co–31Fe, the T_c varied in a non-linear fashion both in the amorphous state and the nanocrystalline state with an expected highest theoretical value at 50Co–50Fe (indicated in figure 7) [7]. Amongst the alloys studied enhanced magnetic moments comparable to this equi-partitioned composition was achievable with the stoichiometry close to Co : Fe :: 50 : 50 in the present alloy with $X = 36$ at% for the sample annealed at 875 K.

4. Discussion

The incorporation of cobalt in the Fe-based system as observed in the previous section has been found to offer a complex effect of stoichiometric variation on the magnetic and structural development for high temperature applications. From the range of the cobalt content, the alloy with $X = 36$ at% revealed stable soft magnetic properties with an extended low coercivity with temperature (figure 5) in combination with enhanced ferromagnetic ordering (figure 7). Structural developments play a strong role in causing the deviation in these properties for a critical content of cobalt in the present alloys. During heat treatment of the amorphous alloys with silicon as the metalloid,

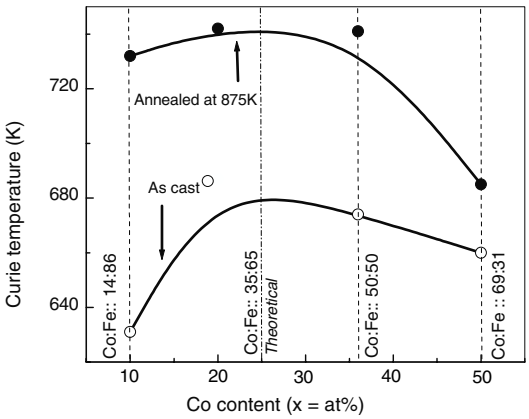

Figure 7. Variation of the Curie temperature with the cobalt content of as-spun as well as annealed samples at 875 K for 15 min.

as and how the crystallization temperature T_{X1} approaches, there are elemental combinations which ultimately catalyse the formation of silicide phases. This was distinctly evidenced from the shift (figure 8) in the primary x-ray diffraction peak of the samples annealed at 875 K. The small span of the diffraction angle about the primary reflection shows the

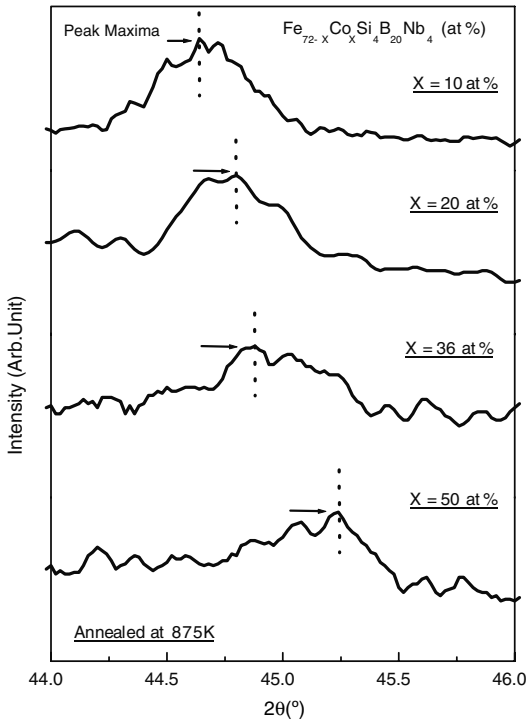

Figure 8. Shift in the primary peak of the XRD plots of the $Fe_{72-X}Co_xSi_4B_{20}Nb_4$ ($X = 10, 20, 36, 50$ at%) ribbons annealed at 875 K. Plots are shown for the small span of 2° about the primary peak.

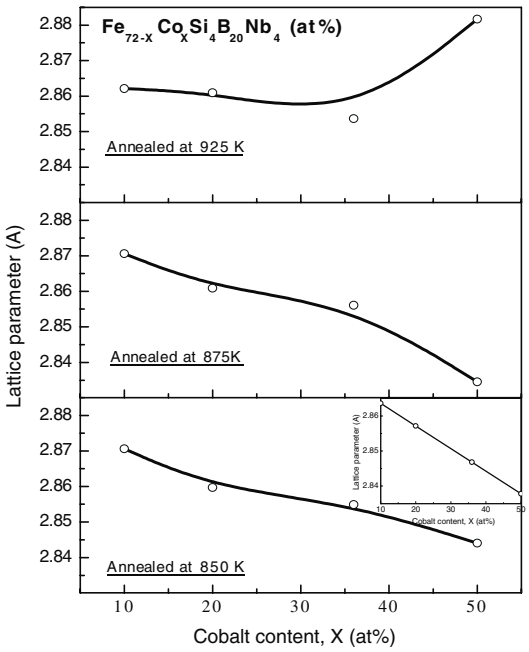

Figure 9. Variation of the lattice parameters with the cobalt content in the $Fe_{72-X}Co_xSi_4B_{20}Nb_4$ ($X = 10, 20, 36, 50$ at%) ribbons annealed at 850, 875 and 925 K. The lattice parameter from equation (2) is shown in the inset.

peak shift towards higher angles, indicating a decrease in the lattice parameter. The lattice parameters were computed from the primary reflection peak (1 1 0) and the corresponding Braggs d spacing. Variation of the lattice parameters with the cobalt content at different temperatures is shown in figure 9. Quantitatively, the lattice parameter a_α for the formation of the α-CoFe solid solution is given by the equation as follows [8, 9].

$$a_\alpha(\mathrm{A}) = [0.282\,36 + 6.4514 \times 10^{-5}(\mathrm{at\%Fe})] \times 10. \quad (2)$$

Using equation (2), the lattice parameter was calculated for the present alloys and its variation is shown in the inset of figure 9. The plot shows a linear reduction in the lattice parameter with cobalt incorporation in Fe. However, in the present multi-component system, the lattice shrinkage is attributed not only due to the element Co going into the solution with Fe [10] but also because of the metalloid Si combining with these ferromagnetic metals [11, 12]. The decrease in the lattice parameter also led to a reduction in the particle size as observed from the transmission electron micrographs of the samples annealed at 875 K (figure 10) with the selected area diffraction (SAD) patterns shown in the inset. However, a deviation in the trend of the lattice parameters was found in the case of alloys with a high cobalt content annealed at higher temperatures. It was observed that at an elevated temperature of 925 K, which was a temperature far above T_{X1}, the lattice parameter decreased in alloys with $X \leqslant 36$ at%, while above this composition there was a rising trend. This increasing trend in alloys with $X > 36$ at% is attributed to the formation of different high temperature phase evolutions such as CoFe-borides which drastically offsets the lattice shrinkage with cobalt addition in Fe.

In amorphous magnetic alloy systems, the partitioning into fine crystalline phase particles led to variation in the soft magnetic properties and has been modelled by Herzer [13]. The model is fitted in the present CoFe-based system for a temperature of 875 K, below which the lattice parameter shift has been found to consistently decrease irrespective of the alloying additions. The mathematical expression for this random anisotropy model is

$$H_C = P_C \frac{K_1^4 D^6}{A^3 J_s}, \quad (3)$$

where H_C is the coercivity of the alloys annealed at 875 K and P_C is a pre-factor which according to fine particle theory becomes 0.64 [10]. K_1 is the magnetocrystalline anisotropy of the nanoparticles, which is 8 KJ m^{-3} [14]. $A = 10^{-11}$ J m^{-1} [15] is the exchange stiffness constant of the system. J_s and D are the saturation magnetization and the particle size, respectively, the variations of which with the cobalt content annealed at 875 K are shown in figure 11(a). D was determined from an assembly of particles bearing a deviation of ±1 nm

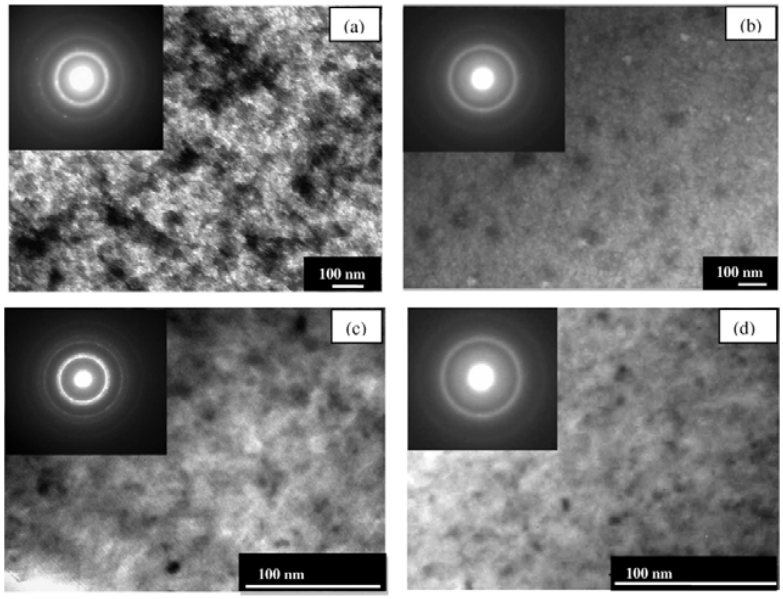

Figure 10. Bright field images of (*a*) $X = 10$ (*b*) $X = 20$ (*c*) $X = 36$ and (*d*) $X = 50$ heat treated at 875 K for 15 min. SAED patterns shown in the inset.

in all the samples. The particle size D was found to drop drastically above $X = 20$ at% compared with the gradual decrease in the saturation magnetization J_s above $X = 36$ at%. These experimental data have been incorporated in Herzer's random anisotropy model (equation (3)) and the coercivity determined is shown in figure 11(*b*). The coercivity values determined from the anisotropy model and the magnetic hysteresis experiment follow a similar trend till $X = 36$ at% with the 50Co–50Fe stoichiometry indicating superior soft magnetic properties than the theoretical high magnetization stoichiometry of the 35Co–65Fe alloy. At higher cobalt contents the experimental value indicated a marked deviation from those predicted by the model. The high magnetic hardness observed may be attributed to a very fine cluster of highly anisotropic cobalt left in the matrix that could not go into the nanophase [16] as well as due to the incipiently formed boride phases. This was also reflected from the deviation in the lattice parameter (figure 9) in the alloy with $X > 36$ though at a higher temperature of 925 K whereby the shrinkage due to Co in Fe did not follow a decreasing trend due to the clustering of cobalt in the matrix. It is also suggested that due to the presence of these cobalt clusters in the matrix, the net magnetization J_s did not drop as drastically as the nanoparticle size as shown in figure 11(*a*).

The partitioning behaviour of cobalt into the nanophase with a critical increase in the phase volume fraction was found to affect the magnetic moment of the system, an essential criterion for ferromagnetic ordering. This was evidenced from the thermal variation of magnetization in the annealed samples as shown in figure 12. The initial drop in magnetization was elevated to a higher temperature when annealed at 875 K, which was around the primary onset for bcc-FeCo nanophase formation. This drop shifted to a lower temperature for the 900 K annealed sample, which may be attributed to the depletion of cobalt and iron from the ferromagnetic matrix. The subsequent enhancement of the magnetization level at a higher nanocrystallization temperature of 800 K and above is attributed to the increase in the volume fraction of the nanophase generated. A typical heat treatment at 925 K raised the level of magnetization considerably with a ferromagnetic stability till 1000 K (figure 12, inset). Beyond this temperature the ferromagnetic disordering started due to the formation of CoFe-borides in the high volume fraction which also affected the trend of lattice contraction due to cobalt partitioning into the bcc-FeCo nanophase.

In high frequency transformer and rotor assemblies with a soft magnet core flux lines in alternating current would contribute towards power losses leading to a major concern for high temperature soft magnetic applications [17]. The coercivity and core loss variation with frequency for the as-cast and the sample annealed at 875 K is shown in figures 13(*a*) and (*b*) respectively. The measurements have been carried out in a magnetizing field of 400 A m^{-1} starting from a frequency of 3 kHz. To observe the effect of nanocrystallization, all the data have been normalized with respect to the data for the 875 K annealed sample obtained at a starting frequency of 3 kHz. This optimally heat treated sample indicated a lower coercivity and core loss compared with the as-cast material. Linear fittings of the data indicated that the nanocrystallized sample has a tendency to approach as-cast material behaviour with increasing frequency. However, the soft magnetic component (coercivity) was stable towards higher frequency compared with the eddy current component (core loss).

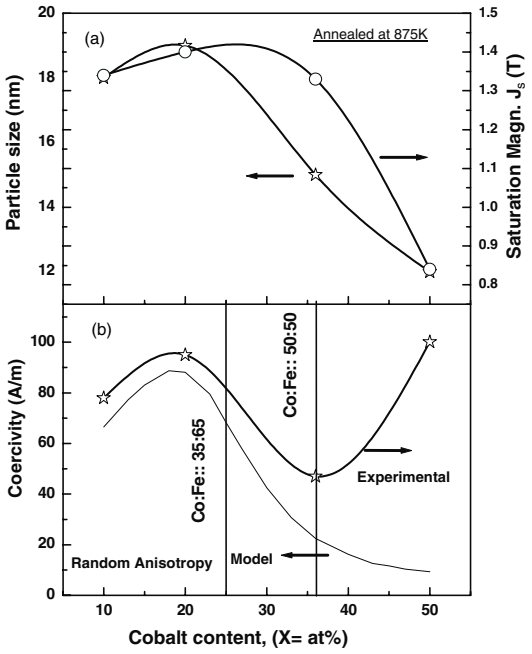

Figure 11. (*a*) Variation of the particle size and the saturation magnetization with the cobalt content for the alloys annealed at 875 K. (*b*) Coercivity variation with the cobalt content as per the experimental data and Herzer's model for the alloys annealed at 875 K.

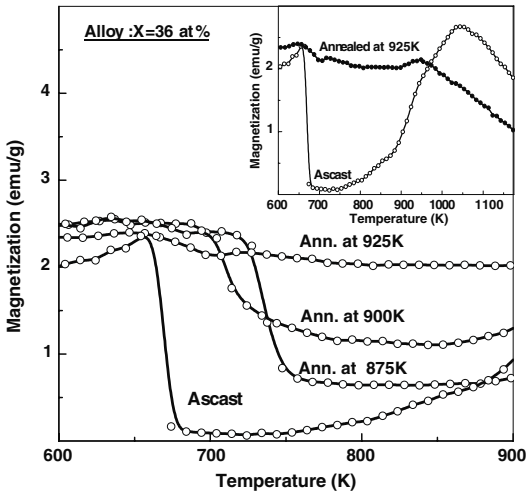

Figure 12. Effect of the annealing temperature on the thermal variation of magnetization in the $Fe_{72-X}Co_xSi_4B_{20}Nb_4$ ($X = 36$ at%) alloy. Inset shows the profile for as-cast and 925 K annealed samples till the onset of ferromagnetic disordering.

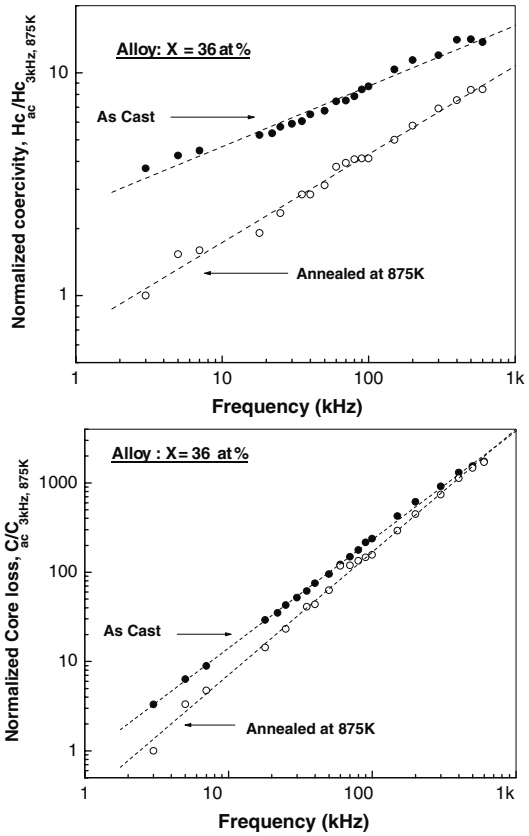

Figure 13. Variation of (*a*) the ac coercivity and (*b*) the core loss normalized with respect to the 875 K annealed data measured at 3 kHz and at a magnetizing field of 400 A m^{-1}.

5. Conclusion

The $(Fe_{72-X}Co_x)Si_4B_{20}Nb_4$ ($X = 10$, 20, 36, 50 at%) alloys were prepared in the form of amorphous ribbons by the melt spinning technique. The alloys exhibited a reduction in the primary crystallization onset (T_{X1}), the secondary crystallization onset (T_{X2}), the glass transition (T_g), the activation energy (E_{X1}) and the particle size (D) with an increase in the cobalt content. The bcc-FeCo nanophase and $(CoFe)_3B$ formation marked the thermodynamic onsets as T_{X1} and T_{X2}, respectively. High temperature and high cobalt content were found to catalyse boride formation leading to deviation in the lattice shrinkage expected for increasing the dissolution of Co and Si in the element Fe. The alloy with $X = 36$ at% with a stoichiometry of 50Co–50Fe revealed superior soft magnetic properties at elevated temperatures. This alloy when optimally annealed in the range 875–925 K generated a bcc-FeCo nanophase enhancing the ferromagnetic ordering temperature to 1000 K for suitability to applications at an elevated temperature. The alloy in its nanostructured state also exhibited low power losses.

Acknowledgments

The authors express their sincere gratitude to the Director, National Metallurgical Laboratory, Jamshedpur, India, for kindly giving permission to publish the work. One of the authors (Ojaswini Mohanta) acknowledges the financial support from CSIR, India.

Reference

[1] Fingers R T and Rubertus C S 2000 *IEEE. Trans. Magn.* **36** 3373
[2] Pfeifer F and Radeloff C 1980 *J. Magn. Magn. Mater.* **19** 190
[3] Yoshizawa Y, Oguma S and Yamauchi K 1988 *J. Appl. Phys.* **64** 6044
[4] Inoue A and Shen B 2003 *J. Mater. Res.* **18** 2799
[5] Mittemeijer E J, Chang L, Van Der Schaaf P J, Brakman C M and Korevaar B M 1988 *Metall. Trans.* A **19** 925
[6] Gallagher K A, Willard M A, Zabenkin V N, Laughlin D E and Mchenry M E 1999 *J. Appl. Phys.* **85** 5130
[7] Johnson F, Um C Y, McHenry M E and Garmestani H 2006 *J. Magn. Magn. Mater.* **297** 93
[8] Ohnuma I *et al* 2002 *Acta Mater.* **50** 379
[9] Sourmail T 2005 *Scr. Mater.* **52** 1347
[10] Bozorth R M 1959 *Ferromagnetism* (New York: Van Nostrand)
[11] Muller M, Mattern N and Illgen L 1991 *Z. Metallk.* **82** 895
[12] Panda A K, Ravikumar B, Basu S and Mitra A 2003 *J. Magn. Magn. Mater.* **260** 70–7
[13] Herzer G 1990 *IEEE Trans. Magn.* **26** 1397
[14] Gengnagel H and Wagner H 1961 *Z. Angew. Phys.* **8** 174
[15] Huller K 1986 *J. Magn. Magn. Mater.* **61** 347
[16] Mao X, Xu F, Tang J, Gao W, Li S and Du Y 2005 *J. Magn. Magn. Mater.* **288** 106
[17] Varga L K, Kovács Gy, Kákay A, Mazaleyrat F, Gercsi Zs, Ferenc J, Fazakas E, Kulik T and Conde C 2004 *J. Magn. Magn. Mater.* **272** 1506

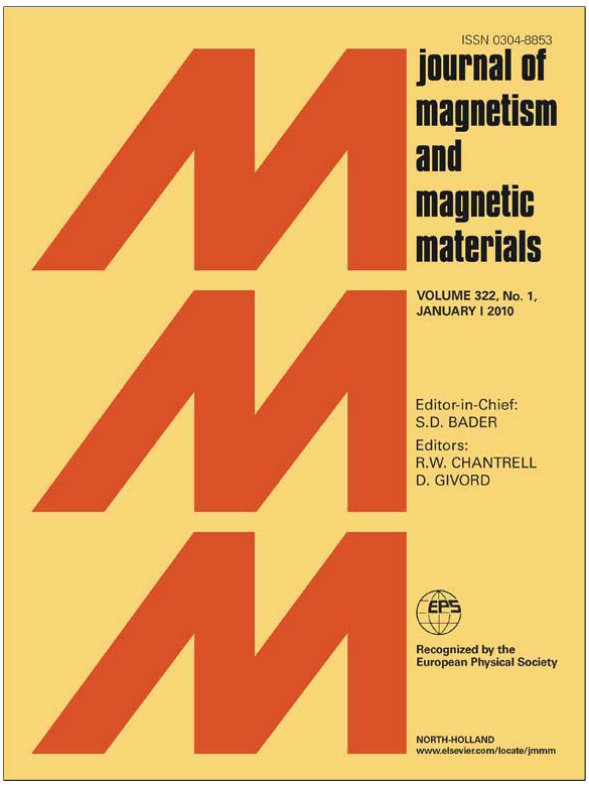

Journal of Magnetism and Magnetic Materials 322 (2010) 112–118

Contents lists available at ScienceDirect

Journal of Magnetism and Magnetic Materials

journal homepage: www.elsevier.com/locate/jmmm

Enhancement in soft magnetic and ferromagnetic ordering behaviour through nanocrystallisation in Al substituted CoFeSiBNb alloys

Ojaswini Mohanta [a], A. Basumallick [b], A. Mitra [a], A.K. Panda [a,*]

[a] Council for Scientific and Industrial Research, National Metallurgical Laboratory, Jamshedpur 831 007, India
[b] Bengal Engineering and Science University, Shibpur, West Bengal, India.

ARTICLE INFO

Article history:
Received 30 April 2009
Available online 6 September 2009

PACS:
75.50.Kj
75.50.Tt
75.50.Bb
75.30.Cr

Keywords:
Melt-spun ribbons
Nanocrystalline
Magnetic anisotropy
Curie temperature

ABSTRACT

The effect of substituting Al for Si in $Co_{36}Fe_{36}Si_{4-x}Al_xB_{20}Nb_4$, ($X$=0, 0.5, 1.0, 1.5, 2.0 at%) alloys prepared in the form of melt-spun ribbons have been investigated. All the alloys were amorphous in their as-cast state. The onset of crystallization as observed using differential scanning calorimetry (DSC) was found to rise at low Al content up to X=1 at% beyond which there was a decreasing trend. The alloys also exhibited glass transition at 'T_g'. Microstructural studies of optimally annealed samples indicated finer dispersions of nanoparticles in amorphous matrix which were identified as bcc-(FeCo)Si and bcc-(FeCo)SiAl nanophases by X-ray diffraction technique. Alloy with optimum content of Al around X=1 at% exhibited stability in coercivity at elevated temperatures. Though Al addition is known to lower magnetostriction, such consistency in coercivity may also be attributed towards lowering in the nanoparticle size compared to X=0 alloy. In the nanostructured state, the alloy containing optimum Al content (X=1) exhibited further enhancement in ferromagnetic ordering or the Curie temperature by 100 K compared to alloy without Al. Such addition also attributed to better frequency response of coercivity and low core losses.

1. Introduction

Nanocrystallisation of Fe-based amorphous precursors has been found to reveal superior soft magnetic properties [1]. The operational temperatures of these alloys were extended with cobalt incorporation in these nanostructured systems [2,3]. The alloying issues addressed to Co addition have been a subject of concern due to simultaneous increase in anisotropy which is deleterious towards soft magnetic properties. In view of this, several attempts are undergoing to modify the nanostructure phase so as to counteract such detrimental effects. Various alloy designs are under investigations to reduce the particle size for effective averaging of magnetocrystalline anisotropy on one hand and reduction in magnetostriction on the other.

The Fe-based nanocrystalline alloys contained a large refractory element Nb which retarded growth of the nanoparticles thus bringing about effective averaging of the anisotropy [4]. In such systems, the amorphous precursor is primarily positively magnetostrictive. Heat treatment induces the generation and dispersion of negatively magnetostrictive Fe–Si nanophase in amorphous matrix. The optimal nanostructured state leads to a very small positive magnetostriction close to zero whereby enhancement in soft magnetic properties is observed. Some recent investigations suggested further improvement in properties with incorporation of aluminium. This idea originated out of the fact that in Sendust class of alloys (FeSiAl), the addition of the element Al significantly improved the soft magnetic properties. This behaviour has been attributed to lowering of magnetocrystalline anisotropy due to addition of Al to the Fe–Si binary system [5]. This enhancement in soft magnetic properties is particularly desirable in view of increasing demand for CoFe-based nanocrystalline materials for high temperature applications like assemblies of jet engine rotors, high frequency transformers [6]. The magnetic losses at high operational temperatures are critically dependent on stability of coercivity at elevated thermal environments. Similarly, stable properties at high frequencies demand low eddy current losses which are consequences of high resistivity. Thus, these attributes are further important for alloying modifications in the CoFe-based nanostructured systems by addition or substitution of Al for elements like Si.

The present investigation addresses the effect of Al substitution for Si in CoFeSiNbB-based alloy system. The structure and soft magnetic behaviour at high temperature for these as-cast as well as annealed alloys were evaluated.

2. Experimental

Pure elements (99.99%) were arc melted in argon atmosphere for several times to ensure effective homogenisation and subse-

* Corresponding author. Tel.: +91 657 2345002; fax: +91 657 2270527.
E-mail addresses: akpanda@nmlindia.org, akpanda2_in@rediffmail.com (A.K. Panda).

0304-8853/$ - see front matter © 2009 Elsevier B.V. All rights reserved.
doi:10.1016/j.jmmm.2009.08.048

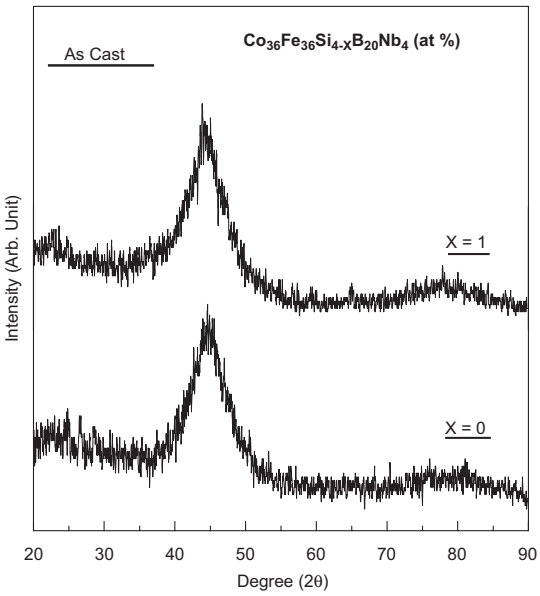

Fig. 1. XRD plots of as-cast $Co_{36}Fe_{36}Si_{4-x}Al_xB_{20}Nb_4$ (X=0, 1) at% alloys.

quently cast into ingots of master alloys with nominal composition of $Co_{36}Fe_{36}Si_{4-x}Al_xB_{20}Nb_4$, ($X$=0, 0.5, 1.0, 1.5, 2.0 at%). The alloy ingots were induction melted and spun into ribbons. The crystallization behaviour of these rapidly quenched ribbons was evaluated using a differential scanning calorimeter (Perkin-Elmer Diamond DSC). Identification of phases was carried out using X-ray diffraction technique (Philips: D-500) with Cu Kα radiation.

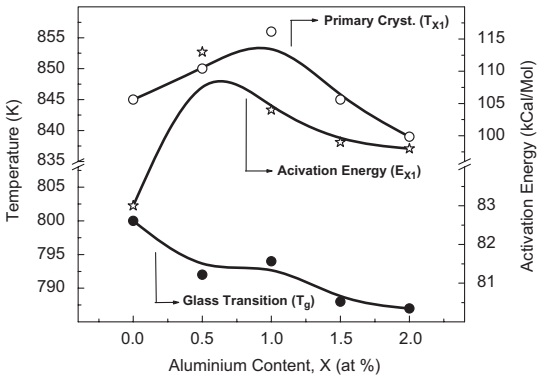

Fig. 3. Variation of crystallization onset (T_{X1}) and glass transition temperatures (T_g) and activation energy (E_{X1}) of $Co_{36}Fe_{36}Si_{4-x}Al_xB_{20}Nb_4$, X=0, 0.5, 1.0, 1.5, 2.0 at% alloys.

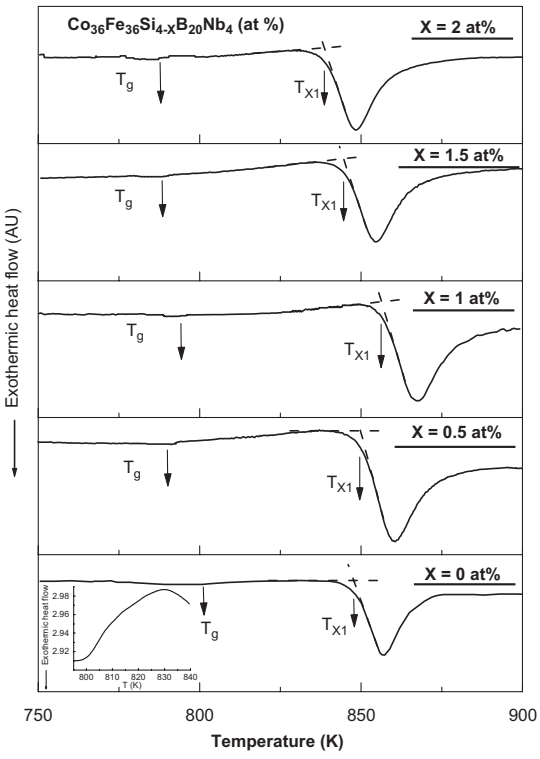

Fig. 2. Differential scanning calorimetry (DSC) plots of as-spun $Co_{36}Fe_{36}Si_{4-x}Al_xB_{20}Nb_4$, X=0, 0.5, 1.0, 1.5, 2.0 at% alloys at a heating rate of 20 K/min.

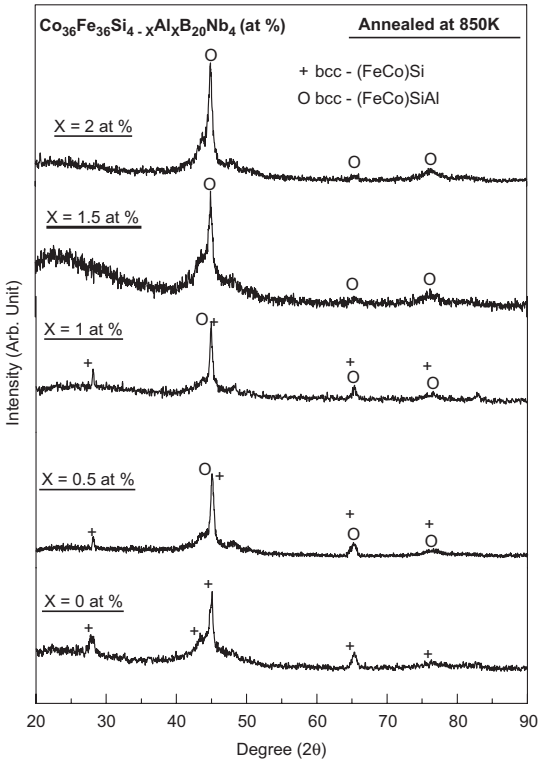

Fig. 4. XRD plots of $Co_{36}Fe_{36}Si_{4-x}Al_xB_{20}Nb_4$, X=0, 0.5, 1.0, 1.5, 2.0 at% alloys annealed at 850 K.

Microstructural evolutions were observed using transmission electron microscopy (Philips, CM-200). Magnetic coercivity was measured at a dc magnetizing frequency of 50 mHz. For determining the stability of ferromagnetic ordering, Curie temperature was observed using a vibrating sample magnetometer (LakeShore VSM Model: 7404). The ac coercivity and core loss were measured using an ac hysteresis loop tracer (Walker, Model: 401 AMH).

3. Results

3.1. Phase transformation

The broad maxima observed in the X-ray diffraction pattern (Fig. 1) showed the amorphous nature of the as-spun ribbons with Al content of $X=0$ and 1 as a representative plots. As observed in these plots, all the other alloys also displayed similar type of peak broadening indicating amorphous nature of the as-cast ribbons. These alloys on thermal scanning up to 900 K at 20 K/min revealed exothermic transformation peaks as shown in the differential scanning calorimetric (DSC) plots of Fig. 2. The peaks were broad indicating an onset of nanocrystallisation at T_{X1} [7] which increased up to $X=1$ and then displayed a decreasing trend when aluminium content was $X>1$ as shown in Fig. 3. The activation energy (E_{X1}) for the primary transformation was calculated using the modified Kissinger's equation [8].

$$\ln(T_p^2/S) = (E_{act}/RT_p) + \ln(E_{act}/RK_o) \quad (1)$$

where T_p is the peak temperature of the exothermic process completion, E_{act} the effective activation energy for the process associated with the peak, S the rate of thermal scanning, R the gas constant and K_o the pre-exponential factor in the arrhenius equation for the rate constant K. The variation of E_{X1} followed similar trend as T_{X1} with Al incorporation. Below the primary crystallization the DSC plots also indicated a glass transition temperature at 'T_g' with a distinct endothermic onset (inset of Fig. 2) as an exemplary for the alloy with $X=0$. The 'T_g' was found to follow a decreasing trend with increase in Al content. Evolution of phases around onset of crystallization was observed using X-ray analysis of samples annealed at 850 K and shown in Fig. 4. The diffractograms showed the formation of bcc-(CoFe)Si nanophase formation in the alloys with a predominant Si content [9]. However, as the Al content increased, the alloys showed the formation of bcc-(CoFe)SiAl nanophase. This suggested the dissolution of Al into the generated bcc-(CoFe)Si phase with increased Al content.

3.2. Soft magnetic properties

The variation of coercivity of the alloys with annealing temperature is shown in Fig. 5. All the alloys exhibited consistent coercivity values up to 850 K beyond which there was rapid degradation. A guide to minimum coercivity before this deterioration was indicated with an extended arrow of range 18 A/m and shown in rescaled Fig. 6. This guide revealed that in Al devoid ($X=0$) or 50%Al substituted ($X=2$) containing alloys, the minimal coercivity values were much higher than the alloys with intermediate Al concentration ($0.5 \le X \le 1.5$). The consistent

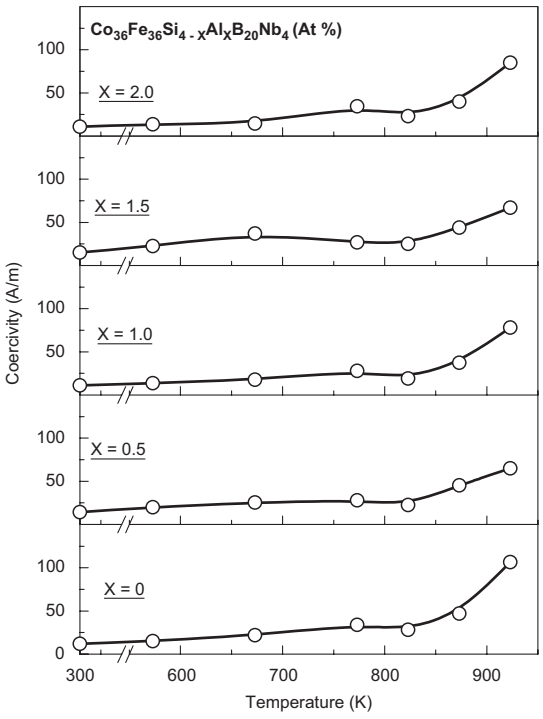

Fig. 5. Variation of coercivity with annealing temperature of $Co_{36}Fe_{36}Si_{4-x}Al_xB_{20}Nb_4$ ($X=0$, 0.5, 1.0, 1.5, 2.0 at%) alloys.

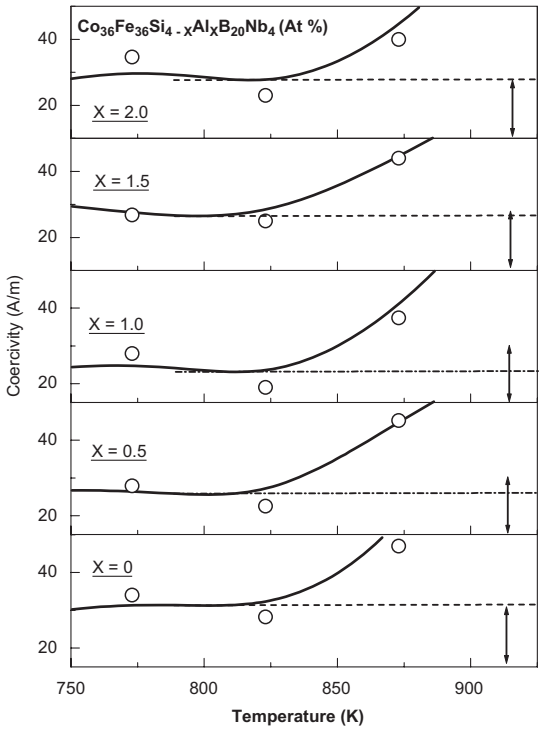

Fig. 6. Optimal values of coercivity variation with annealing temperature in $Co_{36}Fe_{36}Si_{4-x}Al_xB_{20}Nb_4$, ($X=0$, 0.5, 1.0, 1.5, 2.0 at%) alloys. Extended arrow indicates minimal coercivity observed.

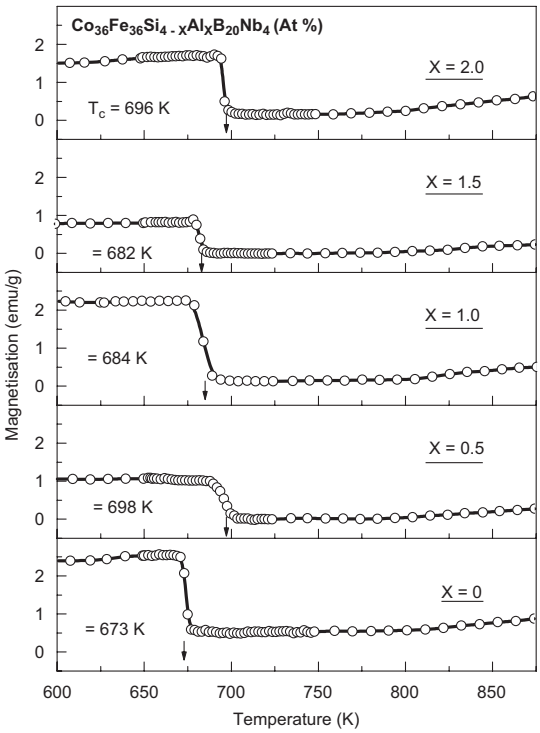

Fig. 7. Temperature dependence magnetization curve of as-spun $Co_{36}Fe_{36}Si_{4-x}Al_xB_{20}Nb_4$ (X=0, 0.5, 1.0, 1.5, 2.0 at%) alloys.

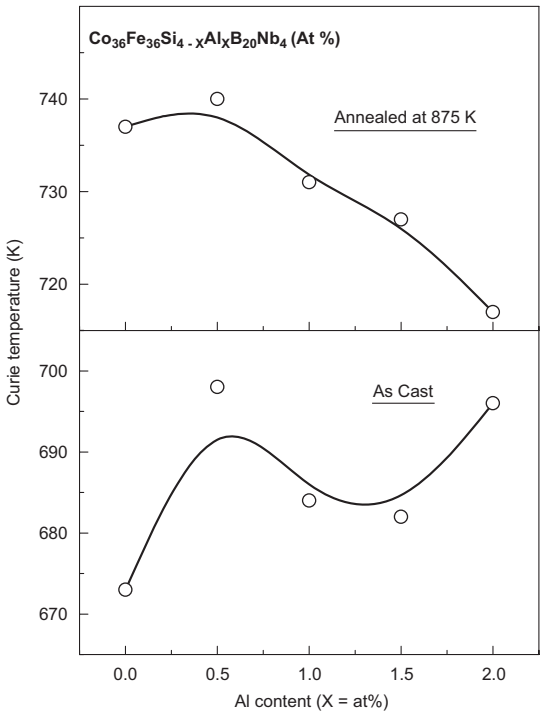

Fig. 8. Variation of Curie temperatures with Al content of as-spun as well as annealed at 875 K for 15 min.

coercivity prior to degradation was observed in alloy with aluminium content of X=1.

Thermal variation of magnetization of as-cast alloys is shown in Fig. 7. The initial drop in magnetization indicated transition of ferromagnetic to paramagnetic state i.e. the Curie temperature 'T_C'. The trend in 'T_C' of the as-cast ribbon with Al content shown in Fig. 8 indicated non-linear variations. However, after annealing at 875 K, 'T_C' showed a decreasing trend with increasing Al content though the drop was only by 25 K with up to 50%Al (X=2). This indicated that the nanophase has higher Curie temperature towards lower Al concentration.

3.3. Results and discussion

Detailed analysis of the effect of Al on the extent of magnetic degradation showed is shown in Fig. 9. In the as-cast state, the coercivity varied non-linearly thereby exhibiting the competing role of Al and Si in the amorphous structure. On annealing at 875 K which is past the onset of crystallizations, the alloys with X=0 and 2 showed much rapid degradation in coercivity compared to those with intermediate Al content. At elevated annealing temperature of 925 K, this deterioration further increased. However it is interesting to observe that at higher temperatures the coercivity variation revealed a shallow profile with a minima around aluminium content of X=1. This enhancement in properties may be attributed to some sort of Al dissolution into a bcc-(CoFe)SiAl during the process of nanophase generation. Such effect of Al dissolution into bcc-(CoFe)Si nanophase was also observed from the X-ray diffractogram peak shift. In the alloys with X=0 the high Si content led to peak shift towards higher diffracting angle as shown in Fig. 10. This was attributed to lattice shrinkage due to Si going into solid solution of bcc-(CoFe) to form the nanostructured silicide phase around T_{X1} [10]. With subsequent replacement of Si by Al, the lattice shrinkage effect was counteracted by lattice expansion [11] and consequent peak shift towards low angle. The variation of lattice parameter as derived from the primary peak of XRD plots of sample annealed at 850 K with Al addition is shown in Fig. 11. Al substitution up to 25% (X=1) showed rapid increase in lattice parameter (inset of Fig. 11) beyond which this rise had a tendency to reach a limiting value. The limiting tendency at an approach of 50%Al may be attributed to a competing role of Si and Al towards lattice shrinkage and expansion respectively.

Al substitution for Si has been found to alter T_X and T_g indicating its influence on the amorphous structure. Scattering factor was determined from X-ray diffraction major peak of alloys annealed at 850 K. The replacement of Si by Al led to a decrease in scattering factor as shown in Fig. 12. The scattering factor was determined [12] from the primary peak using the equation

$$K = 4\pi \sin\Theta/\lambda \quad (2)$$

where Θ is the diffracting angle of the major primary peak obtained from X-ray diffractograms, and λ the wavelength of the CuKα radiation. This decreased scattering constant 'k_p' is due to an increase in Fe–Fe, Fe–Co and Co–Co atomic pair distance for the addition of larger element Al [13]. The increase in atomic spacing with Al incorporation leads to an increase in the vacant regions for

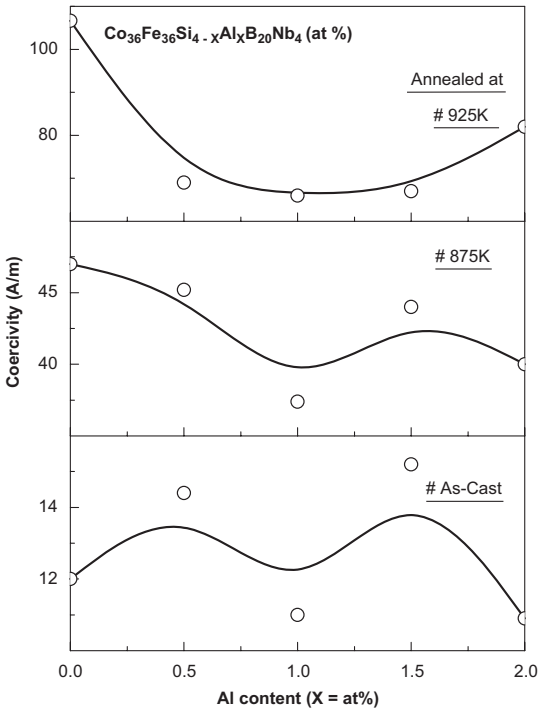

Fig. 9. Variation of coercivity with aluminium content of as-cast and annealed $Co_{36}Fe_{36}Si_{4-x}Al_xB_{20}Nb_4$ (X=0, 0.5, 1.0, 1.5, 2.0 at%) alloys.

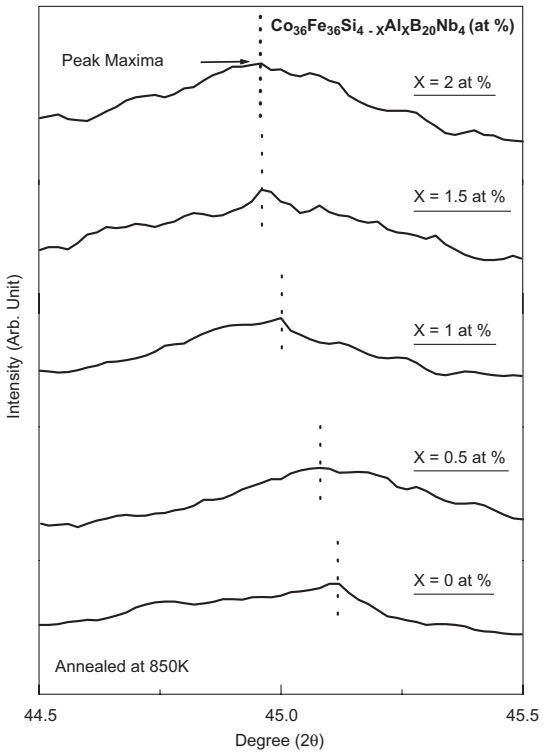

Fig. 10. Shift in the primary peak shift of XRD plots of $Co_{36}Fe_{36}Si_{4-x}Al_xB_{20}Nb_4$ (X=0, 0.5, 1.0, 1.5, 2.0 at%) alloys annealed at 850 K. Plots are shown for the small span of 2° about primary peak.

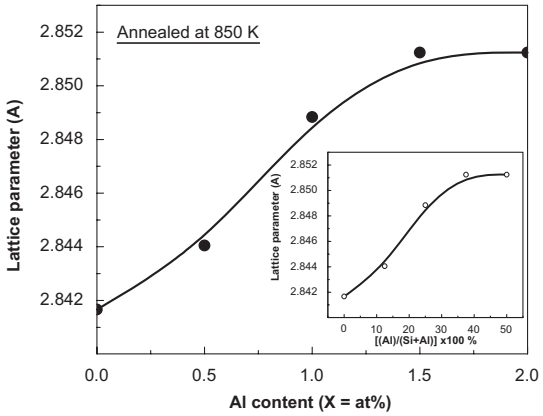

Fig. 11. Variation of lattice parameter obtained from major peak of X-ray diffractograms of $Co_{36}Fe_{36}Si_{4-x}Al_xB_{20}Nb_4$ (X=0, 0.5, 1.0, 1.5, 2.0 at%) alloys annealed at 850 K. Inset shows lattice parameter versus Al(Si+Al)%.

enhanced dissolution of the metalloid required for the amorphous structure. However, the relative reduction in metalloid Si content with Al addition beyond X=1 did not contribute much towards the amorphous stabilization and as a result the glass transition temperature 'T_g' and the corresponding super cooled region [14] was affected. The extent of super cooled region, ΔT_X obtained as ($T_X - T_g$) and shown in Fig. 12 suggests that such an effect on amorphous phase stability is observed with Al substitution up to 25% (X=1). ΔT_X increased continuously up to X=1 beyond which there was a decreasing trend with Al content. Beyond this Al content, the scattering factor also tended to reach a limiting trend. The effect of Al addition was also observed in inducing enhanced amorphous stability as observed from microstructural evaluations. The as-cast alloy without Al (X=0) revealed amorphous microstructure with a diffused halo in selected area diffraction (SAD) pattern as shown in the transmission electron micrograph of Fig. 13a. This alloy when annealed at 875 K revealed much higher nanoparticles size ~15 nm (Fig. 13b) compared to the 6 nm sized particles (Fig. 13c) observed for X=1 alloy. The aluminium containing alloy revealed nanoparticle size ~15 nm after annealing at much higher temperature of 925 K which is comparable to that of X=0 annealed at 875 K (Fig. 13d).

The substitution of Al for Si has also been known to favorably enhance the magnetic moment of system as the element Al having one less P-electron than Si atom, promotes smaller charge transfer from Al to Fe atoms thereby raising the magnetization [15]. This was observed from higher level of magnetization in alloy with X=1 compared to X=0 for samples annealed at 875 K as observed from thermal variation of magnetization in Fig. 14. This may be attributed the process of nanocrystallisation whereby the partitioning of Al along with reduced fraction of Si in X=1 formed (CoFe)SiAl nanophase with enhanced magnetic moment. This plot which also revealed the thermal variation of ferromagnetic ordering also revealed that in X=1 alloy, the

drastic fall in magnetization was subsequently followed by rise in moment around 800 K whereas the alloy without aluminium maintained a low moment range after the drop. This enhanced behaviour of ferromagnetic ordering in the former case was further manifested by a more stable ferromagnetic ordering (inset of Fig. 14) up to 1060 K in Al containing alloy (X=1) compared to reduction in magnetization around 950 K in X=0 alloy. The bcc-(CoFe)SiAl due to its enhanced magnetization is supposed to shift the exchange coupling of nanoparticles through paramagnetic amorphous matrix towards high temperature regions [16–18].

In high temperature applications the efficiency of soft magnetic components in transformers and rotor assemblies depend on the frequency response of coercivity and core loss [19]. As seen in Figs. 15 and 16, the as-cast alloy with aluminium content of X=1 revealed lower values of coercivity and core loss respectively than the alloy without Al (X=0). In the as-cast state, both the alloys revealed a consistent difference in their properties (coercivity, core loss) throughout the evaluated span of frequencies. This behaviour suggests that Al incorporation enhanced the as-cast disordered structure for lower coercivity and higher resistivity for low eddy current loss leading to reduction in core loss. However, in the nanocrystalline state through annealing at 875 K, the alloy with X=1 revealed distinct divergence from X=0 for coercivity and core loss at higher frequencies. This behaviour may attributed to the reduction in anisotropy with Al incorporation into (CoFe)SiAl nanophase. Additionally, the lower particle size ~6 nm in the former alloy compared to 15 nm for X=0 attributed towards greater electron scattering (higher resistivity) for lower core losses at higher frequencies.

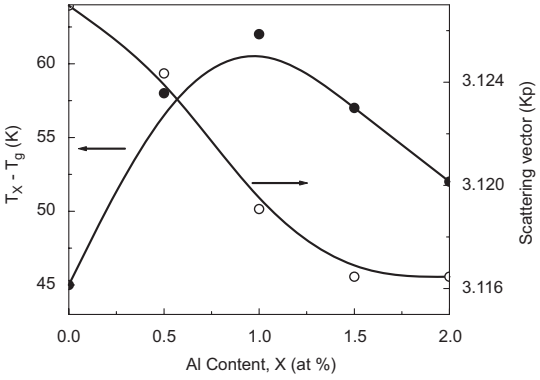

Fig. 12. Variation undercooling ($T_X - T_g$) and the magnitude of the scattering vector of 850 K annealed $Co_{36}Fe_{36}Si_{4-x}Al_xB_{20}Nb_4$ (X=0, 0.5, 1.0, 1.5, 2.0 at%) alloys.

4. Conclusion

The $Co_{36}Fe_{36}Si_{4-x}Al_xB_{20}Nb_4$, ($X$=0, 0.5, 1.0, 1.5, 2.0 at%) alloys were prepared in the form of amorphous ribbons by the melt

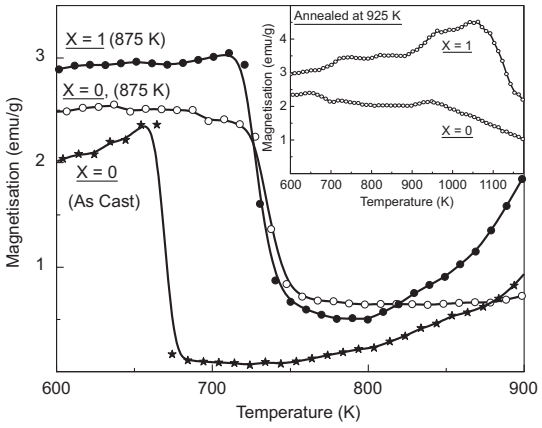

Fig. 14. Effect of annealing temperature on thermal variation of magnetization in $Co_{36}Fe_{36}Si_{4-x}Al_xB_{20}Nb_4$ (X=0, 1 at%) alloys. Inset shows the profile for X=0 and X=1 alloys annealed at 925 K.

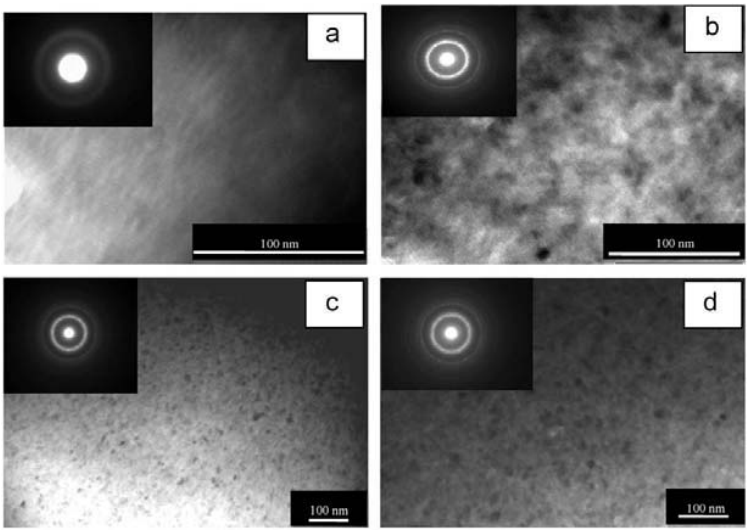

Fig. 13. TEM micrograph of with as-cast (a) X=0 and annealed (b) X=0 at 875 K, (c) X=1 at 875 K and (d) X=1 at 925 K. SAD in the inset.

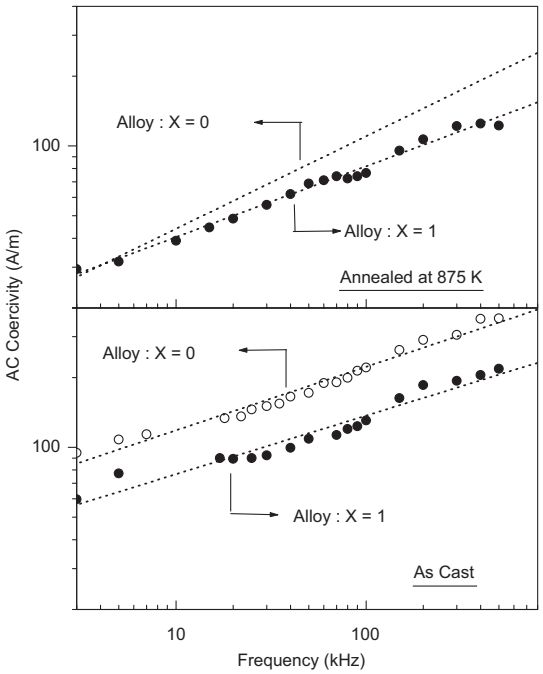

Fig. 15. AC Coercivity for as-spun and annealed at 875 K for $X=0$ and $X=1$ of $Co_{36}Fe_{36}Si_3Al_1B_{20}Nb_4$ alloys.

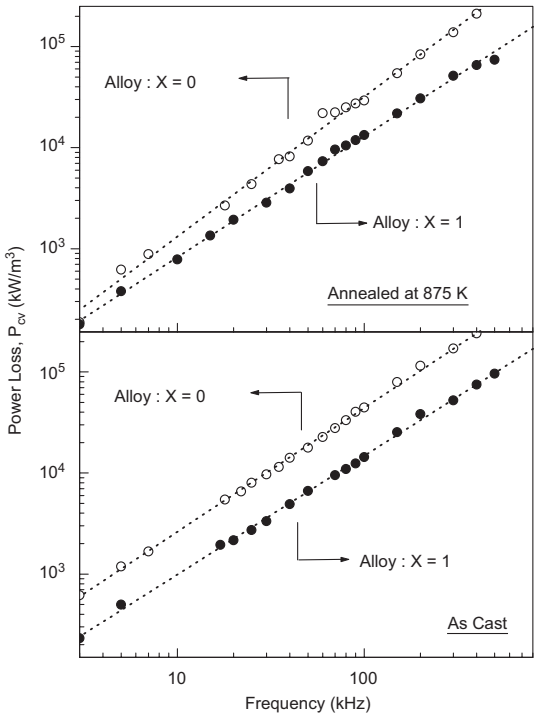

Fig. 16. AC Power loss for as-spun and annealed at 875 K for $X=0$ and $X=1$ of $Co_{36}Fe_{36}Si_3Al_1B_{20}Nb_4$ alloys.

spinning technique. The onset of crystallization temperature increased with Al content up to ($X \leq 1$), whereas at higher Al there was a decreasing trend. The glass transition temperature (T_g) reduced with increasing Al content. Compared to all the other compositions, the alloy with optimum Al content of $X=1$ exhibited stable coercivity values at high temperature. This may be attributed to reduction of magnetostriction with Al incorporation and at the same time smaller nanoparticles bcc-(CoFe)SiAl to induce effective averaging of anisotropy. In the nanostructured state when annealed at 925 K, the alloy without Al ($X=0$) showed reduction in ferromagnetic ordering above 950 K. However, the Al containing alloy with $X=1$ exhibited stable ferromagnetic ordering up to 1050 K i.e. additionally by 100 K. This optimal Al containing alloy also revealed better frequency response of coercivity and low core losses compared to the alloy without Al ($X=0$).

Acknowledgements

The authors express their sincere gratitude to Director, National Metallurgical Laboratory, Jamshedpur, India for kindly giving permission to publish the work. One of the authors (Ojaswini Mohanta) gratefully acknowledges financial support from CSIR, India.

References

[1] Y. Yoshizawa, S. Oguma, K. Yamauchi, J. Appl. Phys. 64 (1988) 6044.
[2] M.E. McHenry, M.A. Willard, D.E. Laughlin, Prog. Mater. Sci. 44 (1999) 291.
[3] C. Gomez-Polo, et al., Phys. Rev. B 66 (2002) 012401.
[4] G. Herzer, IEEE Trans. Magn. 26 (1990) 1397.
[5] R. Boll, In: K.H.J. Buschow (Ed.), Electronic and Magnetic Properties of Metals and Ceramics, in: Materials Science and Technology, vol. 3B, Part II, VCH pub., p. 446.
[6] R.T. Fingers, C. Scott Rubertus, IEEE Trans. Magn. 36 (2000) 3373.
[7] C.F. Conde, A. Conde, Mater. Sci. Forum 179 (1995) 587.
[8] E.J. Mittemeijer, L. Chang, P.J. Van Der Schaaf, et al., Metall. Trans. A 19 (1988) 925.
[9] C. Gomez-Polo, et al., Phys. Rev. B 65 (2002) 024433.
[10] M. Muller, N. Mattern, L. Illgen, Z. Metallk. 82 (1991) 895.
[11] E. Apinaniz, E. Legarra, F. Plazaola, J.J.S. Garitaonandia, J. Magn. Magn. Mater. 320 (2007) e692.
[12] B.D. Cullity, Elements of X-ray diffraction, Addison–Wesley publ.co, Massachusetts.
[13] A. Inoue, H. Yamamoto, T. Masumoto, Mater. Trans., JIM 31 (1990) 1021.
[14] A. Inoue, Mater. Trans. JIM 36 (1995) 866.
[15] E. Apinaniz, E. Legarra, F. Plazaola, J.J.S. Garitaonandia, J. Magn. Magn. Mater. 316 (2007) e470.
[16] A. Hernando, et al., Phys. Rev. B 51 (1995) 3281.
[17] A. Hernando, T. Kulik, Phys. Rev. B 49 (1994) 7064.
[18] A. Slawska-Wanieska, et al., Phys. Rev. B 50 (1994) 6465.
[19] M.E. Mc. Henry, D.E. Laughlin, Acta Mater. 48 (2000) 223.